SWOT: The Surface Water and Ocean Topography Mission

Wide-Swath Altimetric Measurement of Water Elevation on Earth

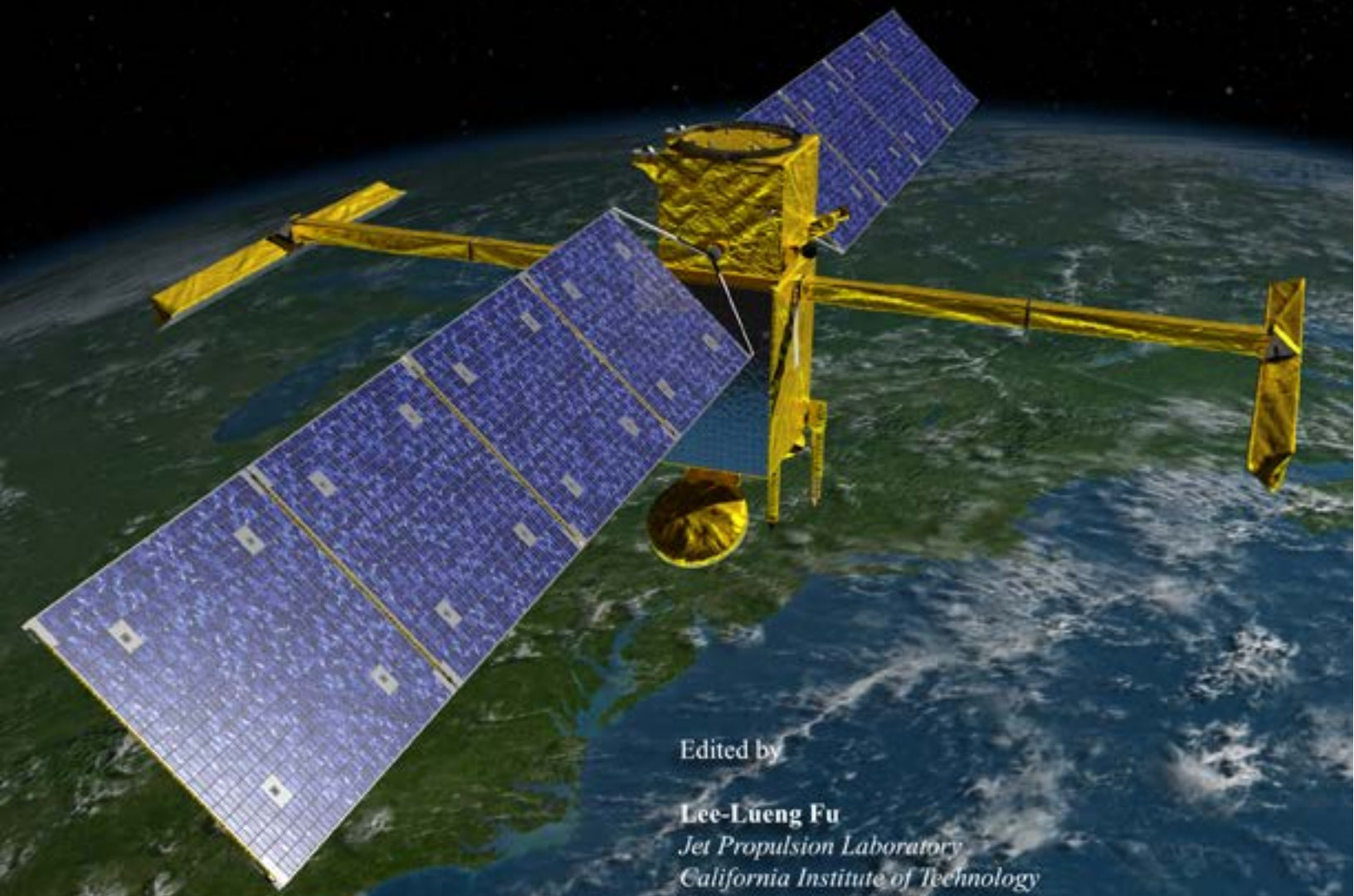

Edited by

Lee-Lueng Fu
Jet Propulsion Laboratory
California Institute of Technology

Douglas Alsdorf
Ohio State University

Rosemary Morrow
Laboratoire d'Etudes en Géophysique
et Océanographie Spatiales (LEGOS)
Centre National d'Etudes Spatiales

Ernesto Rodriguez
Jet Propulsion Laboratory
California Institute of Technology

Table of Contents

Acknowledgments 3
Contributors of Science Articles 4
Preface 5
Abstract 6
1 Introduction 7
2 Scientific Objectives 10
3 Oceanic Mesoscale and Submesoscale Processes 11
3.1 Eddies, Fronts, and Filaments 18
3.2 Three-dimensional Upper Ocean Circulation 32
3.3 Eddy-mean Flow Interaction 36
3.4 Cascade and Dissipation of Oceanic Kinetic Energy 40
3.5 Biogeochemical Processes 44
3.6 Coastal Processes 49
4 Terrestrial Hydrology: Storage and Discharge of Water on Land 54
4.1 The Global Water Cycle 64
4.2 Lake Storage 68
4.3 Reservoirs, Transboundary Issues, and Human Impacts 76
4.4 Floodplain and Wetland Processes 82
4.5 Arctic Hydrology 89
4.6 Floods and Flood Modeling 95
5 Additional Objectives 105
5.1 Ocean Tides 106
5.2 Ocean Bathymetry 113
5.3 Ice Sheets 119
5.4 Sea Ice 125
5.5 Tropical Cyclone Intensification Studies and Forecasts 129
5.6 Sea-Level Change 134
6 Measurement of water elevation 142
6.1 Radar Interferometry 143
6.2 Media Effects 148
6.3 Ocean Tides 155
6.4 Ocean Waves 157
6.5 Layover and Vegetation Effects 159
6.6 Waterbody Delineation 169
7 The SWOT Mission 177
7.1 Orbit and Sampling Issues 178
7.2 Precise Orbit Determination 185
7.3 Science Payload 190
7.4 Mission Operation and Data Products 192
7.5 Calibration and Validation 206
8 Acronyms and Abbreviations 219

ACKNOWLEDGMENTS

This work was carried out in part at the Jet Propulsion Laboratory, California Institute of Technology, under a contract with the National Aeronautics and Space Administration. A significant portion of the document, Sections 3 through 5, is contributed by the science community with interests in the development of the SWOT Mission. The authorship of these science sections is provided on the next page. The rest of the documents draws contributions of the following individuals in addition to the editors: Shannon Brown (JPL), Brian Arbic (University of Michigan), Richard Ray (Goddard Space Flight Center), Roger Fjortoft (CNES), Steve Nerem (University of Colorado), Shailen Desai (JPL), Bruce Haines (JPL), and Phil Callahan (JPL).

CONTRIBUTORS OF SCIENCE ARTICLES

Contributor		Section	Affiliation
Waleed	Abdalati	5.3	University of Colorado
Douglas	Alsdorf	4.4; 4.6	Ohio State University
Kostas	Andreadis	4.4; 4.6	Jet Propulsion Laboratory
Brian	Arbic	5.1	University of Michigan
Paul	Bates	4.4; 4.6	University of Bristol
Sylvain	Biancamaria	4.4; 4.6	LEGOS
Aaron	Boone	4.1	Météo-France
Anny	Cazenave	5.6	LEGOS
Dudley	Chelton	3.1	Oregon State University
Jean-Francois	Cretaux	4.2	LEGOS
Francesco	d'Ovidio	3.5	University of Paris
Michael	Durand	4.3; 4.4; 4.6	Ohio State University
Gustavo	Goni	5.5	NOAA
Faisal	Hossain	4.3	Tennessee Technological University
Patrice	Klein	3.2	LPO/DOPS-IFREMER Brest
Chungyen	Kuo	5.6	National Cheng-Kung University
Ronald	Kwok	5.4	Jet Propulsion Laboratory
Guillaume	Lapeyre	3.2	ENS-IPSL Paris
Hyongki	Lee	4.3	Ohio State University
John	Lenters	4.2	University of Nebraska-Lincoln
Marina	Lévy	3.5	University of Paris
James	McWilliams	3.4	University of California, Los Angeles
Rosemary	Morrow	3.1	LEGOS
Steve	Nerem	5.6	University of Colorado
Josefina	Olascoaga	5.5	University of Miami
Tamlin	Palvesky	4.5	University of North Carolina
Bo	Qiu	3.3	University of Hawaii
Richard	Ray	5.1	Goddard Space Flight Center
David	Sandwell	5.2	Scripps Insitution of Oceanography
Yongwei	Sheng	4.2	Unversity of California, Los Angeles
CK	Shum	5.6	Ohio State University
Ted	Strub	3.6	Oregon State University

PREFACE

In January 2007, the National Research Council released the first decadal survey of Earth science, *Earth Science and Applications from Space: National Imperatives for the Next Decade and Beyond*. The study was sponsored by the National Aeronautics and Space Administration (NASA), the National Oceanic and Atmospheric Administration (NOAA), and the U. S. Geological Survey (USGS) in order to develop community consensus in providing recommendations to guide the agencies' space-based Earth observation programs in the coming decade. The report recommended a set of 17 missions in three time phases (called tiers) to achieve the needed observations while providing for both scientific advance and societal benefit. Among the recommended tier-two missions is the Surface Water and Ocean Topography (SWOT) mission. After the release of the decadal survey, NASA and Centre National d'Etudes Spatiales (CNES) jointly developed SWOT as a collaborative mission.

In October 2007, a SWOT Science Working Group (SWG) was formed under the auspices of NASA and CNES with participants from international communities of oceanography and land surface hydrology. The SWG was charged to provide scientific guidance for the development of the mission, including science objectives and requirements, science payload, orbit selection, and data products. Since the inaugural meeting in October 2007, the SWG has met eight times. Additionally, a town hall meeting on SWOT was held in the 2008 American Geophysical Union (AGU) Fall Meeting. This document summarizes the findings from these meetings with a purpose to provide information on the potential opportunities in science investigation and applications as well as on the preliminary design of the SWOT mission.

ABSTRACT

The elevation of the surface of the ocean and freshwater bodies on land holds key information on many important processes of the Earth System. The elevation of the ocean surface, called ocean surface topography, has been measured by conventional nadir-looking radar altimeter for the past two decades. The data collected have been used for the study of large-scale circulation and sea level change. However, the spatial resolution of the observations has limited the study to scales larger than about 200 km, leaving the smaller scales containing substantial kinetic energy of ocean circulation that is responsible for the flux of heat, dissolved gas and nutrients between the upper and the deep ocean. This flux is important to the understanding of the ocean's role in regulating future climate change.

The elevation of the water bodies on land is a key parameter required for the computation of storage and discharge of freshwater in rivers, lakes, and wetlands. Globally, the spatial and temporal variability of water storage and discharge is poorly known due to the lack of well-sampled observations. In situ networks measuring river flows are declining worldwide due to economic and political reasons. Conventional altimeter observations suffers from the complexity of multiple peaks caused by the reflections from water, vegetation canopy and rough topography, resulting in much less valid data over land than over the ocean. Another major limitation is the large inter track distance preventing good coverage of rivers and other water bodies.

This document provides descriptions of a new measurement technique using radar interferometry to obtain wide-swath measurement of water elevation at high resolution over both the ocean and land. Making this type of measurement, which addresses the shortcomings of conventional altimetry in both oceanographic and hydrologic applications, is the objective of a mission called Surface Water and Ocean Topography (SWOT), which was recommended by the National Research Council's first decadal survey of NASA's Earth science program. This document provides wide-ranging examples of research opportunities in oceanography and land hydrology that would be enabled by the new type of measurement. Additional applications in many other branches of Earth System science ranging from ocean bathymetry to sea ice dynamics are also discussed. Many of the technical issues in making the measurement are discussed as well. Also presented is a preliminary design of the SWOT Mission, which is being jointly developed by NASA and CNES, with contributions from the Canadian Space Agency.

1 INTRODUCTION

Satellite radar altimetry has revolutionized oceanography by providing, since 1993, global measurements of ocean surface topography (e.g., Fu and Cazenave, 2001). The long-term observations of large-scale circulation and heat storage of the global oceans have led to significant advances in our understanding of the interaction of ocean circulation with climate (e.g., El Niño and La Niña). Radar altimetry has also provided high-precision sea-level measurements with global coverage (e.g, Nerem et al., 2010). Coupled with space gravity measurement and in situ observations, satellite altimetry observations were analyzed to separate natural climate variability effects from human-induced changes in sea level, identify most vulnerable coastal areas, and improve climate models used for sea-level projections. Since the late 1990s, radar altimetry has also been used to measure surface water levels on land (i.e., lakes, rivers, and floodplains), extending its applications to land hydrology (e.g., Cazenave et al., 2004, Alsdorf et al., 2006, 2007). However, a critical limitation for both ocean dynamics and land hydrology, is the 200- to 300-km spacing between satellite orbital tracks. This track separation precludes the sampling of small-scale features in oceanography (e.g., currents and oceanic mesoscale processes) and a large number of surface water bodies on land (lakes, reservoirs, wetlands, and rivers).

In physical oceanography, several issues cannot be addressed from the currently available radar altimetry measurements. First, the strongest currents of the ocean (e.g., Gulf Stream, Kuroshio Current, Antarctic Circumpolar Current) have spatial scales less than 100 km in the cross-stream direction. These currents and their meanders and eddies carry most of the kinetic energy of the ocean. The present generation of satellite altimeters can resolve only the eddy energy at scales larger than 100 km. With the information at smaller scales missing, questions are left open regarding the effects of ocean currents and eddies on global climate. Second, the stirring and mixing of ocean properties at scales of 10–100 km are presently not sampled globally, but they are an important process in the lateral transport of mass, heat, salt and nutrients in the ocean. Third, substantial vertical transfers of the ocean properties mentioned above also take place at these scales. This vertical exchange is an important process in many parts of the global oceans. In the coastal oceans, upwelling and cross-shelf circulation have a strong effect on marine life, ecosystems, and waste disposal. In the open ocean, it is estimated that about 50% of the vertical transfer of nutrients in the ocean takes place at the submesoscales of 10–100 km (Lapeyre and Klein, 2006). This is of critical importance for understanding the role of the oceanic circulation and ecosystems in a changing climate.

In contrast to ocean observations, land surface water measurements are limited mostly to in situ networks of gauges that record water surface elevations at fixed points along river channels. Globally, the spatial and temporal distribution of water stored on land surface and moving through river channels is poorly known. Furthermore, water

movement in wetlands and across floodplains throughout the world is essentially unmeasured, significantly limiting our understanding of flood processes. In situ networks measuring river flows are declining worldwide due to economic and political reasons, affecting not only developing countries but also developed countries. While radar altimetry over surface waters has demonstrated the potential of this technique in land hydrology, a number of limitations exist because altimetry has been optimized for observing the ocean surface. Raw radar altimetry echoes reflected from the land surface are complex, with multiple peaks caused by the multiple reflections from water, vegetation canopy and rough topography, resulting in much fewer valid data over land than over the ocean. Another major limitation is the large inter-track distance, which prevents good coverage of rivers and other water bodies.

To address these important issues in physical oceanography and land surface hydrology, high-resolution satellite measurements of the ocean surface topography and the elevation of water on land are urgently needed. Based on the heritage of the Shuttle Radar Topography Mission (SRTM), scientific and technical studies at the Jet Propulsion Laboratory (JPL) over the past 10 years have refined the wide-swath interferometric altimetry concept for high-resolution mapping of the ocean surface topography (Fu and Rodriguez, 2004). An instrument system called the Wide-Swath Ocean Altimeter (WSOA) was developed and prototyped for implementation on the Ocean Surface Topography Mission/Jason-2. Unfortunately, the implementation of WSOA was canceled due to lack of funding. More recently, the potential of this technique has been demonstrated for mapping terrestrial surface waters (e.g., LeFavour and Alsdorf, 2005; Kiel et al., 2006; Alsdorf et al., 2007).

In the U.S., two separate proposals—one for hydrology, one for oceanography—based on this concept were submitted in 2006 to the Decadal Survey conducted by the National Research Council (the National Academies, USA). In Europe (jointly with U.S. scientists), studies were conducted during the past 2–3 years to define a wide-swath altimetry mission for land hydrology. In response to the recommendation by the Decadal Survey, the physical oceanography and the land surface hydrology communities have now joined together in developing a new mission named SWOT (Surface Water and Ocean Topography) based on the concept of wide-swath interferometric altimetry for high-resolution mapping of the elevation of water on Earth. SWOT measurements will address two key aspects on the problem of climate change: the role of the oceanic mesoscale and submesoscale processes in regulating climate change and the consequence of climate change on the distribution of water on land.

This document provides an overall description of the science objectives and anticipated advances for the SWOT mission and the measurement approach and requirements, as well as mission design issues in relation to the science requirements. The document will serve as the basis for the mission's science requirements and mission design trade-offs.

References

Alsdorf, D.E., E. Rodriguez, and D. Lettenmaier, 2007: Measuring surface water from space. Reviews of Geophysics, **45**(2), RG2002 doi:10.1029/2006RG000197.

Cazenave, A., P. C. D. Milly, H. Douville, J. Benveniste, P. Kosuth, and D. Lettenmaier, 2004: Space techniques used to measure change in terrestrial waters. Eos Trans. AGU, **85**(6), 59.

Fu, L.-L., and A. Cazenave, editors, 2001: Satellite Altimetry and Earth Sciences: A Handbook of Techniques and Applications. Academic Press, San Diego, 463 pp.

Fu, L.-L., and R. Rodriguez, 2004: High-resolution measurement of ocean surface topography by radar interferometry for oceanographic and geophysical applications. AGU Geophysical Monograph 150, IUGG Vol. 19: State of the Planet: Frontiers and Challenges, 209–224. Eds. R.S.J. Sparks and C.J. Hawkesworth.

Kiel, B., D. Alsdorf, and G. LeFavour, 2006: Capability of SRTM C and X Band DEM data to measure water elevations in Ohio and the Amazon. Photogrammetric Engineering and Remote Sensing (SRTM Special Issue), **72**(3), 313–320.

Lapeyre, G, and P. Klein, 2006: Imapct of the small-scale elongated filaments on the oceanic vertical pump. J. Mar. Res., **64**, 835–851.

LeFavour, G., and D. Alsdorf, 2005: Water slope and discharge in the Amazon River estimated using the Shuttle Radar Topography Mission digital elevation model. Geophysical Research Ltrs, **32**, L17404, doi:10.1029/2005GL023836.

National Research Council, 2007: Earth Science and Applications from Space: National Imperatives for the Next Decade and Beyond. National Academies Press.

Nerem, R.S., D.P. Chambers, C. Choe, and G.T. Mitchum, 2010: Estimating mean sea level change from the TOPEX and Jason altimeter missions. Marine Geodesy, **33**, 435–446, doi:10.1080/01490419.2010.491031.

2 SCIENTIFIC OBJECTIVES

There are two primary science rationales for the development of SWOT: (1) make high-resolution, wide-swath altimetric measurement of the ocean surface topography to make fundamental advances in the understanding of the oceanic mesoscale and submesoscale processes and (2) measure the elevation of water on land to make fundamental advances in the understanding of the spatial and temporal distribution of the storage and discharge of water on land. In addition to addressing the two primary objectives in oceanography and land hydrology, SWOT measurements will have applications to a host of other topics. These “additional objectives” are not considered main drivers for the mission, and significant resources will not be allocated to meet them. However, within the realm of mission design, and without incurring significant risk and cost, the best possible effort will be made to accommodate the additional objectives.

3 OCEANIC MESOSCALE AND SUBMESOSCALE PROCESSES

Ocean Surface Topography

The oceans distribute heat, salt, carbon, nutrients, and other chemicals around the world. The circulation of the ocean is, therefore, vital for understanding climate change as well as for understanding the ocean's role in the uptake of carbon, in the distribution of biomass, and other societal issues related to the oceans. Direct measurement of ocean current velocity is difficult owing to the turbulent nature of the flow. What is of interest for studying ocean circulation at scales larger than 10 km, however, is not the instantaneous velocity at every point of the ocean. Instead, a spatially and temporally averaged velocity field is required. Such smoothed flow has a special property called geostrophic balance; namely, the ocean velocity can be determined by the gradient of the pressure field at the ocean surface. This surface pressure field can be computed from the elevation of the ocean surface above the geoid, the ocean's equi-geopotential surface. The sea surface elevation relative to the geoid is called the ocean surface topography, which provides a very effective (if not the best) approach to computing the large-scale, low-frequency surface current velocity of the ocean. This geostrophic component of ocean circulation varies vertically in relation to the density distribution in the ocean. Therefore, ocean surface topography is an important dynamic boundary condition for determining the three-dimensional structure of ocean circulation.

Ocean surface topography is only a minor departure from the geoid, which has a range of about 200 m relative to a reference ellipsoid. Therefore, to first order sea surface elevation essentially represents the geoid. Alongtrack nadir altimetry observations have been instrumental in improving our understanding of the small-scale features of the marine geoid, and of the ocean bathymetry after inversion processes are made. However, many small-scale seamounts and bathymetric features between the groundtracks remain unobserved today. Defined as the departure from the geoid, the ocean surface topography varies by a range of about 3 m, and contains information about ocean currents. The measurement of the shape of sea surface thus has profound applications to oceanography, geodesy, and geodynamics.

The New Challenges for SWOT

The measurement of ocean surface topography by satellite radar altimeters since 1993 has made fundamental advances in our understanding of the large-scale ocean circulation and its role in climate change. However, as in the atmosphere, ocean circulation is dominated by turbulent eddies (Robinson, 1983). The most energetic ocean eddies have scales of ~100 km, the mesoscale, which is about 10 times less than the scale of atmospheric storms. Even with combined data from multiple altimeters, the ocean eddy field has not been well sampled by existing altimetry missions. Figure 3-1 shows the characteristics of spatial and temporal sampling by multiple conventional nadir

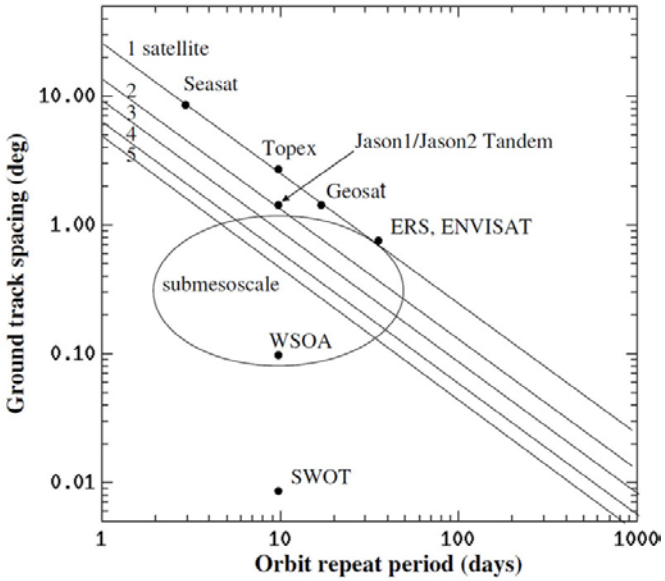

Figure 3-1. Sampling characteristics of satellite altimetry missions. The various straight lines represent the combination of different numbers of satellite altimeters. The ellipse is a schematic representation of the oceanic submesoscales.

altimeters in comparison to that by WSOA and SWOT.

Based on the observations from the TOPEX/Poseidon–Jason-1 tandem mission, which provided only suboptimal sampling of the eddy field, Sharffenberg and Stammer (2009) reported that the eddy kinetic energy overwhelmingly dominated the total kinetic energy of ocean circulation (Figure 3-2). Note that the eddy energy has been underestimated from this data set. Ocean model simulations have suggested that only by including realistic eddies in the model can the simulated oceanic heat transport approach observations (Smith et al., 2000). We need observations that fully resolve ocean eddies to improve models for studying the effects of the ocean in climate change.

The sampling offered by SWOT down to 1-km scale is a significant improvement over the samplings provided by combinations of conventional altimeters, and will give us a unique opportunity to study oceanic variability from the mesoscale to the submesoscale. While conventional altimetry has addressed the large-scale ocean variability associated with the density and mass distribution of the ocean, SWOT will address the small-scale energetic processes responsible for the maintenance and dissipation of the energy of the

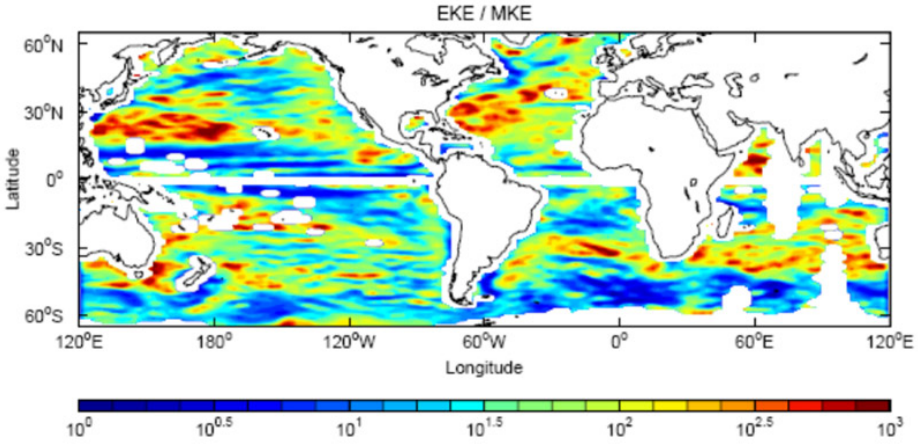

Figure 3-2. Ratio of eddy kinetic energy to the kinetic energy of the mean flow using surface velocities computed from the TOPEX/Poseidon and Jason interleaved mission (Sharffenberg and Stammer, 2009)

ocean circulation. Figure 3-3 illustrates the features of sea surface temperature and ocean color at the various scales observed by infrared and visible channel sensors. While these sensors provide information about the sea surface under clear sky conditions, SWOT will provide sea surface height (SSH) information that can be used to link surface observations to subsurface processes, even through clouds.

The Current State of Knowledge

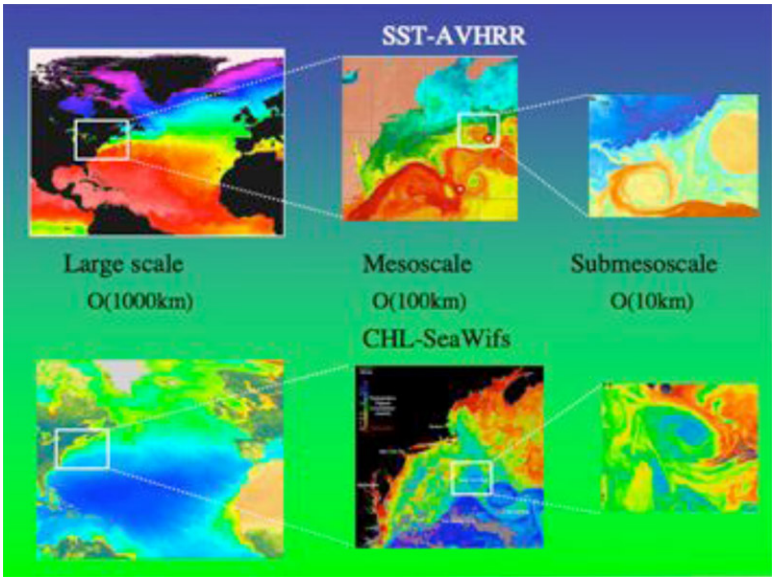

Figure 3-3. Sea surface temperature (upper row) and ocean color (lower row) images showing the progression of large-scale features to mesoscale and submesoscale features. (Courtesy of M. Levy of University of Paris.)

Observations made by satellite altimeters since 1980s have provided progressively improved views of the global ocean mesoscale eddy field (Le Traon and Morrow, 2001). Shown in Figure 3-4 is a snapshot of global SSH anomalies from combined data from Jason-1 and Jason-2, revealing the ubiquitous ocean eddies of scales larger than about 200 km. In parallel to these observations, ocean models have also progressed from coarse-resolution, highly dissipative mesh grids to higher resolutions where mesoscale eddies dominate the solutions. We are now able to produce simulations of the present state of the ocean which compare increasingly well to observations. Figure 3-5 displays a comparison of the standard deviation of ocean surface topography variability between altimetry observation and simulation by an eddy-permitting model at resolution of 18 km produced by the ECCO-2 Project, showing reasonable agreement. Figure 3-6 shows a snapshot of the speed of global ocean surface currents simulated by a model running at much higher resolution of 1/16° in latitude and longitude (~ 7 km at the equator and decreasing with latitude) as part of the ECCO-2 Project, showing the ubiquitous presence of mesoscale and submesoscale features—currents, eddies, fronts, and filaments. Most of the small eddies, fronts and filaments are not resolved by the available altimetry observations, nor by the majority of global ocean models today.

Indeed, the skill of the state-of-the-art models in making long range predictions of the ocean is still very limited, because they lack a physically-based representation of the submesoscales, i.e., scales of 10-100 km that are important for turbulent transport and energy dissipation. Ocean models running at sufficient resolutions (less than 1 km) to address submesoscale dynamics have just begun to emerge (e.g., Capet et al., 2008), but we need global observations at these scales to guide the model development.

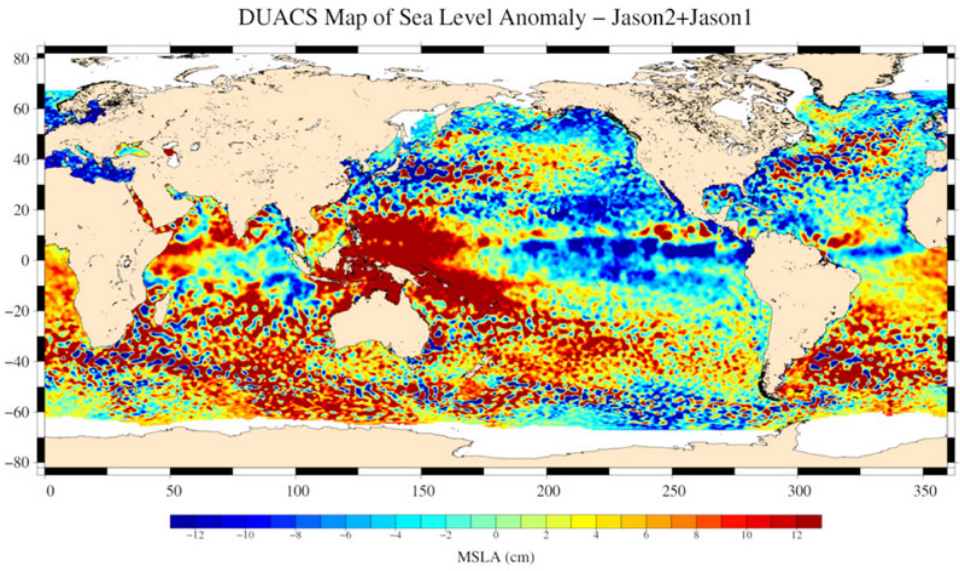

Figure 3-4. A snapshot of the sea surface height anomaly mapped by the Jason-1 and Jason-2 tandem mission (a 10-day composite) (Courtesy of G. Dibarboure.)

Conventional nadir-looking radar altimeters have a footprint on the order of 2–10 km. Even with thousands of pulses averaged over 1 second, the noise level of the sea surface height (SSH) measurement is substantial, making ocean SSH signals at wavelengths less than 100 km not well observed. A typical wavenumber spectrum of SSH deviations from a time mean, sampled along a long satellite pass (from the Jason-1 mission) from Bering Sea to Drake Passage in the Southern Ocean, is shown in Figure 3-7a (from Fu and Ferrari, 2008). At wavelengths longer than 100 km, the spectrum shows a typical "redness," with power density increasing with wavelength. The spectral slope levels off at wavelengths shorter that 100 km, showing the dominance of measurement and geophysical noise at the submesoscales. However, very high-resolution models that resolve the submesoscale (Capet et al., 2008) show a cascade of energy from the mesoscale to the submesoscale, such that the ocean spectra remains "red" down to kilometric wavelengths (Fig. 3-7b).

When the noisy measurements along nadir tracks are smoothed and merged to produce two-dimensional maps (e.g., Figure 3-4), the spatial resolution is on the order of 200 km even with combined data from two altimeters (Ducet et al., 2000). This resolution is not even sufficient to resolve the details of the two-dimensional structure of ocean currents like the Gulf Stream and Kuroshio, whose cross-current dimension is on the order of 100 km. Although combined data from TOPEX/Poseidon and European Remote Sensing satellite (ERS have been used extensively to study the characteristics of ocean eddies (e.g., Chelton et al, 2007), the size of the eddies has been limited to diameters larger than 100 km.

Mesoscale eddies larger than about 100 km are effective in transporting ocean properties (nutrients, heat, salt, carbon) horizontally in a systematic way in the upper ocean, as illustrated by Figure 3-8. The horizontal transport, diffusion, and mixing

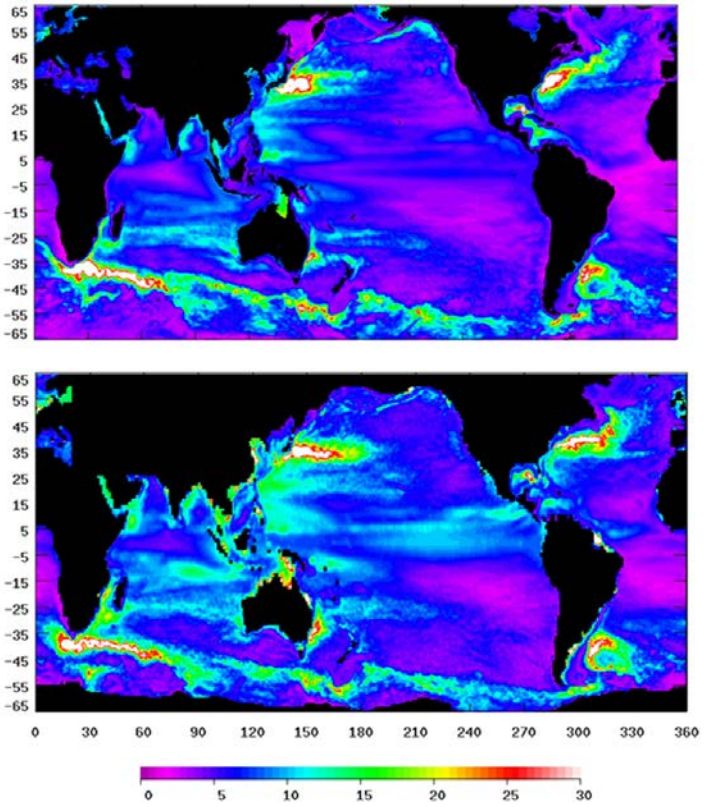

Figure 3-5. Standard deviation of sea surface height from ECCO-2 ocean general circulation model (18-km resolution) (Upper panel) and from Aviso altimetry observations (lower panel). The unit is in centimeters.

associated with the smaller mesoscale eddies (10–150 km) is not well observed or understood today. Ocean variability at the submesoscales in the form of fronts and filaments is most effective in vertical transport of ocean properties between the upper layers of the ocean and the deep ocean (Lapeyre and Klein, 2006). This vertical transport of ocean properties is important to understanding the ocean's role in climate change, in terms of the rate of oceanic uptake of heat and CO_2.

The vertical transport of nutrients is also important for the biogeochemical cycle of the ocean, which has important effects on climate.

The Breakthrough of SWOT

To make an order of magnitude advance in horizontal resolution and precision for resolving the submesoscales, the measurement noise must be reduced to less than the signal at a wavelength of 10 km, as shown by the horizontal dashed line in Figure 3-7, in which the SSH spectrum is extended from the power law to wavelengths of 10 km. The threshold of noise level corresponds to a power density of 1 cm/cycle/km, about two orders of magnitude less than that of the Jason-1 altimeter. This performance in SSH measurement translates to a geostrophic velocity error of 3 cm/s at 10 km scale at 45° latitude. The two-dimensional SSH maps from SWOT will then allow the study of the submesoscale ocean eddies, fronts, narrow currents, and even the vertical velocity at these scales. Described below are the science objectives enabled by SWOT for furthering our understanding of the oceanic mesoscale and submesoscale fields, including the physical processes in the open ocean as well as the coastal zones, the high-latitude oceans, and biogeochemical-physical interactions.

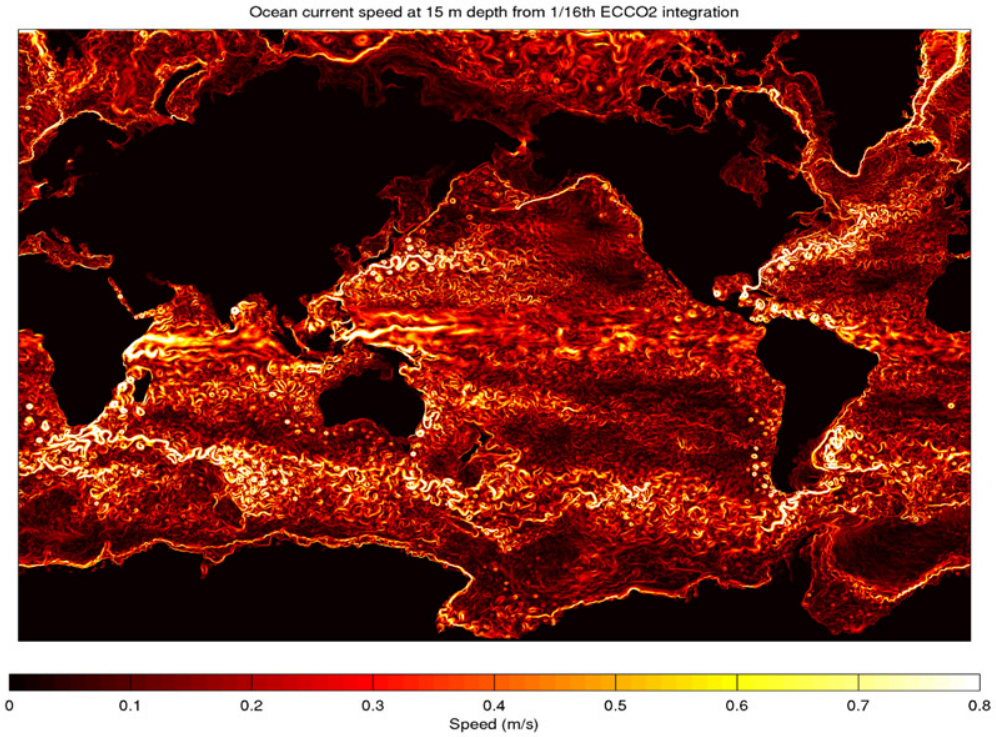

Figure 3-6. A snapshot of ocean current speed (in meters per second) at 15 m simulated by the ECCO-2 ocean general circulation model at 1/16 deg resolution.

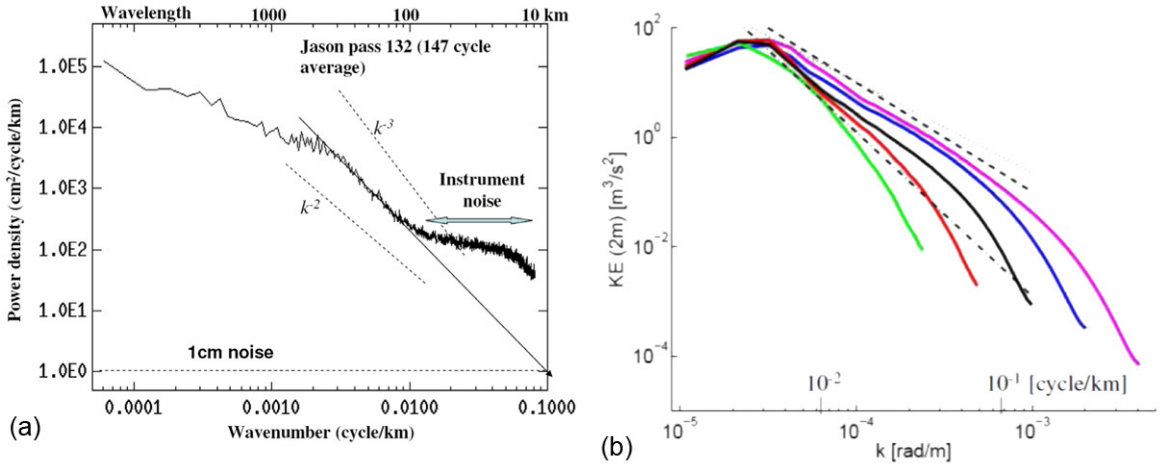

Figure 3-7. (a) Spectrum of sea surface height anomaly from Jason altimeter data (solid line). The two slanted dashed lines represent two spectral power laws with k as wavenumber. The horizontal dashed line represents the threshold of measurement noise at 1/km sampling rate. The slanting solid straight line represents a linear fit of the spectrum between 0.002 and 0.01 cycles/km. It intersects with the threshold noise level at 10 km wavelength (from Fu and Ferrari, 2008). (b) Wavenumber spectra for simulated kinetic energy at 10- m depth. Straight lines indicate −5/3 (dotted), −2 (dashed), and −3 (dot–dash) spectrum slopes. The five other lines correspond to different simulations whose resolutions increase from 12 (green), 6 (red), 3 (black), 1.5 (blue) to 0.75 km (purple). (From Capet et al., 2008.)

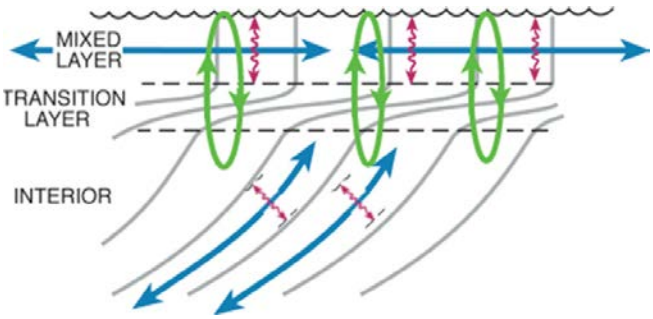

Figure 3-8. The oceanic motion at submesoscales (10–100 km, in green color) are effective in transferring heat, carbon dioxide, and other water properties from ocean surface to the deep ocean. Blue color represents motions at mesoscales (100–500km) transferring ocean properties mostly horizontally and red color represents mixing processes at scales less than 1 km. (Courtesy of R. Ferrari of MIT.)

References

Capet, X., P. Klein, B.L. Hua, G. Lapeyre, and J.C. McWilliams, 2008: Surface kinetic energy transfer in surface quasi-geostrophic flows. J. Fluid Mech., **604**, 165–174.

Chelton, D. B., M. G. Schlax, R. M. Samelson, and R. A. de Szoeke, 2007: Global observations of large oceanic eddies. Geophys. Res. Lett., **34**, L15606, doi:10.1029/2007GL030812.

Ducet, N., P.Y. Le Traon, and G. Reverdin, 2000: Global high resolution mapping of ocean circulation from the combination of TOPEX/POSEIDON and ERS-1/2J. Geophys. Res., **105**, 19477-19498.

Fu, L-L., and R. Ferrari, 2008: Observing oceanic submesoscale processes from space. Eos, Transactions, American Geophysical Union, **89** (48), pp. 488.

Lapeyre, G, and P. Klein, 2006: Imapct of the small-scale elongated filaments on the oceanic vertical pump. J. Mar. Res., **64**, 835–851.

Le Traon, P-Y., and R. Morrow, 2001: Ocean currents and eddies. In Satellite Altimetry and Earth Sciences: A Handbook for Techniques and Applications, pp. 171–210, Academic Press, San Diego, 423 pp. Eds. L.-L. Fu and A. Cazenave.

Robinson, A.R., editor, 1983: Eddies in Marine Science, Springer-Verlag, 609 pp.

Scharffenberg, M.G., and D. Stammer, 2010: Seasonal variations of the large-scale geostrophic flow field and eddy kinetic energy inferred from the TOPEX/Poseidon and Jason-1 tandem mission data. J. Geophys. Res., **115**, C2, doi:10.1029/2008JC005242

Smith, R. D., M. E. Maltrud, F. O. Bryan, and M. W. Hecht, 2000: Numerical simulation of the North Atlantic Ocean at 1/10. J. Phys. Oceanogr., **30**, 1532–1561.

3.1 Eddies, Fronts, and Filaments

3.1.1 Introduction

The availability of sea-surface height (SSH) measurements from two simultaneously operating altimeters since October 1992 (one in a 10-day exact repeat orbit and the other in a 35-day exact repeat orbit) has provided a 19-year altimetric record of mesoscale variability (Ducet et al., 2000; Fu et al., 2010). The temporal resolution of SSH fields constructed from this merged data set is about 20 days, and the spatial resolution corresponds to wavelengths of about 2º of longitude and latitude. For Gaussian eddies, this is equivalent to an e-folding scale of about 50 km. As summarized below, this data set has been analyzed extensively in synergy with other satellite and in situ data to investigate mesoscale dynamics, eddy fluxes of heat and salt, ocean interactions with topography, air-sea interaction, and physical-biological interaction. While somewhat improved resolution has been possible during periods of 3 and 4 simultaneously operating altimeters (Pascual et al., 2006; Dussurget et al., 2011), to date it has not been possible to resolve variability on wavelength scales shorter than about 100 km (Gaussian eddy e-folding scales of ~25 km). The present understanding of mesoscale dynamics is thus limited to the dynamics of the larger, and longer-lived, eddies. Much of the wavenumber-frequency spectrum of mesoscale and submesoscale variability remains unresolved, whereas this part of the ocean spectra is most important for understanding ocean mixing and energy dissipation. As discussed in later chapters, new technology such as SWOT will be required to investigate the smaller-scale range of mesoscale variability and the even smaller scales of submesoscale variability.

3.1.2 Mesoscale Eddies

3.1.2.1 Large Eddies, Their Nonlinearity and Dispersion

The merged altimeter data set has revealed the near ubiquity of coherent structures that propagate systematically westward with very little meridional deflection (Chelton et al., 2007a; 2011). During the 16-year period 14 October 1992–31 December 2008, more than 35,000 of these features were tracked for more than 4 months, and about 4300 were tracked for more than a year (Figure 3.1-1). From their scales and rotational velocities, it is clear that these features are significantly nonlinear. The ratio of particle velocity to translation speed exceeds 1 for 98% of the observed features poleward of 20º latitude (Figure 3.1-1). Even within the tropics, about 90% of the observed features have nonlinearity ratios greater than 1. Except in regions of strong eastward flow, these features propagate nearly due west with little evidence of dispersion. Their propagation speeds are approximately equal to the westward phase speeds of nondispersive Rossby waves, and there are preferences for slight poleward and equatorward deflections of cyclonic and anticyclonic features, respectively (Morrow et al., 2004a; Chelton et al., 2011). These characteristics are all consistent with theories for large, nonlinear eddies

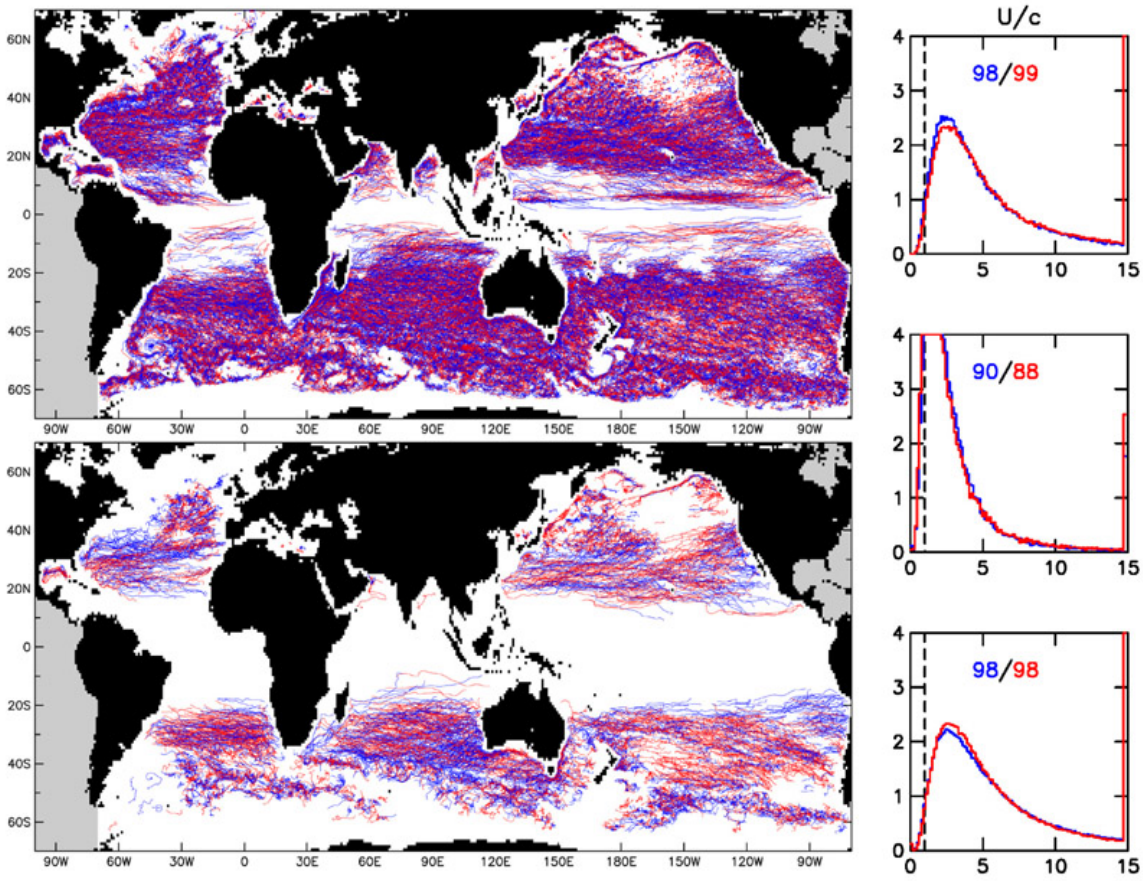

Figure 3.1-1. The trajectories of cyclonic (blue) and anticyclonic (red) eddies with lifetimes longer than 4 months (top left) and longer than 1 year (bottom left). Histograms of the nonlinearity parameter U/c, where U is the maximum fluid speed within an eddy and c is its translation speed, are shown in the right panels for cyclonic (blue curves) and anticyclonic (red curves) eddies in three different latitude bands. The blue and red numbers in each panel indicate the percentages of cyclonic and anticyclonic eddies, respectively, with U/c>1. (After Chelton et al., 2011.)

(McWilliams and Flierl, 1979). Globally, there are about 6% more cyclonic eddies with lifetimes longer than 4 months than anticyclonic eddies with lifetimes longer than 4 months. Regionally, however, either polarity can dominate.

The nonlinear eddies observable from the merged altimeter data set were not resolvable in the SSH fields constructed from TOPEX/Poseidon data alone. Early studies based on the TOPEX/Poseidon data thus misinterpreted the westward propagating features as linear Rossby waves variously modified by the vertical shear of background mean currents (Killworth et al., 1997), bottom roughness (Tailleux and McWilliams, 2001), and the combined effects of vertical shear and bottom slope (Killworth and Blundell, 2005). While the dynamical importance of Rossby waves is indisputable, it is clear from the merged data set that most of the SSH variance at mid to high latitudes is attributable to nonlinear eddies (Figure 3.1-1). The distinction is important since nonlinear eddies can transport water masses and their associated physical, chemical, and

biological properties, while Rossby waves cannot. Eddies thus have important influences on heat and momentum flux and marine ecosystem dynamics, as described below.

Many questions about the observed mesoscale eddy field have yet to be answered. One of the most fundamental is the question of the generation mechanism. A comparison of the geographical distribution of eddies with a global map of the Eady growth rate (Smith, 2007) suggests that the most likely generation mechanism is baroclinic instability. However, since we cannot observe the smaller-scale or coastal eddy processes, other mechanisms may also be important (barotropic or mixed instabilities, current-bathymetric interactions, etc.). SWOT offers the potential in particular to improve the global mapping of sea-floor bathymetry (see section 5.2) and therefore to foster greater understanding of eddy interactions with small-scale topography (e.g., Gille et al., 2000; Decloedt and Luther, 2010; Nikurashin and Legg, 2011). Secondly, although the propagation characteristics of the larger eddies are now understood, there is a paucity of observations on how the smaller mesoscale eddies propagate, mix, and decay. Indeed, these smaller eddies dominate the ocean circulation at mid to high latitudes, yet they are not well observed or understood.

3.1.2.2 Horizontal Fluxes of Heat, Salt, and Carbon

Mesoscale eddies of all scales play an important role in the horizontal transports of heat, nutrients, and carbon. Horizontal eddy heat and salt fluxes have been calculated in a number of oceanic regions from mapped altimetry data. High-resolution hydrographic sections or Argo profiles that cross the eddies are used to establish a typical eddy vertical structure. Altimetry is then used to determine population statistics, such as the number of eddies generated per year, their decay time, and their propagation direction. Annual mean heat and salt transports are then estimated.

This technique has been successfully applied in the Agulhas region by numerous authors (see review by de Ruitjer et al., 1999), and in the southeast Indian Ocean (Morrow et al., 2003). In the Southern Ocean south of Tasmania, cyclonic eddies were found to transport as much cool, fresh water across the Subantarctic Front as the northward Ekman transport (Morrow et al., 2004b). In the North Pacific, a combination of altimetric SSH, satellite sea-surface temperature (SST), and vertical temperature profiles from Argo floats were analyzed to estimate eddy-induced heat transport (Qiu and Chen, 2005). The largest poleward eddy heat flux was found to occur in the upper 200 m in the region of the subtropical front. It is noteworthy that the annual mean heat or salt flux estimates from these various studies differ from those calculated across model sections (e.g., Treguier et al., 2003). This may be due to the resolution limitations of the merged altimeter data set, which cannot resolve rapidly evolving small mesoscale and submesoscale eddies.

In addition to their horizontal transport, eddy shear velocities can induce an eddy diffusion of properties. Different techniques have been used to estimate eddy diffusivities

and eddy property fluxes from traditional altimetry. Horizontal eddy diffusivities have been calculated based on the statistics of dispersion, from surface drifters or altimetry (Zhurbas and Oh, 2004; Sallee et al., 2008b), with maximum diffusivities (~ 10^4 m^2s^{-1}) in the energetic currents. In contrast, eddy diffusivity based on altimeter-derived tracer transport studies (Marshall et al., 2006, Shuckburg et al., 2009) show a minimum transport in the jet axes. Studies are under way to resolve this paradox. Observations of the energy spectra of horizontal currents over the full range of wavelengths are needed to resolve the issue, especially in mid to high latitudes.

3.1.2.3 Vertical Processes—The Interaction of Mesoscale Eddies and Filaments

For climate studies, one of the important key issues to resolve in oceanography is how water masses are exchanged between the surface mixed layer and the ocean interior. Intermediate and deep waters are formed by two dominant wintertime mechanisms: deep convection at mid to high latitudes, and subduction. Subduction occurs when the denser large-scale intermediate ocean layers are drawn under lighter layers by a combined horizontal and downward flow (see Price, 2001, for a review). During the Programme Océan Multidisciplinaire Méso Echelle (or Multidisciplinary Meso Scale Ocean Program, POMME) experiment, high-resolution modeling and observational studies suggested that mode water subduction does not occur along a north-south gradient as previously thought, but rather within the submesoscale filament structures generated by the evolving mesoscale eddy field (Paci et al., 2005). The filaments greatly increase the mixed layer depth range (see Figure 3.1-2), and the entrainment of surface waters into the deeper layers. These deep-reaching filament structures also allow denser mode waters to form.

Winter deep convection cells can occur in the open ocean, in polynyas between the sea ice, and close to continents (especially ice-covered continents). Observations are limited, as the processes have such small spatial scales (1–10 km) and are sporadic in time. Deep winter convection in the Mediterranean Sea has been recently monitored from 7-km alongtrack altimetry (Herrmann et al., 2009), and the results of the convective overturning can be observed with in- itu data (see Lazier et al., 2001, for a review). However, understanding the dynamics of the overturning requires observations with much higher spatial and temporal coverage. The ~1 km-resolution sea level and velocity observations from SWOT will provide unprecedented insight into these processes, including the ocean-ice boundaries. Although the 22-day repeat sampling will not allow us to monitor the full evolution of these processes, there should be sufficient temporal coverage to observe cases of convection, especially with the improved temporal coverage from overlapping passes at high latitudes, where most of the convection processes occur.

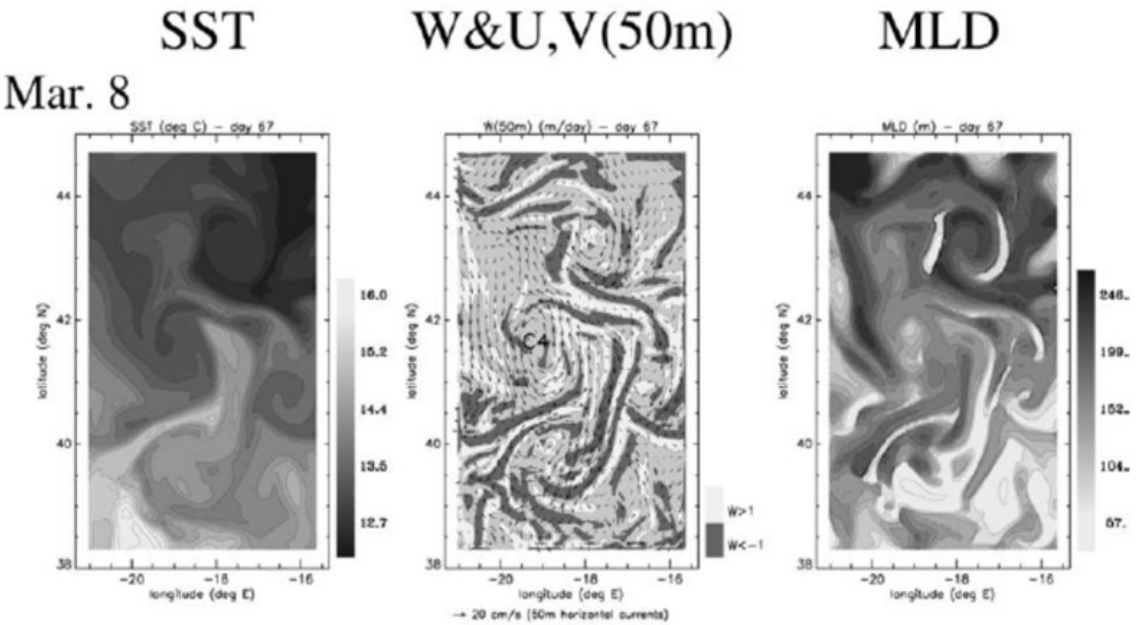

Figure 3.1-2. Surface snapshots of (left) temperature, (middle) the velocity field: vertical velocity is shaded, horizontal velocity vectors are overlaid, and (right) mixed layer depth, from a high-resolution numerical model of the POMME region in the northeastern Atlantic, forced by high-resolution atmospheric fields and constrained by altimetry and in situ observations. Note that the submesoscale filaments give rise to strong vertical velocities and large changes in the mixed layer depth. (After Paci et al., 2005.)

3.1.3 Meandering Jets and Fronts

3.1.3.1 Eastern Boundary Current Systems

Energetic mesoscale variability is found along the midlatitude eastern margins of all of the major ocean basins, with the best-defined seasonal development occurring in the California Current System. In the California system, poleward winter flow next to the coast is replaced in late spring by wind-driven coastal upwelling, which creates an SST front and a shallow equatorward jet near the coast. Continued upwelling moves the SST fronts offshore, where they connect to form a narrow and meandering equatorward jet that extends the length of the U.S. west coast by early summer. The vertical shear between this equatorward jet and a year-round poleward undercurrent generates baroclinic instabilities that lead to growing meanders and cut-off eddies in the surface jet (Figure 3.1-3). This seasonal evolution that begins near the coast in spring moves offshore during summer and fall at speeds similar to those of baroclinic Rossby waves (Kelly et al, 1998; Strub and James, 2000). The dominant wavelengths of the meandering jet and eddy system are approximately 300 km, differentiating the coastally generated mesoscale features from the weaker offshore eddy field, which has dominant scales of 120–150 km (Strub and James, 2000). A rich distribution of submesoscale variability forms around the peripheries of the nearshore mesoscale features (Figure 3.1-3). Since conventional altimetry cannot resolve either the coastal variability or the submesoscale

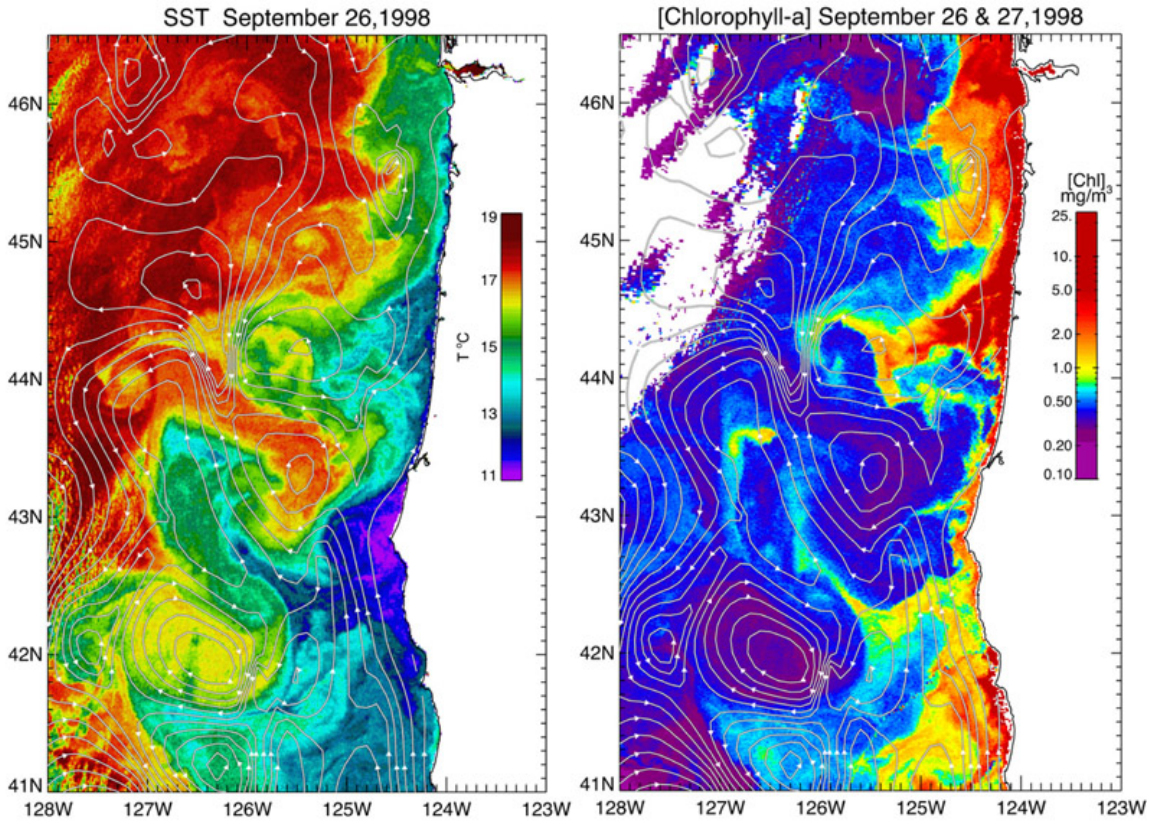

Figure 3.1-3. Sea surface temperature (left) and chlorophyll (right) with contours of SSH overlaid during September 1998 in the California Current System. The white area in the upper left corner of the chlorophyll image corresponds to clouds. Some degree of cloud contamination in this region is also evident in the SST image. It is readily apparent that the merged altimeter data set resolves the mesoscale features, but the rich distribution of submesoscale variability is undetectable by conventional altimetry.

variability, SWOT will contribute greatly to the understanding of these nearshore and offshore features, and their dynamical significance.

The westward movement of the meandering jet and eddy system transports nutrient-rich coastal water offshore (Figure 3.1-3) and plays an important role in ecosystem dynamics (e.g., Barth et al., 2002). The mechanisms by which the offshore waters are enriched (direct advection, trapping of water within eddy cores, simple vertical displacements of nutriclines) are the focus of ongoing research.

3.1.3.2 Open Ocean Fronts and Filaments

Multi-mission altimetry has been used to monitor the structure of jets and meanders in the Southern Ocean (Sokolov and Rintoul, 2007). The traditional view of the polar fronts, derived from hydrographic sections, is that the Antarctic Circumpolar Current (ACC) is composed of three or four nearly continuous circumpolar fronts (e.g., Orsi et al., 1995). However, altimetric maps of the gradient in sea level reveal that the ACC

consists of multiple frontal branches or filaments that are strongly correlated with a particular value of absolute sea level. Absolute sea level contours have been used to monitor the meandering position of the polar fronts south of Australia (Sokolov and Rintoul, 2007), and over the entire Southern Ocean (Sallee et al., 2008a). The positions of the fronts are strongly constrained by bathymetry (e.g., Gille et al., 2004), but in deep basins the fronts move meridionally in response to the dominant climate mode forcing (Sallee et al., 2008a). The poleward shift of the fronts during the 1990s in response to large-scale wind forcing changes may contribute to the observed Southern Ocean sea level rise (Morrow et al., 2008).

These studies track the larger-scale frontal movements with scales >200 km, which are observable in the mapped altimeter data set. Although the smaller-scales eddies are highly smoothed by the mapping process, the temporal evolution of the altimetry maps can reveal some smaller-scale structures. Lagrangian statistics based on the temporal evolution of altimetry maps have been used to derive ocean filaments, stirred around the larger mapped eddies, using Lyapunov exponents for example (d'Ovidio et al., 2009). Stirring a large-scale tracer field with altimetric geostrophic currents can also introduce sharper hydrological fronts, as demonstrated in the North Atlantic (Despres et al., 2011).

These fronts and filaments are generated around the presently observed larger-scale eddies. At present it is not possible to observe the full spectra of smaller-scale eddies, their perturbations on the observed stirring by larger-scale eddies, or the full frontogenesis processes. The fine-resolution sampling of SWOT, in combination with satellite SST observations and improved seafloor bathymetry derived from SWOT (see section 5.2), will provide a greatly improved insight into frontal movements, topographic influence on fronts, frontogenesis, and the important vertical exchanges induced at the fronts (see also sections 3.2 and 3.5). Improved bathymetry may ultimately give us better estimates of diapycnal mixing, which impacts water mass properties and the overall assessment of ocean mixing (Jayne et al, 2004).

3.1.3.3 Alternating Quasi-Zonal Jets

Studies from the merged altimeter data set by Maximenko et al. (2005) and others have revealed the existence of alternating quasi-zonal jets that have been interpreted as evidence of the reverse energy cascade expected from two-dimensional turbulence on a beta-plane. Similar structures have also been identified in time averages of historical observations of subsurface thermal measurements (Maximenko et al., 2008), as well as in the surface and subsurface velocity fields in eddy-resolving ocean models (e.g., Nakano and Hasumi, 2005; Maximenko et al., 2005). Ongoing research is attempting to determine the extent to which these features are eddy artifacts (Schlax and Chelton, 2008), as opposed to the quasi-zonal jets expected from two-dimensional turbulence theory.

3.1.4 Mesoscale Ocean-Atmospheric Interaction

Scatterometer and microwave radiometer measurements of surface winds and SST have revealed a strong coupling between surface winds and SST associated with oceanic mesoscale variability (see Small et al., 2008, for a review). The wind stress magnitude is linearly related to SST on scales of 100–1000 km with locally higher winds over warmer water and lower winds over cooler water (Figure 3.1-4). This SST influence is evident in atmospheric models but is generally too weak by at least a factor of 2 (Maloney and Chelton, 2006; Song et al., 2009). A key factor in this coupling is that vertical mixing in the atmospheric boundary layer is enhanced over warmer water, which increases surface winds through downward mixing of momentum. Diminished vertical mixing over cooler water decouples the surface winds from the stronger winds aloft, resulting in decreased surface winds. Spatial variability in the SST field thus generates a wind stress curl that is linearly related to the crosswind SST gradient (Chelton et al., 2004). The associated Ekman upwelling consists of order 1 perturbations of the large-scale background Ekman upwelling (O'Neill et al., 2003; Chelton et al., 2007b). Since Ekman upwelling alters the ocean circulation, as well as the SST itself, this SST influence on surface winds has potentially important feedback effects on the ocean.

The ramifications of this two-way air-sea coupling are only beginning to be investigated. Spall (2007) showed that the coupling can alter the growth rate of baroclinic instability when winds blow across SST fronts. On basin scales, Hogg et al. (2009) showed that the small-scale forcing by SST-induced Ekman pumping substantially

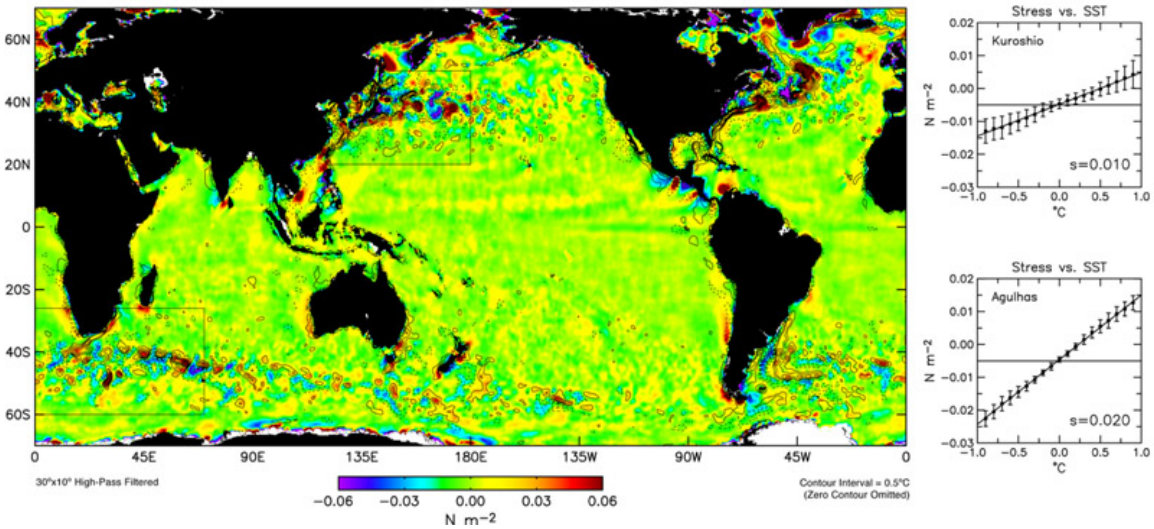

Figure 3.1-4. The 4-month average (November 2002–February 2003) wind stress magnitude from QuikSCAT with contours of SST from the Advanced Microwave Scanning Radiometer (AMSR). Both fields have been spatially high-pass filtered to remove scales longer than 30º of longitude and 10º of latitude. Binned scatter plots of wind stress magnitude as a function of SST are shown in the right panels for the Kuroshio Extension and Agulhas Return Current regions. The slopes of the lines through the binned scatter plots are labeled in the lower right corner of each panel. (After Maloney and Chelton, 2006.)

changes the time-mean circulation in an idealized eddy-resolving ocean model. The feedback destabilized the western boundary current where it separates from the coast and shifted the midlatitude oceanic jet southward, resulting in a mean circulation with 30%–40% weaker jet and comparably reduced gyre circulations.

In another recent idealized model simulation, Jin et al. (2009) showed that two-way coupling strongly influences all of the salient features of eastern boundary current systems. Cold water generated by coastal upwelling reduces the equatorward winds within ~100 km of the coast, resulting in a positive wind stress curl that broadens and strengthens the poleward undercurrent. The reduced coastal upwelling weakens the alongshore SST front and reduces the rate of baroclinic instability and consequently the eddy kinetic energy. Mesoscale SST-induced Ekman upwelling preferentially weakens the cyclones, resulting in a preponderance of anticyclonic eddies in the idealized coupled simulation.

The importance of this air-sea coupling to the evolution of mesoscale eddies is under investigation. SWOT will provide fine-scale observations of the mesoscale and submesoscale eddy field. In combination with satellite observations of winds and SST, this will enable the study of the implications of this coupling. In particular, the ability to resolve fronts will provide important insight into the time and space scales of adjustment of the atmospheric boundary layer to SST forcing and the feedback effects on mesoscale and submesoscale oceanic variability.

3.1.4.1 Mesoscale Physical-Biological Interaction

Coherent westward propagation of SSH and ocean color is observed in many regions of the World Ocean (e.g., Killworth et al., 2004, and references therein). Early studies interpreted this as an influence of Rossby waves on the chlorophyll distribution. From the improved resolution of the merged altimeter data set, it has become apparent that the co-propagation of SSH and ocean color is attributable to nonlinear eddies rather than Rossby waves.

A variety of mechanisms have been proposed to explain the observed mesoscale physical-biological interaction. The dominant near-surface chlorophyll signature is a simple distortion of the ambient chlorophyll distribution by rotational advection of fluid within the eddies (Killworth et al., 2004; Siegel et al., 2008). Examples can be seen in Figure 3.1-3 Other mechanisms include trapping and transport of marine organisms and nutrients from one biogeographic region to another within eddy cores and “eddy pumping” of nutrients into the euphotic zone from the shoaling of isopycnal surfaces during intensification or decay of eddies (e.g., Siegel et al., 2008, and references therein). Attempts to distinguish between these various mechanisms have met with mixed success and sometimes contradictory conclusions. Different processes are likely important at different life stages of an eddy. For example, high chlorophyll trapped during the formation of an eddy can rapidly decay as the nutrients trapped within the eddy core are

consumed. Replenishment of nutrients by eddy pumping during phases of eddy intensification is likewise ephemeral. Moreover, the injection of nutrients by eddy pumping and the associated phytoplankton blooming often occurs too deep within eddies to be consistently detectable in satellite measurements of ocean color (Siegel et al., 2008).

Martin and Richards (2001) suggested an alternative mechanism for eddy pumping that is likely to be more persistent and therefore more important in mesoscale eddies. The stress on the sea surface is determined by the difference between the wind and surface ocean currents. Since the wind field is relatively constant across the scales of mesoscale eddies, this results in an enhanced stress on the portion of an eddy where the wind and current are in opposition, and a reduced stress on the opposite side of the eddy where the wind and current are in the same direction. The resulting curl of the surface stress generates Ekman upwelling within the eddy interior. The negative surface geostrophic vorticity within anticyclonic eddies generates positive Ekman upwelling within the eddy cores. For mode-type anticyclonic eddies, this upwelling will raise the shallow domed isopycnals, thus injecting nutrients into the euphotic zone that stimulate phytoplankton growth. McGillicuddy et al. (2007, 2008) observed this eddy-wind interaction and Ekman upwelling in a mode-type eddy in the North Atlantic. Their estimated eddy-Ekman upwelling velocity of 0.4 m s^{-1} for the winds and currents observed during their experiment was confirmed from upward movement of a tracer released in the core of the eddy.

As reviewed by Klein and Lapeyre (2009), recent global biogeochemical estimates have concluded that the injection of nutrients by mesoscale eddies can only account for 20%–30% of the observed primary production in the ocean interior. Modeling studies suggest that the bulk of phytoplankton production must occur through ageostrophic processes in the submesoscale filaments that surround mesoscale eddies. (A detailed discussion is given in section 3.5.) The association of chlorophyll with submesoscale variability is readily apparent from the California Current example in Figure 3.1-3. The high-resolution measurements from SWOT will enable an investigation of this hypothesized biological importance of submesoscale variability.

References

Barth, J. A., T. J. Cowles, P. M. Kosro, R. K. Shearman, A. Huyer, and R. L. Smith, 2002: Injection of carbon from the shelf to offshore beneath the euphotic zone in the California Current. J. Geophys. Res., 107, doi:10.1029/2001JC000956.

Chelton, D. B., M. G. Schlax, M. H. Freilich, and R. F. Milliff, 2004: Satellite measurements reveal persistent small-scale features in ocean winds. Science, **303**, 978–983.

Chelton, D. B., M. G. Schlax, R. M. Samelson, and R. A. deSzoeke, 2007a: Global observations of large oceanic eddies. Geophys. Res. Lett., **34**, L15606, doi:10.1029/2007GL030812.

Chelton, D. B., M. G. Schlax, and R. M. Samelson, 2007b: Summertime coupling between sea surface temperature and wind stress in the California Current System. J. Phys. Oceanogr., **37**, 495–517.

Chelton, D. B., M. G. Schlax, and R. M. Samelson, 2011: Global observations of nonlinear mesoscale eddies. Prog. Oceanogr., **91**, 167–216.

d'Ovidio, F., J. Isern-Fontanet, C. López, E. García-Ladona, and E. Hernández-García, (2009). Comparison between Eulerian diagnostics and the finite-size Lyapunov exponent computed from altimetry in the Algerian Basin. Deep Sea Res. I, **56**, 15–31.

Decloedt, T., and D. S. Luther, 2010: On a simple empirical parameterization of topography-catalyzed diapycnal mixing in the Abyssal Ocean. J. Phys. Oceanogr., **40**, 487–508, doi: http://dx.doi.org/10.1175/2009JPO4275.1. Last accessed December 31, 2011.

de Ruijter, W. P. M., A. Biastoch, S. S. Drijfhout, J. R. E. Lutjeharms, R. P. Matano, T. Pichevin, P. J. van Leeuwen, and W. Weijer, 1999: Indian-Atlantic inter-ocean exchange: Dynamics, estimation and impact. J. Geophys. Res., **104**, 20,885–20,910.

Desprès, A., G. Reverdin, and F. d'Ovidio, 2011: Summertime modification of surface fronts in the North Atlantic subpolar gyre, J. Geophys. Res., **116**, C10003, doi:10.1029/2011JC006950.

Ducet, N., P.-Y. Le Traon, and G. Reverdin, 2000: Global high resolution mapping of ocean circulation from TOPEX/Poseidon and ERS-1/2. J. Geophys. Res., **105**, 19,477–19,498.

Dussurget, R., F. Birol, R. Morrow, and P. Demey, 2011: Fine resolution alitmetry data for a regional application in the Bay of Biscay. Marine Geodesy, **34**, 447–476.

Fu, L.-L., D. B. Chelton, P.-Y. Le Traon, and R. Morrow, 2010: Eddy dynamics from satellite altimetry. Oceanography, **23**(4):14–25.

Gille, S. T., M. M. Yale, and D. T. Sandwell, 2000: Global correlation of mesoscale ocean variability with seafloor roughness from satellite altimetry. Geophys. Res. Lett., **27**, 1251–1254.

Gille, S. T., E. J. Metzger, and R. Tokmakian, 2004: Sea floor topography and ocean circulation, Oceanography, **17**(1), 47–54.

Herrmann, M., J. Bouffard, and K. Béranger, 2009: Monitoring open-ocean deep convection from space, Geophys. Res. Lett., **36**, L03606, doi:10.1029/2008GL036422.

Hogg, A. McC., W. K. Dewar, P. Berloff, S. Kravstov, and D. K. Hutchinson, 2009: The effects of mesoscale ocean-atmosphere coupling on the large-scale ocean circulation. J. Climate, **22**, 4066–4082.

Jayne, S. R., L. C. St. Laurent, and S. T. Gille, 2004: Connections between ocean bottom topography and Earth's climate. Oceanography, **17**(1), 65–74.

Jin, X., C. Dong, J. Kurian, J. C. McWilliams, D. B. Chelton, and Z. Li, 2009: SST-wind interaction in coastal upwelling: Oceanic simulation with empirical coupling. J. Phys. Oceanogr., **39**, 2957–2970.

Kelly, K. A., R. C. Beardsley, R. Limeburner, K. H. Brink, J. D. Paduan, and T. I. Chereskin, 1998: Variability of the near-surface eddy kinetic energy in the California Current based on altimeter, drifter, and moored current data. J. Geophys. Res., **103**, 13067–13083.

Killworth, P. D., P. Cipollini, B. M. Uz, and J. R. Blundell, 2004: Physical and biological mechanisms for planetary waves observed in satellite-derived chlorophyll. J. Geophys. Res., **109**, C07002, doi: 10.1029/2003JC001768.

Killworth, P. D., and J. R. Blundell, 2005: The dispersion relation for planetary waves in the presence of mean flow and topography. Part II: Two-dimensional examples and global results. J. Phys. Oceanogr., **35**, 2110–2133.

Killworth, P. D., D. B. Chelton, and R. A. de Szoeke, 1997: The speed of observed and theoretical long extra-tropical planetary waves. J. Phys. Oceanogr., **27**, 1946–1966.

Klein, P., and G. Lapeyre, 2009: The oceanic vertical pump induced by mesoscale and submesoscale turbulence. Ann. Rev. Mar. Sci., **1**, 351–375.

Lazier, J. R. Pickart, and P. Rhines, 2001: Deep convection In Ocean Circulation and Climate, Int. Geophys. Ser., **77**, Eds. G. Siedler, J. Church, and J. Gould, Academic, New York, 373–386.

Maloney, E. D., and D. B. Chelton, 2006: An assessment of the sea surface temperature influence on surface wind stress in numerical weather prediction and climate models. J. Climate, **19**, 2743–2762.

Marshall, J., E. Shuckburgh, H. Jones, and C. Hill, 2006: Estimates and implications of surface eddy diffusivity in the Southern Ocean derived from tracer transport. J. Phys. Oceanogr., **36**, 1806–1821.

Martin A. P., and K. J. Richards, 2001: Mechanisms for vertical nutrient transport within a North Atlantic mesoscale eddy. Deep-Sea Res. II, **48**, 757–773.

Maximenko, N. A., B. Bang, and H. Sasaki, 2005: Observational evidence of alternating zonal jets in the World Ocean, Geophys. Res. Lett., **32**, doi:10.1029/2005GL022728.

Maximenko, N. A., O.V. Melnichenko, P. P. Niiler, and H. Sasaki, 2008: Stationary mesoscale jet-like features in the ocean, Geophys. Res. Lett., **35**, L08603, doi:10.1029/2008GL033267.

McGillicuddy, D. J., and Coauthors, 2007: Eddy/wind interactions stimulate extraordinary mid-ocean plankton blooms. Science, **316**, 1021–1026.

McGillicuddy, D. J., J. R. Ledwell, and L. A. Anderson, 2008: Response to comment on “Eddy/wind interactions stimulate extraordinary mid-ocean plankton blooms.” Science, **320**, 448.

McWilliams, J. C., and G. R. Flierl, 1979: On the evolution of isolated, nonlinear vortices. J. Phys. Oceanogr., **9**, 1155–1182.

Morrow, R.A., F. Fang, M. Fieux and R. Molcard, 2003: Anatomy of three warm-core Leeuwin Current eddies. Deep Sea Res.II, **50**, 2229–2243.

Morrow R. A, F. Birol, D. Griffin, and J. Sudre, 2004a: Divergent pathways of cyclonic and anti-cyclonic ocean eddies, Geophys. Res. Lett., **31**, L24311, doi:10.1029/2004GL020974.

Morrow R., J. R. Donguy, A. Chaigneau, and S. Rintoul, 2004b: Cold core anomalies at the Subantarctic Front, south of Tasmania. Deep-Sea Research I, **51**, 1417–1440.

Morrow, R., G. Valladeau, and J. B. Sallee, 2008: Observed subsurface signature of Southern Ocean decadal sea level rise. Prog. Oceanogr., **77**(4), 351–366.

Nakano, H., and H. Hasumi, 2005: A series of zonal jets embedded in the broad zonal flows in the Pacific obtained in eddy-permitting ocean general circulation models. J. Phys. Oceanogr., **35**, 474–488.

Nikurashin, M., S. Legg, 2011: A mechanism for local dissipation of internal tides generated at rough topography. J. Phys. Oceanogr., **41,** doi: http://dx.doi.org/10.1175/2010JPO4522.1, 378–395. Last accessed December 31, 2011.

O'Neill, L. W., D. B. Chelton, and S. K. Esbensen, 2003: Observations of SST-induced perturbations of the wind stress field over the Southern Ocean on seasonal time scales. J. Climate, **16**, 2340–2354.

Orsi, A., T. Whitworth III, and W. Nowlin Jr., 1995: On the meridional extent and fronts of the Antarctic Circumpolar Current. Deep-Sea Res. II, **42**, 641–673.

Paci, A., G. Caniaux, M. Gavart, H. Giordani, M. Levy, L. Prieur, and G. Reverdin, 2005: A high-resolution simulation of the ocean during the POMME experiment: Simulation results and comparison with observations, J. Geophys. Res., **110**, doi:10.1029/2004JC002712.

Pascual, A., Y. Faugere, G. Larnicol, and P.-Y. Le Traon, 2006: Improved description of the ocean mesoscale variability by combining four satellite altimeters. Geophys. Res. Lett., **33**, L02611, doi:10.1029/2005GL024633.

Price, J., 2001: Subduction In Ocean Circulation and Climate, Int. Geophys. Ser., **77**, edited by G. Siedler, J. Church, and J. Gould, Academic, New York, 373–386.

Qiu, B., and S. Chen, 2005: Eddy-induced heat transport in the subtropical North Pacific from Argo, TMI and altimetry measurements. J. Phys. Oceanogr., **35**, 458–473.

Sallée, J. B., K. Speer, and R. Morrow, 2008a: Southern Ocean fronts and their variability to climate modes. J. Climate, **21**, 3020–3039.

Sallée, J. B., K. Speer, R. Morrow, and R. Lumpkin, 2008b: An estimate of Lagragian eddy statistics and diffusion in the mixed layer of the Southern Ocean. J. Mar. Res., **66**, 441–463.

Schlax, M. G., and D. B. Chelton, 2008: The influence of mesoscale eddies on the detection of quasi-zonal jets in the ocean. Geophys. Res. Lett., **35**, L24602, doi:10.1029/2008GL035998.

Shuckburgh, E., H. Jones, J. Marshall, and C. Hill, 2009: Robustness of effective diffusivity diagnostic in oceanic flows. J. Phys. Oceanogr., 39, 1993–2009.

Siegel, D. A., D. B. Court, D. W. Menzies, P. Peterson, S. Maritorena, and N. B. Nelson, 2008: Satellite and in situ observations of the bio-optical signatures of two mesoscale eddies in the Sargasso Sea. Deep-Sea Res. II, **55**, 1218–1230.

Small, R. J., et al., 2008: Air-sea interaction over ocean fronts and eddies. Dyn. Atmos. Oceans, doi:10.1016/j.dynatmoce.2008.01.001.

Smith, K. S., 2007: The geography of linear baroclinic instability in Earth's oceans. J. Mar. Res., **65**, 655–683.

Sokolov, S., and S. R. Rintoul, 2007: Multiple jets of the Antarctic Circumpolar Current south of Australia. J. Phys. Oceanogr., 37, doi:10.1175/JPO3111.1, 1394–1412.

Song, Q., D. B. Chelton, S. K. Esbensen, N. Thum, and L. W. O'Neill, 2009: Coupling between sea surface temperature and low-level winds in mesoscale numerical models. J. Climate, **22**, 146–164.

Spall, M. A., 2007: Effect of sea surface temperature-wind stress coupling on baroclinic instability in the ocean. J. Phys. Oceanogr., **37**, 1092–1097.

Strub, P. T., and C. James, 2000: Altimeter-derived variability of surface velocities in the California Current System: 2. Seasonal circulation and eddy statistics. Deep-Sea Res. II, **47**, 831–870.

Tailleux, R., and J. C. McWilliams, 2001: The effect of bottom pressure decoupling on the speed of extratropical, baroclinic Rossby waves. J. Phys. Oceanogr., **31**, 1461–1476.

Treguier, A. M., O. Boebel, B. Barnier, and G. Madec, 2003: Agulhas eddy fluxes in a 1/6° Atlantic model. Deep Sea Res. II, **50**, 251–280.

Zhurbas, V., and I. Oh. 2004: Drifter-derived maps of lateral diffusivity in the Pacific and Atlantic Oceans in relation to surface ciculation patterns. J. Geophys. Res., **109**, 1–10.

3.2 Three-dimensional Upper Ocean Circulation

Conventional altimetry allows us to capture structures at the ocean surface with wavelengths larger than 100 km and to retrieve the related surface currents using the geostrophic approximation. So far these data have revealed a rich dynamic that is now interpreted, in particular at mid-latitudes, in terms of mesoscale eddies that strongly interact. On the other hand, these data provide no information on the smaller structures—such as the much smaller vortices and elongated filaments—that are ubiquitous on high-resolution (1 km) ocean color and SST images. These smaller structures clearly result from the nonlinear interaction of mesoscale eddies; but, contrary to mesoscale eddies, they are often assumed to have no dynamical impact on the larger scales.

High-resolution (1 km) studies—both experimental (Ferrari and Rudnick, 2000) and numerical (Capet et al., JPO, 2008 and Klein et al., JPO 2008)— have, however, pointed out that these smaller scales are much more energetic than previously thought and have a significant dynamical impact on the larger scales. These studies have provided some evidence that the surface velocity wavenumber spectrum has a shallower slope (in k-2) than the classical expected k-3 slope, which means that horizontal currents associated with these smaller structures are non-negligible. They have further revealed a spectral relationship between surface density and sea surface height (SSH) close to what is expected from surface quasigeostrophic (SQG) dynamics. In addition, these high-resolution numerical simulations have revealed that these smaller-scale structures are associated with active surface frontogenesis and, as a consequence, trigger most of the vertical velocity field in the first 500 m below the surface. This explains why these smaller-scale structures drive a large part of the horizontal and vertical fluxes of momentum— in particular, a large part of the inverse kinetic energy cascade (Capet et al., JPO, 2008 and Klein et al., JPO 2008)—and, consequently, why they have a significant impact on the ocean circulation at larger scales. Furthermore, the smaller-scale structures drive most of the vertical fluxes of tracers such as nutrients from the interior to the mixed-layer, a feature crucial for the biogeochemistry (see section 3.5).

For these reasons, the knowledge of the dynamics associated with scales smaller than 100 km is highly needed. This knowledge, not accessible at the present time from satellite data, should be accessible in the future with the new space missions (using wide swath radar interferometer such as SWOT) that aim to measure SSH at much higher resolution (Fu and Ferrari, EOS, 2008): such missions should allow us to capture the surface signature of structures with wavelengths as small as 10 km. But an additional outcome, which may represent a major advance compared with conventional altimetry, is that these data, combined with theoretical results (Lapeyre and Klein, JPO 2006), should allow us to diagnose not only the surface currents associated with these smaller-scale structures, but also and principally the three-dimensional ocean circulation, including the vertical velocity in the first 500 m below the surface. These theoretical results involving SQG and QG dynamics indicate that, in the first 500 m, the spectral characteristics of the stream function at a given level are related to those of the SSH through a transfer function that

depends only on the large-scale properties of the ocean flow (such as the vertical stratification) that can be obtained from climatology. This means that knowledge of high-resolution SSH combined with climatological data should allow us to diagnose the stream function at any level in the upper oceanic layers. Then the three-dimensional circulation in the upper oceanic layers, including the vertical velocity field, can be retrieved from high-resolution SSH (using the geostrophic approximation and the well-known Omega equation). Because of the assumptions considered, the resulting diagnosis method (called the eSQG method) can only be used to estimate the low-frequency motions with scales smaller than O (400 km).

The validity of the eSQG diagnosis has been tested using an Ocean General Circulation Model (Parallel Ocean Program, or POP) simulation at 1/10°resolution in the North Atlantic Ocean with realistic winter atmospheric forcing (Isern et al., 2008). Results show that the reconstruction of horizontal velocities from SSH is reasonably good for the upper 500 m, in particular in the Gulf Stream region and the North Atlantic drift. The simulation resolution was, however, not high enough to use it for the vertical velocity diagnosis.

This vertical velocity diagnosis has been recently evalutated using much higher resolution (1/50°) simulations performed on the Earth Simulator, characterized by a turbulent eddy field with larger Rossby numbers and the presence of an active mixed-layer (ML) forced by realistic high-frequency winds (Klein et al., GRL 2009). The velocity field includes a high-frequency component (at the inertial frequency) which is non-negligible compared to the lower frequency component related to the mesoscale eddy field (see Figure 3.2-1). However, these simulations show that the near-inertial motions have almost no signature on the SSH, as illustrated by Figure 3.2-2.

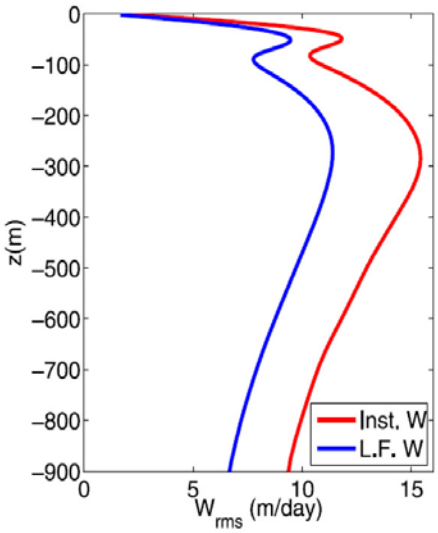

Figure 3.2-1. Vertical profiles of the rms values of the instantaneous vertical velocity (red curve) and of the vertical velocity averaged over an inertial period (blue curve).

An additional property is that the wind-driven motions become significant only for scales smaller than 20 km. This means that high-resolution SSH can be used to diagnose in the upper layers the three-dimensional circulation associated with mesoscale eddies for scales between O (400 km) and 20 km. Then the stream function, relative vorticity, buoyancy, and vertical velocity at any depth can be diagnosed from SSH using the eSQG relation; and the diagnosed fields can be compared to the observed ones, averaged over an inertial period (Klein et al, GRL 2009). An example of such observed and diagnosed

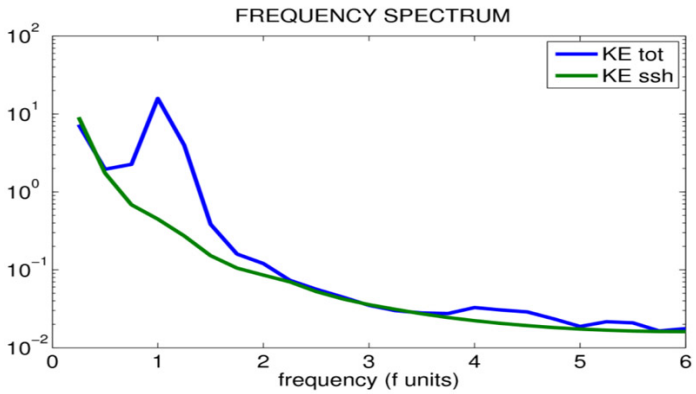

Figure 3.2-2. Frequency spectrum of the surface kinetic energy deduced from observed currents (red line) and from currents estimated from the SSH using the geostrophic approximation (green line).

fields at 200 m is shown on Figures 3.2-3a and b. The fields exhibit remarkable visual coincidence. Evaluation of this diagnosis, done by calculating the correlation between diagnosed and observed fields as well as their rms amplitudes at any depth, has revealed a quite good agreement from the base of the ML down to 500 m depth (Klein et al., GRL 2009).

These results reveal the significant potential of a snapshot of high-resolution SSH to reconstruct the three-dimensional motions, including vertical velocities, for scales between 400 km and 20 km in the first 500 m below the surface. As such, the results highlight the potential of high-resolution SSH to assess the low-frequency horizontal and vertical fluxes of momentum and tracers in the upper ocean driven by mesoscale and smaller scale dynamics. More work has still to be done to improve this simple diagnostic method. Firstly, a more appropriate estimation of the transfer function between SSH and the stream function at depth needs to be investigated. One approach would be to use the climatological data in conjunction with the sea surface temperature and/or the existing Argo float data. Secondly, the skill of the SSH reconstruction must be tested in a broader range of mesoscale eddy and ML dynamics regimes. For example, concerning the surface ML, work has shown that frontal instabilities can drive vertical transports largely in excess of what would be estimated with the eSQG diagnostic method (Fox-Kemper et al.,

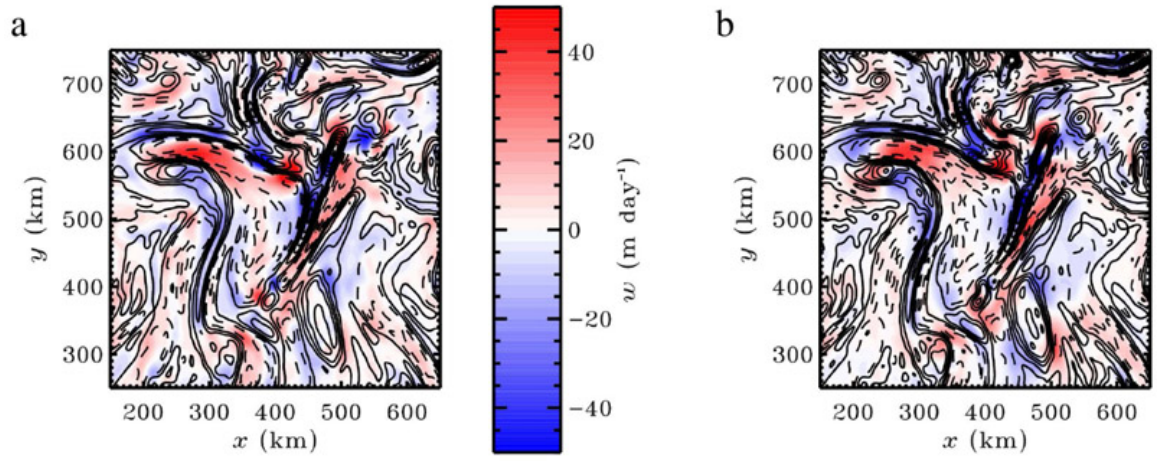

Figure 3.2-3. (a) Observed low-frequency vertical velocity (in colors) and relative vorticity (contours) at 200 m. (b) eSQG reconstructed vertical velocities (in colors) and relative vorticity (contours) at 200 m.

JPO, 2008; Thomas and Ferrari, JPO, 2008). It appears that these dynamics become dominant only on scales shorter than O (10) km, but efforts must be carried out to evaluate under what conditions and at what scales the ML dynamics are not captured by the eSQG approach and what improvements can be proposed.

References

Capet, X., P. Klein, B. L. Hua, G. Lapeyre, and J. C. McWilliams, 2008: Surface kinetic energy transfer in surface quasi-geostrophic flows. J. Fluid Mech., **604**, 165–174.

Ferrari, R., and D. L. Rudnick, 2000: Thermohaline structure of the upper ocean. J. Geophys. Res., **105**, 16857–16883.

Fox-Kemper, B., R. Ferrari, and R. W. Hallberg, 2008: Parameterization of mixed layer eddies. Part I: Theory and diagnosis. J. Phys. Oceanogr., **38**(6):1145–1165.

Fu, L-L., and R. Ferrari, 2008: Observing oceanic submesoscale processes from space, Eos, Transactions. American Geophysical Union, **89**(48), 488.

Isern–Fontanet, J., G. Lapeyre, P. Klein, B. Chapron, and M. W. Hecht, 2008. Three-dimensional reconstruction of oceanic mesoscale currents from surface information. J. Geophys. Res., **113**, C09005, doi:10.1029/2007JC004692.

Klein, P., B. L. Hua, G. Lapeyre, X. Capet, S. Le Gentil, and H. Sasaki, 2008: Upper ocean turbulence from high-resolution 3D simulations. J. Phys. Oceanogr., **38**, 1748–1763.

Klein, P., J. Isern-Fontanet, G. Lapeyre, G. Roullet, E. Danioux, B. Chapron, S. Le Gentil, and H. Sasaki, 2009: Diagnosis of vertical velocities in the upper ocean from high resolution Sea Surface Height. Geophys. Res. Lett., **36**, L12603.

Lapeyre, G., and P. Klein, 2006: Dynamics of the upper oceanic layers in terms of surface quasigeostrophy theory. J. Phys. Oceanogr., **36**, 165–176.

Thomas, L. N., and R. Ferrari, 2008: Friction, frontogenesis, and the stratification of the surface mixed layer. J. Phys. Ocean., **38**, 2501–2518.

3.3 Eddy-mean Flow Interaction

Large-scale mean ocean circulation is predominantly driven by surface wind stress and buoyancy forcings. For the mean circulation to maintain its equilibrium state, the energy supplied by the surface forcings must be dissipated through motions with smaller scales. An effective way to accomplish this is through eddies that are generated as a result of instability of the mean circulation. The high-quality SSH measurements from satellite altimeters over the past 17 years have provided us with an unprecedented observational data set to explore the dynamics underlying the eddy-mean flow interaction. One important feature revealed by the altimeter measurements is that the level of the mesoscale eddy variability in eddy-rich regions of the world oceans modulates on various timescales. In the Pacific Ocean, for example, the mesoscale eddy variability undergoes a large-amplitude decadal modulation in the Kuroshio Extension (KE) region; in contrast, the mesoscale eddy variability exhibits a well-defined annual cycle in the subtropical countercurrent (STCC) band (see Figure 3.3-1). These contrasting behaviors reflect the differences in the intrinsic ocean dynamics and how the background mean circulation is forced.

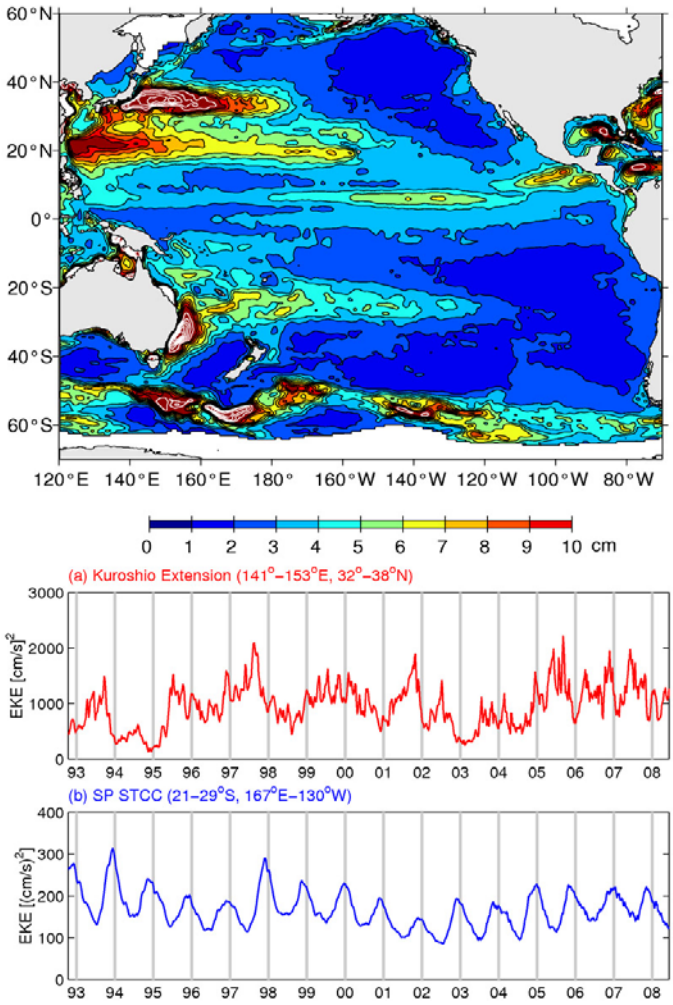

Figure 3.3-1. (Top) rms SSH variability in the Pacific Ocean based on high-pass filtered satellite altimeter SSH data from Oct 1992 to Dec 2006. The high-pass filter has a half-power at 180 days. Contour intervals are 0.01 m for black lines and 0.02 m for white lines starting from 0.12 m. (Bottom) Eddy kinetic energy time series in the regions of (a) Kuroshio Extension and (b) South Pacific Subtropical Countercurrent.

In the KE region, the background mean circulation oscillated between a stable and an unstable dynamic state on a decadal timescale. During the stable state (i.e., October 1992–June 1995; January 2002–December 2005), the KE jet was intense and had a northerly zonal mean path and a well-defined southern recirculation gyre. During the unstable state,

the KE jet had a reduced eastward transport and a more southerly flow path. Transitions between the two dynamic states are caused by the basin-scale wind stress curl forcing in the eastern North Pacific related to the Pacific decadal oscillations (PDO; Figure 3.3-2). During the positive PDO phase, the intensified Aleutian Low generates negative SSH anomalies in the eastern North Pacific through Ekman divergence. As these wind-induced negative SSH anomalies propagate to the west as baroclinic Rossby waves, they weaken the zonal KE jet and shift its path southward. As its path is pushed southward (~32° N), the deep-reaching KE jet has to ride over the shallow Shatsky Rise, generating localized disturbances that develop west of the Shatsky Rise. An opposite sequence occurs when the PDO changes to its negative phase. The large-scale, PDO-forced SSH variability can be adequately modeled by the linear vorticity dynamics (cf. Figures 3.3-2c and b). In the KE band of 140° E–180° E, the linear model, however, underestimates the observed SSH signals; and the larger observed SSH variability is due to the eddy's feedback upon the slowly varying, background KE jet. (For more details about the eddy potential vorticity flux convergence analysis, see Qiu et al., 2010.)

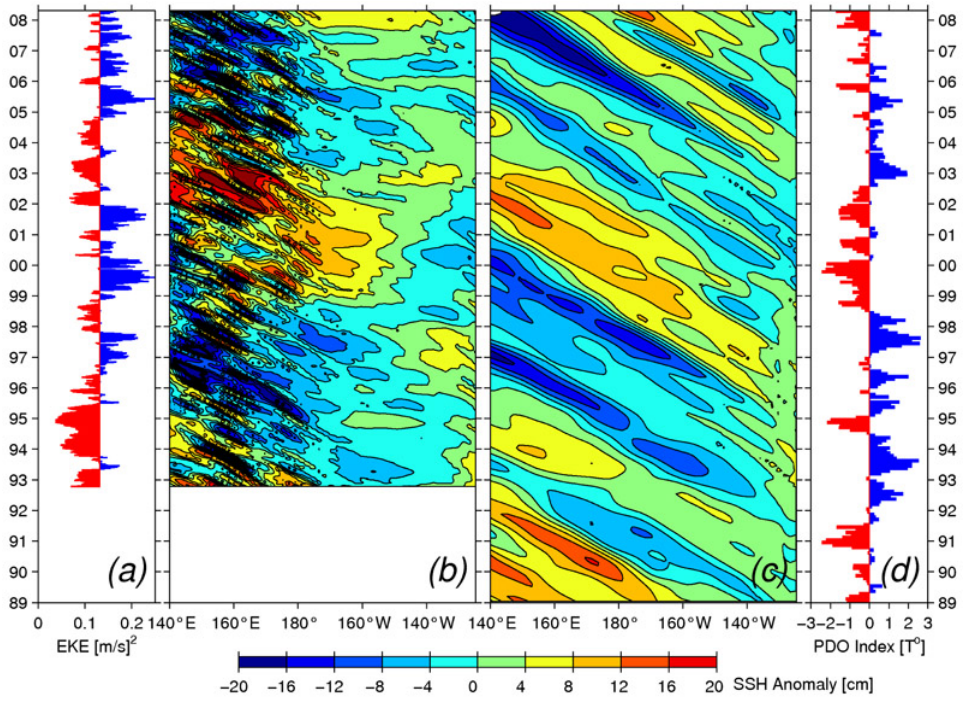

Figure 3.3-2. (a) Time series of eddy kinetic energy (EKE) in the upstream KE region of 141° E–153° E and 32° N–38° N. Here, EKE is calculated using the weekly SSH anomaly data by assuming geostrophy. For comparison with the PDO index, the time series is plotted as the deviation from the regional mean EKE value. (b) SSH anomalies along the zonal band of 32–34° N from the satellite altimeter data. (c) Same as panel (b) but from the wind-forced baroclinic Rossby wave model driven by the NCEP-NCAR reanalysis wind stress curl data. (d) PDO index from http://jisao.washington.edu/pdo/PDO.latest.

Enhanced eddy variability signals in the STCC band in the South Pacific (20° S–30° S) is due to baroclinic instability of the vertically sheared eastward-moving STCC and westward-moving South Equatorial Current (SEC). The well-defined seasonal modulation in the eddy kinetic energy level in this band (Figure 3.3-1) is due to the seasonally modulating vertical shear and stratification: greater vertical shear and weaker stratification in the southern hemisphere winter lead to a stronger growth of instability, followed by an elevated eddy kinetic energy (EKE) level in the STCC band in November/December. A stability analysis reveals that the STCC-SEC system favors generation of anomalies with larger meridional-length scales. Subsequent nonlinear eddy–eddy interactions work to redistribute the EKE to larger total horizontal length scales, and larger zonal scales in particular. This is confirmed by diagnosing the spectral transfer of EKE in the surface geostrophic flow, which is found to drive an anisotropic inverse cascade, being redirected as with the beta-effect (Qiu et al., 2008). Due to the seasonal renewal of meridionally elongated anomalies by baroclinic instability and possibly due to the barotropization process, however, the net outcome for the formation of surface zonal flows is limited.

As the nadir-looking altimeters are unable to adequately resolve scales shorter than ~200 km, our understanding about the eddy-mean flow interaction—in particular, how eddies interact and decay—remains incomplete. In the South Pacific STCC band, the existing merged satellite data capture only part of the SSH anomaly signals (see Figure 3.3-3). In order to fully understand how the upper ocean evolves dynamically, it is crucial to capture the SSH anomaly signals with finer spatial scales. For example, Figure 3.3-4 shows the spectral energy fluxes as a function of wavenumber based on the Naval Research Laboratory Layered Ocean Model (NLOM) model simulation at different subsampled spatial scales. From the 1/3°smoothed model result, the scale separating the forward and inverse energy cascades is located at 100 km, whereas this scale is at ~25 km in the

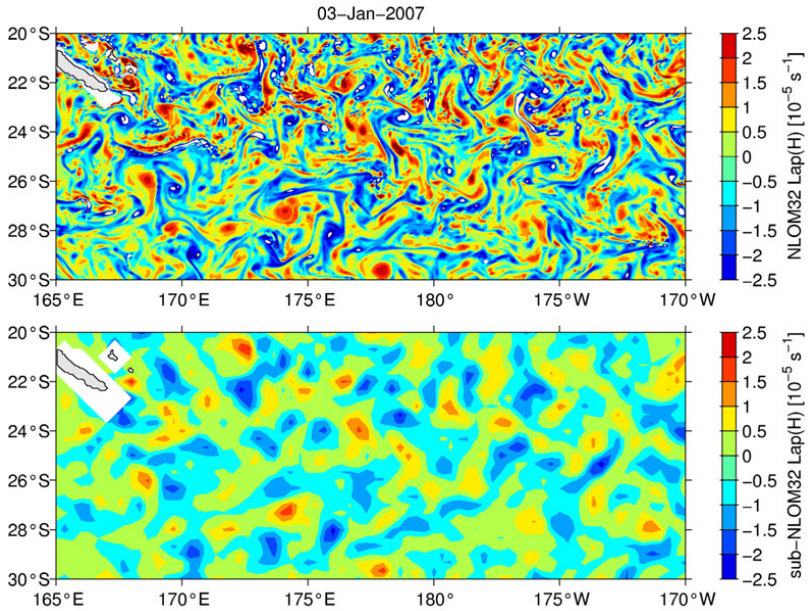

Figure 3.3-3. (Top) Snapshot of surface vorticity field on 3 January 2007 in the South Pacific STCC region from the 1/32° resolution NLOM simulation. (Bottom) The same vorticity field sampled at the 1/3°resolution. This spatial resolution is currently resolvable by multiple nadir satellite altimeter missions.

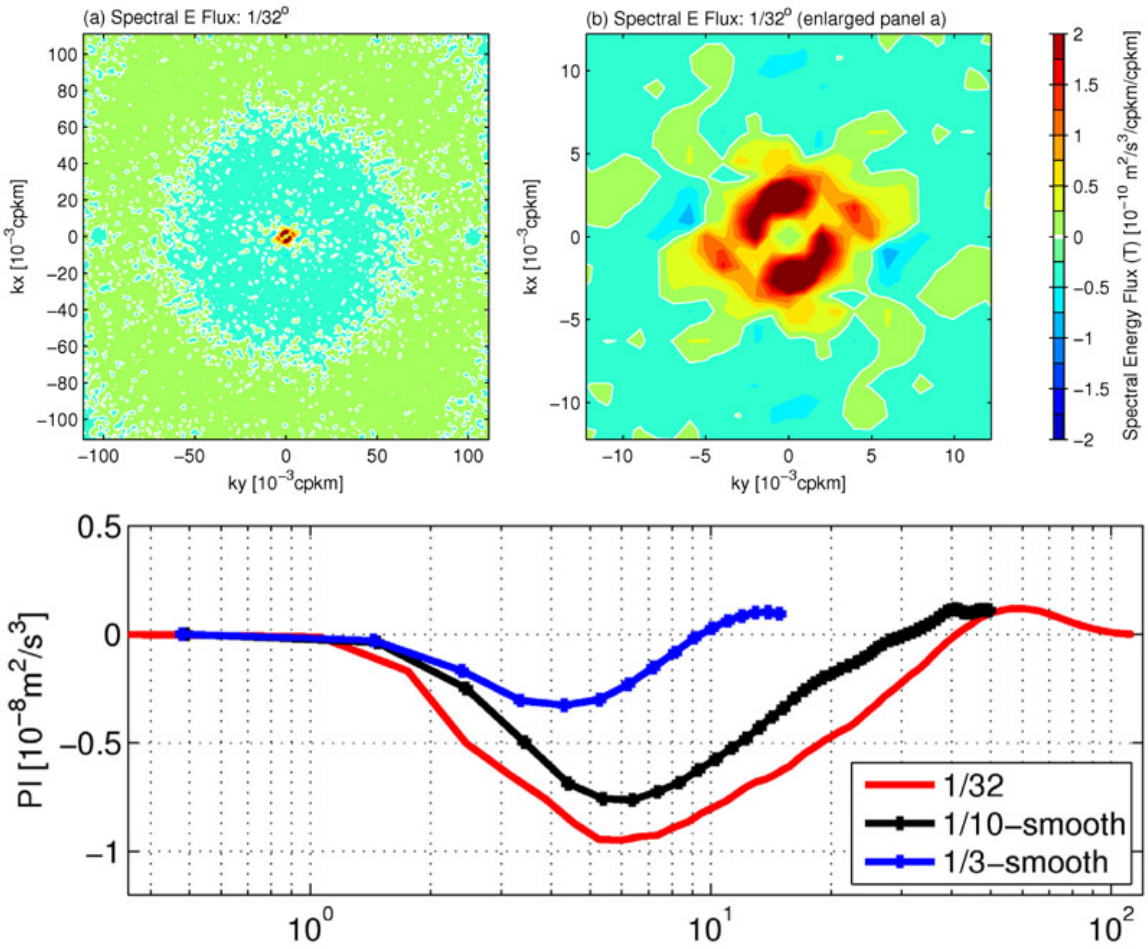

Figure 3.3-4. (Top) Spectral energy transfer values in the South Pacific band from the NLOM simulation result shown in Figure 3.3-3a. The left panel shows the details with small wavenumbers. (See Qiu et al.2008 for more details.) (Bottom) Spectral energy fluxes as a function of total wavenumber. The red and blue curves are based on the original and 1/3°subsampled model output shown in Figures 3.3-3a and b, respectively.

original 1/32°model result. Physically, it indicates that while the instability in the original model occurs at scales longer than 25 km, sampling by the nadir-looking altimeters will miss those instability signals between 25 and 200 km. These signals correspond to the instability of the density front associated with the STCC, known as the Subtropical Front, and they are likely to be important for regulating the EKE decay in March/April in the South Pacific STCC region.

References

Qiu, B., R. Scott, and S. Chen, 2008: Length scales of eddy generation and nonlinear evolution of the seasonally-modulated South Pacific Subtropical Countercurrent. J. Phys. Oceanogr., **38**, 1515–1528.

Qiu, B., and S. Chen, 2010: Eddy-mean flow interaction in the decadally-modulating Kuroshio Extension system. Deep-Sea Res. II, **57**, 1098–1110.

3.4 Cascade and Dissipation of Oceanic Kinetic Energy

The general circulation of the ocean still has an incompletely determined kinetic energy cycle. (See Ferrari and Wunsch 2009 for a modern estimate.) The primary power source is large-scale wind stress, which is reasonably well estimated from global analyses. The primary power sinks must be viscous and diffusive dissipation at the microscale of approximately millimeters. What is poorly known are the mechanisms and locations that provide the pathways to dissipation, and hence to climatic equilibration of the general circulation. The pathway starts with mesoscale instabilities of the large-scale circulation, primarily through baroclinic energy conversion. Energy flows into mesoscale eddies that have an approximately quasi-static force balance, geostrophic in the horizontal direction and hydrostatic in the vertical. (These balances are the basis for the successful altimetric diagnosis of mesoscale surface currents.) A major unsolved question is what processes set the characteristic speed (U) and spatial scale (L) of the equilibrated mesoscale eddy field, i.e., how the eddy loses its kinetic energy. Geostrophic, hydrostatic fluid dynamics has a characteristic turbulent behavior of inverse energy cascade (Charney 1971) whereby momentum and density advection transfer eddy energy toward larger scales, and hence away from the effective action of viscosity. Exceptions occur in the top and bottom boundary layers where small-scale turbulence can provide a local route to dissipation, but the bulk of the mesoscale kinetic energy is in the upper ocean outside the boundary layers, and it is uncertain how efficiently energy can be fluxed toward the boundaries. Another possibility receiving much recent attention is the breakdown of the quasi-static force balances at the smaller-scale end of the mesoscale eddy spectrum, referred to as the submesoscale regime. Numerical models confirm that mesoscale energy flows into the submesoscale when the grid resolution is fine enough (a few kilometers); and since submesoscale dynamics are partly unbalanced, a forward energy cascade ensues for both kinetic and available potential energy down to microscale dissipation (Capet et al., 2008a–c; McWillliams, 2008; Molemaker et al., 2010a–b). Illustrations are shown and described in Figures 3.4-1 through 3.4-3 for simulated sea level and surface temperature fields; kinetic energy spectrum $K(k_h)$ (where k_h is the horizontal wavenumber); and the spectral energy flux $\Pi(k_h)$ (defined such that the influence of advection in the spectrum evolution equation appears as $\partial_t K = -\partial_{k_h} \Pi$).

The energy cascades into the submesoscale range can arise through frontogenesis and frontal instability or baroclinic instability of the weakly stratified surface layer or spontaneous emission of inertia-gravity waves, especially in flow over topography. With models, the particular mixes of these different behaviors are now being discovered to vary with location and season (and perhaps climate state). In global oceanic models, the forward-cascade dissipation route is implicit in artificial eddy viscosities, but it is important to determine the true nature of submesoscale processes and to accurately parameterize their effects. The submesoscale is highly active in the upper ocean, and hence measurable by high-resolution altimetry. It has a spectrum signature of a rather

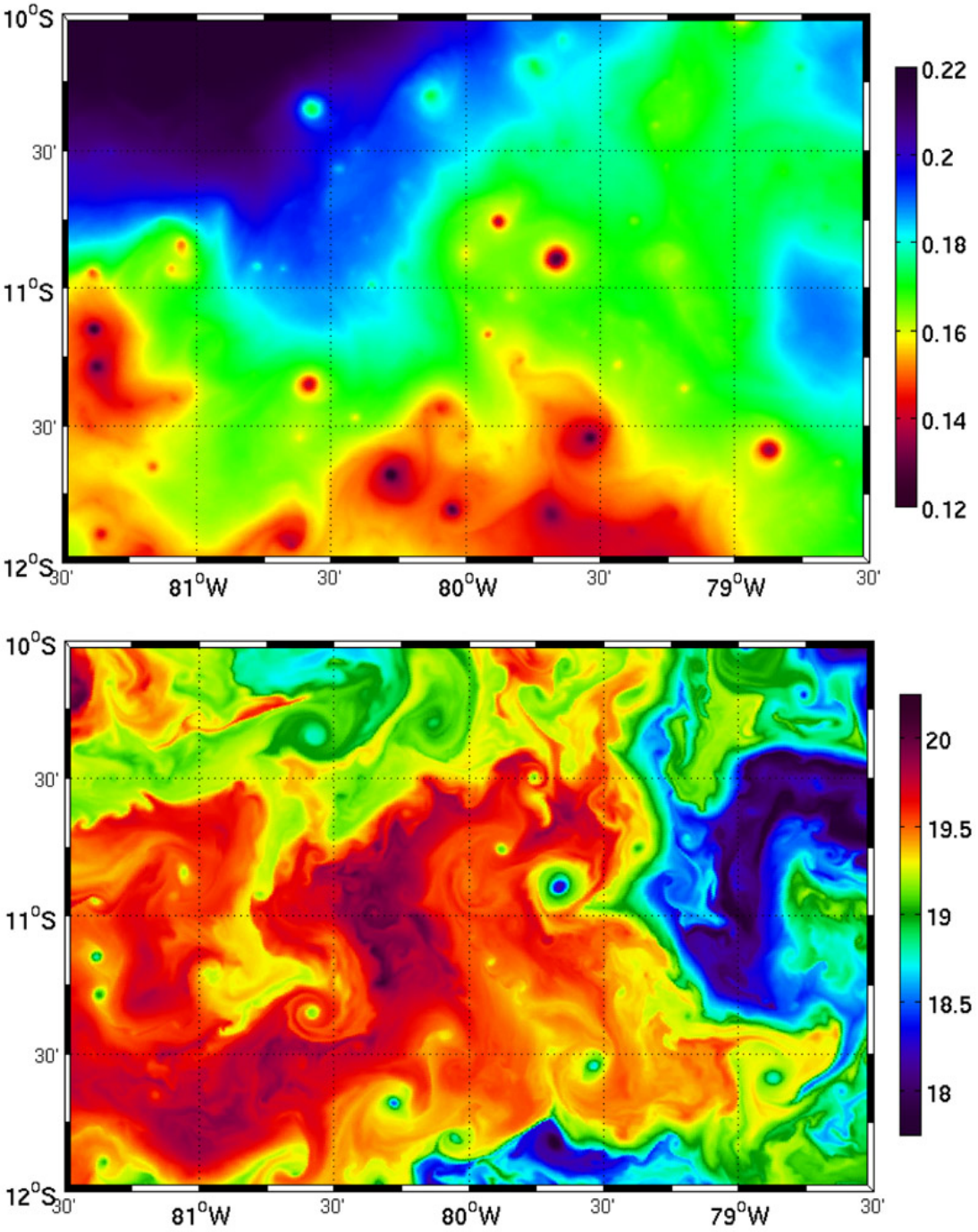

Figure 3.4-1. Snapshots of sea-surface height (m) (top) and temperature (ºC) (bottom) in a high-resolution numerical simulation of the Peru-Chile Current region in Austral winter. Note the submesoscale fronts and coherent vortices between the mesoscale eddies.

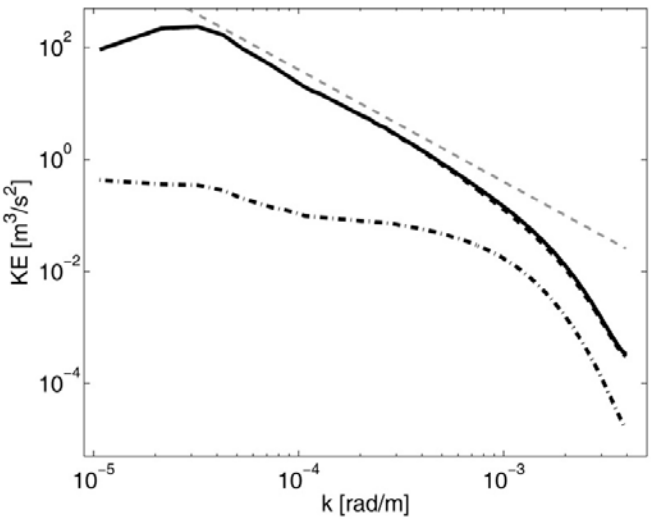

Figure 3.4-2. Horizontal wavenumber spectrum of surface horizontal eddy kinetic energy $K(k_h)$ in a numerical simulation of an idealized Subtropical Eastern Boundary Current: total (solid line), horizontally non-divergent (i.e., geostrophic) component (dark dash), and divergent (ageostrophic) component (dash-dot). Also shown is a k^{-2} power-law (light dash), which is an approximate fit in the submesoscale range for kh larger than the mesoscale spectrum peak. Note that most of the energy is geostrophic throughout this range, even though local breakdowns of geostrophic balance do occur. (Capet et al., 2008c)

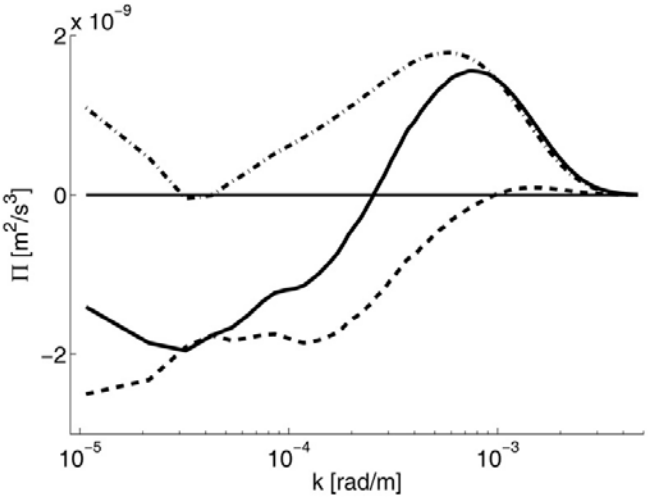

Figure 3.4-3. Horizontal wavenumber spectrum of the advective spectral flux of kinetic energy $\Pi(k_h)$ in the same numerical simulation as Figure 3.4-2: total (solid line), contribution from non-divergent (geostrophic) velocity alone (dash), and residual contribution involving the divergent velocity (dash-dot). $\Pi < 0$ at smaller k_h is the inverse kinetic energy cascade associated with the mesoscale and the larger submesoscale flows, and $\Pi > 0$ at larger k_h is the forward energy cascade associated with smaller submesoscale flows. Notice that the relatively small ageostrophic velocities are essential to the forward energy cascade behavior. (Capet et al., 2008c)

shallow kinetic energy spectrum shape, typically either k_h^{-2} for frontogenesis (Ferrari and Rudnick 2000) or $k_h^{-5/3}$ for surface-geostrophic and frontal-instability processes. The simplest altimetric analysis for horizontal currents is based on geostrophic balance, and it leads directly to estimates of the surface kinetic energy spectrum (Le Traon et al., 2008). This approach has been extended to diagnose the upper-ocean vertical velocity (Lapeyre and Klein 2006) and the kinetic energy spectral flux (Scott and Wang 2005), and these results are reliable for the mesoscale. However, since the submesoscale is only partially geostrophic, it is an important task to develop more general interpretative analysis methods for high-resolution altimetry. Nevertheless, the new altimetric measurements of sea level, together with high-resolution sea surface temperature, will be an extremely valuable means of exploring and better understanding oceanic mesoscale and submesoscale currents, their energy cascades, and oceanic routes to dissipation.

References

Capet, X., J. C. McWilliams, M. J. Molemaker, and A. Shchepetkin, 2008a–c: Mesoscale to submesoscale transition in the California Current System. I: Flow structure, eddy flux, and observational tests. II: Frontal processes. III: Energy balance and flux. J. Phys. Ocean., **38**, 29–43, 44–64, 2256–2269.

Charney, J., 1971: Geostrophic turbulence. J. Atmos. Sci., **28**, 1087–1095.

Ferrari, R., and D. Rudnick, 2000: Thermohaline variability in the upper ocean. J. Geophys. Res., **105**, 16857–16883.

Ferrari, R., and C. Wunsch, 2009: Ocean circulation kinetic energy: Reservoirs, sources and sinks. Ann. Rev. Fluid Mech., **41**, 253–282.

Lapeyre, G., and P. Klein, 2006: Dynamics of the upper oceanic layers in terms of surface quasigeostrophy theory. J. Phys. Ocean., **36**, 165–176.

Le Traon, P. Y., P. Klein, and B. L. Hua, 2008: Do altimeter wavenumber spectra agree with interior or surface quasigeostrophic theory? J. Phys. Ocean., **38**, 1137–1142.

McWilliams, J. C., 2008: Fluid dynamics on the margin of rotational control. Environ. Fluid Mech., **8**, 441–449.

Molemaker, M. J., J. C. McWilliams, and X. Capet, 2010a: Balanced and unbalanced routes to dissipation in an equilibrated Eady flow. J. Fluid Mech., **654**, 35–63.

Molemaker, M. J., and J. C. McWilliams, 2010b: Local balance and cross-scale flux of available potential energy. J. Fluid Mech., **645**, 295–314.

Scott, R., and F. Wang, 2005: Direct evidence of an oceanic inverse kinetic energy cascade from satellite altimetry. J. Phys. Ocean., **35**, 1650–1666.

3.5 Biogeochemical Processes

The photosynthesis of phytoplankton represents roughly half of the biological production on the planet. This Primary Production (PP) supports almost all marine life. It plays a key role in the global carbon cycle because phytoplankton growth, and its subsequent death and sinking, transports vast quantities of carbon out of the surface layer where it can be sequestrated for long times. Phytoplankton generally have limited or no swimming ability and are advected through the water by currents. Moreover, phytoplankton requires nutrients for growth and reproduction, and these inorganic nutrients are provided to the sunlit surface layer (where photosynthesis can take place) by hydro-dynamic transport. Thus, phytoplankton growth and distribution is strongly controlled by oceanic currents.

Observations from ocean-color satellites have shown that this control occurs over a large range of temporal and spatial scales. At the basin scale, productive regions are found where winter convection is important, such as the North Atlantic, or over strong upwellings, such as eastern boundary upwelling systems. Without losing sight of the large scale, the most remarkable phenomenon revealed by ocean-color is the ubiquitous imprint of mesoscale and submesoscale dynamical features on the distribution of phytoplankton. This discovery has raised the question of the importance of submesoscale biophysical coupling for the estimation of PP, for the functioning of the oceanic carbon pump, and for the distribution of phytoplankton in general. Given the space (1–10 km) and time (1–10 days) scales associated with submesoscale dynamics, their impact on phytoplankton can hardly be examined with standard in situ observations on a regional scale. A regional characterization of the processes is needed, however, to quantify the importance of the small-scale structures (e.g., filaments) on global primary production budgets. Such a regional approach at high resolution will hopefully reduce the errors in global PP estimates due to the misrepresentation of the submesoscale processes, both from models and from observation networks.

So far, the question of biophysical coupling at the submesoscale has been addressed mostly with models. In the past few years, high-resolution model studies have universally suggested that ocean biogeochemistry is extremely sensitive to submesoscale physics (see Lévy, 2008, for a review). The physical processes at play include dynamical re-stratification, horizontal stirring, and vertical advection. More precisely, frontogenesis triggers intense vertical velocities within submesoscale filaments and thus potentially stimulates PP under oligotrophic conditions (Figure 3.5-1, Lévy et al., 2001). A second mechanism, at play during the onset of the spring bloom when nutrients are plentiful, is related with the capacity of submesoscale dynamics to stratify the surface mixed-layer, thus accelerating the bloom over specific submesoscale features (Figure 3.5-2, Lévy et al., 2005). Models have also suggested that horizontal stirring is important in shaping the ecosystem (Abraham et al., 2000; Lévy and Klein, 2004) and in enhancing vertical nutrient supplies (Martin et al., 2002).

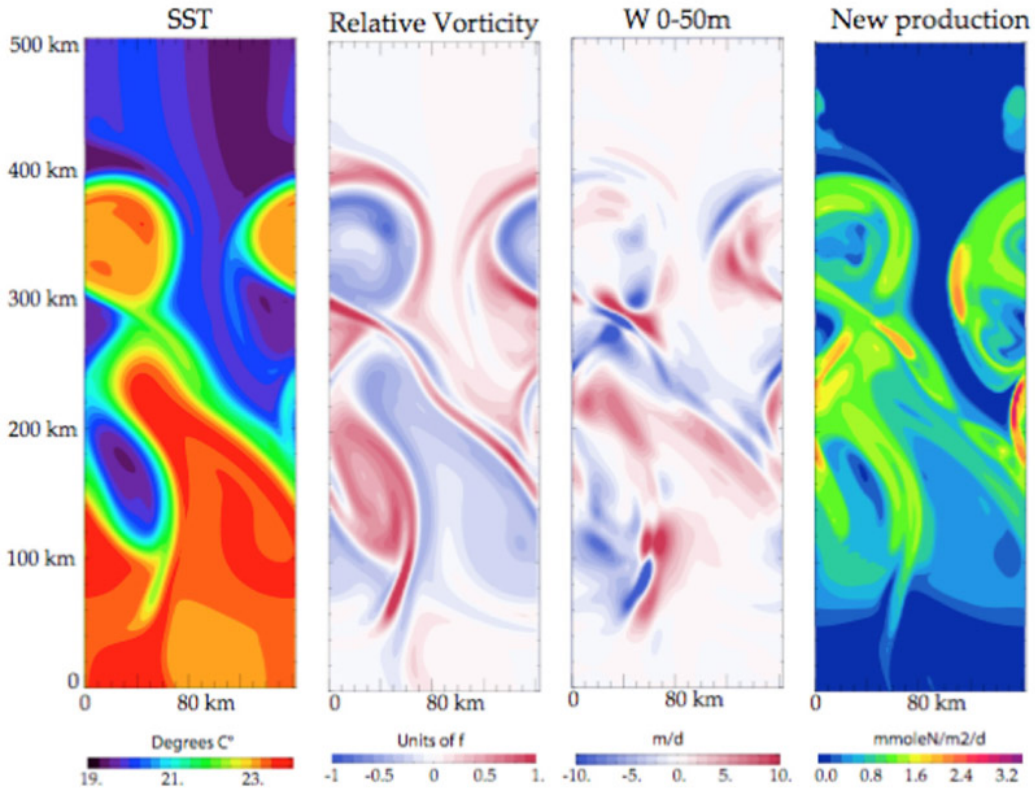

Figure 3.5-1. Model simulations of SST, vorticity, vertical velocity, and phytoplankton new production (NP), showing the increase of NP in submesoscale filaments in response to vertical advection, within an oligotrophic regime (after Lévy et al., 2001).

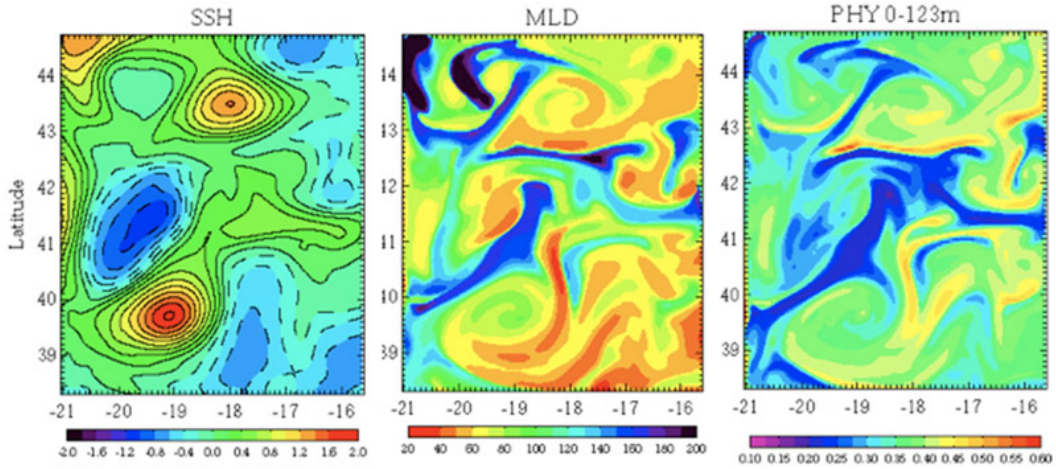

Figure 3.5-2. Model simulation of SSH, mixed-layer depth (MLD), and phytoplankton, showing the increase of phytoplankton in filaments of shallow MLDs, during the onset of the spring bloom (after Lévy et al., 2005).

However, the validation of these models is very limited, because we lack concomitant observations of biological and physical parameters at the submesoscale that would help to connect the response of the biology to the physics. Moreover, this validation is complicated by the fact that the physical and biological fields are not directly correlated; indeed, the distribution of phytoplankton reflects the cumulative effects of advective transport, nutrient supplies, and other biological processes. This apparent decorrelation was shown for instance by Lehahn et al. (2007), who examined phytoplankton filaments in the light of altimetry derived geostrophic currents (Aviso products). Their examination showed that the phytoplankton filaments do not follow the instantaneous stream lines; rather, they follow the lines of strong Lyapunov exponent, which integrate the information about the time variation of the flow and are thus better descriptors of stirring by advection (Figure 3.5-3).

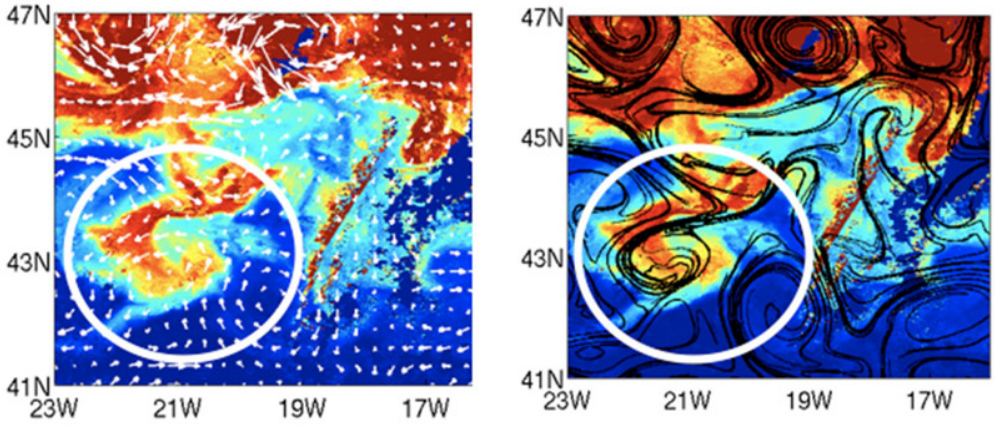

Figure 3.5-3. Sea-surface distribution of chlorophyll in the Northeast Atlantic observed by SeaWiFS during the spring bloom (colors), overlaid with geostrophic currents derived from altimetry (white arrows) and with lines of strong Lyapunov exponent (black lines). The region circled in white highlights a spiralling phytoplankton filament whose shape is consistent with the dynamical fronts deduced from the time-evolving flow (right panel) but not with the instantaneous circulation (left panel) (after Lehahn et al., 2007).

Thus, understanding submesoscale biophysical coupling requires following oceanic currents and the concentration of phytoplankton at the scale of a filament. This is difficult with the resolution of current altimeters. The method is also currently limited by the scarcity of high-resolution, cloud-free ocean-color images. The next generation of altimeters will enable us to precisely locate the submesoscale filaments, with information on the horizontal and vertical velocities, which is crucial for phytoplankton. The use of such an instrument in conjunction with high-frequency, high-resolution ocean-color data—such as those expected from ocean-color missions on geostationary orbits (such as the Korean ocean-color mission GOCI, to be launched by the end of 2009)—will enable the monitoring of the increase of phytoplankton at the scale of filaments and will pave the way to global and systematic detection and understanding of submesoscale biophysical coupling, and of its impact on phytoplankton.

A second important gap that next-generation altimetry is expected to fill is the high-precision, near-real time detection of filaments for campaign studies. A novel type of biogeochemical in situ studies is currently been designed in which a relatively isolated water mass (like the filament forming the core of a stable eddy) is monitored in the course of the bloom. The main advantages expected from this approach with respect to more traditional sampling strategies are (i) the reduction of the synopticity problem, since the same water mass is followed in time, and (ii) an improved observation of the coupling between physical and biological processes, since the temporal evolution of the filament is observed. Current altimetry provides some capabilities for the identification and tracking in near–real time of relatively isolated filaments, but its use is limited to large and stationary eddy cores. (See for instance the LOHAFEX campaign, Figure 3.5-4.) The possibility of having higher-resolution surface velocity field in support of these campaign studies would extend this approach to other ocean regions where large, stationary eddies may not necessarily be present. Even more importantly, such higher-resolution velocities would be instrumental in better quantifying the dilution processes occurring in filaments, allowing scientists to compute accurate biogeochemical budgets from the campaign measurements.

Finally, Lagrangian reanalyses of altimetry data, when complemented to other reanalyses of satellite data (SeaWiFS-PHYSAT), have been shown to open new perspectives for marine ecology. It has been shown that this multisatellite approach can reveal water patches with homogeneous physicochemical characteristics, and with lifetimes that are long enough for important ecological processes to take place, such as phytoplanktonic competition or predation (d'Ovidio et al., 2010). In this landscape of fluid dynamical niches, dynamical fronts appear to be colocalized with ecological fronts. This approach has been applied to the community structure of dominant phytoplanktonic types. Other studies have also considered higher levels of the trophic chain

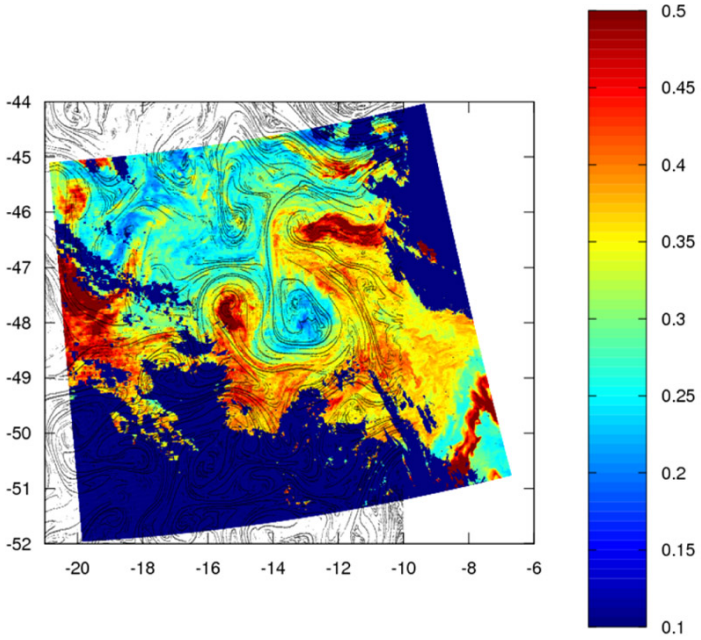

Figure 3.5-4. Observed chlorophyll concentration (color, mg/m^3) and lines of altimetry-derived fronts obtained with the Lyapunov exponent technique during the LOHAFEX* campaign (26 February 2009). The possibility of locating an isolated eddy core was a key aspect of the campaign, which aimed to follow the evolution of an iron-induced plankton bloom for several weeks. The fertilized eddy core is the one in 15° E, 48° S. Altimetry allowed to select the eddy and to track its core in near–real time for the entire duration of the experiment. (*LOHA is Hindi for iron, FEX stands for Fertilization Experiment.)

(including whales and marine birds (see Cotté et al., 2011 and references therein), showing that the distribution of marine predators is preferentially associated to altimetry-derived fronts. These studies are a first step towards understanding how the ecosystem inside a fluid dynamical niche can age and how the biomass can be transferred across the trophic chain. These studies have a strong interdisciplinary and societal interest, where the submesoscale regime plays a special role, as seen by the ocean-color images. The present generation of nadir altimetry data, once reanalyzed with Lagrangian diagnostics, allows us only to approach the submesoscale regime. The improved altimetric resolution available with SWOT data will change this substantially, allowing marine ecologists to fully explore a domain where transport and ecological interactions are expected to be strongest.

References

Abraham, E. R., C. S. Law, P. W. Boyd, S. J. Lavender, M. T. Maldonado, and A. R. Bowie, 2000: Importance of stirring in the development of an iron-fertilized phytoplankton bloom. Nature, **407**, 727–730.

Cotté, C., F. d'Ovidio, A. Chaigneau, M. Lévy, I. Taupier-Letage, C. Guinet, 2011: Scale-dependent interactions of resident Mediterranean whales with marine dynamics. 23. Limnology and Oceanography, **56**, 219–232

d'Ovidio, F., S. De Monte, S. Alvain, Y. Danonneau, and M. Lévy, 2010: Fluid dynamical niches of phytoplankton types. Proc. Nat'l. Acad. of Sciences, **107**, doi:10.1073/pnas.1004620107, 18366–18370.

Lehahn, Y., F. d'Ovidio, M. Lévy, and E. Heitzel, 2007: Stirring of the Northeast Atlantic spring bloom: a lagrangian analysis based on multi-satellite data. J. Geophys. Res., **112**, C08005, doi:10.1029/2006JC003927.

Lévy, M., 2008: The modulation of biological production by oceanic mesoscal turbulence. Lect. Notes Phys., **744**, doi10.1007/978-3-540-75215-8_9. In Transport in Geophysical Flow: Ten Years After. Eds. J. B. Weiss and A. Provenzale, Springer, 219–261.

Lévy, M., and P. Klein, 2004: Does the low frequency variability of mesoscale dynamics explain a part of the phytoplankton and zooplankton spectral variability? Proc. Royal Soc. Lon, **460**(2046), doi:10.1098/rspa.2003.1219, 1673–1683.

Lévy, M., P. Klein, and A.-M. Treguier, 2001: Impacts of sub-mesoscale physics on phytoplankton production and subduction. J. Mar. Res., **59**, doi: 10.1357/002224001762842181, 535–565.

Lévy, M., M. Gavart, L. Mémery, G. Caniaux, and A. Paci, 2005: A 4D-mesoscale map of the spring bloom in the northeast Atlantic (POMME experiment): results of a prognostic model. J. Geophys. Res., **110**(C7), C07S21, doi: 10.1029/2004JC002588

Martin, A. P., K. J. Richard, A. Bracco, and A. Provenzale, 2002: Patchy productivity in the open ocean. Global Biogeochem. Cycles, **16**(2), doi:10.1029/2001GB001449, 1025–9pp.

3.6 Coastal Processes

Even more than they do in the deep ocean, several processes in the coastal ocean create strong currents with short spatial and temporal scales (~10 km, 2–10 days) that cannot be resolved by conventional altimeters, even in combinations of 2 or 3. These coastal ocean regions are of increasing societal concern, due to the importance (and vulnerability) of coastal ecosystems and the increased use of the coastal oceans by human populations.

In regions with narrow shelves, alongshore winds create alongshore upwelling and downwelling jets with cross-jet scales of 10–20 km that can change position (onshore-offshore) by tens of kilometers or reverse directions (responding to winds) over periods of 2–5 days. Figure 3.6-1 (left) shows vertical cross-shelf sections of temperature and alongshore velocity next to the coast of Oregon at 45° N with examples of alongshore jets next to the coast with alternating directions and widths of 5–20 km. Figure 3.6-1 (right) shows a map of the current field at 25 m depth from the same period as the sections. The sections in Figure 3.6-1 (left) are from the northern end of the map in Figure 3.6-1 (right). These sections demonstrate the result of a reversal of narrow nearshore jets (from southward to northward) during a 2-day relaxation of the southward winds (Barth et al., 2005a).

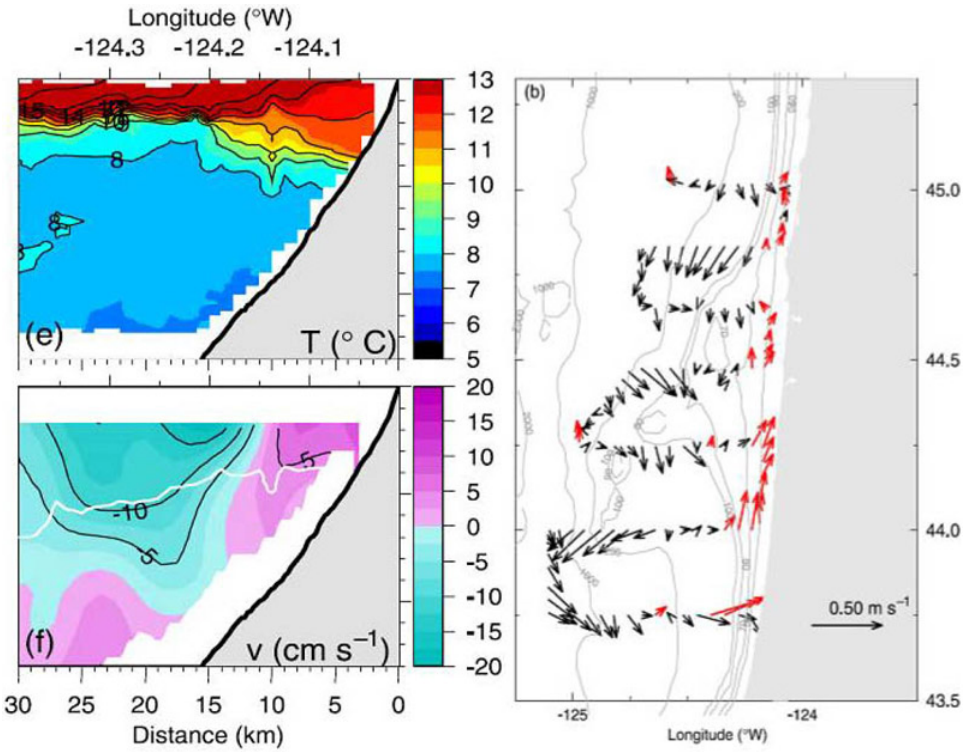

Figure 3.6-1. (Left) Cross-shelf section of temperature (top) and alongshore velocity (bottom) at 45° N on August 25 during a 2-day reversal of winds from southward to northward during August 24-25, 2001. (Right) Velocity vectors at 25-m depth from shipboard Acoustic Doppler Current Profiler (ADCP) measurements during the same 2-day period.

Over wider shelves (or where narrow shelves widen, as in Figure 3.6-1), variations in bottom bathymetry exert strong control of the location of jets and eddies, which interact with the wind-driven currents. Figure 3.6-2 shows the tracks of surface drifters off the Oregon coast, demonstrating pathways that initially follow the bathymetry around a local submarine bank but that ultimately overshoot and follow several different paths. Some go offshore; some recirculate around an eddy southeast of the bank, proceed southward along the shelf-break, and then go offshore, deflected by a prominent cape, etc. (Barth et al., 2005b).

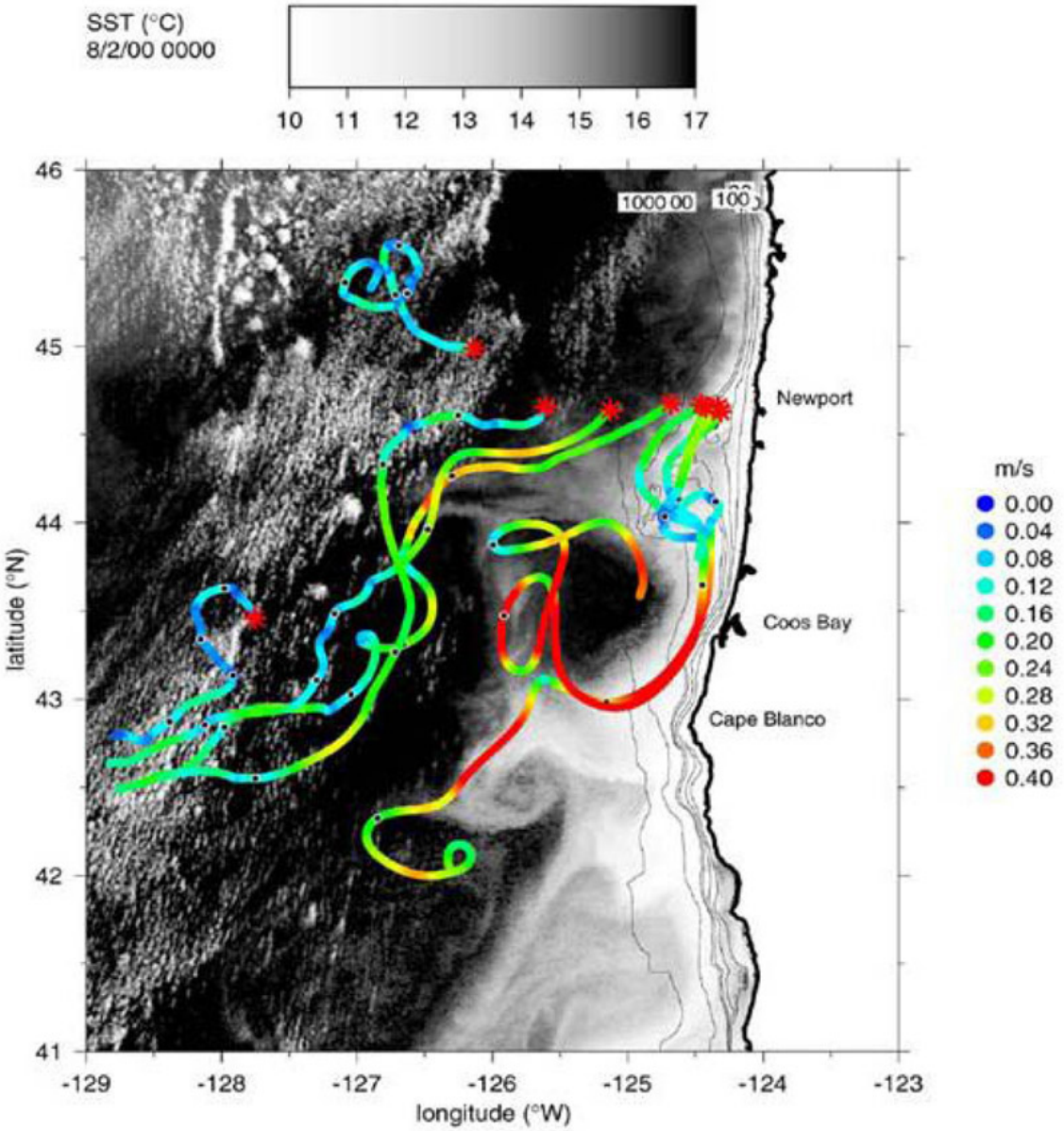

Figure 3.6-2. Drifter trajectories from July 8-August 11, 2000, overlaid on an SST image from August 2. Tracks are color coded by drifter speed; black bullets are at 7-day intervals. Red asterisks mark the initial locations on July 8. The 50-, 70-, 90-, 100-, 200-, and 1000-m isobaths are shown.

Currents in these jets transport substances 10–100 km/day (6–60 miles/day), both in the alongshore and onshore-offshore directions. In operational settings, coastal managers need to know and/or predict these currents accurately to determine pathways for spills of toxic materials, movement of blooms of toxic algae or anoxic water conditions, most probable search areas for missing persons or disabled boats, originating locations for material discharged from ships or shore, etc. Changes in these currents also bring different water properties to a region, affecting the growth and survival of kelp beds and larval/juvenile coastal fish and benthic invertebrate species, populations of aquacultured fish and shellfish, etc. The currents also create the patterns of SST that affect the creation of local fog and coastal weather.

The proposed SWOT altimeter, with horizontal resolution of 0.5–1.0 km, will help to resolve these small-scale coastal currents within each 120 km-wide swath, extending to within 0.5–1.0 km of the coast. To retrieve these data, several technical improvements need to be made in the geophysical and atmospheric corrections used with the raw altimeter data. The primary challenges are the tidal corrections and wet troposphere delay. Resolving the tidal and other high-frequency barotropic signals is discussed separately (see section 5.1). Atmospheric fronts in the coastal region produce strong gradients in atmospheric moisture that affect the wet troposphere path delay, which are not resolved well by the onboard microwave radiometer used to estimate the integrated atmospheric water vapor along the radar path. The radiometer's signal is also affected by the presence of land in its footprint. These problems are presently being addressed by a combination of: (1) improved radiometer retrieval techniques that take into account the land's contribution to the radiometer signal; and (2) use of atmospheric moisture fields from very high-resolution atmospheric models, developed for regional coastal weather forecasts. Other altimeter-correction terms are also the subject of ongoing research and improvement.

Even with perfect retrieval of the altimeter data within each swath, the time between swath repeats at a given location (every 2–20 days, depending on the geographical position) will not provide the temporal resolution needed to observe rapid changes in coastal currents. Furthermore, the altimeter measures only the surface height and geostrophic currents, missing subsurface shears and ageostrophic currents (such as surface Ekman drift). Numerical models are needed to assimilate the altimeter data, along with other coastal ocean observations, and to provide the dynamical interpolation of the surface currents, their extension to depth, and the inclusion of ageostrophic effects. Fortunately, the coastal ocean provides several advantages for dynamical modeling: (1) Currents over the shelf are strongly wind-driven, allowing models to fairly accurately predict the non-tidal currents, given accurate wind fields (from improved weather forecast models). Currents are also fairly deterministic, through coastal trapped wave dynamics, due to the presence of the coastal boundary and bottom topography. (2) Coastal observing systems are being put in place that will provide an increased number of observations to constrain the models between altimeter repeats. These observations

include surface currents from coastal radars (which have their own sampling limitations), moored current and density measurements at fixed locations, and sections of density and currents from autonomous underwater vehicles. The last two systems provide information about the subsurface fields.

As an example of the utility of altimeter data in improving coastal models through assimilation, Figure 3.6-3 shows SST fields from a coastal model without data assimilation (left), with assimilation of SSH data from the single track decending from 46° N to the southeast (middle) and from a satellite infrared field from the same period (right). Since SST was not assimilated, the improvement in agreement of model and satellite SST gives greater confidence in the model surface velocities and subsurface fields.

For most purposes, the standard coverage planned for the SWOT oceanographic sampling (0.5–1.0 km resolution SSH) will suffice for coastal ocean regions. For a few applications, however, the higher-resolution, but noisier, raw data will be useful. These applications primarily involve interactions of the nearshore ocean and "inland" waters—rivers, bays, and shallow wetlands. Strong changes in sea surface heights in these regions are caused by tides, inland flood waters, and wind-driven storm surges. For tide-driven

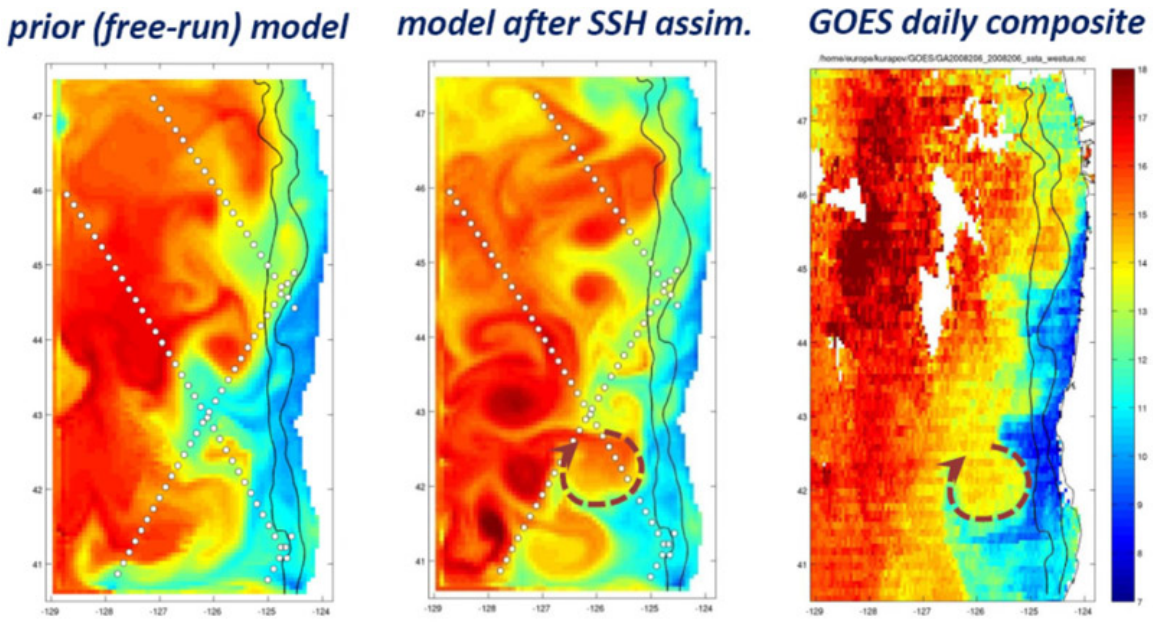

Figure 3.6-3. Comparison of the SST (July 24, 2008) in the model before SSH assimilation (left), model after SSH assimilation (middle), and geostationary satellite (right) shows that assimilation of alongtrack SSH helps to improve geometry of the upwelling front. For instance, the anticyclonic eddy is apparent in both the model after altimetry assimilation and in the satellite SST (outlined with arrows). This eddy is not found in the model without assimilation. Also, as a result of SSH assimilation, the cold SST tongue extending westward at 43° N is reduced, in better correspondence with the observed SST. [NOTE: In this case SST is not assimilated, but used only to validate SSH assimilation results]. (Unpublished results from the coastal Regional Ocean Modeling System (ROMS) model provided by Alexandre Kurapov)

changes, the repeatability of the cycles will allow repeated sampling of each phase of the tides to reduce the noise and reveal high-resolution details of tidal circulations into and out of bays and harbors, changes in sea level over wide and shallow shelves, periodic wetting and drying of wetlands and mangroves, etc. For non-tidal forcing over shallow regions with complex bathymetry, new methods of data assimilation into high-resolution, nearshore models will be encouraged by the availability of these data. As with standard SWOT data, the temporal coverage will not allow the high resolution data to resolve the evolution of the nearshore SSH fields, but the coverage will provide snapshots for testing of new assimilation techniques and for model validation.

In summary, the SWOT altimeter will provide data needed to resolve the small-scale spatial variability in coastal currents within each swath. In remote locations without additional data or modeling efforts, this will provide information allowing a statistical and phenomenological description of SSH and transports by coastal currents (retrospectively). In regions with operational coastal observing systems, combination of the SWOT altimeter fields with other observations and dynamical models will provide real-time fields and predictions needed for a variety of applications with societal impacts. These include the prediction of trajectories for toxic/noxious substances, search and rescue, fisheries, navigation (fuel conservations), etc. As with weather prediction, the number of applications will grow as the observing and modeling systems mature and new products are developed from the surface current fields.

References

Barth, J. A., S. D. Pierce, and R. M. Castelao, 2005a: Time-dependent, wind-driven flow over a shallow midshelf submarine bank. J. Geophys. Res., **110**, C10S05, doi:10.1029/2004JC002761.

Barth, J. A., S. D. Pierce, and T. J. Cowles, 2005b: Mesoscale structure and its seasonal evolution in the northern California Current system. Deep-Sea Res., Part II, **52**, 5–28.

4 TERRESTRIAL HYDROLOGY: STORAGE AND DISCHARGE OF WATER ON LAND

Discharge and Changes in Storage

Given our basic need for fresh water, perhaps the most important hydrologic observations that can be made are of the temporal and spatial variations in surface water distributed across the continents. These observations include discharge (Q) of water flowing in rivers and the changes in stored water volumes (ΔS) in lakes, reservoirs, wetlands, and floodplains. There is widespread recognition of the need for better observations and understanding of surface water distribution globally (e.g., Marburger and Bolten, 2004, 2005; United Nations, 2004; IWGEO, 2005; NSTC, 2004) especially in view of the fact that over one-third of the world's population is not served by adequate supplies of clean water (Gleick, 2003). Even in the United States, where existing in situ stream gauging networks include thousands of monitoring stations, we are still left with the question of unknown water availabilities (NSTC, 2004). The problem is worse outside of the industrialized world (IAHS, 2001; Stokstad, 1999; Shiklomanov et al., 2002).

Lacking global observations of surface water dynamics leads to many basic questions. The following are only just a sampling of these questions. (1) What is the global distribution of freshwater runoff delivered to rivers, lakes, and ultimately to oceans; and, importantly, how does this influence interseasonal and interannual water budgets across basins? (2) How much water is stored on a floodplain and subsequently exchanged with its main channel, and how do these exchanges influence biogeochemical fluxes of carbon and nutrients on both local and global scales? (3) What are the local-to-global scale responses of surface waters to climate-induced changes? (4) What are the water surface elevations across a flood wave in urbanized and natural environments, and what are the corresponding extents of inundation? (5) What are the policy implications that freely available water storage data would have for water management, particularly for rivers that cross international boundaries? (6) Can health issues related to waterborne diseases be predicted through better mappings? All of these questions are addressed in sections 4.1 through 4.6.

Alsdorf and Lettenmaier (2003) have considered these questions and determined that answering them will require fundamentally different approaches to measuring surface water storage and rates of change. Hydraulic measurements that are central to the fluid equations of motion include elevations of the water surface (h), temporal changes in water levels ($\partial h/\partial t$), water surface slope ($\partial h/\partial x$), and inundated area. Essentially, temporally repeated measurements of h provide a basis for estimating $\partial h/\partial t$, which summed over an inundated area is a measure of the volume of water lost or gained over a time interval (i.e., ΔS). Water storage is an essential variable in continuity-based

estimates of mass balance, whereas h is a state variable in hydrodynamic models that predict flow hydraulics through channels and wetlands.

The New Challenges for SWOT

Because SWOT represents a fundamentally new approach to measuring discharge and storage change, there are many scientific and application opportunities, and hence new challenges, that SWOT will allow us to address. The following presents just a couple of these challenges. Sections 4.1 through 4.6 highlight additional exciting challenges.

A 2006 study has suggested that there are over 300 million lakes in the world that are larger than 0.1 hectare and 30 million larger than 1.0 hectare (Downing et al., 2006). This study is based on local-to-regional studies and log-log statistical extrapolations of these to global scales. Ideally, existing remote sensing data would constrain these numbers, but as shown by Frey and Smith (2007), such classifications are often in error. For example, four different classifications of West Siberian wetlands and open water bodies agree with each other or with ground truth as little as 2% (Frey and Smith, 2007). Most of the world's lakes occur north of 45° N (Lehner and Doll, 2004), and yet almost none have been gauged or measured with altimetry.

This lack of knowledge has led to a key paper in *Science* by Smith et al., (2005), which showed that Arctic lakes are disappearing because permafrost beneath these lakes is degrading in local spatially heterogeneous patterns (e.g., Figure 4-1). On a regional scale, a pattern emerges showing that southern lakes are disappearing at a greater rate than northern lakes and hence suggests a connection of storage changes to increased temperatures, i.e., global warming causing the permafrost to degrade.

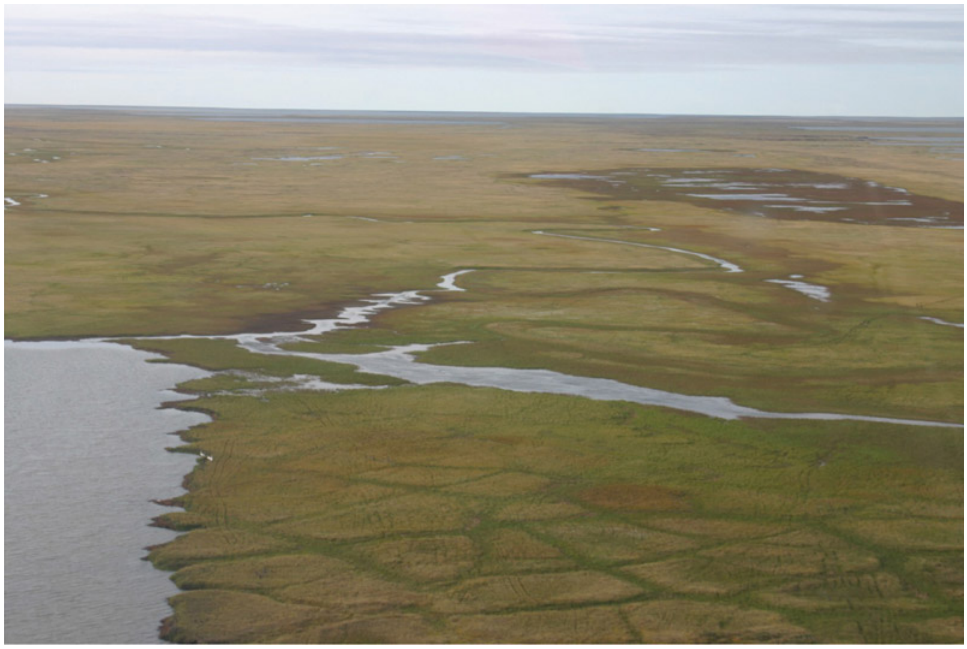

Figure 4-1. Disappearing arctic lakes in Barrow, Alaska (Smith et al., 2005).

This lack of knowledge also calls into question the amount of storage change that can be ascribed to the numerous small lakes. Biancamaria et al. (2010) used log-normal statistics to estimate variations in lake water elevations and combined their results with the global lakes abundance work of Downing et al. (2006, noted above) to suggest that 50% of the total storage change (i.e., as summed from all lakes) is from lakes having a surface area of 1 km^2 or less. This estimate, if correct, represents about 4500 km^3 of annual storage variation, which is about eight times larger than the annual discharge of the Mississippi River—yet, it presently goes unmeasured.

Another example of one of the challenges that SWOT will allow us to address is wetland flows and flooding dynamics. Floods, whether driven by fluvial processes or coastal storms, are the number one natural hazard in terms of life or economic losses (Cutter and Emrich, 2005). Outside of the Florida Everglades, essentially no wetland or floodplain is gauged, and thus we have almost no measurements to constrain hydrodynamic modeling predictions of floodwater dynamics (e.g., rising waters, inundation changes, flow velocities and related forces). Floodplains and wetlands fill and empty via several processes, including water exchanged with the mainstem river or with local tributaries, overland flows from adjacent higher, nonflooded ground, precipitation falling directly on the floodplain, and exchange with groundwater (Mertes, 1997). All of these processes represent different sources of carbon, nutrients, and sediment and hence a mix within the floodplain or wetland. They also alter conventional viewpoints that floodplain waters are dominated by simple exchange with the mainstem river. Thus, we are left with open questions regarding the global carbon fluxes from wetlands (e.g., Richey et al., 2002), the sediments deposited on the floodplain or the nutrients exchanged with the main river (Dunne et al., 1998; Smith and Alsdorf, 1998), and the dynamics of floods (Alsdorf et al., 2007a; 2007b).

The Current State of Knowledge

Interseasonal and interannual variations in surface water storage volumes—as well as their impact on precipitation, evaporation, infiltration, and runoff—are not well known. The terrestrial water balance equation used in hydrologic models and as applied to a river basin is:

$$\boldsymbol{P} - \boldsymbol{E} = Q_s + Q_g + d\boldsymbol{S}/dt \qquad (4\text{-}1)$$

where $\boldsymbol{P}$ and $\boldsymbol{E}$ are basin-average precipitation and evaporation, respectively; Q_s is river discharge; Q_g is groundwater discharge across the basin boundary; and $\boldsymbol{S}$ is the total surface and subsurface storage (summed from soil moisture, snow water content, surface water storage, vegetation water content, ground water, and glaciers (e.g., Lettenmaier, 2005). Each of the variables in equation 4-1 is known only with considerable (in most cases) uncertainty because of disparate sampling densities, poor political or economic support, or inability to make an accurate measure. Estimation of $\boldsymbol{E}$, and the storage change term, however, is particularly problematic. $\boldsymbol{E}$ is often estimated as the closure

term; and over long-term averages, d***S***/dt is often ignored.However, the latter approach precludes consideration of surface water dynamics, and even over long periods of time, storage change can be important.

So, essentially, the current state of measurement-based knowledge is poor. As a simple example, the stream gauge density (expressed as number of gauges per unit discharge) in the Amazon River is roughly four orders of magnitude less than a typical area in the eastern United States. The situation is worse in the Congo River. Conventional altimetry has offered some promise to make water surface elevation measurements (e.g., Birkett, 1998; 1995; Birkett and Doorn, 2004, Birkett et al., 2002; Cretaux et al., 2005; Frappart et al., 2006; Hwang et al., 2005; Kouraev et al., 2004; Maheu et al., 2003; Mercier et al., 2002), but these suffer key problems. (1) Profiling altimetry has significant gaps between orbits—usually on the order of hundreds of kilometers. Thus, because of their small size, the disappearing Arctic lakes (Smith et al., 2005; noted above) cannot be measured, even with a large collection of simultaneously operating altimeters. Quantitatively, pulse-limited altimeters collecting samples only along a profile severely under-sample rivers and lakes. For example, using a profiling instrument and a 16-day orbital repeat cycle, like that of Terra, misses ~30% of the world's rivers and ~70% of its larger lakes (Alsdorf et al., 2007b). (2) Altimetry methods measure the water surface elevation at a point where the orbit crosses the river. To convert this point observation to discharge, researchers rely on in situ gauges to provide the discharge estimate, which is then correlated with the altimeter elevation measurement. Clearly, this approach does not work where gauges are lacking, e.g., the entire Congo Basin and its discharge, which is second only to the Amazon. Furthermore, water slope measurements from altimetry are not dh/dx; rather, they are created from two orbital overpasses separated by significant gaps in space and time (e.g., dx is well over 100 km and dt is involved in the slope estimate as (dh/dt)/dx). Because rivers change slope on shorter time and spatial scales, conventional altimetry will not provide the hydraulic measurements necessary to understand river flows. (See Alsdorf et al., 2007b for more details.)

The Breakthrough of SWOT

SWOT will provide two-dimensional measurements of surface waters. This breakthrough is a substantial change from our existing collection of one-dimensional gauge and altimetric measurements. Water flow and storage changes are fundamentally a two-dimensional process. (The third, or vertical, dimension can be ignored because surface water flow is often shallow compared to the two lateral dimensions; e.g., consider the long distances that water flows along a river compared to the depth of the river.)

The Breakthrough for Discharge

Figure 4-2 provides an example of the expected breakthrough from SWOT's two-dimensional measurement capabilities. The model-based simulation shows discharge along 400 km of flow distance on the Kanawha River, a tributary of the Ohio River, located in southern West Virginia, and draining about 32,000 km^2 (Durand et al., 2010).

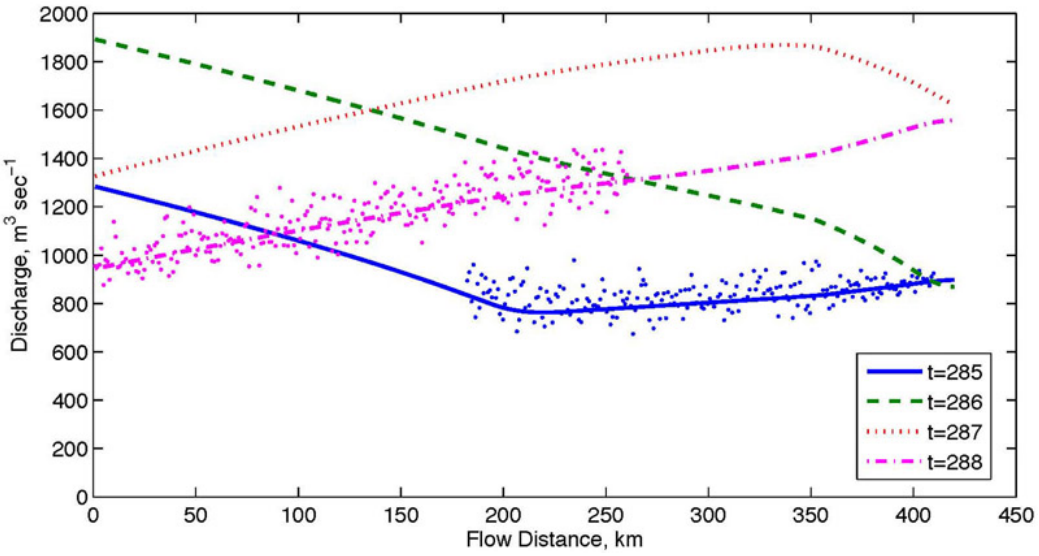

Figure 4-2. SWOT simulated discharge along the Kanawha River (Durand et al., 2010)

SWOT will provide discharge estimates all along the river channel, rather than at just a couple of gauging points. This simulation shows some of the expected errors from SWOT, such as those from the height accuracy of the technology (i.e., the distribution of the dots along the model discharge profiles). Polynomial averaging schemes will significantly reduce these errors (e.g., LeFavour and Alsdorf, 2005). As demonstrated by the simulation, SWOT will allow a mapping of discharge and its changes along entire river reaches and with time, and hence, an ability to map flood waves progressing downstream. By combining SWOT's measurements with hydrodynamic and hydrologic modeling in a data assimilation (Durand et al., 2008; Andreadis et al., 2007), discharge throughout entire stream networks will be produced on a regular basis. For example, Figure 4-3 shows a mapping of the Ohio Basin stream network, where SWOT is expected to provide discharge estimates. Such data products are expected from SWOT for all basins throughout the world.

The Breakthrough for Storage Change

Figure 4-4 shows an example of the expected SWOT accuracies when estimating storage changes in Arctic lakes. Because of the paucity of lake measurements, a "truth" data set (blue lines) was created using a statistical combination of gauge- and altimetry-derived water surface elevations, with lake areas derived

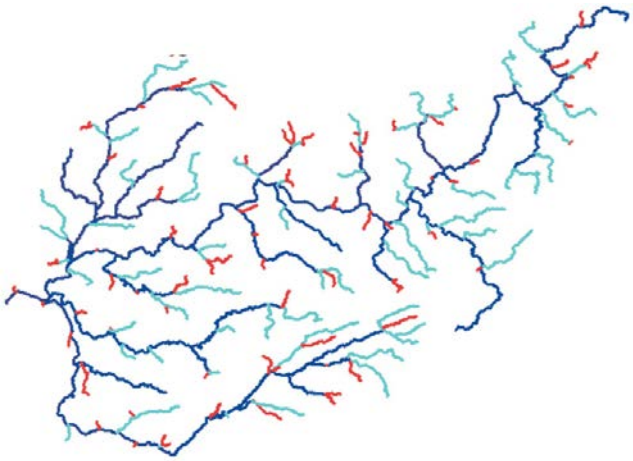
Figure 4-3. Expected SWOT coverage of rivers in the Ohio Basin. (Personal Communication, Elizabeth Clark, University of Washington, 2012.)

from satellite imagery (Lee et al., 2010). This truth was sampled using the SWOT orbit and using the instrument height and spatial accuracies to create the expected storage changes estimated by SWOT (red lines). Because height errors decrease with the number of pixels averaged, large lakes have a better relative accuracy compared to smaller lakes. Nevertheless, small lakes will still be sampled with significant accuracy. Even lakes one-hectare in size will be well sampled, with only ~20% errors in storage change.

On a global basis, SWOT science requirements will result in an accurate sampling of about half of all storage change occurring globally (Figure 4-5). The SWOT science goal of sampling 250 m×250 m–sized water bodies will result in about two-thirds of global storage changes being sampled. If, as expected, the mission successfully samples one hectare–sized lakes (i.e., Figure 4-4), then about 80% of all storage change in the world will be measured on a regular basis.

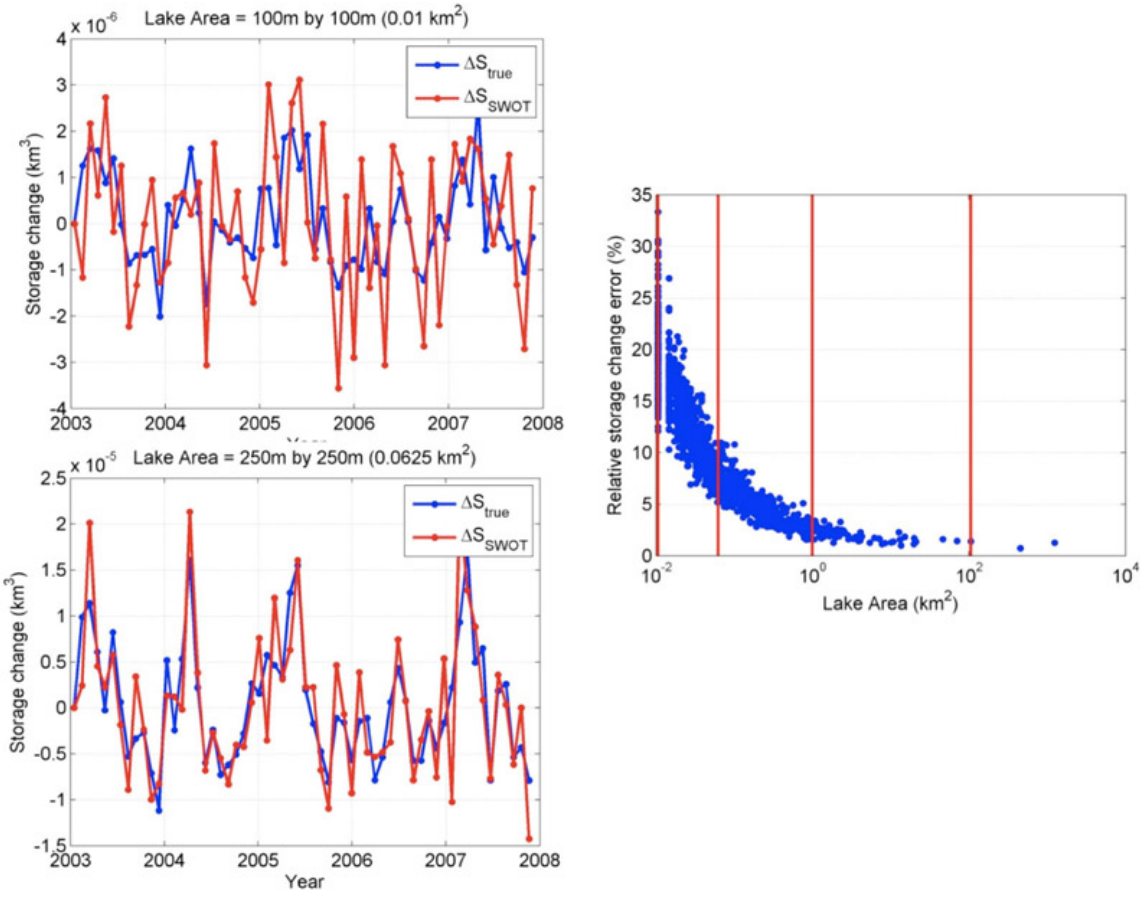

Figure 4-4. Expected SWOT accuracies when measuring storage changes (Lee et al., 2010).

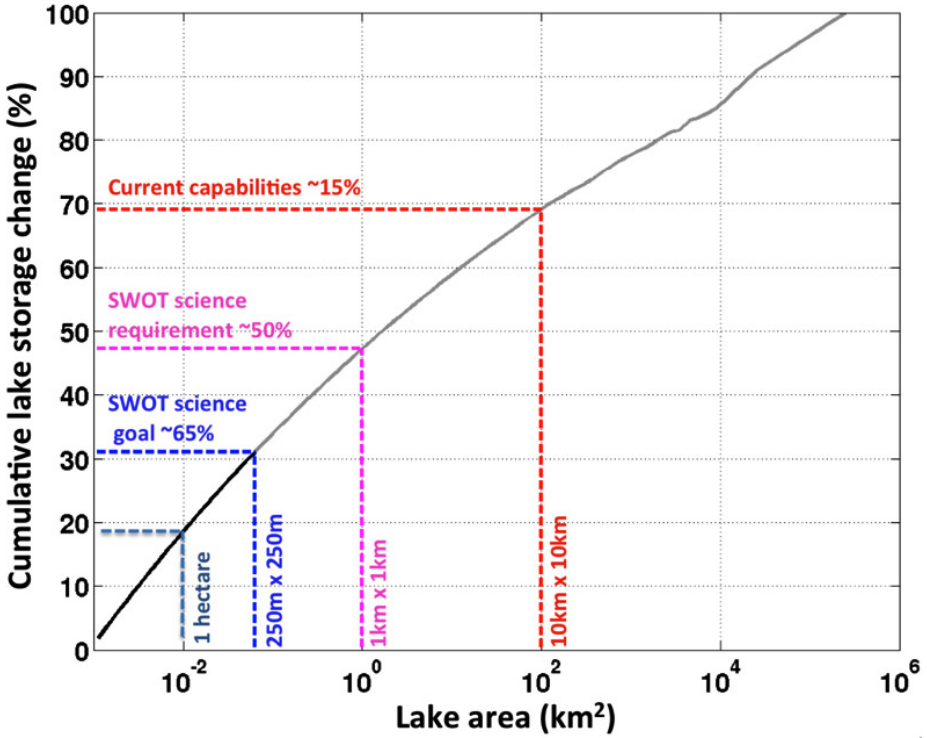

Figure 4-5. Improvement in global storage changes from SWOT (Bianacmaria et al., 2009)

These two breakthroughs are only possible with SWOT. No other method—whether in situ, airborne, or combination of satellites—allows a global comprehensive coverage with sufficient height and spatial accuracy to provide the measurements necessary for answering the many hydrologic science questions.

References

Alsdorf, D. E., and D. P. Lettenmaier, 2003: Tracking fresh water from space. Science, **301**, 1485–1488.

Alsdorf, D., P. Bates, J. Melack, M. Wilson, and T. Dunne, 2007a: The spatial and temporal complexity of the Amazon flood measured from space. Geophysical Research Ltrs., **34**, L08402, doi:10.1029/2007GL029447.

Alsdorf, D. E., E. Rodriguez, and D. Lettenmaier, 2007b: Measuring surface water from space. Reviews of Geophysics, **45**(2), RG2002 doi:10.1029/2006RG000197.

Andreadis, K. A., E. A. Clark, D. P. Lettenmaier, and D. E. Alsdorf, 2007: Prospects for river discharge and depth estimation through assimilation of swath-altimetry into a raster-based hydrodynamics model. Geophysical Research Ltrs., **34**, L10403, doi:10.1029/2007GL029721.

Biancamaria, S., K. M. Andreadis, M. Durand, E. A. Clark, E. Rodriguez, N. M. Mognard, D. E. Alsdorf, D. P. Lettenmaier, and Y. Oudin, 2010: Preliminary characterization of SWOT hydrology error budget and global capabilities. IEEE Journal of Selected Topics in Applied Earth Observations and Remote Sensing,**3**(1), 6–19.

Birkett, C. M., 1998: Contribution of the TOPEX NASA radar altimeter to the global monitoring of large rivers and wetlands. Water Resources Research, **34**, 1223–1239.

Birkett, C. M., 1995: The contribution of TOPEX/Poseidon to the global monitoring of climatically sensitive lakes. J. Geophys. Res., **100**, 25179–25204.

Birkett, C., and B. Doorn, 2004: A new remote-sensing tool for water resources management. Earth Observation Magazine, **13**(6), 20–21.

Birkett, C. M., L. A. K. Mertes, T. Dunne, M. H. Costa, and M. J. Jasinski, 2002: Surface water dynamics in the Amazon basin: Application of satellite radar altimetry. J. Geophys. Res., **107**, 10.1029/2001JD000609.

Cretaux, J.-F., A. V. Kouraev, F. Papa1, M. Bergé-Nguyen, A. Cazenave, N. Aladin, and I. S. Plotnikov, 2005: Evolution of sea level of the Big Aral Sea from satellite altimetry and its implications for water balance. J. Great Lakes Res. **31**(4), 520–534.

Cutter, S. L., and C. Emrich, 2005: Are natural hazards and disaster losses in the U.S. increasing? EOS Transactions of the American Geophysical Union, **86**(41), 2005.

Downing, J. A., and 10 others, 2006: The global abundance and size distribution of lakes, ponds, and impoundments. Limnology & Oceanography, **51**(5), 2388–2397.

Dunne T., L. A. K. Mertes, R. H. Meade, J. E. Richey, and B. R. Forsberg, 1998: Exchanges of sediment between the flood plain and channel of the Amazon River in Brazil. Geol. Soc. Amer. Bull., **110**, 450–467.

Durand, M., K. Andreadis, D. Alsdorf, D. Lettenmaier, and D. Moller, 2008: Estimation of bathymetric depth and slope from data assimilation of swath altimetry into a hydrodynamic model. Geophys. Research Ltrs., **35**, L20401, doi:10.1029/2008GL034150.

Durand, M., E. Rodriguez, D. E. Alsdorf, and M. Trigg, 2010: Estimating river depth from remote sensing swath interferometry measurements of river height, slope, and width. IEEE Journal of Selected Topics in Applied Earth Observations and Remote Sensing,**3**(1), 20–31.

Frappart, F., S. Calmant, M. Cauhope, F. Seyler, and A. Cazenave, 2006: Preliminary results of ENVISAT RA-2-derived water levels validation over the Amazon basin. Remote Sensing of Environment, **100**, 252–264.

Frey, K. E., and L. C. Smith, 2007: How well do we know northern land cover? Comparison of four global vegetation and wetland products with a new ground-truth database for West Siberia. Global Biogeochemical Cycles, **21**, GB1016, doi:10.1029/ 2006GB002706.

Gleick, P. H., 2003: Global freshwater resources: Soft-path solutions for the 21st century. Science, **302**, 1524–1528.

Hwang, C., M.-F. Peng, J. Ning, J. Luo, and C.-H. Sui, 2005: Lake level variations in China from TOPEX/Poseidon altimetry: Data quality assessment and links to precipitation and ENSO. Geophysical Journal International, **161**, 1–11.

IAHS (Ad Hoc Group on Global Water Data Sets), 2001: Global water data: A newly endangered species. Forum article in EOS Transactions of AGU, **82**, 54–58.

IWGEO, Interagency Working Group on Earth Observations, 2005: Strategic Plan for the U.S. Integrated Earth Observation System. U.S. President's National Science and Technology Council, http://www.whitehouse.gov/sites/default/files/microsites/ostp/eocstrategic_plan.pdf. Last accessed December 31, 2011.

Kouraev, A. V., E. A. Zakharovab, O. Samainc, N. M. Mognard, and A. Cazenave, 2004: Ob' river discharge from TOPEX/Poseidon satellite altimetry (1992–2002). Remote Sensing of Environment, **93**, 238–245.

Lee, H., M. Durand, H.-C. Jung, D. Alsdorf, C. K. Shum, and Y. Sheng, 2010: Characterization of surface water storage changes in Arctic lakes using simulated SWOT measurements, International Journal of Remote Sensing, **31**(14), 3931.

Lehner, B., and P. Döll, 2004: Development and validation of a global database of lakes, reservoirs, and wetlands. J. Hydrol., **296**, 1–22.

Lettenmaier, D. P., 2005: Observations of the global water cycle—Global monitoring networks. In Encyclopedia of Hydrologic Sciences. Eds. M. G. Anderson and J. J. McDonnell, J. Wiley and Sons Publishers, **5**, 2719–2732.

LeFavour, G., and D. Alsdorf, 2005: Water slope and discharge in the Amazon River estimated using the shuttle radar topography mission digital elevation model. Geophys. Res. Ltrs., **32**, L17404, doi:10.1029/2005GL023836.

Maheu, C., A. Cazenave, and C. R. Mechoso, 2003: Water level fluctuations in the Plata Basin (South America) from TOPEX/Poseidon satellite altimetry. Geophys. Res. Ltrs., **30**, 10.1029/2002GL016033.

Marburger, J. H., and J. B. Bolten, 2004: Updated administration research and development budget priorities, Memorandum M-04-23 from Executive Office of U.S. President, OMB and OSTP, http://www.whitehouse.gov/files/documents/ostp/pdf/m04_23.pdf. Last accessed December 31, 2011.

Marburger, J. H., and J. B. Bolten, 2005: FY 2007 administration research and development budget priorities, Memorandum M-05-18 from Executive Office of U.S. President, OMB and OSTP, http://www.ods.usf.edu/plans/fed/Federa%20Research%20Priorities%20FY07.pdf. Last accessed December 31, 2011.

Mercier, F., A. Cazenave, and C. Maheu, 2002: Interannual lake level fluctuations (1993–1999) in Africa from TOPEX/Poseidon: Connections with ocean–atmosphere interactions over the Indian Ocean. Global and Planetary Change, **32**, 141–163.

Mertes, L. A. K., 1997: Documentation and significance of the perirheic zone on inundated floodplains. Water Resources Research, **33**, 1749–1762.

NSTC, Natl. Science & Technology Council, 2004: Report on science and technology to support fresh water availability in the United States, http://water.usgs.gov/owq/swaq.pdf. Last accessed December 31, 2011.

Richey, J. E., J. M. Melack, A. K. Aufdenkampe, V. M. Ballester, and L. L. Hess, 2002: Outgassing from Amazonian rivers and wetlands as a large tropical source of atmospheric CO_2. Nature, **416**, 617–620.

Shiklomanov, A. I., R. B. Lammers, and C. J. Vörösmarty, 2002: Widespread decline in hydrological monitoring threatens Pan-Arctic research. Eos Trans., AGU, **83**, 13–16.

Smith, L. C., Y. Sheng, G. M. MacDonald, and L. D. Hinzman, 2005: Disappearing Arctic lakes. Science, **308**, 1429.

Smith, L. C., and D. E. Alsdorf, 1998: Control on sediment and organic carbon delivery to the Arctic Ocean revealed with space-borne synthetic aperture radar: Ob' River, Siberia. Geology, **26**, 395–398.

Stokstad, E., 1999: Scarcity of rain, stream gages threatens forecasts. Science, **285**, 1199.

United Nations, 2004: International Decade for Action: Water for Life, 2005–2015. General Assembly resolution A/RES/58/217, http://daccess-dds-ny.un.org/doc/UNDOC/GEN/N03/507/54/PDF/N0350754.pdf?OpenElement. Last accessed December 31, 2011.

4.1 The Global Water Cycle

Land water storage and the associated fresh water fluxes or discharge play a fundamental role in the global water cycle. They have a significant impact on climate and on the management of natural resources. However, measurements of the land water storage and fluxes are scarcely available at regional to global scales, particularly in closed basins. This situation is generally worse in regions where anthropogenic pressures on the already limited water resources are high, such as the Sahélien zone of West Africa (Redelsperger et al., 2006). A better understanding and monitoring of hydrological processes are needed to improve food security and socio-economic stability in such regions, especially because of the uncertainty in the future evolution of water resources in response to anticipated global climate change. But instead of increasing observational networks in response to such needs, the coverage in such regions (and in general, globally) is currently decreasing.

Atmospheric Global Climate Models (AGCMs) currently are used extensively to study the global water and energy budgets. Certain global numerical weather prediction (NWP) models are also used for this purpose, but not in forecast mode. The analysis (which consists in model initialization fields that are usually available four or even up to six times per day) or re-analysis (extensive atmospheric and surface information) is assimilated into the models in a hind-cast type mode. Examples include the multi-year re-analysis products of the National Center for Environmental Prediction, NCEP, and of the European Centre for Medium Range Weather forecasts, ECMWF. However, the AGCM represents the best scientific tool currently available to study the impact of climate change. Future projections from such models are being used by the Intergovernmental Panel on Climate Change (IPCC) as the basis for estimating the most probable range of impacts of both natural and anthropogenic changes, and are having a profound influence on shaping public perception of the threat and government policy.

Many numerical studies with AGCMs have suggested that land surface hydrology contributes to atmospheric variability and predictability over a large range of spatial and temporal scales (e.g., Dirmeyer, 2000; Koster et al., 2000; Gedney et al., 2000; Douville, 2003). The coupling of continental hydrology and atmosphere is accomplished mainly through the precipitation evaporation feedback mechanism. The hydrological parameterization is contained within the land surface model (LSM) component of the AGCM. LSMs were originally developed to provide the lower boundary condition to atmospheric models (fluxes of mass, heat, and momentum, in addition to radiative fluxes) over continental land areas. However, LSMs have now become much more sophisticated; and many now contain more realistic representations of photosynthesis, carbon dynamics, vertical heat and mass transfer, snow and soil freeze-thaw processes, and hydrology. The LSM hydrological parameterization exerts a powerful constraint on the evolution of the soil water storage, which then modulates the partitioning of the surface sensible and

latent heat flux (evapotranspiration) exchanges with the overlying atmosphere. It also controls the amount of water stored in lakes and discharged to the oceans.

Detailed studies of terrestrial hydrology using fully coupled land-atmosphere models can be quite difficult owing to atmospheric model biases, and most importantly, the relatively poor spatial and temporal distribution of predicted precipitation. For example, Roads et al. (2003) performed a comprehensive assessment of global and regional weather forecast models, using their predicted precipitation over the Mississippi River basin and routing the runoff produced by an LSM over the Mississippi River basin. They found that the resulting model predictions of streamflow were often in error by 50%, with values often exceeding this threshold. There have also been efforts at the regional scale over Europe using model forecast ensemble precipitation (e.g., Rousset-Regimbeau et al., 2007); however, global weather model predicted precipitation still poses problems for accurate streamflow predictions.

In order to avoid the biases related to using fully coupled models, most LSMs have used the "offline" strategy to evaluate and improve their hydrology parameterizations at regional to global scales. This consists in forcing the LSMs with a blend of observed, satellite-based, and NWP precipitation, radiative fluxes, and near-surface atmospheric state variables. Wood et al. (1998) performed one of the first offline model inter-comparison studies at the regional scale; these studies showed the importance of including sub-grid runoff parameterizations, as most LSMs at that time only generated overland flow if the soil was saturated. (Saturated soil is a relatively rare occurrence in coupled GCM models owing to the large spatial scales and model integration time step, both of which tend to lead to light precipitation rates.) The result was that many LSMs improved their sub-grid runoff parameterizations. The offline method was first used at the global scale for an ensemble of LSMs under the auspices of the Global Soil Wetness Project (GSWP: Dirmeyer et al., 1999). This project led many modeling groups to develop or use simple river routing schemes to convert the simulated runoff fluxes into discharge, which can then be evaluated at various gauging stations located throughout the world (Oki et al., 1999; Ngo-Duc et al., 2005; Decharme and Douville, 2006). This strategy is being increasingly used, and represents a useful method to detect major deficiencies in LSMs (Lohmann et al., 1998; Dirmeyer et al., 1999; Boone et al., 2004). The main offshoot of this work is that such parameterizations will permit an explicit computation of the discharge of freshwater into oceans and seas in fully coupled ocean-AGCMs.

Despite recent improvements, the aforementioned river routing parameterizations use very simple assumptions, largely owing to parameter uncertainty and a lack of high-quality spatially distributed evaluation data (such as discharge) over large parts of the globe. Moreover, it has been shown by inter-comparing a large ensemble of independent LSMs driven by realistic atmospheric forcing that on a global scale, the land surface flux with the highest uncertainty (least agreement defined as the largest inter-model

variability) is the runoff (Dirmeyer et al., 2006). Indeed, once such a parameterization has been transferred to the AGCM or NWP model, it is applied over the entire globe (even for basins where offline precipitation estimates might have been poor or where discharge for evaluation was not available). The seemingly logical choice to address this issue is to use remotely sensed data in offline mode. Indeed, spaceborne platforms can be used to estimate certain hydrological variables to within a reasonable accuracy (Alsdorf et al., 2007). However, current monitoring strategies do not give complete global coverage of these variables. SWOT would provide the first possibility to improve the river routing, the representation of lakes and hydrological model parameterizations within LSMs at a relatively high spatial resolution over the entire globe using a data assimilation strategy. Tendencies in water height change and spatial coverage could be directly assimilated into river routing and floodplain parameterizations, which would then result in improved estimates of discharge on a global scale. The more realistic estimates of river routing could then be used to improve LSM runoff parameterizations and, by extension, estimates of evaporation.

A realistic simulation of the hydrological impacts of seasonal climate anomalies and global warming by AGCMs will be critical to study ecology and human activities. While the continental land component of such models continue to improve through incorporation of better soils, topography, land use and land cover maps—not to mention advances in soil physics, cold-season processes and the representation of the carbon cycle—the models' representations of the surface water balance are still greatly in error in large part because of the absence of a coherent observational basis for quantifying river discharge and surface water storage globally (Alsdorf et al., 2007). The improved representation of global-scale hydrology will not only have an impact on the estimates of freshwater discharge into the oceans, but it also has the potential to improve the estimate of continental evaporation and therefore have an influence on the atmospheric circulation and precipitation simulated by such models. Such improvements would be useful not only for climate scenarios, but also for seasonal weather prediction and water resource management.

References

Alsdorf, D. E., E. Rodriguez, and D. P. Lettenmaier, 2007: Measuring surface water from space. Rev. Geophys., **45**, RG2002, doi:10.1029/2006RG000197.

Boone, A., F. Habets, J. Noilhan, D. Clark, P. Dirmeyer, S. Fox, Y. Gusev, I. Haddeland, R. Koster, D. Lohmann, S. Mahanama, K. Mitchell, O. Nasonova, G.-Y. Niu, A. Pitman, J. Polcher, A. B. Shmakin, K. Tanaka, B. van den Hurk, S. V'erant, D. Verseghy, P. Viterbo, and Z.-L. Yang, 2004: The Rhone Aggregation Land Surface Scheme Intercomparison Project: An overview. J. Climate, **17**, 187–208.

Decharme, B., and H. Douville, 2006: Uncertainties in the GSWP-2 precipitation forcing and their impacts on regional and global hydrological simulations. Climate Dyn., **27**, 695–713.

Dirmeyer, P. A., 2000: Using a global soil wetness dataset to improve seasonal climate prediction. J. Climate, 13, 2900-2922.

Dirmeyer, P. A., A. J. Dolman, and N. Sato, 1999: The Global Soil Wetness Project: A pilot project for global land surface modeling and validation. Bull. Am. Meteorol. Soc., **80**, 851–878.

Dirmeyer, P. A., X. Gao, M. Zhao, Z. Guo, T. Oki, and N. Hanasaki, 2006: The Second Global Soil Wetness Project (GSWP-2): Multi-model analysis and implications for our perception of the land surface. Bull. Am. Meteorol. Soc., **87**, 1381–1397.

Douville, H., 2003: Assessing the influence of soil moisture on seasonal climate variability with AGCMs. J. Hydrometeor., **4**, 1044–1066.

Gedney, N., P. M. Cox, H. Douville, J. Polcher, and P. J. Valdes, 2000: Characterising GCM land surface schemes to understand their responses to climate change. J. Climate, **13**, 3066–3079.

Koster, D. R., M. J. Suarez, and M. Heiser, 2000: Variability and predictability of precipitation at seasonal to interannual time-scales. J. Hydrometeor., **1**, 26–46.

Lohmann, D., X. Liang, E. F. Wood, D. Lettenmaier, A. Boone, S. Chang, F. Chen, Y. Dai, C. Desborough, Q. Duan, M. Ek, Y. Gusev, F. Habets, P. Irannejad, R. Koster, O. Nasanova, J. Noilhan, J. Schaake, A. Schlosser, Y. Shao, A. Shmakin, D. Verseghy, J. Wang, K. Warrach, P. Wetzel, Y. Xue, Z.-L. Yang and Q. Zeng, 1998: The Porject for Intercomparison of Land-Surface Parameterization Schemes (PILPS) Phase-2c Red-Arkansas River Basin Experiment: 3. Spatial and temporal analysis of water fluxes. Glob. Plan. Change, **19**, 161–179.

Ngo-Duc, T., J. Polcher, and K. Laval, 2005: A 53-year forcing data set for land surface models. J. Geophys. Res., **110**, D06116, doi:10.1029/2004JD005434.

Oki, T., T. Nishimura, and P. Dirmeyer, 1999: Assessment of annual runoff from land surface models using Total Runoff Integrating Pathways (TRIP). J. Meteorol. Soc. Jpn., **77**, 235–255.

Redelsperger, J.-L., C. D. Thorncroft, A. Diedhiou, T. Lebel, D. J. Parker, and J. Polcher, 2006: African monsoon multidisciplinary analysis: An international research project and field campaign. Bull. Amer. Meteor. Soc., **87**, 1739–1746.

Roads, J., et al., 2003: GCIP Water and Energy Budget Synthesis (WEBS). J. Geophys. Res., **108**(D16), doi:10.1029/2002JD002583, 8609.

Rousset-Regimbeau, F. Habets, E. Martin, and J. Noilhan, 2007: Ensemble streamflow forecasts over France. ECWMF Newsletter, **111**, Spring 2007.

Wood, E. F., D. Lettenmaier, X. Liang, D. Lohmann, A. Boone, S. Chang, F. Chen, Y. Dai, C. Desborough, Q. Duan, M. Ek, Y. Gusev, F. Habets, P. Irannejad, R. Koster, O. Nasonova, J. Noilhan, J. Schaake, A. Schlosser, Y. Shao, A. Shmakin, D. Verseghy, J. Wang, K. Warrach, P. Wetzel, Y. Xue, Z.-L. Yang and Q. Zeng, 1998: The Project for Intercomparison of Land-Surface Parameterization Schemes (PILPS) Phase-2c Red-Arkansas River Basin Experiment: 1. Experiment description and summary intercomparisons. Glob. Plan. Change, **19**, 115–139.

4.2 Lake Storage

Access to adequate supplies of clean, fresh water proves to be a severe social and developmental constraint in many nations, particularly those in arid and semi-arid regions (O'Sullivan and Reynolds, 2004). As the most readily accessible water resource, lakes and reservoirs house the dominant source of liquid freshwater on the Earth's surface, providing domestic, agricultural, and industrial water supplies. In addition, they support dynamic, complex, and diverse aquatic ecosystems; provide significant sources of food through commercial and recreational fishing; contribute aesthetic appeal and spectacular beauty to the landscape; and support commercial shipping, hydropower, and major recreational interests (Herdendorf, 1984; Kalff, 2002). In terms of their contributions to food production, recreation, and water supply regulation, lakes and rivers are estimated to provide annual ecosystem services of over $8,000 per hectare of water surface (Costanza et al., 1997). Variations in lake water storage have important effects on the landscape, regional climate, and aquatic ecosystems through changes in the terrestrial hydrologic cycle and changes in lake / wetland habitat.

The SWOT mission will provide systematic and comprehensive assessments of natural and human-induced lake changes at regional and global scales. A lake system represents complex interactions between the atmosphere and surface and underground water. Hence, lakes are a system that responds to climatic conditions, yet is tempered by upstream water uses for agriculture, industry, or human consumption. The volume of water stored within lakes and reservoirs is a proxy for precipitation and for other climatic parameters through evaporation, i.e., temperature, surface pressure, wind stress, and radiation (both short and long wave). The stored water volume is also important for hydrologic parameters such as groundwater and runoff. Lakes may hence be used to study the combined impacts of climate change and water resources management. Water management generally affects directly the water balance parameters of a lake, through irrigation or hydropower usage, while climate change alters the water balance of a lake through long-term changes in temperature and precipitation.

4.2.1 Lakes and the Terrestrial Water Balance

Lakes serve as integrative, water storage reservoirs within the terrestrial hydrologic cycle; and the very existence of persistent, standing water bodies is a reflection of the local water balance – one in which the inputs of water to the lake (precipitation, runoff, etc.) are significant enough to balance the losses of water to evaporation, groundwater seepage, and/or runoff into an outflowing stream. Any imbalances in the lake water budget lead to variations in storage (i.e., water volume), which are manifested as changes in lake level and/or surface area. Such changes can be quantified by means of the water budget equation (i.e., mass conservation):

$$dS/dt = d(A \cdot L)/dt = A(dL/dt) + L(dA/dt) = A(P - E) + Q_{in} - Q_{out}, \qquad (4.2\text{-}1)$$

where S represents lake storage, A is lake surface area, L is water level, P is over-lake precipitation, E is lake evaporation, and Qin and Qout represent terrestrial inputs and outputs of water from streams and/or groundwater (expressed in units of volume per unit time). Changes in water volume can also result from thermal expansion and contraction, but the impact on lake level is generally negligible, except for deep lakes with strong seasonal variations in water temperature, such as Lake Superior (Lenters, 2004). Although temporal variations in lake area, dA/dt, are often ignored in equation 4.2-1, such variations can be significant for the water balance of closed-basin lakes, lakes with gently sloping bathymetry, and/or very small lakes (i.e., those in which the percent change in lake area is nontrivial for a given change in lake level).

4.2.2 Global Lake Dynamics and the Role of SWOT

Global measurements of changes in lake storage require observations of lake level and surface area across space and time. Such measurements are well suited for satellite remote sensing and the previously noted capabilities of the SWOT mission. In addition to directly quantifying changes in the amount of available surface water (i.e., the left-hand side of equation 4.2-1), SWOT will also provide valuable information about the regional climatic and terrestrial hydrologic processes that drive lake storage dynamics. This includes not only direct measurements of stream discharge for some of the larger rivers (i.e., Qin and Qout), but also inferred fluxes of water due to groundwater seepage or lake evaporation (e.g., when over-lake precipitation is either negligible or directly measured). And since lakes act as integrators of the terrestrial water balance across a given watershed, changes in lake water storage can even provide inferences about land surface hydrologic processes such as snowmelt and evapotranspiration. Each of these aforementioned processes—while critical to our understanding of the regional and global water cycle—is notoriously difficult to measure. Furthermore, the processes are poorly observed at regional and global scales. Thus, SWOT observations of changes in lake water storage will provide an unprecedented global perspective of surface water availability and the terrestrial water balance.

Lakes are generally considered to cover only about 3% of the terrestrial surface area (Meybeck, 1995). 1,522 of the world's lakes are larger than 100 km^2 and contribute importantly to the total lake surface area and volume. Although we have a reasonable understanding of some (but not all) of the world's largest lakes, our knowledge about small lakes is much more limited primarily due to the exponentially larger number of small lakes. It is estimated that approximately 2.1% of the world's land area is covered by lakes and ponds exceeding one hectare (Meybeck, 1995), but it is still not certain how many lakes, in total, currently populate the surface of the Earth and how much surface area and volume those lakes occupy. The geographic distribution of lakes is problematic. In some countries the lakes cover vast areas. For example, in Canada, 7.9% of the total area is covered by lakes, in northwestern regions of Russia, the coverage is 10%, and in Finland it is 12%. On a global scale, existing lakes and reservoir monitoring systems are

inadequate; thus, data sets from different parts of the world are difficult to compare. The total number of world lakes can be calculated only approximately. According to one study, there are about 300 million lakes on the Earth that cover 4 million km^2 (Downing et al., 2006). Moreover, the data on water level and surface variations are available only for the largest lakes in most regions of the world. But in some countries, the data on water resources even for the largest lakes are sparse and approximate.

No single, comprehensive, and systematic high-resolution database of lake distribution is currently available at the global scale, let alone an inventory of lake dynamics (i.e., changes through time). Lakes have simply not been analyzed or monitored in sufficient detail at the global scale, due to the lack of global data sets such as those that SWOT will provide.

A global lake dynamics inventory represents an important challenge, since lakes are abundant at small sizes, and since changes in lake storage are manifested not only in terms of lake level, but also through changes in surface area around lake margins, requiring fine-resolution satellite imagery for accurate assessment. Coarse-resolution images are simply not able to resolve many of the abundant small lakes, much less discern the even smaller changes in lake area. In addition, cloud contamination imposes significant challenges to the widely used optical remote sensing techniques for surface water. In general, clouds cover about 60% of the land surface at any given time (Rossow and Schiffer, 1999). Designed using microwave sensors at ~50-m resolution, SWOT penetrates cloud cover and is effective during both night and day, providing all-weather observations at high resolution and overcoming the limitations of its optical counterparts. The SWOT mission will provide—at regular intervals and independent of ambient weather conditions—two-dimensional global lake maps at a spatial scale of tens of meters, as well as observations of vertical changes in water level. With measurements of both surface water area and lake level change, the SWOT mission will produce unprecedented observations of water storage change in lakes. This is a revolutionary product that is desirable in many fields, including limnology, hydrology, aquatic ecology, climate modeling, agriculture, water resources management, and water law, policy, and economics.

4.2.3 Inventory of Small Reservoirs

The monitoring of hundreds to millions of small reservoirs is a key issue for countries that rely on this important source of freshwater. For example, man-made ponds have historically been dug over the years to create reservoirs of just a few hectares in size, which store water from rainfall and surface runoff. These reservoirs, sometimes called “tanks,” are for agriculture use and are widespread across India. Water usage in India is constrained by increasing water need from a growing population, and India could face an eventual lack of water from an increasing drought. Thus, the assessment and monitoring of water stored in this myriad of small reservoirs has become a socio-economical challenge for the country. Indeed, integrated water management at the scale of the entire country suffers from inadequacy of traditional methods, which are based on

ground measurements, and from administrative complexity split into several independent layers of decision.

Remote sensing techniques such as the classification of satellite imagery may partially solve the issue, but are limited by the availability of the satellite data. Moreover, these methods do not provide a direct measurement of water storage variations. SWOT will provide for the first time a tool to solve this question at global to local scales. For example, Mialhe et al., 2008 have monitored small reservoirs using a classification of Landsat data over a river watershed of Tamil Nadu in South India, which has a total area of 11,000 km^2. Small reservoirs cover about 7.6% of the total land area, with 56% of the water surface covered by reservoirs each having an area less than 100 hectares. Based on an assumption of 50 m sized pixels, SWOT will measure the storage changes in reservoirs as small as one hectare with an accuracy within 80% of the true storage change (Lee et al., 2010). For slightly larger sized reservoirs of just over six hectares, SWOT-based storage change estimates are expected to be within 90% of truth (Lee et al., 2010). Using this one-hectare size for SWOT, it is expected for such regions to monitor more than 90% of the total water storage, which will be an unprecedented achievement. This is true over all of India. Other countries in arid climate zones also base their water storage capabilities on small reservoirs (northeast of Brazil, for example); and they face the same challenge as India: How do they carry out efficient water management policy of thousands of small reservoirs over the entire country? SWOT will help considerably in answering this question.

4.2.4 Lake Response to Regional and Global Change

Lakes can be an indicator of changes in regional and global climate. As noted above and in equation 4.2-1, the water balance of a lake is a function of climatic factors such as precipitation and evaporation. In Arctic lakes, the groundwater exchange is also important, particularly as permafrost degrades, which can result in the complete loss of all stored surface water (i.e., Smith et al., 2005).

When considering this climate-limnology signal, there are two main types of lakes: open lakes with outflow draining to rivers and closed lakes with no outflow. The first class of lakes depends closely on the balance of inflows (precipitation and runoff of rivers) and evaporation. They hence could be considered as proxies of climate change, since a small change in the temperature or precipitation in the lake basin can have a direct consequence on the lake water level. In addition, Hostetler (1995) noted that deep lakes with steep shore topography are good proxies for high amplitude–low frequency changes, while shallow water basins are better indicators for rapid low-amplitude changes. The latter are sensitive for revealing decreased water input and rising evaporation. Observations of many lakes in different climatic and regional zones, and with different morphometric characteristics, can, therefore, be used to discriminate between regional or global climate change.

Precipitation changes during the next hundreds of years as well as the retreat of glaciers and changes in the snow cover predicted by the IPCC (Intergovernmental Panel for Climate Change) will have impacts on annual to decadal changes of the amount of stored lake water. As an illustration, for South America the IPCC scenarios predict an increase in temperature going from 1 ºC to 6 ºC, and an increase in precipitation anomalies by about 20% before the end of the 21st century (Bates et al., 2008). But the geographical distribution of these anomalies is not homogeneous: Most GCM (Global Climate Model) projections indicate larger (positive or negative) rainfall anomalies for the tropical region, and smaller for the extra-tropical part of South America. This will have an impact on river runoff, which feeds the South American lakes.

Indeed, the Andean chain in South America is covered with hundreds of lakes from the arid north Altiplano to the boreal South Patagonia. They are located in a region that is under the influence of various climatic forcings: Southern Atlantic Oscillation, Pacific Decadal Oscillation, El Niño, Glacier melting, etc. (Garreaud and Battisti, 1999; Garreaud and Aceituno, 2001; Zola and Bengtson, 2006). Studying these lakes in a continental framework would be, therefore, very useful for a better understanding of the climate change impact on surface water resources; in particular, for the large Andean cities fed in the summer by melt water outpouring from glaciers and from winter snowfall.

Although the monitoring of water storage in such large, continental-scale mountain chains is essential to understanding the impact of climate change on water resources, very few of the lakes (the biggest) in the Andean chain can be monitored from current satellite data. This limits our ability to characterize the hydro-climatic mechanisms involved in this region. SWOT has the potential to solve this question. While SWOT will not measure multi-decadal changes (due to short lifetime of the mission), the mission will allow discrimination of different climate forcings and help establish the linkage between changes in ocean and atmosphere water circulation with changes in surface water storage in the Andean chain. Moreover, the quantification at seasonal time scales of surface water changes at high spatial resolution from SWOT will help to better constrain the GCM via assimilation of this lake information into the models.

4.2.5 Conclusion

Lakes serve as integrative “sentinels” of change—responding both to human-induced stressors as well as other climatic and environmental pressures (Williamson et al., 2009; Adrian et al., 2009; Williamson et al., 2008). The extent of physical and human-induced changes to lakes and their landscapes has increased tremendously over the past century—at the watershed, regional, and global scales. Population growth and increased human water demand have imposed greater stress on lake systems and freshwater availability in general. In addition, it is now recognized that global and regional climate change has had—and continues to have—important impacts on terrestrial and aquatic ecosystems. Recent studies, for example, have revealed significant warming of lakes throughout the world (e.g., Schneider and Hook, 2010; Hampton et al., 2008; Coats et al., 2006; Vollmer

et al., 2005; Livingstone, 2003). Remarkably, the observed rate of lake warming is, in many cases, greater than that of the ambient air temperature (Schneider and Hook, 2009; Austin and Colman, 2008; Lenters 2004). These rapid, unprecedented changes in lake temperature have profound implications for lake hydrology, hydrodynamics, productivity, and biotic communities (e.g., Kirillin, 2010; Tierney et al., 2010; Peeters et al., 2007; Verburg et al., 2003, O'Reilly et al., 2003).

The scientific community is just beginning to understand the global extent, regional patterns, and physical mechanisms of lake warming, as well as the consequences of this rapid warming for lake water storage and aquatic ecosystems. Lake evaporation, for example, is a highly temperature-dependent process, and further increases in water temperature could result in reduced lake storage through increased evaporative loss (particularly for lakes with seasonal ice cover). Arctic lakes are further susceptible to warmer temperatures as a result of permafrost thawing and catastrophic lake drainage via thermokarst processes. Together with increased pressure from irrigation and other consumptive uses of water, many inland water bodies, such as the Aral Sea or Lake Urmia, have already suffered serious consequences as a result of drastic reductions in water storage and ecosystem collapse (Oelkers, 2011; Micklin, 2007; Micklin, 1988; Crétaux et al., 2005, 2010; Eimanifar and Mohebbi, 2007). The SWOT mission will provide a unique opportunity to more extensively map and monitor patterns of lake storage and changes in storage and will, in turn, provide a means of relating lake storage dynamics to the observed patterns of lake warming and other key environmental stressors.

References

Adrian, R., C. M. O'Reilly, H. Zagarese, S. B. Baines, D. O. Hessen, W. Keller, D. M., Livingstone, R. Sommaruga, D. Straile, E. Van Donk, G. A. Weyenmeyer, and M. Winder, 2009. Lakes as sentinels of climate change. Limnology and Oceanography, **54**(Part 2), 2283–2297.

Austin, J., and S. Colman, 2008. A century of temperature variability in Lake Superior. Limnology and Oceanography, **53**, 2724–2730.

Bates, B. C., Z. W. Kundzewicz, S. Wu, J. P. Palutikof, 2008: Climate change and water. (technical paper of the Intergovernmental Panel on Climate Change). IPCC Secretariat, Geneva, 210.

Coats, R., J. Perez-Losada, G. Schladow, R. Richards, and C. Goldman, 2006. The warming of Lake Tahoe. Climatic Change, **76**, 121–148.

Costanza, R., R. d'Arge, R. de Groot, S. Farber, M. Grasso, B. Hannon, K. Limburg, S. Naeem, R. V. O'Neill, J. Paruelo, R. G. Raskin, P. Sutton and M. van den Belt, 1997. The value of the world's ecosystem services and natural capital. Nature, **387**, 253–260.

Crétaux, J.-F., A. V. Kouraev, F. Papa, M. Bergé Nguyen, A. Cazenave, N. V. Aladin, and I. S. Plotnikov, 2005: Water balance of the Big Aral Sea from satellite remote sensing and in situ observations. Journal of Great Lakes Research, **31**(4).

Crétaux J.-F., R. Letolle, and A. V. Kouraev, 2010: Aral Sea level variability, Handbook of Environmental Chemistry, Vol 7 Water Pollution. Eds. A. G. Kostianoy, A. N. Kosarev, Springer, 181–194.

Downing, J. A., Y. T. Prairie, J. J. Cole, et al., 2006: The global abundance and size distribution of lakes, pounds, and impoundments. Limnol. Oceanog., **51**(5), 2388–2397.

Eimanifar A., and F. Mohebbi, 2007: Urmia Lake (northwest Iran): A brief review, http://www.salinesystems.org/content/3/1/5. Last accessed January 12, 2012.

Garreaud, R., and P. Aceituno, 2001: Interannual rainfall variability over the South American Altiplano. J. Climate, **14**, 2779–2789.

Garreaud, R. D., and D. S. Battisti, 1999: Interannual (ENSO) and interdecadal (ENSO-like) variability in the Southern Hemisphere tropospheric circulation. J. Climate, **12**, 2113–2123.

Hampton, S. E., L. R. Izmest'eva, M. V. Moore, S. L. Katz, B. Dennis, and E. A. Silow, 2008: Sixty years of environmental change in the world's largest freshwater lake—Lake Baikal, Siberia. Global Change Biology, **14**, 1947–1958.

Herdendorf, C. E., 1984: Inventory of the morphometric and limnologic characteristics of the large lakes of the world. Columbus, OH: The Ohio State University Sea Grant Program.

Hostetler, S.W., 1995: Hydrological and thermal response of lakes to climate: Description and modeling. In Physics and Chemistry of Lakes, Springer-Verlag.

Kalff, J., 2002: Limnology: Inland Water Ecosystems. Upper Saddle River, NJ: Prentice Hall.

Kirillin, G., 2010: Modeling the impact of global warming on water temperatures and seasonal mixing regimes in small temperate lakes. Boreal Environment Research, **15**, 279–293.

Lee, H., M. Durand, H.-C. Jung, D. Alsdorf, C. K. Shum, and Y. Sheng, 2010: Characterization of surface water storage changes in Arctic lakes using simulated SWOT measurements. Intl. J. Remote Sensing, **31**(14), 3931–3953.

Lenters, J. D., 2004: Trends in the Lake Superior water budget since 1948: A weakening seasonal cycle. Journal of Great Lakes Research, **30**, 20–40.

Livingstone, D. M., 2003: Impact of secular climate change on the thermal structure of a large temperate central European lake. Climatic Change, **57**, 205–225.

Meybeck M., 1995: Global distribution of lakes. In Physics and Chemistry of Lakes. Eds. A. Lerman, D. M. Imboden, and J. R. Gat, Berlin: Springer-Verlag, 1–35.

Mialhe, F., Y. Gunnell, and C. Mering, 2008: Synoptic assessment of water resource variability in reservoirs by remote sensing: General approach and application to the runoff harvesting systems of South India. Water Resour. Res., 44, W05411, doi:10.1029/2007WR006065.

Micklin, P. P., 1988: Desiccation of the Aral Sea: A water management disaster in the Soviet Union. Science, **241**(4870), doi:10.1126/science.241.4870.1170, 1170–1176.

Micklin, P. P., 2007: The Aral Sea disaster. Annual Review of Earth and Planetary Sciences, **35**, doi:10.1146/annurev.earth.35.031306.140120, 47–72.

Oelkers, E. H., J. G. Hering, and C. Zhu, 2011: Water: Is there a global crisis? Elements, **7**(3), doi:10.2113/gselements.7.3.157, 157–162.

O'Reilly, C. M., S. R. Alin, P.-D. Plisnier, A. S. Cohen, & McKee, 2003: B. A. Nature **424**, 766–768.

O'Sullivan, P. E., and C.S. Reynolds (Eds.), 2004: The Lakes Handboo. Malden, MA. Blackwell.

Peeters, F., D. Straile, A. Lorke, and D. M. Livingstone, 2007: Earlier onset of the spring phytoplankton bloom in lakes of the temperate zone in a warmer climate. Global Change Biology, **13**, 1898–1909.

Rossow, W. B., and R. A. Schiffer, 1999: Advances in understanding clouds from ISCCP. Bull. Amer. Meteorol. Soc., **80**, 2261–2287.

Schneider, P., and S. J. Hook, 2010: Space observations of inland water bodies show rapid surface warming since 1985. Geophysical Research Letters, **37**, L22405, doi:10.1029/2010GL045059.

Schneider, P. S. J. Hook, R. G. Radocinski, G. K. Corlett, G. C. Hulley, S. G. Schladow, and T. E. Steissberg, 2009: Satellite observations indicate rapid warming trends for lakes in California and Nevada. Geophysical Research Letters, **36**, L22402, doi:10.1029/2009GL040846.

Smith, L. C., Y. Sheng, G. M. MacDonald, and L. D. Hinzman, 2005: Disappearing Arctic lakes. Science, **308**, 1429.

Tierney, J. E., M. T. Mayes, N. Meyer, C. Johnson, P. W. Swarzenski, A. S. Cohen, and J. M. Russell, 2010: Late-twentieth-century warming in Lake Tanganyika unprecedented since AD 500. Nature Geoscience, **3**, 422–425.

Verburg, P., R. E. Hecky, and H. Kling, 2003. Ecological consequences of a century of warming in Lake Tanganyika. Science, **301**, 505–507.

Vollmer, M. K., H. A. Bootsma, R. E. Hecky, G. Patterson, J. D. Halfman, J. M. Edmond, D. H. Eccles, and R. F. Weiss, 2005: Deep-water warming trend in Lake Malawi, East Africa. Limnology and Oceanography, **50**, 727–732.

Williamson, C. E., J. D. Saros, and D. W. Schindler, 2009: Climate change: Sentinels of change. Science, **323**, 887–888.

Williamson, C. E., W. Dodds, T. K. Kratz, and M. A. Palmer, 2008: Lakes and streams as sentinels of environmental change in terrestrial and atmospheric processes. Frontiers in Ecology and Environment, **6**, 247–254.

Zola, R. P., and L. Bengtsson, 2006: Long-term and extreme water level variations of the shallow Lake Poopo, Bolivia. Hydrological Sciences Journal, **51**(1), 98–114.

4.3 Reservoirs, Transboundary Issues, and Human Impacts

One of the most common public infrastructures with the longest heritage of modern design and operations experience is perhaps dams and their impounded water reservoirs. Water supply, hydropower generation, and flood control are the three most common needs for which most reservoirs are built. According to Graf (1999 and 2006), the United States alone has about 75,000 dams capable of storing a volume of water approximately equaling one year's mean runoff of the nation. Although the estimation of mean annual runoff is subject to considerable uncertainty due to inadequate in situ measurement of surface runoff, the vast number of dams built today leave no doubt that a nonnegligible portion of surface runoff has already been impounded. The World Commission on Dams (WCD) reports that there have been at least 45,000 large dams[1] built around the world since the 1930s. It is estimated that half of the world's rivers have at least one dam somewhere along the reach. With a changing climate and increasing water scarcity (Vorosmarty et al., 2005; Gleick, 2002), more reservoirs are likely to be commissioned or maintained (rather than removed) in this century in order to secure a steady supply of surface water for humans. A good example of this continued trend is India's recently revived mega-project concept, called the Indian River Linking Project. This project proposes to divert surface water from humid northern regions to the arid southern regions through a network of canals and dams connecting the Brahmaputra and Ganges rivers (Misra et al., 2007).

Large reservoirs, given their scale, are intimately impacted by humans, national interests, and transboundary issues. We live in a world where terrestrial water flow does not recognize political boundaries of nations, only the topographic limits of the catchments. Yet, more than 260 river systems of the world are subject to international political boundaries (Wolf et al., 1999). These river systems flow through multiple nations within the basin before draining out. An International River Basin (IRB) is such a basin within the jurisdiction of many nations. Today, IRBs account for more than 50% of global surface flow (Wolf et al., 1999) that is shared by multiple riparian nations. Hence, the reservoirs, built mostly in the upstream regions having sufficient topographic relief for storage, have vital implications on water supply for other nations in the downstream regions (Figure 4.3-1). Examples manifesting this transboundary impact are the reservoir built in the Danube River by Slovakia (former Czechoslovakia) in Europe, the Southeast Anatolia Project or GAP (Güneydoğu Anadolu Projesi in Turkish) plan in Turkey for the Euphrates river in Asia, and the Namibian plan to impound water from the Okavango River in Africa (De Villiers, 2000).

[1] According to the International Commission on Large Dams (ICOLD) and UNESCO, a large dam is defined as having a height higher than 15 m from the foundation or holding a reservoir volume of more than 3 million m^3.

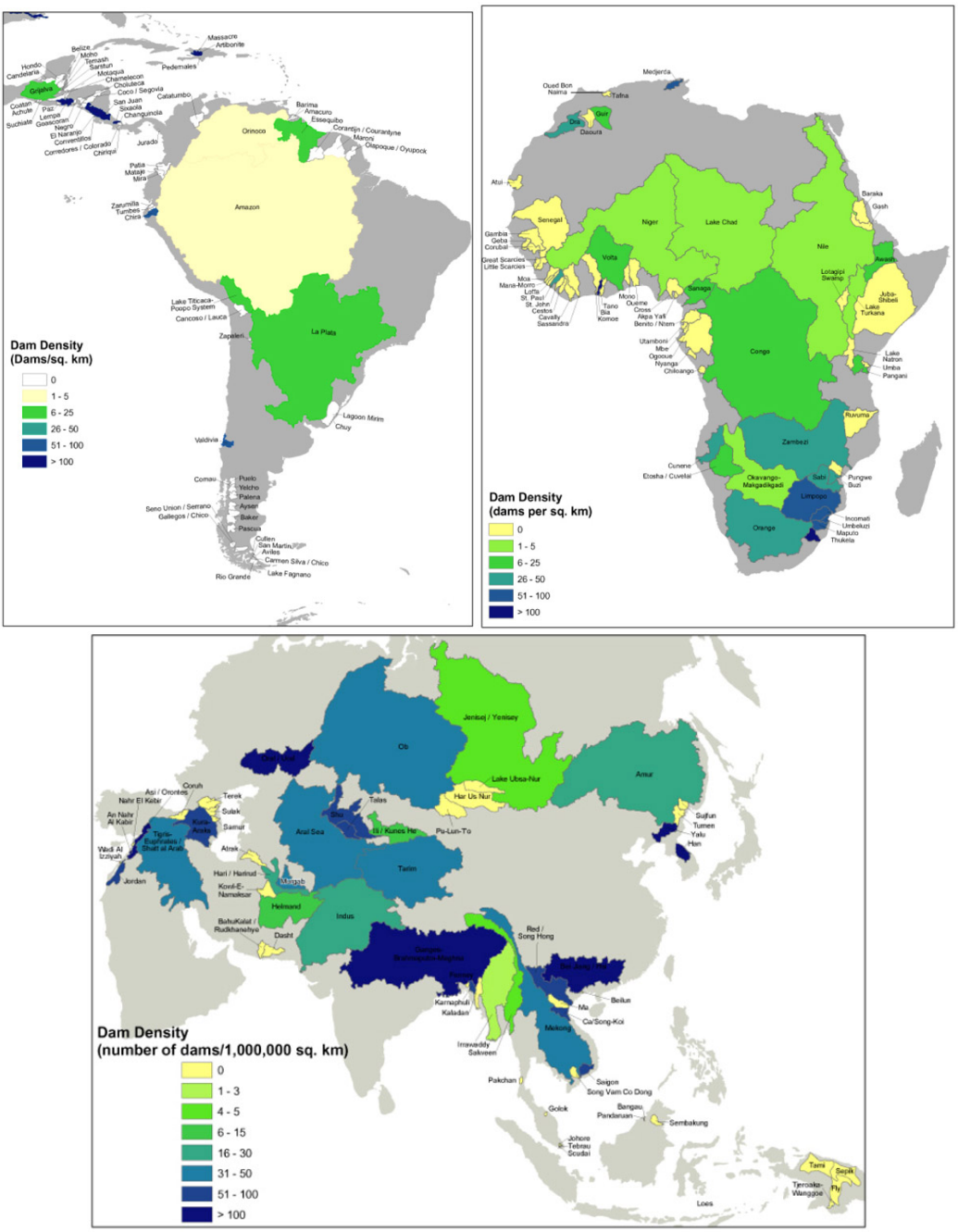

Figure 4.3-1. Map showing the density of large dams in international river basins in South America (upper left panel), Africa (upper right panel) and Asia (bottom panel). Source: Transboundary Freshwater Dispute Database available online at http://www.transboundarywaters.orst.edu (Courtesy of Dr. Aaron Wolf, Oregon State University)

Historically, the knowledge of storage (reservoir level) and spillway discharge has been controlled by nations in which the reservoir is located. Without adequate treaties for transboundary cooperation at operational time scales for water resources management (Balthrop and Hossain, 2010), the controlling nation has no legal obligation to share reservoir information with downstream nations in a timely manner. This has traditionally

made forecasting of water supply and flooding in downstream nations a very challenging task (Hossain and Katiyar, 2006). With the launch of the SWOT mission, repeat observations of surface water elevation and impounded area of the reservoirs across the globe will be obtained. These two variables will then be leveraged to measure storage changes for the reservoirs. Average revisit times of SWOT will depend upon latitude, with two to four revisits at low to mid latitudes and up to 10 revisits at high latitudes per the planned 22-day orbit repeat period. Storage change accuracy from SWOT is expected to vary as a function of reservoir size.

Storage change errors over reservoirs of 1 km^2 (1 ha) will be generally less than 5% (25%), which is a quantum leap from storage information generally available now in the pre-SWOT era (Lee et al., 2009).

So what does this globally evolving scenario of freely available reservoir storage and outflow information from SWOT bode for us in a changing climate where the availability of water resources is likely to shift during this century? Will such availability solve many of the fundamentally intractable problems, such as real-time forecasting of transboundary water flow? Will nations in IRBs become more and more ‘‘independent’’ and ‘‘sovereign’’ in forecasting and managing water resources flowing from and to other nations? Will the increased transparency of data increase trust among nations for greater cooperation on transboundary water issues? Preliminary studies clearly show that there is a direct relationship between the institutional capacity of nations to routinely gather information on surface water and the effectiveness of operational water resources management, particularly in the area of transboundary flooding (Bakker, 2009).

The global impact of SWOT on the management of transboundary water resources is better understood by analyzing the areal makeup of an IRB by multiple nations. Table 4.3-1 summarizes the distribution of nations that occupy a given portion of an IRB. About 33 such nations have more than 95% of their territory locked within such basins (Giordano and Wolf, 2003). Many of these locked nations are, thus, forced to manage a large proportion of the runoff that is generated beyond their borders. Some examples of these ‘locked’ nations are (1) Bangladesh in the Ganges-Brahmaputra-Meghna (GBM) basin comprising Bhutan, Nepal, and India (Paudyal, 2002); (2) Cambodia in the Mekong River basin comprising Myanmar, Laos, Vietnam, and Thailand; and (3) Senegal in the Senegal River basin comprising Senegal, Mali, Mauritania, and Guinea. As an example, Bangladesh, situated at the most downstream region of the GBM basin, does not receive any upstream river flow in real time from India (for lack of an adequate water treaty) during the critical monsoon rainy season spanning June–September. Yet, more than 90% of the surface runoff that flows into Bangladesh is generated upstream beyond its borders (Hossain and Katiyar, 2006). Bangladeshi authorities, therefore, measure river flow at staging points where the three major rivers enter Bangladesh (Ganges, Brahmaputra, and Meghna) and at other points downstream. On the basis of these data, it is possible to forecast flood levels in the interior and south of Bangladesh with only 2–3 days lead time

(Paudyal, 2002). If discharge information was available further upstream in India and Nepal, it is estimated that the flood forecasting lead time could be increased from 7 to 14 days, which is considered ideal for improving food security in Asian climates (Hossain and Katiyar, 2006). Flood warnings with such longer lead times can help farmers plan better through early harvesting or delayed sowing of crops. Hence, it is expected that SWOT will be found vitally useful for more accurate management of water resources by many downstream nations that do not receive discharge and reservoir storage information from upstream nations at timescales of operational management.

Table 4.3-1. Percentage of an IRB occupied by a riparian nation: a global summary

Percentage Area (of an IRB)	Number of Countries
91–99	39
81–90	11
71–80	14
61–70	11
51–60	17
41–50	10
31–40	10
21–30	13
11–20	9
1–10	11

With a more accurate assessment of the storage changes in artificial reservoirs on land, SWOT should also be able to facilitate better quantification of the sources of negative impact to global sea level rise, starting from the first SWOT data records. According to Chao et al. (2008), the reconstruction of the rise of global sea level, accounting for the volume of water impounded by artificial reservoirs, reveals a nonnegligible contribution to negate global sea level rise. In terms of the accuracy of storage volume data that are available today on the world's major reservoirs, Chao et al. (2008) reports that impoundments should have reduced global sea level rise by 0.55 mm/year during the last century. This lends credence to the possibility of other unaccounted sources (anthropogenic and natural) of sea level rise when assessed in context of observed sea level rise of 1.7–1.8 mm/year during the last century. With the more accurate spatio-temporal characterization of storage of impoundments that will be available from SWOT, modeling efforts to close the budget for global sea level rise should exhibit smaller discrepancy in the future. For instance, absolute reservoir volume will be known at all water levels above the minimum water elevation measured during the course of the SWOT mission. This will provide a lower bound on the total amount of water storage on a per-reservoir basis. SWOT should help us quantify the anthropogenic sources that reduce global sea level rise much more accurately than we can today (see section 5.6).

SWOT will not completely resolve all the open issues highlighted in this section related to reservoirs, transboundary issues, and human impacts. But SWOT may encourage us to adopt a more cooperative approach among nations towards information sharing on water storage and discharge in international river basins and help overcome some of the transboundary hurdles that are fundamentally intractable when using conventional ground-based measurements.

References

Alsdorf, D. E., E. Rodríguez, and D. P. Lettenmaier, 2007: Measuring surface water from space. Rev. Geophys., **45**, RG2002, doi:10.1029/2006RG000197.

Balthrop, C., and F. Hossain, 2010: A review of state of the art on treaties in relation to management of transboundary flooding in international river basins and the global precipitation measurement mission. Water Policy,**12**(5), 635–640.

Bakker, M. H. N., 2009: Transboundary river floods and institutional capacity. Journal of American Water Resources Association, **45**(3), doi. 10.1111/j.1752-1688.2009.00325.x., 553–566.

Chao, B. F., Y. H. Wu, and Y. S. Li, 2008: Impact of artificial reservoir impoundment on global sea level. Science, **320**(5873), 212–214.

De Villiers, M., 2000: Water: The fate of our most precious resource. Mariner Books, USA.

Giordano, M. A., and A. T. Wolf, 2003: Sharing waters: Post-Rio international water management. Natural Resources Forum, **27**, 163–171.

Gleick, P. H., 2002: The world's water: The biennial report on freshwater resources (2002–2003). Island Press, Washington D.C.

Graf, W. L., 1999: Dam nation: a geographic census of large American dams and their hydrologic impacts. Water Resources Research, **35**, 1305–1311.

Graf, W. L., 2006: Downstream hydrologic and geomorphic effects of large dams on American rivers. Geomorphology, **79**(3,4), 336–360.

Hossain, F., I. Jeyachandran, and R. Pielke, Sr., 2009: Have large dams altered extreme precipitation patterns during the last century? EOS (AGU), in revision.

Hossain, F., and N. Katiyar, 2006: Improving flood forecasting in international river basins. EOS (AGU), **87**(5), 49–50.

Lee, H., M. Durand, H. C. Jung, D. Alsdorf, C. K. Shum, and Y. Sheng, 2009: Characterization of surface water storage changes in Arctic lakes by SWOT measurements. International Journal of Remote Sensing, submitted.

Misra, A. K., A. Saxena, M. Yaduvanshi, A Mishra, Y. Bhauduriya, and A. Takur, 2007: Proposed river linking project of India: Boon or bane to nature? Environmental Geology, **51**(8), doi: 10.1007/s00254-006-0434-7, 1361–1376.

Oregon State University Program in Water Conflict Management and Transformation (PWCMT) database http://www.transboundarywaters.orst.edu Last accessed December 31, 2011.

Paudyal, G. N., 2002: Forecasting and warning of water-related disaster in a complex hydraulic setting—the case of Bangladesh. Hydrological Sciences Journal, **47**(S), S5–S18.

Vorosmarty, C. J., E. M. Douglas, P. A. Green, and C. Revenga, 2005: Geospatial indicators of emerging water stress: An application to Africa. Ambio-Journal of the Human Environment (Royal Swedish Academy of Sciences), **34**(3).

Wolf, A., J. Nathrius, J. Danielson, B. Ward, and J. Pender, 1999. International river basins of the world. International Journal of Water Resources Development, **15**(4), 387–427.

4.4 Floodplain and Wetland Processes

Floodplains and wetlands cover approximately 4% of the Earth's land surface but exert a critical influence on global biogeochemical cycles (Richey et al., 2002; Frey and Smith, 2005, Zhuang et al., 2009), terrestrial runoff to the world's oceans (Richey et al., 1989), sediment and nutrient transport (Beighley et al., 2008), basin wide flood response (Turner-Gillespie et al., 2003), and global biodiversity (Tockner and Stanford, 2002) as a result of the multitude of landscapes generated by floodplain geomorphologic complexity (Mertes et al., 1996). Moreover, over longer timescales, floodplains and wetlands form sedimentary basins where significant oil and natural gas reserves are found. Floodplains and wetlands are also profoundly important to human society because of their ability to mitigate the impact of floods and environmental pollution, and because floodplains are the locations for the majority of urban developments. All floodplain and wetland processes are regulated and constrained by the terrestrial hydrological cycle; yet, despite a number of ground-breaking studies (e.g., Alsdorf et al., 2000; Hamilton et al., 2002; Mertes et al., 1995; Wilson et al., 2007), the hydrological dynamics of seasonally flooded wetlands and floodplains remain poorly quantified through ground observations, satellite observations, or modelling. For example, current estimates of global inundated area from ground and satellite instruments vary from 1 to 12 million km^2 (Zhuang et al., 2009) and do not capture seasonal variations adequately. As a consequence, estimates of the magnitude of other processes driven by such dynamics—such as methane emissions from flooded wetlands that form a significant contribution to global atmospheric methane—also cannot be well estimated. Models of floodplain processes are also constrained in many areas of the globe by lack of detailed digital elevation model (DEM) data of sufficient resolution and vertical accuracy to represent geomorphologically complex and low gradient terrain. SRTM is the current best available data set, yet at 3 arc second resolution this data set has vertical errors of approximately ±6 m (Rodriguez et al., 2006); this accuracy is clearly inadequate given that floodplain slopes can be as low 1 cm per km. Moreover, SRTM does not cover latitudes above 60° N, and therefore cannot be used to model flows in arctic rivers and wetlands (Biancamaria et al., 2009).

On the basis of a small number of unique and opportunistically acquired data sets, we know that floodplain inundation shows significant variability in time over periods of 24 hours or less and in space over length scales down to 10–100 m, yet currently available observations are incapable of capturing this. For example, Alsdorf et al. (2007) use radar interferometry based on consecutive images from the Japanese Earth Resources Satellite (JERS)-1 satellite acquired 44 days apart over the central Amazon floodplain to show spatially complex changes in water surface elevation. Moreover, the pattern of water surface elevation change varies dramatically through the annual cycle, implying dynamic interactions between the main channel and floodplain flow depending on the hydraulics of the flood pulse and local topography (see Figure 4.4-1). In another example, Bates et al. (2006) describe a sequence of four images acquired using a military-use

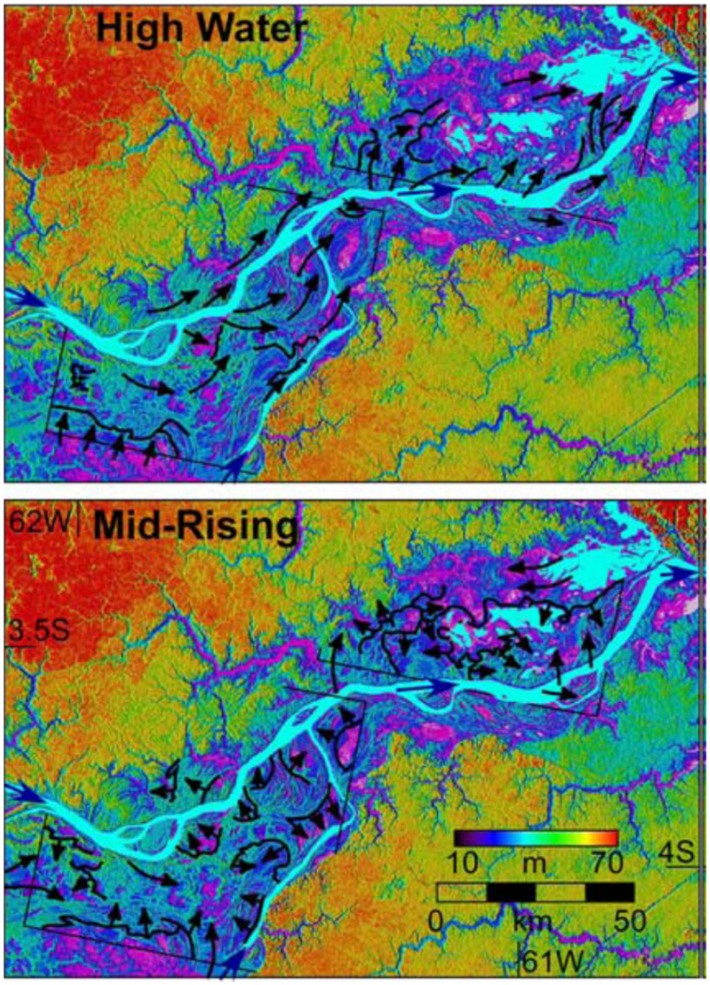

Figure 4.4-1. Water flow directions within the central Amazon floodplain interpreted from dh/dt measurements. Flow arrows are based on continuity with directions pointing toward areas of greater water accumulation. Black lines mark channels that deliver water to the floodplain during mid-rising conditions or serve as leaky barriers to broad floodplain flows during high water. Mid-rising flow is multi-directional across the floodplain, whereas high water flow is unidirectional, subparallel to the Amazon River (taken from Alsdorf et al., 2007).

airborne radar system that show the dewatering of an ~20 km reach of the River Severn in the UK after a large flood event (see Figure 4.4-2). To date, this sequence remains the only synoptic, wide-area, and fine-resolution view of inundation dynamics available globally, yet shows complex patterns of flow in both space and time that cannot be sampled with any current observing system, as we demonstrate below. Without such data our understanding of floodplain and wetland flow processes and the biogeochemical cycles driven by these is fundamentally limited. It is effectively impossible to calibrate and validate predictive models of these systems.

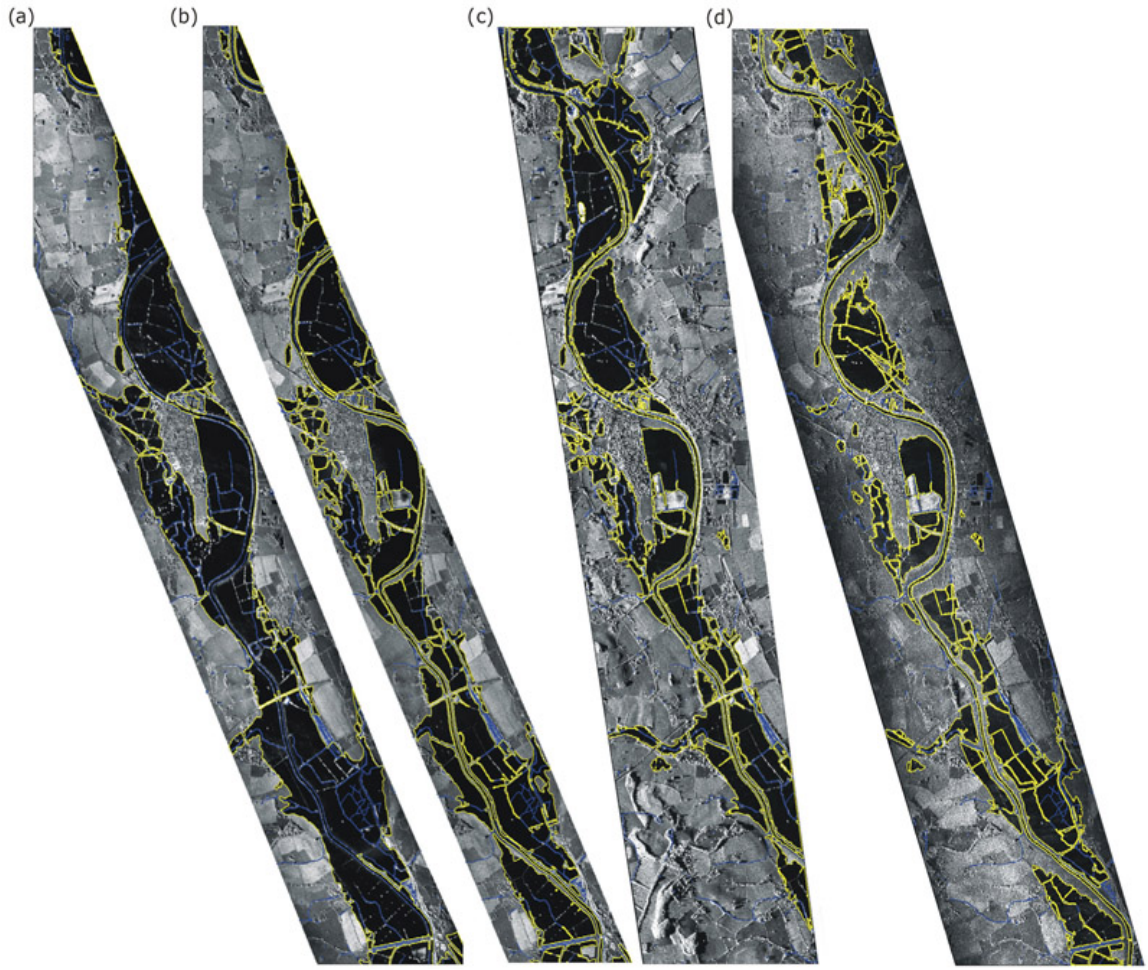

Figure 4.4-2. Airborne synthetic-aperture radar (SAR) images of an ~20 km reach of the River Severn, UK, at a spatial resolution of 1 m acquired on (a) 8 November 2000, (b) 14 November 2000, (c) 15 November 2000, (d) 17 November 2000. The flood extent delineated using an active statistical contour algorithm is shown in yellow. The flow direction is north to south (taken from Bates et al., 2006).

Ground observations of surface waters are made through discharge gauging stations; however, these are only located on main rivers where flow is confined to a single channel and can be fully sampled by a single measurement. Floodplain flow is two dimensional and cannot be measured in such a way, such that floodplains, which may convey ~25% of total flow (Richey et al., 1989), are entirely ungauged. At the same time, existing satellite systems provide only a limited view of floodplain and wetland surface water dynamics. Satellite observations of inundation extent and water level can only be achieved using (a) profiling altimeters with wide (100s of kilometers) spacing between tracks that can only see water bodies >1 km wide, and which miss many of the world's rivers and most of the world's lakes; (b) passive microwave instruments such as special sensor microwave/imager (SMM/I) with good temporal but limited spatial resolution (0.25° pixels); or (c) synthetic aperture radars which have good spatial resolution (~4–25 m pixels) but long revisit times (up to 35 days for ERS). None of these satellite systems can capture the detail of surface flows in floodplains and wetlands (e.g., Alsdorf

et al., 2000; Bates et al., 2006; Alsdorf et al., 2007) and hence provide only limited insight into processes driven by surface water dynamics. For example, estimates of methane emission from seasonally flooded wetlands, such as in the Amazon basin, depend on accurate and fine spatial resolution time series of flood extent, yet such data do not yet exist. In the absence of reliable flow observations, it is also impossible to build, calibrate, and validate models that can be applied with confidence to floodplain systems (see also section 4.6). For example, Horritt and Bates (2001) show that current typically available validation data are sparse in time and space, and contain high error. Their analysis shows that such data are unable to discriminate between simulations using a wide variety of hydraulic models and parameter sets, yet these models may then give very different results in prediction. The consequent uncertainty is, therefore, a severe constraint on our ability to effectively manage flood hazards.

Thus—despite the huge damage caused by flooding every year (see section 4.6), the significant contribution of inundation-driven wetland methane emissions to the carbon cycle, and the importance of wetland ecology to global biodiversity—we do not have a clear understanding of how inundation patterns develop and recede, and we have yet to make any reliable, wide-area observations of flooding dynamics. The lack of such measurements also severely hampers our ability to estimate the magnitude of terrestrial runoff, sediment and nutrient transport to the oceans, and wetland carbon storage. Hence, we cannot adequately constrain key components of global hydrological, biogeochemical, and carbon cycles. Critical science questions that we are currently unable to address are therefore:

(1) How does inundated area vary annually across the globe, and how do these spatial and temporal variations impact processes, such as methane emission, that are strongly determined by such dynamics?

(2) What volume of water is exchanged between rivers and their floodplains, and how does this storage and release of water affect the downstream propagation of the flood pulse? Does this floodplain storage (which is entirely ungauged) lead to an underestimation of global terrestrial runoff?

(3) What are the residence times and flow paths of floodplain flow, and what are the implications for spatial patterns of biogeochemical cycling and ecology?

(4) Where in the floodplain does terra firma runoff mix with river water, and how does this mixing of waters with different chemical and ecological signatures change dynamically? What are the implications of these dynamics for the nutrient concentration (and hence productivity) of floodplain waters?

(5) How do floodplain and wetland flows interact with complex topography, vegetation, and buildings; and how do the storage effects and energy losses so generated control the development of hazardous flooding?

(6) How significant is the timing and propagation of backwater effects in determining flooding along mainstem tributaries and how does this vary? How do floodplains affect basin-wide flood response?

(7) How do floodplain-channel interactions control sediment exchanges to the floodplain, and how does this lead to the development of floodplain geomorphologic complexity?

SWOT will address the above questions either directly, through measurements of inundation extent; water surface elevation, h, its temporal and spatial derivatives dh/dt and dh/dx; change in storage, ΔS and channel discharge, Q; or indirectly, by better constraining models of the above processes. SWOT will provide accurate data for these variables with unprecedented spatial and temporal resolution that will be, for the first time, consistent with the known real-world variability of floodplain flow processes (see for example Bates et al., 2006; Alsdorf et al., 2007). Furthermore, a SWOT mission by-product will also be the first global DEM of floodplain and wetland area with decimetric accuracy that can at last be used to parameterize hydraulic and hydrologic models of these systems adequately. Despite the nonuniform revisit time and opportunistic nature of imaging transient floods, the ubiquity of flooding events globally means that very soon after launch, SWOT will begin to capture detailed sequences of images of flood development in many river systems with basins areas >10,000 m^2, especially during the fast sampling phase. In basins of this scale, typical flood wave travel speeds are such that it becomes highly likely that SWOT will image the same flood on multiple occasions. In very large river systems with an annual flood pulse and in seasonally flooded wetlands, SWOT will provide 1–2 orders of magnitude more images than are currently available, and the SWOT images will be of unprecedented spatial resolution. Moreover, the ability of the instrument to map, for the first time, dh/dt will be a step change advance on current capability. Even for very small rivers (i.e., with basin areas <10,000 km^2 and channels <50 m wide) where in-channel flow may not be visible to SWOT, overbank flows will still cover substantial areas and can be imaged, although the orbit revisit time may mean that only 1 image per flood can be acquired. Finally, assimilation of such data sets into hydraulic models will allow surface water dynamics between SWOT overpasses to be accurately simulated for the first time (Andreadis et al., 2007), thereby filling the gaps in the instrumental record. Taken as a whole, the capability offered by SWOT will lead to a step change in our ability to image, measure, and understand floodplain and wetland processes.

We expect that the outcomes of this increase in data and understanding will be:

(1) A new generation of hydraulic models for predicting flooding to be achieved through fundamental advances in our understanding of the physics of floodplain flow and better constraint of model parameters (see also section 4.6).

(2) New estimates of global terrestrial runoff in large river systems, such as the Amazon, that will be used to better constrain global and regional climate models. Through such studies we will also be able to provide better initial conditions for climate models and develop better parameterizations of flow routing and floodplain processes in global and regional climate models (which will in turn improve predictions of the impact of climate change).

(3) Revised estimates of global wetland methane emissions and carbon storage to help constrain future projections of atmospheric greenhouse gas concentrations and the impact of climate change on these.

(4) Fundamental advances in our understanding of links between floodplain flow, nutrient and sediment transport, floodplain landscape development, and ecology.

References

Alsdorf, D. E., J. M. Melack, T. Dunne, L. A. K. Mertes, L. L. Hess, and L. C. Smith, 2000: Interferometric radar measurements of water level changes on the Amazon floodplain. Nature, **404**, 174–177.

Alsdorf, D. E., P. D. Bates, J. M. Melack, M. D. Wilson, and T. Dunne, 2007: The spatial and temporal complexity of the Amazon flood measured from space. Geophys. Res. Lett., **34**, L08402.

Andreadis, K. M., E. A. Clark, D. P. Lettenmaier, and D. E. Alsdorf, 2007: Prospects for river discharge and depth estimation through assimilation of swath-altimetry into a raster-based hydrodynamics model. Geophysical Research Letters, **34**(10), 5.

Bates, P. D., M. D. Wilson, M. S. Horritt, D. Mason, N. Holden, and A. Currie, 2006: Reach scale floodplain inundation dynamics observed using airborne Synthetic Aperture Radar imagery: Data analysis and modelling. Journal of Hydrology, **328**, 306–318.

Beighley, R. E., T. Dunne, and J. M. Melack, 2008: Impacts of climate variability and land use alterations on frequency distributions of terrestrial runoff loading to coastal waters in southern California. Journal of the American Water Resources Association, **44**(1), 62–74.

Biancamaria, S., P. D. Bates, A. Boone, and N. M. Mognard, 2009: Large-scale coupled hydrologic and hydraulic modelling of an arctic river: The Ob river in Siberia. Journal of Hydrology, **379**, 136–150.

Frey, K. E., and L. C. Smith, 2005: Amplified carbon release from vast west Siberian peatlands by 2100. Geophys. Res. Lett., **32**, L09401.

Hamilton, S. E., et al., 2002: Comparison of inundation patterns among major South American floodplains. J. Geophys. Res. Atmos., **107**(D20), art. no. 8308.

Horritt, M. S., and P. D. Bates, 2002: Evaluation of 1-D and 2-D numerical models for predicting river flood inundation. Journal of Hydrology, **268**, 87–99.

Mertes, L. A. K., et al., 1995: Spatial patterns of hydrology, geomorphology and vegetation on the floodplain of the Amazon River in Brazil: A remote sensing perspective. Geomorphology, **13**, 215–232.

Mertes, L. A. K., T. Dunne, and L. A. Martinelli, 1996: Channel–floodplain geomorphology along the Solimoes-Amazon River, Brazil. Geological Society of America Bulletin, **108**(9), 1089–1107.

Richey, J. E., J. M. Melack, A. K. Aufdenkampe, V. M. Ballester, and L. L. Hess, 2002: Outgassing from Amazonian rivers and wetlands as a large tropical source of atmospheric CO_2. Nature, **416**, 617–620.

Richey, J. E., L. A. K. Mertes, T. Dunne, R. L. Victoria, B. R. Forsberg, A. C. N. S. Tancredi, and E. Oliveira, 1989: Sources and routing of the Amazon River flood wave, Global Biogeochem. Cycles, **3**, 191–204.

Rodriguez, E., C. S. Morris, and J. E. Belz, 2006: A global assessment of the SRTM performance. Photogrammetric Eng. and Remote Sens., **72**(3), 249–260.

Tockner, K., and J. A. Stanford, 2002: Riverine flood plains: present state and future trends. Environmental Conservation, 29(1), 308–330.

Turner-Gillespie, D.F., J. A. Smith, and P. D. Bates, 2003: Attenuating reaches and the regional flood response of an urbanising drainage basin. Advances in Water Resources, **26**, 673–684.

Wilson, M. D., P. D. Bates, D. Alsdorf, B. Forsberg, M. Horritt, J. Melack, F. Frappart, and J. Famiglietti, 2007: Modeling large-scale inundation of Amazonian seasonally flooded wetlands. Geophysical Research Letters, **34**, L15404.

Zhuang, Q., J. M. Melack, S. Zimov, K. M. Walter, C. L. Butenhoff, and M. A. K. Khalil, 2009: Global methane emissions from wetlands, rice paddies, and lakes. EOS (AGU), **90**(5), 37–44.

4.5 Arctic Hydrology

Rivers and lakes in the Arctic and Subarctic north of 55º N represent approximately one third of the global terrestrial, nonagricultural surface water area; and more than half of all lakes larger than 10 ha are in the Arctic/Subarctic (Figure 4.5-1; from Lehner and Döll, 2004). However, despite its central role in physical, biological, and human systems, the high-latitude terrestrial hydrologic cycle remains poorly observed and imperfectly understood. Existing databases of lake extent put the number of boreal lakes (north of 55º N) larger than 10 ha at ~160,000 (Lehner and Döll, 2004); but field-based studies of lake extent suggest that this value is almost certainly too low, perhaps by as much as 100% in some regions (Walter et al., 2007; Frey and Smith, 2007). Nearly all Arctic lakes remain ungauged, and many of the most basic hydrologic parameters (e.g., the magnitude of the seasonal cycle in lake water level) are largely unknown.

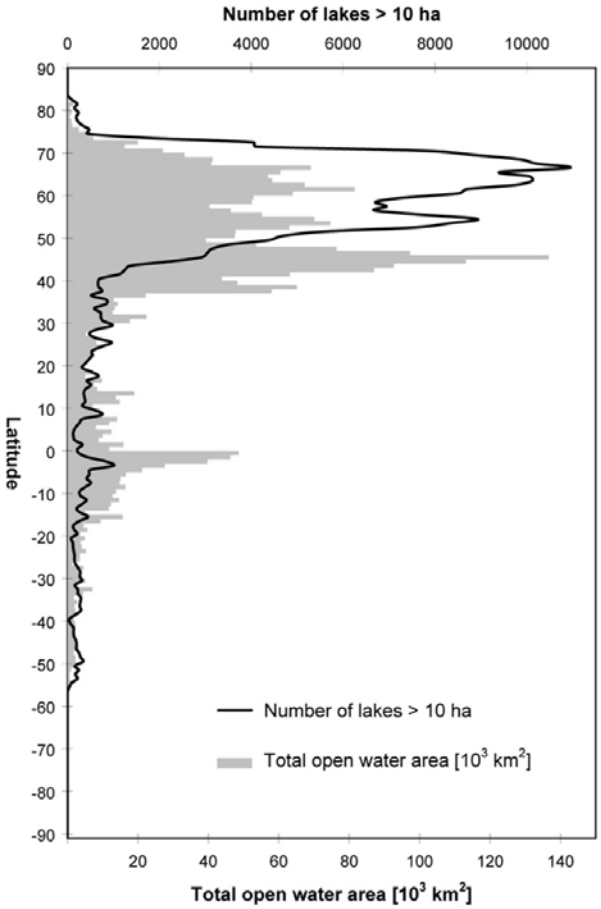

Figure 4.5-1. Histograms of the total number of lakes >10 ha per degree latitude (in black) and total open water area (rivers and lakes) per degree latitude (in grey) from the Global Lakes and Wetlands Database. Note the preponderance of both quantities at high northern latitudes. Figure prepared by B. Lehner from data described by Lehner and Döll (2004).

Observations of river discharge in the Arctic are somewhat more common, with historical time series of monthly discharge available at the mouths of most large (>100,000 km^2) river basins and for some smaller rivers and major tributaries through the R-ArcticNet 4.0 Database (Lammers et al., 2001). Daily discharge values, however, are necessary for most hydrologic applications, and these are available for a much smaller subset of rivers, especially in the former Soviet Union. Moreover, the number of Arctic discharge gauges has declined by nearly 40% (>70% in some regions) since 1986 (Shiklomanov et al., 2002), and current data from Russian rivers are largely unavailable to the international scientific community. Overall, availability of daily in situ river discharge measurements in the Arctic is inadequate for many current science needs.

Other hydrologic processes in the Arctic are impossible to observe with in situ methods. For example, the hydrodynamics of large wetland systems such as the West Siberian Lowland, the Hudson Bay Lowlands, and the Mackenzie and Lena River Deltas remain almost entirely unobserved. Current remote sensing–based methods can be used to track variations in the spatial extent of Arctic surface water (Smith et al., 2005; Smith and Pavelsky, 2008) but give little information on variations in water level or storage. By providing simultaneous observations of water surface elevation, storage change, discharge, and inundation extent, SWOT will fundamentally improve understanding of Arctic surface water hydrology and associated climatic and biogeochemical processes.

4.5.1 Hydrology and Biogeochemistry of Arctic Lakes

In order to understand how climate change and other natural and anthropogenic influences may impact the Arctic hydrologic cycle, it is first necessary to observe the fundamental dynamics of the seasonal cycle and interannual variability. In the case of Arctic surface water storage in lakes and wetlands, these quantities remain largely unknown. While present satellite technology can track variations in inundated area (Smith et al., 2005; Papa et al., 2010), published estimates of pan-Arctic lake extent remain unreliable. Because SWOT will provide high-resolution measurements of inundation extent, the mission will decrease the high level of uncertainty associated with current estimates of Arctic lake area. Except in the largest lakes, current satellite observations are also unable to provide regular and reliable information on lake stage. Because it will observe variations in water surface elevation and water storage in lakes larger than approximately 10 ha with root-mean-square error (rmse) of 5–10 cm, SWOT will for the first time provide measurements of inundated area, water level, and water storage variation in all but the smallest Arctic lakes. These measurements will provide an important validation mechanism for climate, land surface, and hydrology models in Arctic environments (Rouse et al., 1997).

Because surface water hydrology plays a central role in the biogeochemistry and ecology of Arctic lakes and wetlands, SWOT measurements will have substantial scientific value in understanding these systems. The ecological function of floodplains and deltas, among the most biologically productive environments in the Arctic, is strongly dependent on recharge of water and sediment from rivers. There is substantial concern regarding drying of Arctic floodplain wetlands due to decreases in spring flooding associated with dam construction and climate change (Rouse et al., 1997; Prowse et al., 2006). However, currently available remote sensing and in situ techniques cannot adequately capture river-floodplain interactions in boreal environments (Pavelsky and Smith, 2008). SWOT time series of water level fluctuations on rivers and adjacent floodplain lakes will allow, for the first time, detailed observation of the hydrologic connectivity on which boreal lake and wetland systems depend.

Walter et al. (2007) demonstrate that Arctic lakes represent a substantial source of atmospheric methane (CH_4) that may be sensitive to lake extent variations associated

with changing permafrost conditions. However, estimates of total contemporary methane flux from Arctic lakes remain uncertain due to poorly characterized estimates of inundated area. Moreover, changes in surface water hydrology may also result in increased emissions of CO_2 to the atmosphere (Smith et al., 2004) and dissolved organic carbon into the Arctic Ocean (Frey and Smith, 2005) from Arctic peatlands such as the West Siberian and Hudson Bay Lowlands. Improved knowledge of mean inundation extent and seasonal dynamics in water level from SWOT will decrease uncertainty in current fluxes of CH_4 and CO_2. Additionally, examination of current spatial patterns in hydrology driven by permafrost extent will inform estimates of changing greenhouse gas emissions from lakes and wetlands caused by future permafrost degradation.

4.5.2 Variations in Arctic River Discharge

Among the most intractable problems in Arctic hydrology over the last decade is determining the source of recently observed increases in river discharge into the Arctic Ocean (Peterson et al., 2002; McClelland et al., 2006; Pavelsky and Smith, 2006; Rawlins et al., 2009). While discharge at the mouths of the largest rivers is adequately measured in situ, the sources of changes in runoff regime remain poorly understood because of limited knowledge of heterogeneous discharge signals within these basins and in smaller, ungauged basins. Reasons for this lack of knowledge include the extreme remoteness of many rivers and the presence of braiding, which makes in situ gauging difficult or impossible. While optical and radar imagery can be used to estimate relative discharge where river flow width varies substantially with discharge (e.g., Smith and Pavelsky, 2008), currently available techniques cannot be used to reliably track discharge in most rivers. In nearly all Arctic river basins, the majority of annual runoff occurs during the open water season, when SWOT will be capable of estimating variations in discharge. As such, SWOT will provide reliable estimates of discharge variations from all major Arctic subbasins on weekly or better timescales. When combined with climate and land surface data sets, these observations will improve understanding of the physical mechanisms that drive both local and basin-wide river discharge anomalies.

4.5.3 Links Between Arctic Hydrology and the Cryosphere

Arctic surface water hydrology is uniquely linked to cryospheric processes associated with ice sheets, glaciers, river and lake ice, and permafrost. SWOT observations will address outstanding research questions in several of these areas. Discharge through glacial outlet streams represents an important barometer of outflow from glaciers and ice sheets, yet most such streams remain ungauged due to remoteness and pervasive braiding. Existing remote sensing–based methods for tracking discharge variability are often impractical due to limited spatial or temporal resolution. Because SWOT temporal resolution in the Arctic will be as high as 4–9 passes per 22 day orbit, it will be possible to track variations in glacial outflow through rivers on both seasonal timescales and for individual melt events and perhaps even glacial outburst floods. Studies suggest that changing hydrology plays a central role in observed mass loss from

glaciers and ice sheets through direct melt and, more importantly, subglacial bed lubrication (e.g., Thomas et al., 2000). Using SWOT measurements to characterize the timing and magnitude of discharge, it may be possible to employ glacial rivers as barometers of glacier and ice sheet dynamics at time scales and over spatial extents currently unavailable.

Flooding associated with the spring freshet on Arctic rivers plays a central role in exchange of water and sediment between rivers and floodplains. The most extensive flooding is often associated with the formation of large ice jams, yet the hydrologic response of rivers during ice jam floods remains poorly understood (Beltaos, 2003). For the first time, SWOT will provide simultaneous observations of water surface elevation, flow direction, and inundation extent in flooded areas behind ice jams. These observations will substantially improve understanding of ice jam flood dynamics.

Characteristics of rivers and lakes in the Arctic are strongly dependent on the presence or absence of permafrost (Hinzman et al., 2005), and projections suggest substantial degradation in near-surface permafrost in the next century (Lawrence and Slater, 2005). Because permafrost impacts infiltration rates during spring snowmelt and summertime precipitation events, discharge characteristics of Arctic rivers depend strongly on permafrost extent in the contributing watershed. Using spatially continuous estimates of discharge variability provided by SWOT, it will be possible to examine how discharge timing and magnitude vary with changing permafrost extent both within a single large drainage basin and among several different subbasins. Permafrost extent is also important in regulating the presence and seasonal dynamics of Arctic lakes (Smith et al., 2007). Temporal changes in lake extent over the last four decades may be associated with changing permafrost conditions. However, changes are likely also occurring in the mean and seasonal cycle of lake water level, and these cannot be detected using currently available methods. By allowing substitution of contemporary, permafrost-driven spatial variations in hydrologic regime for future temporal changes in permafrost extent, SWOT observations will improve projections of climate change impacts on Arctic lake hydrology.

References

Beltaos, S., 2003: Numerical modeling of ice-jam flooding on the Peace-Athabasca delta. Hydrol. Process., **17**, 3685–3702.

Frey, K. A., and L. C. Smith, 2007: How well do we know northern land cover? Comparisons of four global vegetation and wetland products with a new ground-truth database for West Siberia. Global Biogeochemical Cycles, **21**, 201–208.

Frey, K. A., and L. C. Smith, 2005: Amplified carbon release from vast West Siberian peatlands by 2100. Geophys. Res. Lett., **32**, L09401.

Hinzman, L. D., N. D. Bettez, W. R. Bolton, et al., 2005: Evidence and implications of recent climate change in northern Alaska and other Arctic regions. Climatic Change, **72**, 251–298.

Lammers R. B., A. I. Shiklomanov, C. J. Vorosmarty, B. M. Fekete, and B. J. Peterson, 2001: Assessment of contemporary Arctic river runoff based on observational discharge records. J. Geophys. Res., **108**, 3321–3334.

Lawrence, D. M., and A. G. Slater, 2005: A projection of severe near-surface permafrost degradation during the 21st century. Geophys. Res. Lett., **32**, L24401.

Lehner, B., and P. Döll, 2004: Development and validation of a global database of lakes, reservoirs, and wetlands. J. Hydrol., **296**, 1–22.

McClelland, J.W., S. J. Dery, B. J. Peterson, R. M. Holmes, and E. F. Wood, 2006: A pan-Arctic evaluation of changes in river discharge during the latter half of the 20th century. Geophys. Res. Lett., **33**, L06715.

Papa, F., C. Prigent, C. Jimenez, F. Aires, W. B. Rossow, and E. Matthews, 2010: Interannual variability of surface water extent at global scale, 1993–2004. J. Geophys. Res., **115**, D12111, 17 pages.

Pavelsky, T. M., and L. C. Smith, 2008: Remote sensing of hydrologic recharge in the Peace-Athabasca Delta, Canada. Geophys. Res. Lett., **35**, L08403.

Pavelsky, T. M., and L. C. Smith, 2006: Intercomparison of four global precipitation data sets and their correlation with increased Eurasian river discharge to the Arctic Ocean. Journal of Geophysical Research-Atmospheres, **111**, D21112.

Peterson, B. J., R. M. Holmes, J. W. McClelland, C. J. Vorosmarty, R. B. Lammers, A. I. Shiklomanov, and S. Rahmstorf, 2002: Increasing river discharge to the Arctic Ocean. Science, **298**, 2171–2173.

Prowse, T. D., S. Beltaos, J. T. Gerdner, J. J. Gibson, R. J. Granger, R. LeConte, D. L. Peters, A. Pietroniro, L. A. Romolo, and B. Toth, 2006: Climate change, flow regulation, and land-use effects on the hydrology of the Peace-Athabasca-Slave system; findings from the Northern Rivers Ecosystem Initiative. Environmental Monitoring and Assessment, **113**, 167–197.

Rawlins, M. A., H. Ye, D. Yang, A. Shiklomanov, and K. C. McDonald, 2009: Divergence in seasonal hydrology across northern Eurasia: Emerging trends and water cycle linkages. J. Geophys. Res., **114**, D18119.

Rouse W. R., M. S. V. Douglas, R. E. Hecky, et al., 1997: Effects of climate change on the freshwaters of arctic and subarctic North America. Hydrological Processes, **11**(8), 873–902.

Shiklomanov, A. I., R. B. Lammers, and C. J. Vorosmarty, 2002: Widespread decline in hydrologic monitoring threatens pan-Arctic research. EOS Trans. (AGU), **83**(2), 13, 16–17.

Smith, L. C., and T. M. Pavelsky, 2008: Estimation of river discharge, propagation speed and hydraulic geometry from space: Lena River, Siberia. Water Resources Research, **44**, W03427.

Smith, L. C., Y. Sheng, and G. M. MacDonald, 2007: A first pan-Arctic assessment of the influence of glaciation, permafrost, topography and peatlands on Northern

Hemisphere lake distribution, permafrost and periglacial processes. Permafrost and Periglac. Process., **18**, 201–208.

Smith, L. C., Y. Sheng, G. M. MacDonald, and L. Hinzman, 2005: Disappearing Arctic lakes. Science, **308**, 1429.

Smith, L. C., G. M. MacDonald, A. A. Velichko, et al., 2004: Siberian peatlands a net carbon sink and global methane source since the early Holocene. Science, **303**, 353–356.

Thomas, R. H., W. Abdalati, T. L. Atkins, B. M. Csatho, E. B. Frederick, S. P. Gogineni, W. B. Krabill, S. S. Manizade, and E. J. Rignot, 2000: Substantial thinning of a major east Greenland outlet glacier. Geophys. Res. Lett., **27**, 1291–1294.

Walter, K. M., L. C. Smith, and F. S. Chapin, 2007: Methane bubbling from northern lakes: Present and future contributions to the global methane budget. Phil. Trans. R. Soc. A., **365**, 1657–1676.

4.6 Floods and Flood Modeling

In 2004 the UNESCO World Disasters Report estimated that flooding affected 116 million people globally, causing 7000 deaths and leading to $7.5 B in losses (see http://www.unisdr.org/files/5401_2005disasterinnumbers.pdf). In the UK alone, 5 million people (i.e., 1 in 12 of the population) in 2 million properties live on coastal and fluvial floodplains, and over 200,000 of these properties have less than the standard of protection mandated by the UK government (1 in 75-year recurrence interval). The proportion of at-risk population is likely to be similar in many other developed countries and perhaps worse in developing nations. Moreover, when they do inevitably occur, floods cause major social disruption, civil unrest, economic loss, and insurance sector bankruptcies (e.g. Mozambique, 2000; New Orleans, 2005; UK, summer 2007).

From records of flood events all around the world since 1985 collected by the Dartmouth Flood Observatory (1985–2002), it appears that the mean duration of floods is around 9.5 days and the median duration is 5 days. At the global scale, there is an annual periodicity in the occurrence of floods: the first six months (November to April) correspond to a "low" flood likelihood during which floods are least likely to occur. These six months are followed by two months (May, June) of increasing flood frequency. Floods are most likely to occur during the two months (July and August) of "high" flood likelihood, and finally the two last months (September and October) correspond to a decrease of flood events. These flood events are mainly due to heavy rain, brief torrential rain, tropical cyclones, the monsoon, and snowmelt. As stated previously, floods can have a huge impact on human societies, especially deadly floods occurring principally in June and July in South Asia, in September and October in Central America, and in February in South America. Moreover, huge flood events occur in the Arctic due to snowmelt and ice jams between April and June. From these data, it seems that the biggest floods should be observable by satellite data (i.e., at least one observation of the floodplain inundation) if the revisit time between two measurements is less than 5 days. Moreover, the time period from May to October should be the most important to study, as many floods occur during these months.

Because we are often concerned with either extreme events that may not have been observed in the instrumental record or because we wish to forecast into the future, flood risk is typically assessed with computational hydraulic models. For risk assessment, these models are calibrated against data from floods much smaller than the design event and then used to predict the potential consequences of extreme flooding. Alternatively, models calibrated against historic data can be used as part of flood forecasting and warning systems to predict the downstream propagation of flood waves. The robustness of such models therefore depends critically on the quality of data used to build, calibrate, and validate them. Observations can also be assimilated into such models (see Andreadis et al., 2007, for an example) and used to dramatically improve forward predictions.

Most lowland rivers consist of a main channel with one or two adjacent floodplain areas. During the passage of a flood wave, the flow depth may exceed bankfull height, and water may extend and retreat over the low-lying and flat floodplains. Floodplains, therefore, act either as storage areas for flood water or provide an additional route for flow conveyance. In fluid dynamics terms, a flood is a long, low-amplitude wave passing through a compound channel of complex geometry. In the very largest basins, such waves may be up to ~103 km in length or greater but with amplitude of only ~101 m, and they may take several months to traverse the whole system. Flood waves are translated downstream with speed or celerity, c[LT^{-1}], and attenuated by frictional losses such that in downstream sections the hydrograph is flattened out (see Figure 4.6-1). Wave speeds can be shown (see NERC, 1975) to vary with discharge such that maximum wave speed occurs at approximately two-thirds bankfull capacity (Knight and Shiono, 1996). Typical observed values for c for UK rivers with widths in the range 10–50 m are in the ranges 0.5–1.8 ms^{-1} and 0.3–0.67 ms^{-1}, reported by NERC (1975) and Bates et al. (1998), respectively.

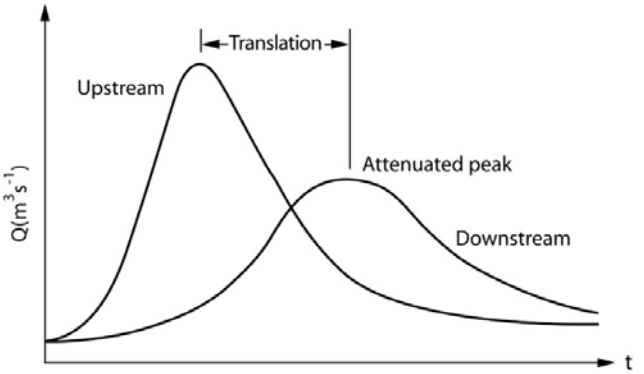

Figure 4.6-1. Translation and attenuation of a flood wave between two gauging stations.

Below the scale of the flood wave itself, other significant in-channel processes can be identified, each with a characteristic length scale. These include shear layers forming at the junction between the main flow and slower moving floodplain flow (Knight and Shiono, 1996), secondary circulations (Bridge and Gabel, 1992; Nezu et al., 1993), and turbulent eddies. The latter range in size from heterogeneous structures at the scale of roughness elements and obstructions on the bed (Ashworth et al., 1996; McLelland et al., 1999; Shvidchenko and Pender, 2001) down through the turbulent energy cascade (Hervouet and Van Haren, 1996) to the Kolmogorov length scale, η [L], where turbulent kinetic energy is finally dissipated. In typical channel flows, these smallest eddies may be only ~10^{-2} mm across (Hervouet and Van Haren, 1996) and are highly transient. All these scales may be fully described with the Navier–Stokes equation (Schlichting, 1979):

$$\rho \frac{\mathrm{D}\mathbf{u}}{\mathrm{D}t} = -\nabla p + \mu \nabla^2 \mathbf{u} + F \tag{4.6-1}$$

where ρ is the fluid density [with dimensions ML^{-3}], $\mathbf{u}$ is the velocity vector [LT^{-1}], t is the time [T], p is the pressure [$ML^{-1}T^{-2}$], μ is the viscosity [$ML^{-1}T^{-2}$], and F is the set of

terms (for example gravity, coriolis, and friction) to be included in the specification of a particular problem. When equation 4.6-1 is combined with the equation of continuity:

$$\nabla.\mathbf{u} = 0 \tag{4.6-2}$$

one obtains a system of equations that can be solved to yield the three-dimensional velocity vector $\mathbf{u} = (u, v, w)$, where *u*, *v*, and *w* are the three components of **u** in the *x*, *y*, and *z* directions respectively, and pressure, *p*, for a given point in time and space. In free surface models the pressure, *p*, is typically replaced with the flow depth, *h* [L].

Solution of equations 4.6-1 and 4.6-2 over a suitably refined grid (i.e., $\Delta x << \eta$) using a suitably small time step can, in theory, simultaneously simulate all flow features described above. However, for typical flood wave flows (i.e., unsteady, nonuniform flows of high Reynolds number in a complex geometry), the direct numerical simulation of the Navier–Stokes equations is computationally prohibitive. Hydrologists have, therefore, sought to isolate from this complex assemblage those processes that are central to the problem of flood routing and inundation prediction in order to build appropriate models.

A starting point for such approximations is to consider the forces acting on the flow. For fluvial flood routing problems, the dominant driving and resisting forces are clearly gravity and friction, respectively; and this realization led in the 18th and 19th centuries to the development of resistance laws for steady and uniform open channel flow by Chezy, Manning, and Darcy–Weisbach. (See Chanson, 1999, pp. 72–91, for a discussion.) For example, the Manning equation is given as:

$$Q = \frac{AR^{2/3}S_f^{1/2}}{n} \tag{4.6-3}$$

where *Q* is the discharge [L^3T^{-1}], *A* is the channel cross sectional area [L^2], *R* is the hydraulic radius [L, calculated by dividing the channel cross sectional area, *A*, with the length of the wetted perimeter], S_f is the friction slope [LL^{-1}], and *n* is the Manning friction coefficient [$L^{1/3}T^{-1}$].

However, to describe unsteady flows requires the development of equations of motion based on principles of mass and momentum conservation for which the critical decision is the number of dimensions in which significant flow field variation occurs. Clearly, for the hydrologist concerned with calculating the translation and attenuation of a flood wave over long river reaches, significant variations in the flow field occur dominantly in the streamwise direction. Hence, despite known three-dimensional processes, channel flows are often considered as one-dimensional in the streamwise direction; and variations in velocity in the vertical and cross-stream directions may be neglected. Such a flow is described by the one-dimensional St. Venant or shallow water equations:

Conservation of momentum

$$\frac{\partial Q}{\partial t} + \frac{\partial \left(Q^2 / A \right)}{\partial x} + gA\left(\frac{\partial h}{\partial x} + S_f - S_o \right) = 0 \tag{4.6-4}$$

where Q is the flow discharge [L^3T^{-1}]; A is the flow cross-section area [L^2], g is the gravitational acceleration [LT^{-2}], S_f is the friction slope [LL^{-1}], and S_o is the channel bed slope [LL^{-1}], and:

Conservation of mass

$$\frac{\partial Q}{\partial x} + \frac{\partial A}{\partial t} = q \tag{4.6-5}$$

where q is the lateral inflow or outflow per unit length [L^2T^{-1}].

Equations 4.6-4 and 4.6-5 have no exact analytical solution, but with appropriate boundary and initial conditions they can be solved using numerical techniques (e.g., Preissmann, 1961; Abbott and Ionescu, 1967) to yield estimates of Q and h in both space and time at a series of irregularly spaced cross sections (see Figure 4.6-2).

For many channel flood routing applications, this is a reasonable approximation; however Knight and Shiono (1996) suggest that when flow exceeds bankfull capacity and begins to spread over adjacent low-lying floodplains, a series of further processes—such as channel-floodplain momentum exchange and water spilling out of channel and across meander loops—are initiated in which higher dimensional effects begin to be important.

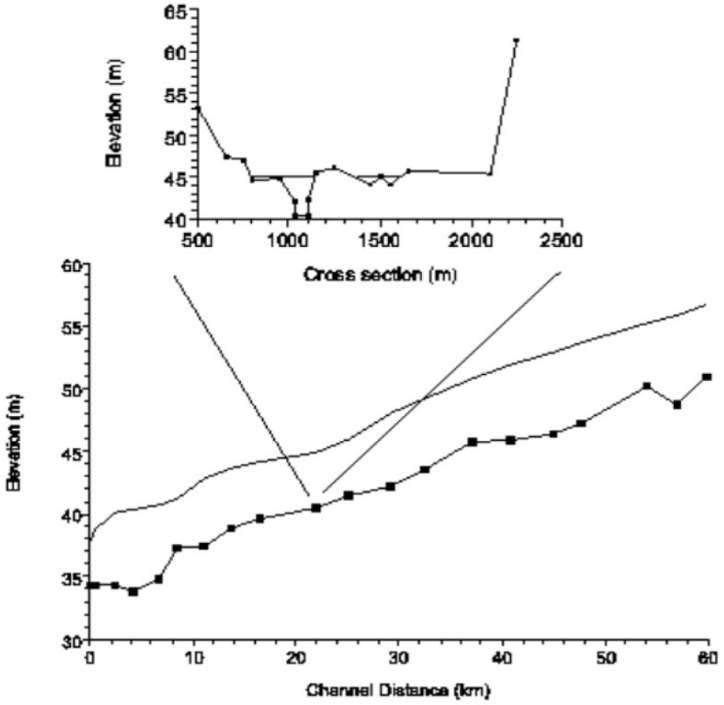

Figure 4.6-2. A typical discretization from a one-dimensional hydraulic model, in this case the Hydrologic Engineering Center-River Analysis System (HEC-RAS) scheme, applied to a 60-km reach of the River Severn in the UK by Horritt and Bates (2002). Shown are the bed elevation profile, with model crosssection locations marked by squares, and a typical simulated water free-surface profile. A sample cross section is also shown.

Flow in the floodplain itself is also clearly at least a two-dimensional process given that flows may be several kilometers in horizontal extent but only a few meters deep, and many inundation prediction studies make the assumption that the variation in vertical velocity is negligible compared to variation in the horizontal. Such shallow water flows over low-lying topography are characterized by rapid extension and retreat of the inundation front over considerable distances, potentially with distinct processes occurring during the wetting and drying phases (see Nicholas and Mitchell, 2003). One-dimensional models cannot easily be applied to floodplain flows as the flow paths cannot be specified a priori. Instead, models based on the two-dimensional shallow water equations are usually required, and these can be given in nonconservative form as:

Conservation of mass

$$\frac{\partial h}{\partial t} + \vec{u}_d \,.\, \overrightarrow{grad}\,(h) + h\,div(\vec{u}_d) = 0 \tag{4.6-6}$$

Conservation of momentum

$$\frac{\partial u_d}{\partial t} + \vec{u}_d \,.\, \overrightarrow{grad}\,(u_d) + g\frac{\partial h}{\partial x} - div(\nu_t \,.\, \overrightarrow{grad}\,(u_d)) = S_x - g\frac{\partial Z_f}{\partial x} \tag{4.6-7}$$

$$\frac{\partial v_d}{\partial t} + \vec{u}_d \,.\, \overrightarrow{grad}\,(v_d) + g\frac{\partial h}{\partial y} - div(\nu_t \,.\, \overrightarrow{grad}\,(v_d)) = S_y - g\frac{\partial Z_f}{\partial y} \tag{4.6-8}$$

where u_d,v_d are the depth-averaged velocity components [with dimensions LT^{-1}] in the x and y cartesian directions [L]; Z_f is the bed elevation [L]; ν_t is the kinematic turbulent viscosity [L^2T^{-1}]; S_x, S_y are the source terms (friction, coriolis force, and wind stress) and g is the gravitational acceleration [LT^{-2}]. These can then be solved using some appropriate numerical procedure over structured or unstructured grids (see Figure 4.6-3) to obtain predictions of the water depth, h, and the two components of the depth-averaged velocity, u_d and v_d.

Despite the different physical processes represented by models based on equations 4.6-1 to 4.6-8, the data requirements for such simulations are actually very similar. Principally, any hydraulic model requires (1) boundary condition data, (2) initial condition data, (3) topography data, (4) friction data, and (5) hydraulic data for use in model validation. These are discussed in detail below.

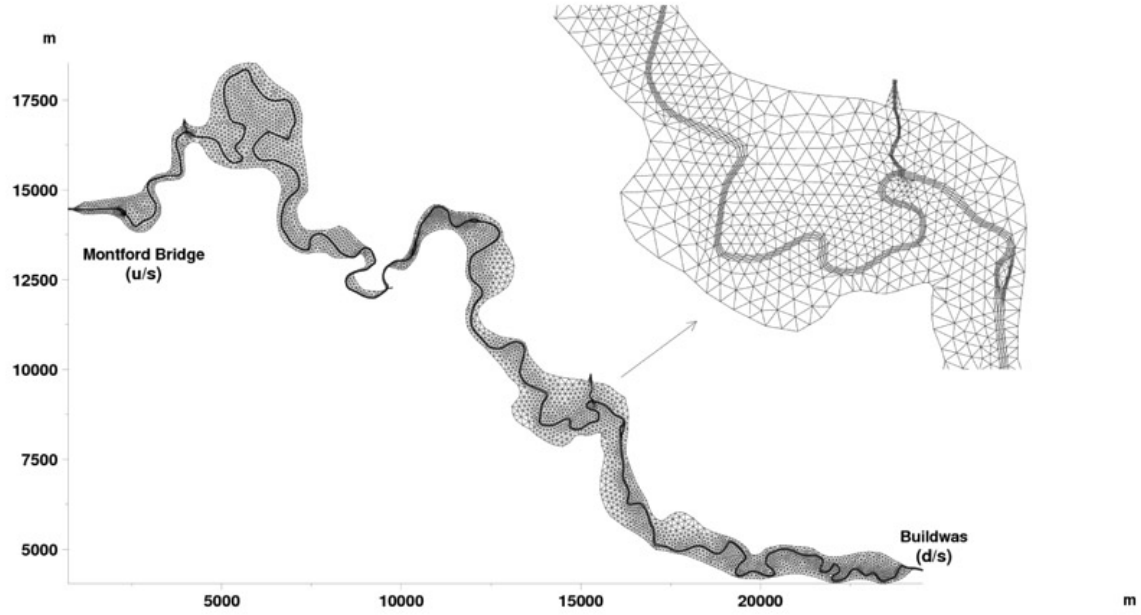

Figure 4.6-3. Unstructured grid of a 60 km reach of the River Severn in the UK used to solve the two-dimensional shallow water equations (equations 2-8 to 2-10) using the finite element technique.

Boundary condition data typically come from ground gauging stations or from flood frequency relationships derived from these. However, gauging stations are lacking for many areas of the globe; and even when such data do exist, they may be subject to large errors during flood events when flow is out of bank. Data to specify an initial state for a hydraulic model at each of its computational nodes can sometimes be obtained by intersecting synthetic aperture radar data showing flood extent with high-resolution terrain models to give water heights along the shoreline. However, in most situations, data to define the model initial state is almost wholly lacking. Simulating shallow flows over low-gradient floodplains with complex microtopography and structures (e.g., flood defenses) requires high (i.e., decimetric) vertical accuracy terrain data, and these are increasingly being obtained for specific areas from airborne laser altimetry (see Marks and Bates, 2000). However, globally available DEMs are insufficient to support inundation modeling (see Sanders, 2007 for a review and Biancamaria et al., 2009 for an example) unless the flood wave amplitude is much larger than the noise in the terrain data signal (see Wilson et al., 2007, for an example of this). Lastly, hydraulic models require reliable observations of flow processes for the friction terms that appear in equations 4.6-3 to 4.6-8 to be accurately calibrated and for model quality to be independently assessed in a split-sample calibration-validation experiment.

Typical data available to calibrate and validate models include (a) point-scale measurements of water stage, discharge, or velocity made at established gauging stations, taken during field campaigns (e.g., Lane et al., 1999), determined from satellite altimetry (e.g., Wilson et al., 2007), or estimated by intersecting flood extent maps with high-

resolution DEMs (Mason et al., 2007; Schumann et al., 2008); (b) vector data on flood inundation extent determined by ground surveys either during or after an event or from remotely sensed images of flooding (e.g. Horritt, 1999; Romanowicz and Beven; 2003; Bates et al., 2006; Pappenberger et al., 2005); and (c) interferometric measurements of water surface height change determined from repeat-pass satellite radar images (e.g., Alsdorf et al., 2007). However, very little of the above data is systematically collected; and for the majority of sites where flood risk assessments or flood warnings are required, there are no adequate data with which to constrain hydraulic models. Without such data flood risk predictions are subject to considerable uncertainty (see for example Aronica et al., 2002; Pappenberger et al., 2006).

SWOT can contribute in all 5 areas of data-need identified above. River discharge will be estimated globally, thereby filling gaps in the instrumental record; while a by-product of the mission will be the first global floodplain DEM with decimetric accuracy that can at last be used to parameterize hydraulic models of these systems adequately. More directly, SWOT measurements of inundation extent; water surface elevation, h; and its temporal and spatial derivatives, dh/dt and dh/dx can be used to provide initial conditions for hydraulic model simulations, calibrate spatial distributions of friction parameters and their variation over time, and independently assess the quality of hydraulic models through more rigorous validation. There is also considerable potential to assimilate SWOT data into hydraulic models (see for example Andreadis et al., 2007), as equations 4.6-3 to 4.6-8 contain many terms that are directly measured by SWOT. For example, the two-dimensional shallow-water equation (equations 4.6-6 to 4.6-8) include the variation of water depth with time (dh/dt) and the water surface gradient (dh/dx), both of which SWOT measures directly. However, the main difference that SWOT will make to flood modeling will be the volume of data that it will contribute as a result of its orbit characteristics. As we argue in section 4.4, the ubiquity of flooding events globally means that very soon after launch SWOT will begin to capture detailed sequences of images of flood development in many river systems with basins areas greater than 10,000 km^2, especially during the fast sampling phase. SWOT will, therefore, create at least an order of magnitude step change in the volume of data available for flood modeling and will allow global applications of such codes that have hitherto been impossible because of a fundamental lack of data. Analysis of SWOT data will also make a fundamental contribution to our understanding of the dynamics of floodplain inundation (see also section 4.4) and in particular to our knowledge of dynamic flow interactions with vegetation, buildings, and microtopography (see for example Alsdorf et al., 2007) and to our knowledge of the model physics and length scales necessary to describe these.

We expect that the outcomes of this increase in data and understanding will be:

(1) A new generation of hydraulic models for predicting flooding to be achieved through fundamental advances in our understanding of the physics of floodplain flow (see also section 4.4).

(2) A step change in the volume of data available to calibrate and validate hydraulic models with, as a consequence, significant improvements in flood risk assessment and flood warning.

(3) An ability, for the first time, to build first-order flood inundation models for anywhere on the globe as a result of the availability of (1) global discharge estimates for use as model boundary conditions and (2) a global floodplain DEM with decimetric accuracy. We anticipate this will make a profound difference to flood risk management in developing countries where terrain mapping and hydrometric programs either do not exist or are being scaled back.

References

Abbott, M., and F. Ionescu, 1967: On the numerical computation of nearly horizontal flows. Journal of Hydraulic Research, 5(2), 97–117.

Alsdorf, D.E., E. Rodriguez, and D. Lettenmaier, 2007: Measuring surface water from space, Reviews of Geophysics, v. 45, no. 2, RG2002 doi:10.1029/2006RG000197. [Note: This is a “by invitation” journal with the highest Earth science impact rating.]

Andreadis, K.A., E.A. Clark, D.P. Lettenmaier, and D.E. Alsdorf, Prospects for river discharge and depth estimation through assimilation of swath-altimetry into a raster-based hydrodynamics model, Geophysical Research Ltrs., **34**, L10403, doi:10.1029/2007GL029721, 2007.

Aronica, G., P. D. Bates, and M. S. Horritt, 2002: Assessing the uncertainty in distributed model predictions using observed binary pattern information within GLUE. Hydrological Processes, 16, 2001–2016.

Ashworth, P. J., S. J. Bennett, J. L. Best, and S. J. McLelland, 1996: Coherent flow structures in open channels. John Wiley and Sons, Chichester.

Bates, P. D., M. D. Stewart, G. B. Siggers, C. N. Smith, J.-M. Hervouet, and R. H. J. Sellin, 1998: Internal and external validation of a two-dimensional finite element model for river flood simulation. Proceedings of the Institution of Civil Engineers, Water Maritime and Energy, **130**, 127–141.

Bates, P. D., M. D. Wilson, M.S. Horritt, D. Mason, N. Holden, and A. Currie, 2006: Reach scale floodplain inundation dynamics observed using airborne Synthetic Aperture Radar imagery: Data analysis and modelling. Journal of Hydrology, 328, 306–318.

Biancamaria, S., P. D. Bates, A. Boone, and N. M. Mognard, 2009: Large-scale coupled hydrologic and hydraulic modelling of an arctic river: The Ob river in Siberia. Journal of Hydrology, 379, 136–150.

Bridge, J. S., and S. L. Gabel, 1992: Flow and sediment dynamics in a low sinuosity, braided river—Calamus River, Nebraska sandhills. Sedimentology, 39(1), 125–142.

Chanson, H., 1999: The hydraulics of open channel flow: An introduction. Arnold, London.

Dartmouth Flood Observatory 1985–2002: World Atlas of Large Flood Events. http://www.dartmouth.edu/~floods/archiveatlas/index.htm . Last accessed December 31, 2011.

Hervouet, J.-M., and L. Van Haren, 1996: Recent advances in numerical methods for fluid flows. In Floodplain Processes. Eds. M. G. Anderson, D. E. Walling, and P. D. Bates, John Wiley and Sons, Chichester, 183–214.

Horritt, M. S., 1999: A statistical active contour model for SAR image segmentation. Image and Vision Computing, **17**, 213–224.

Horritt, M. S., and P. D. Bates, 2002: Evaluation of 1-D and 2-D numerical models for predicting river flood inundation. Journal of Hydrology, **268**, 87–99.

Knight, D. W., and Shiono, K., 1996: River channel and floodplain hydraulics. In Floodplain Processes. Eds. M. G. Anderson, D. E. Walling, and P. D. Bates, John Wiley and Sons, Chichester, 139–182.

Lane, S.N., K. F. Bradbrook, K.S. Richards, P. M. Biron, and A. G. Roy, 1999: The application of computational fluid dynamics to natural river channels: Three-dimensional versus two-dimensional approaches. Geomorphology, **29**, 1–20.

Marks, K., and P. D. Bates, 2000: Integration of high resolution topographic data with floodplain flow models. Hydrological Processes, **14**, 2109–2122.

Mason, D. C., M. S. Horritt, N. M. Hunter, and P. D. Bates, 2007: Use of fused airborne scanning laser altimetry and digital map data for urban flood modelling. Hydrological Processes, **21**, 1436–1477.

McLelland, S. J., P. J. Ashworth, J. L. Best, and J. R. Livesey, 1999: Turbulence and secondary flow over sediment stripes in weakly bimodal bed material. American Society of Civil Engineers, Journal of Hydraulic Engineering, **125**(5), 463–473.

NERC, 1975: Flood studies report. Natural Environment Research Council, London, 5 volumes. Bates, P. D., M. D. Stewart, G. B. Siggers, C. N. Smith, J.-M. Hervouet, and R. H. J. Sellin, 1998: Internal and external validation of a two-dimensional finite element model for river flood simulation. Proceedings of the Institution of Civil Engineers, Water Maritime and Energy, **130**, 127–141.

Nezu, I., A. Tominaga, and H. Nakagawa, 1993: Field-measurements of secondary currents in straight rivers. American Society of Civil Engineers, Journal of Hydraulic Engineering, **119**(5), 598–614.

Nicholas, A. P., and C. A. Mitchell, 2003: Numerical simulation of overbank processes in topographically complex floodplain environments. Hydrological Processes, **17**(4), 727–746.

Pappenberger, F., K. Beven, M. Horritt, and S. Blazkova, 2005: Uncertainty in the calibration of effective roughness parameters in HEC-RAS using inundation and downstream level observations. Journal of Hydrology, **302**(1-4), 46–69.

Pappenberger, F., P. Matgen, K. Beven, J. B. Henry, L. Pfister, and P. De Fraipont, 2006: Influence of uncertain boundary conditions and model structure on flood inundation predictions. Advances in Water Resources, **29**, 1430–1449.

Preissmann, A., 1961: Propagation of translatory waves in channels and rivers. In Proceedings of the 1st Congress de l'Association Francaise de Calcul, Grenoble, France, 433–442.

Romanowicz, R., and K. Beven, 2003: Estimation of flood inundation probabilities as conditioned on event inundation maps. Water Resources Research, **39**(3), 1073.

Sanders, B.F., 2007: Evaluation of on-line DEMs for flood inundation modeling, Advances in Water Resources, **30**(8) 1831–1843

Schlichting, H., 1979: Boundary-layer theory, Seventh edition. McGraw-Hill, New York.

Schumann, G., F. Pappenberger, and P. Matgen, 2008: Estimating uncertainty associated with water stages from a single SAR image. Advances in Water Resources, **31**(8), 1038–1047.

Shvidchenko, A. B. and G. Pender, 2001: Macroturbulent structure of open-channel flow over gravel beds. Water Resources Research, **37(**3), 709–719.

UNESCO, 2005: 2005 disasters in numbers. Source of data: EM-DAT: The OFDA/CRED, International Disaster Database, http://www.emdat.be/, Université Catholique de Louvain, Brussels – Belgium. Report at http://www.unisdr.org/files/5401_2005disasterinnumbers.pdf. Last accessed January 12, 2012.

Wilson, M. D., P. D. Bates, D. Alsdorf, B. Forsberg, M. Horritt, J. Melack, F. Frappart, and J. Famiglietti, 2007: Modeling large-scale inundation of Amazonian seasonally flooded wetlands. Geophys. Res. Lett., **34**, L15404.

5 ADDITIONAL OBJECTIVES

SWOT measurements will be of value to a host of applications in addition to the primary objectives in mesoscale oceanography and terrestrial hydrology. These “additional objectives” are not considered main drivers for the mission. Significant resources will not be allocated to meet them. However, within the realm of mission design, and without incurring significant risk and cost, the best possible effort will be made to accommodate the additional objectives.

5.1 Ocean Tides

As in previous altimeter missions, tides will present important challenges and opportunities for the SWOT mission. However, the exact nature of these challenges and opportunities differs from those in previous missions, because of the higher horizontal resolutions of the SWOT data. In particular, considerable attention must be given to internal tides, which can perturb sea-surface elevations over wavelengths of order 100 km with amplitudes sometimes approaching 5 cm.

The success of using any altimeter for studying nontidal motions relies on accurate prior corrections to remove the dominant tidal signals. The challenge of doing that for SWOT is discussed in section 6.3. Here we address the opportunities that SWOT presents for increasing our knowledge of tides. We foresee advances in three areas: high-latitude tides, near-coastal tides, and internal tides.

5.1.1 Tides In High Latitudes

SWOT's nominal inclination of 78° implies that SWOT will map a large swath of the ocean polewards of the TOPEX/Poseidon–Jason latitude limit of 66.1°. Currently the tides in that region have been determined by hydrodynamic modeling, sometimes constrained by a handful of tide-gauge stations, and by ERS-1/2 and Envisat altimetry, although the ERS and Envisat results are problematic owing to their sun-synchronous orbits. Figure 5.1-1 highlights the current level of uncertainty in tidal charts over the 66°–78° band; note in particular the large increase in model differences in Baffin Bay just north of 66°.

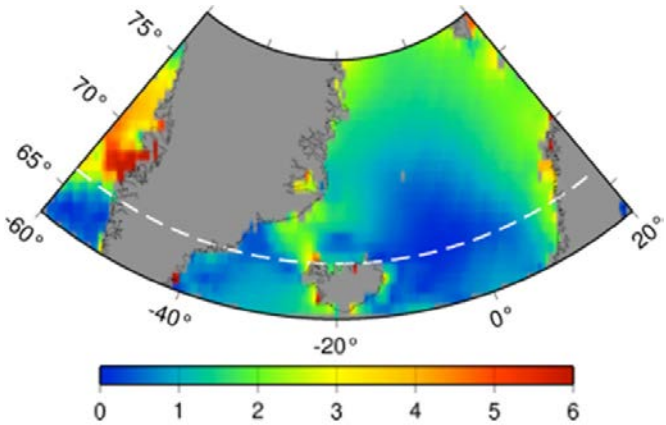

Figure 5.1-1. Maximum differences (cm) between the S2 tide models of FES2004 and TPXO7.1 for the seas near Greenland. The white dashed line marks 66° N, the northernmost latitude reached by the TOPEX/Poseidon and Jason satellites. Large model differences south of 66° are mostly coastal problems; differences increase markedly north of 66°. Both models used data from ERS-1/2 altimetry north of 66°, but those data reveal nothing about S2 owing to the sun-synchronous orbits. SWOT should remedy this situation.

New SWOT data should considerably improve all tidal charts in this region. As discussed in section 6.3, the orbit of SWOT is designed in part to facilitate mapping tides. Although the tidal alias frequencies are not perfect—some sacrifices are necessary to reach near-polar latitudes—they should adequately allow for empirically mapping tides in regions such as those in Figure 5.1-1.

Moreover, SWOT's high resolution will enhance its ability to measure sea level in the presence of sea ice (see section 5.4). This should also improve tidal mapping. In fact, tide models in some regions below ±66° latitude are problematic now because of persistent sea ice. For example, TOPEX/Poseidon obtained few valid returns in the northern Weddell Sea east of the Larsen Ice Shelf, and existing tide models have been impacted by this lack of data. Other regions that will benefit include the Bering Sea, the Okhotsk Sea, Hudson Bay, and the Canadian Arctic Archipelago.

5.1.2 Near-Coastal and Shelf Tides

Tidal wavelengths in shallow water are generally much shorter than those in the deep ocean, reflecting reduced propagation speeds. It is thus rather obvious that the high horizontal resolution of SWOT will add to knowledge of near-coastal and shelf tides. Many features of near-coastal tides have been inadequately sampled or completely missed with present-day altimetry. An example, taken almost at random from the literature (Canhanga and Dias, 2005), is shown in Figure 5.1-2. In this case—a small bay along the southern coast of Mozambique—TOPEX/Poseidon and Jason altimeter data could conceivably supply open boundary conditions for tidal modeling, but otherwise only data at a single tide gauge at the port city of Maputo can be used for testing. In particular, the relatively high amplitudes within the bay proper are totally unconstrained by in situ measurements. SWOT will provide a wealth of data for modeling tides in such regions.

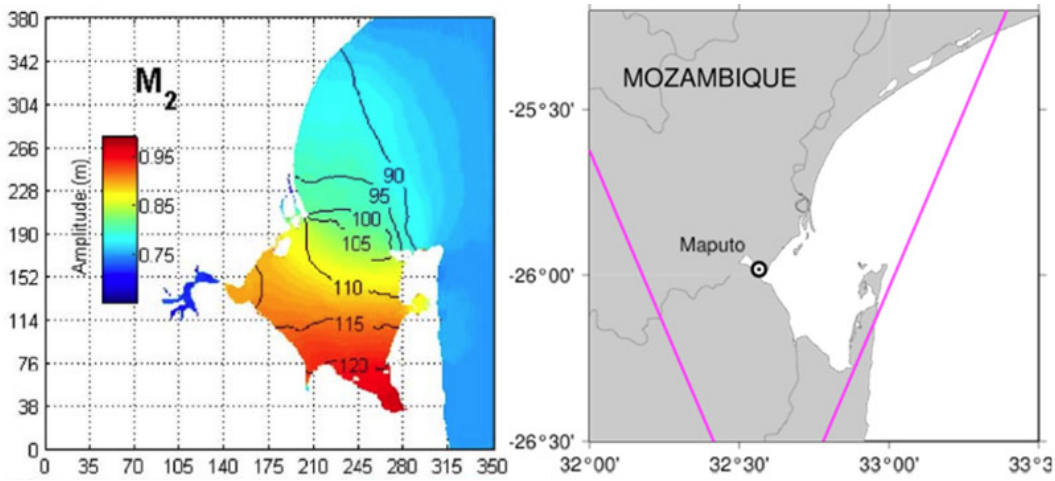

Figure 5.1-2. (Left) Simulated M_2 tide in Maputo Bay, along the southern coast of Mozambique, from Canhanga and Dias (2005). Color scale depicts model amplitudes in meters; contour lines depict phases in degrees. Canhanga and Dias had only data from a single tide gauge at Maputo to test their model. Labels along axes are in grid units, which were 250 m. (Right) The ground tracks of TOPEX/Poseidon and Jason over this region. Data along those tracks could conceivably supply valuable open boundary conditions for modeling Maputo Bay tides, but they completely miss the bay itself. SWOT will provide elevation measurements at a resolution comparable to the Canhanga–Dias numerical model.

Short wavelengths, however, are but one reason that present-day models of shallow-water tides are deficient on a global scale. In many regions nonlinear interactions present additional complications: They distort normally smooth tidal admittances, a result that confounds inference of smaller constituents, and they generate potentially dozens of compound tides that must be determined before accurate predictions can be computed. A recent review (Ray et al., 2011) discusses many aspects of shallow-water tides in the context of satellite altimetry. The main conclusion is that determination of shallow-water tides requires a considerably longer time series of elevation measurements than do tides in deep water. Thus, the longer the SWOT time series lasts, the more valuable the data become for determining shallow-water tides.

In addition to their role in providing critical corrections to nontidal altimeter studies and to other kinds of geodetic measurements (e.g., ocean loading), accurately mapped tides in near-coastal environments have a wide range of scientific and practical applications. The latter include navigation, sedimentation, pollution dispersal, and, more generally, the distribution of tracers and nutrients. These important applications all require knowledge of tidal currents. Similarly, understanding processes such as tidal stirring and mixing, diffusion, and formation of tidal fronts requires knowledge of currents, usually three-dimensional (e.g., Simpson, 1998). Nonlinear rectification, where the tidal flow adds to the mean circulation, can be significant near steep bottom topography (Zimmerman, 1981). Tidal currents tend to exhibit much greater small-scale variability than tidal elevations (Prandle, 1997), so such problems are ideally matched to SWOT's fine-scale horizontal resolution.

Based on our experience in using deep-ocean altimetry to address fundamental questions of barotropic tidal dynamics (e.g., Egbert and Ray, 2000), we have every expectation that SWOT data can similarly be employed to constrain models of the complex three-dimensional processes occurring in shelf and coastal seas. However, the methods of data assimilation currently used in three-dimensional regional tidal models often tend to be too simplistic. (For example, it is common to invert only the open boundary conditions.) Further development of methodologies for data assimilation and inference will be needed to fully exploit SWOT data for shallow-water tidal problems.

5.1.3 Deep-Ocean Internal Tides

Our knowledge of the sea-surface height signature of internal tides derives primarily from analysis of alongtrack altimeter data (Ray and Mitchum, 1997), although numerical models at regional (e.g., Kang et al., 2000; Merrifield et al., 2001) and global (Simmons et al., 2004; Arbic et al., 2004, 2010) scales are continually improving. The altimetry is most sensitive to the lowest-order baroclinic mode, since that mode generally has the largest displacement at the sea surface (Wunsch, 1975) and—at least some evidence suggests—tends to be more temporally coherent (phase-locked) with the astronomical tide (e.g., Ray and Zaron, 2011). The wavelength of first-mode semidiurnal tides is of order 100 km. This is much shorter than the resolution achievable with current satellite

altimetry, except in the alongtrack direction, so altimetry currently provides us with a very incomplete picture of the surface field of internal tides. Inferred dynamics (e.g., horizontal energy fluxes) are likewise incomplete, but can surely be improved with better spatial resolution (Zhao and Alford, 2009). It seems evident that SWOT can considerably fill in these partial views of the internal-tide field with a nearly complete mapping of the phase-locked tide, of the sort that numerical simulations suggest exists (see Figure 5.1-3).

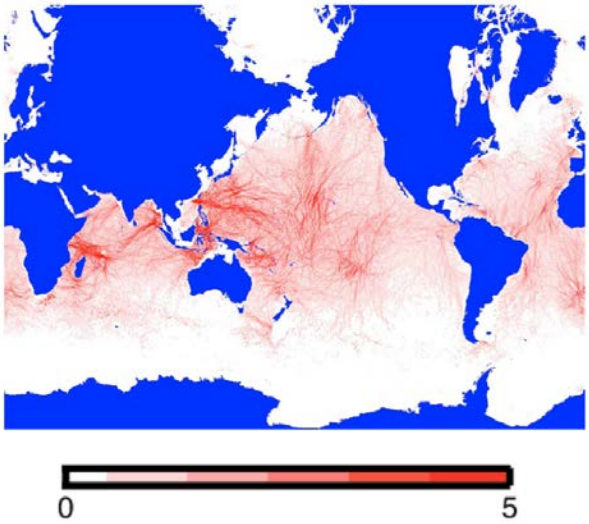

Figure 5.1-3. Amplitude (cm) of M_2 internal tide signature in steric SSH of HYbrid Coordinate Ocean Model (HYCOM) experiment with 32 layers, 1/12.5° horizontal resolution, horizontally nonuniform stratification, and wind-, buoyancy-, and M_2-forcing included. From Arbic et al. (2010).

It is of interest to examine the state of current modeling capabilities regarding the global internal tide field (e.g., Figure 5.1-3) and the manner in which SWOT may add to this capability. As an example, Figure 5.1-4 shows the M_2 internal (baroclinic) tide amplitude, computed as high-passed perturbations to the total (baroclinic plus barotropic) M_2 amplitude, at the sea surface. The computation is done from both altimetric data and from a global simulation of the HYbrid-Coordinate Ocean Model with 32 layers in the vertical direction, 1/12.5° horizontal resolution, and tidal forcing in addition to wind- and buoyancy-forcing (Arbic et al., 2010). HYCOM will soon become the workhorse U.S. Navy operational global model, and the HYCOM simulations shown here represent an early attempt by the Navy to include tides in a high-resolution general circulation model. Figure 5.1-4 demonstrates that, generally speaking, models display high internal tide activity in the same hotspots documented by altimetry data (e.g. Hawai‘i, east of the Philippines, tropical central and southwestern Pacific, and Madagascar region). Figure 5.1-5 shows the perturbations to the M_2 elevation amplitudes due to the internal tides (computed as in Figure 5.1-4, except that now absolute values are not taken), shown in the northeastern Pacific. The HYCOM simulation matches some of the altimetrically observed features, but there are other features that are not well captured in the model. It is likely that improvements in the agreement between models and observations will be realized, for example by increasing

the model resolution. Additionally, data assimilation has already been shown to produce improved internal-tide fields (Zaron et al., 2009), and further efforts in assimilation are ongoing. Moreover, assimilation results can undoubtedly be improved when the dense elevation data provided by SWOT become available.

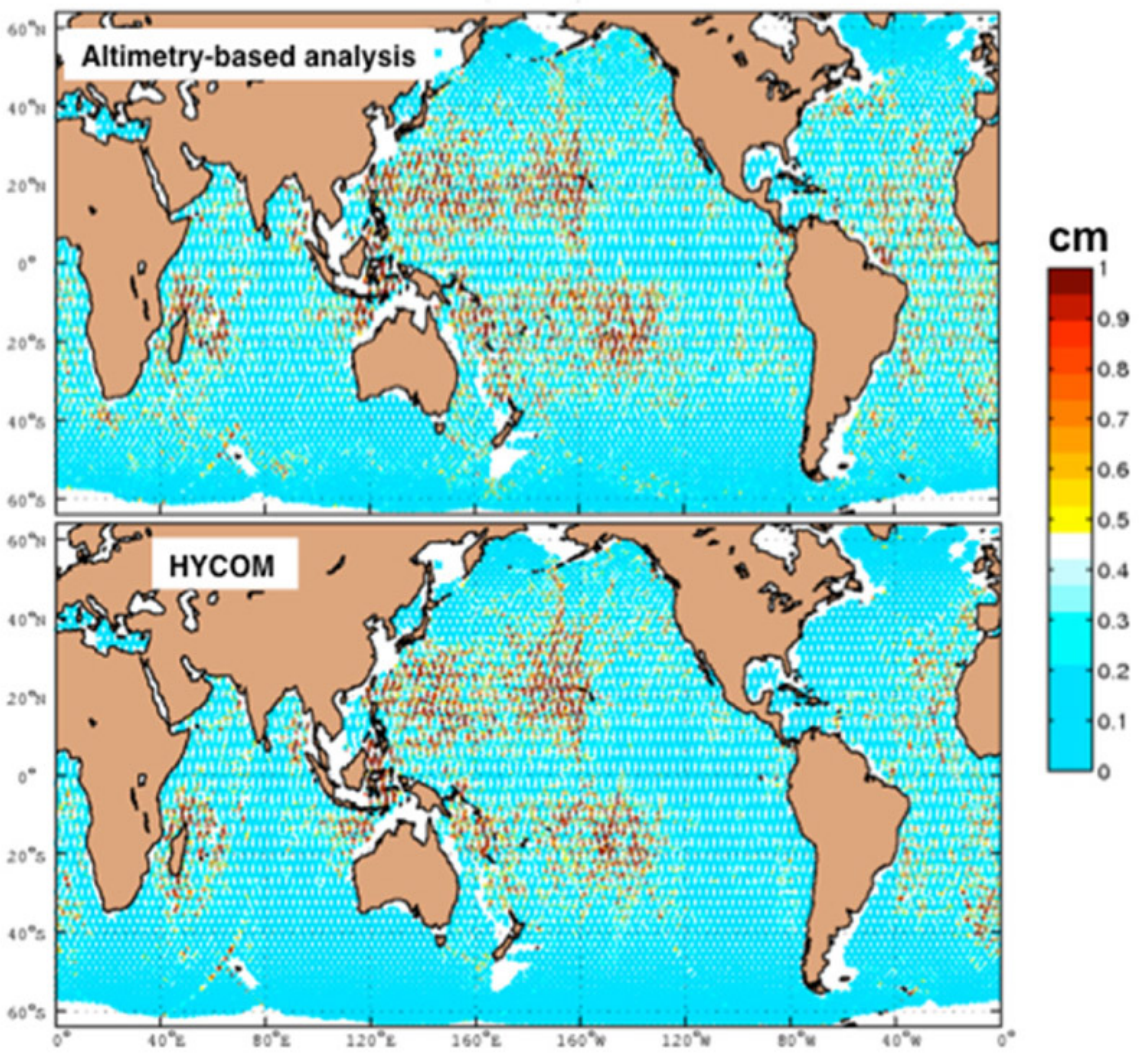

Figure 5.1-4. Amplitudes (top, altimetric and bottom, HYCOM) of the M_2 internal tide signature in sea surface elevation along altimeter tracks. HYCOM output is interpolated to altimeter tracks for comparison. HYCOM simulation shown is a 32-layer, wind-, buoyancy-, and M_2- forced simulation. For both subplots the internal (baroclinic) tide amplitudes are computed from high-passing the total (baroclinic plus barotropic) M_2 signal. This yields an amplitude—or more precisely, a perturbation to the amplitude—that has both positive and negative values. In the plot above absolute values (always positive) are shown. (Plot courtesy Jay Shriver, 2011.)

An important question regarding internal tides that has critical implications for correcting SWOT data for internal-tide signals (section 6.3) is the degree to which the internal-tide surface elevations maintain phase-lock with the tidal potential. That is, how temporally varying are these signals? This is a topic of ongoing research with TOPEX/Poseidon and Jason altimetry and with numerical modeling. In particular, models that combine baroclinic tides with the eddy-permitting general circulation (Arbic et al., 2010) are ideal for studying temporal stability in the presence of background flows such as mesoscale eddies. Initial studies with satellite altimetry (Ray and Zaron, 2011) suggest that the mode-1 tides are surprisingly coherent over most of the global ocean, with some

important exceptions; strong seasonal variability, for example, has been detected in the South China Sea. Further research on these issues before the launch of SWOT will be conducted and is likely to have a bearing on how SWOT data are corrected for tides (section 6.3).

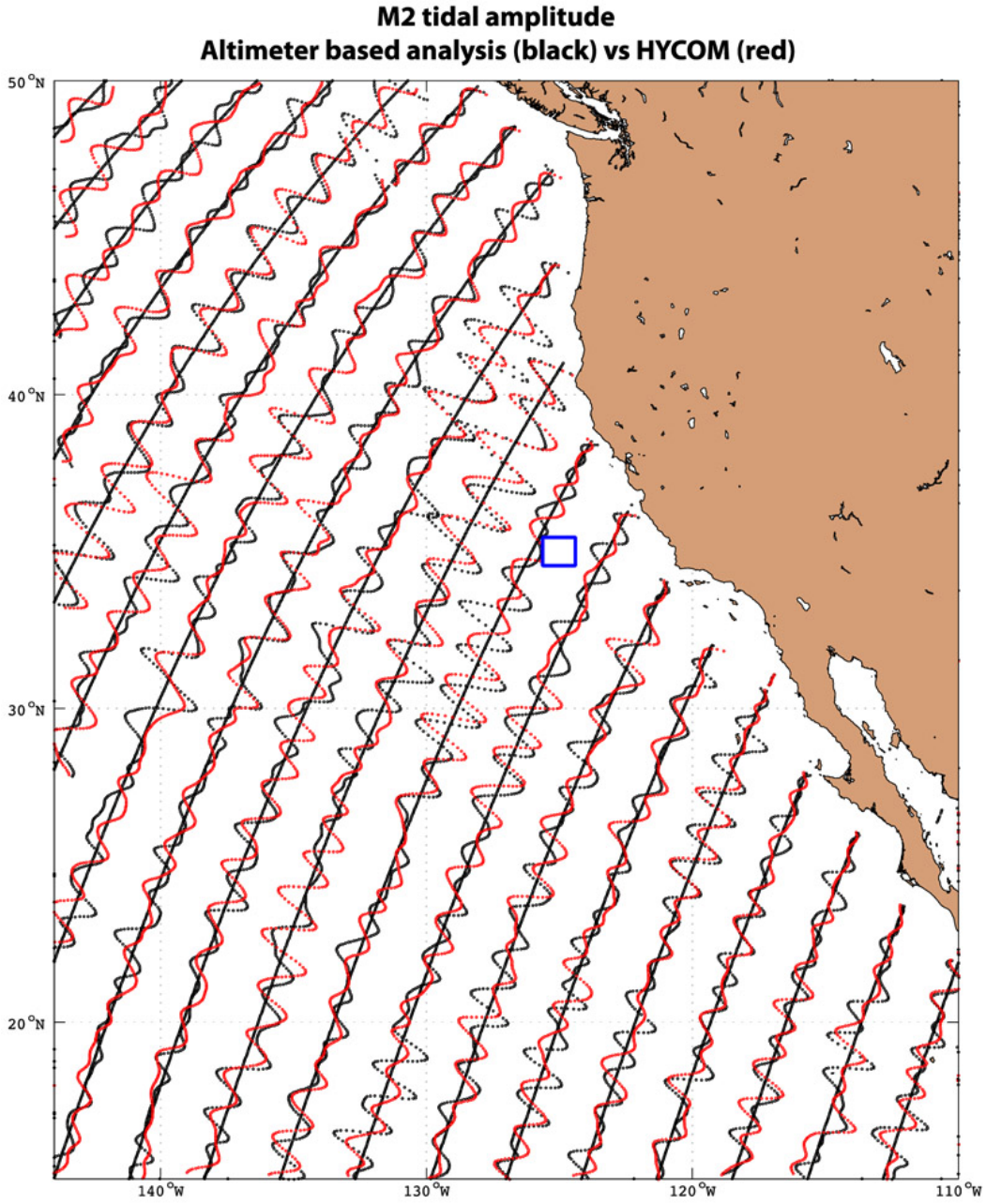

Figure 5.1-5. Internal tide perturbations to amplitude of M_2 sea surface elevation along ascending altimetric tracks in North Pacific. Blue box is a site considered for the AirSWOT mission. (Plot courtesy Jay Shriver, 2011.)

References

Arbic, B. K., S. T. Garner, R. W. Hallberg, and H. L. Simmons, 2004: The accuracy of surface elevations in forward global barotropic and baroclinic tide models. Deep-Sea Research II, **51**, 3069–3101.

Arbic, B. K., A. J. Wallcraft, and E.J. Metzger, 2010: Concurrent simulation of the eddying general circulation and tides in a global ocean model. Ocean Modelling, **32**, 175–187.

Canhanga, S., and J. M. Dias, 2005: Tidal characteristics of Maputo Bay, Mozambique. J. Marine Sys., **58**, 83–97.

Egbert G. D., and R. D. Ray, 2000: Significant dissipation of tidal energy in the deep ocean inferred from satellite altimeter data. Nature, **405**, 775–778.

Kang, S. K., M. G. G. Foreman, W. R. Crawford, and J. Y. Cherniawsky, 2000: Numerical modeling of internal tide generation along the Hawaiian Ridge, J. Phys. Oceanogr., **30**, 1083–1098.

Merrifield, M. A., P. E. Holloway, and T. M. S. Johnston, 2001: The generation of internal tides at the Hawaiian Ridge. Geophys. Res. Lett., **28**, 559–562.

Prandle, D., 1997: Tidal currents in shelf seas—their nature and impacts. Progr. Oceanogr., **40**, 245–261.

Ray, R. D., and G. T. Mitchum, 1997: Surface manifestation of internal tides in the deep ocean: Observations from altimetry and tide gauges. Progr. Oceanogr., **40**, 135–162.

Ray, R. D., and E. D. Zaron, 2011: Non-stationary internal tides observed with satellite altimetry. Geophys. Res. Lett., **38**, L17609.

Ray, R. D., G. D. Egbert, and S. Y. Erofeeva, 2011: Tide predictions in shelf and coastal waters: Status and prospects. In Coastal Altimetry. Eds. S. Vignudelli et al., Springer, 191–216.

Simmons, H. L., R. W. Hallberg, and B. K. Arbic, 2004: Internal wave generation in a global baroclinic tide model. Deep-Sea Research II, **51**, 3043–3068.

Simpson, J. H., 1998: Tidal processes in shelf seas. In The Sea, Vol. 10. Eds. K. H. Brink and A. R. Robinson, Wiley, 113–150.

Wunsch, C., 1975: Internal tides in the ocean. Rev. Geophys. Space Phys., **13**, 167–182.

Zaron, E. D., C. Chavanne, G. D. Egbert, and P. Flament, 2009: Baroclinic tidal generation in the Kauai Channel inferred from high-frequency radio Doppler current meters. Dyn. Atmos. Oceans, **48**, 93–120.

Zhao, Z., and M. H. Alford, 2009: New altimetric estimates of mode-1 M_2 internal tides in the central North Pacific Ocean. J. Phys. Oceangr., **39**, 1669.

Zimmerman, J. T. F., 1981: Dynamics, diffusion and geomorphological significance of tidal residual eddies. Nature, **290**, 549–555.

5.2 Ocean Bathymetry

The depth to the ocean floor and the roughness of the bottom vary throughout the oceans as a result of numerous geologic processes (Brown et al., 1998). This seafloor topography influences the ocean circulation and mixing that moderate Earth's climate (Kunze and Llewellyn Smith, 2004; Munk and Wunch, 1998), and the biological diversity and food resources of the sea. The ocean floor records the geologic history and activity of the ocean basins (Mueller et al., 1997), revealing areas that may store resources such as oil and gas (Fairhead et al., 2001), and generate earthquakes and tsunamis (Mofjeld et al., 2004). Despite the importance of Earth's ocean floor to our quality of life, we have made much better maps of the surfaces of other planets, moons, and asteroids.

After five decades of surveying by ships carrying echosounders, most of the ocean floor remains unexplored, and there are vast gaps between survey lines (Figure 5.2-1). The primary reason for this lack of data is that ships are slow and expensive to operate. For example, a systematic mapping of the deep oceans by ships would take more than 120 years of survey time. Moreover, because the swath width of a multibeam echo sounder is proportional to depth, it takes much longer (750 ship-years) to survey the shallow (<500 m) continental margins (Carron et al., 2001). While shipboard surveys offer the only means for high-resolution seafloor mapping, moderate accuracy and resolution (12–17 km full wavelength) can be achieved using satellite radar altimetry at a fraction of the time and cost (Figure 5.2-2). Radar altimeters aboard the ERS-1 and Geosat spacecraft have surveyed the marine gravity field over nearly all of the world's oceans to a high accuracy and moderate spatial resolution of 25–45 km (Cazenave et al., 1996; Sandwell and Smith, 1997; Tapley and Kim, 2001). In the wavelength band 10 to 160 km, variations in gravity anomaly are highly correlated with seafloor topography (Figure 2-49) and thus, in principle, can be used to recover topography (Baudry and Calmant, 1991; Dixon et al., 1983; Jung and Vogt, 1992; Ramillien and Cazenave, 1997; Smith and Sandwell, 1994). The sparse ship soundings constrain the long wavelength (160 km) variations in seafloor depth and are also used to calibrate the local variations in topography to gravity ratio associated with varying tectonics and sedimentation.

Satellites have another advantage in comparison to the present database of echosoundings; namely, globally uniform resolution. By carrying the same sensor all over the globe, a satellite makes measurements of the same quality everywhere, a requirement for mapping the global distribution patterns of bathymetric features. Ships have not done this. The era of frontier exploration, when scientists could take ships into remote areas merely for curiosity's sake, was an era of single-beam echosounders and relatively poor navigation. The last two decades have seen great technical advances in echosounding (multi-beam swath mapping systems, Figure 5.2-2) and navigation (Global Positioning System), but these have been deployed over only a few percent of the ocean's area. The focus has been on coastal regions and Exclusive Economic Zones, and research

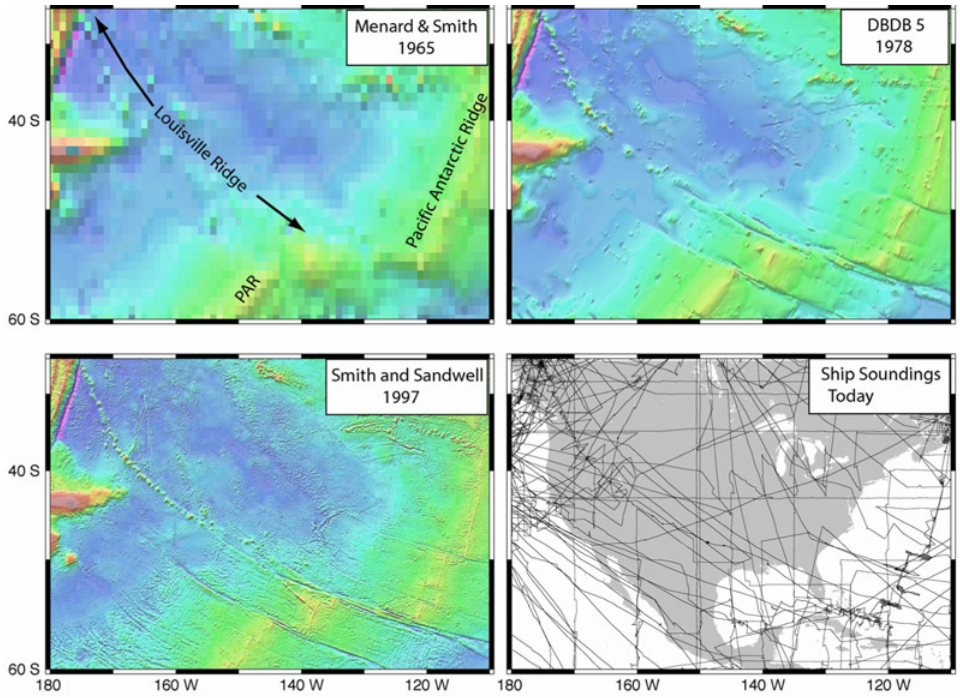

Figure 5.2-1. The Pacific-Antarctic rise, which has an area about equal to North America, is a broad rise of the ocean floor caused by seafloor spreading between two major tectonic plates. To the west of the ridge lies the Louisville seamount chain, which is a chain of large undersea volcanoes having a length equal to the distance between New York and Los Angeles. The Louisville seamount chain was first detected in 1972 using depth soundings collected along random ship crossings of the South Pacific. Six years later, the full extent of this chain was revealed by a radar altimeter aboard the Seasat (NASA) spacecraft (Haxby et al., 1983). More recently, high-density data collected by the Geosat (U.S. Navy) and ERS-1 (European Space Agency) spacecraft show the Pacific-Antarctic Rise and the Louisville Ridge in unprecedented detail (Smith and Sandwell, 1997).

emphasizing "hypothesis testing," which requires ships to revisit previously surveyed areas. The result is that even today, most of the data available in the remote oceans are the old-style, low-tech data.

5.2.1 Sensing Gravity and Bathymetry from Space

The ocean's surface has broad bumps and dips that reflect variations in the pull of gravity. In the deep ocean where sediments are thin, seafloor features such as seamounts produce minor variations in gravity, which in turn produce tiny variations in ocean surface height (Figure 5.2-3). On the shallow continental margins, where sediments are thick and the seafloor is relatively flat, gravity anomalies reflect the structure of the sedimentary basins. Gravity can be measured at orbital altitude using spacecraft such as CHAMP, GRACE, and GOCE (Tapley and Kim, 2001). However, because these spacecraft measure gravity at altitudes higher than 200 km, they are unable to recover wavelengths shorter than about 160 km. In contrast, satellite altimeters offer much higher

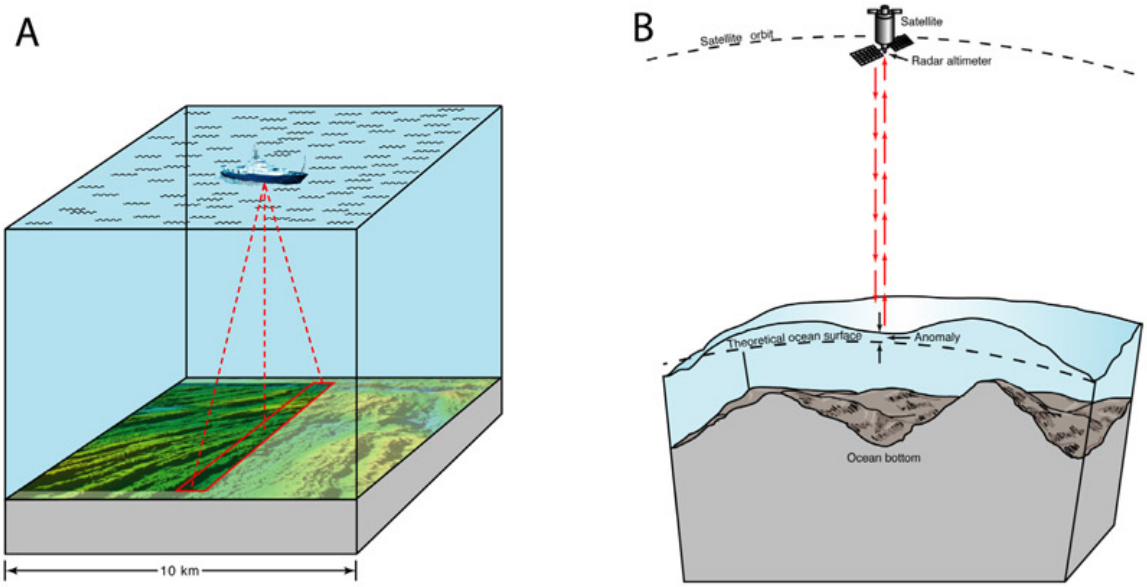

Figure 5.2-2. Modern tools for mapping the deep ocean floor. (A) A shipboard multibeam echo sounders uses sound waves to map 10–20 km wide swaths at ~200 horizontal resolution. (B) An Earth-orbiting radar cannot see the ocean bottom, but it can measure ocean surface height variations induced by ocean floor topography. While the resolution of the echo sounder technique is far superior to the ultimate resolution of the satellite altimeter technique (~8 km), complete mapping of the deep oceans using ships would take 200 ship-years at a cost of billions of dollars (Carron et al., 2001). Indeed, the shipboard and altimeter methods are highly complementary. The current distribution of ship soundings provides the long-wavelength (160 km) information that cannot be obtained from gravity because of spatial variations in isostasy (Figure 5.2-3). Satellite altimeters provide the global uniform coverage in the 16–160 km wavelength band. When interesting features are discovered in satellite gravity, they can be surveyed in fine detail by ships.

spatial resolution gravity measurements because they sense the gravity field at the ocean surface, which is typically only 4 km above the seafloor. In the deep ocean basins, where sediments are thin and seabed geology is simple, satellite altimeter data may be used to predict bathymetry at a half-wavelength scale of 6–9 km (Figure 5.2-3). Existing satellite altimeter data have proved the feasibility of the technique and revealed the overall, large-scale tectonic features of the ocean basins. A properly designed mission could bring significant new resolution, capturing a critical scale of features and facilitating new science and applications.

The radar altimeter measures sea surface bumps and dips by measuring the travel time of microwave pulses. For gravity field recovery and bathymetric estimation, alongtrack sea surface height differences (slopes) are needed, instead of absolute heights. The major error source is the roughness of the ocean surface due to ocean waves. The absolute height—and any component of height that changes only over wavelengths much longer than a few hundred kilometers—is irrelevant, as it contributes to negligible slope. For example, most of the standard altimeter corrections, such as radial orbit error,

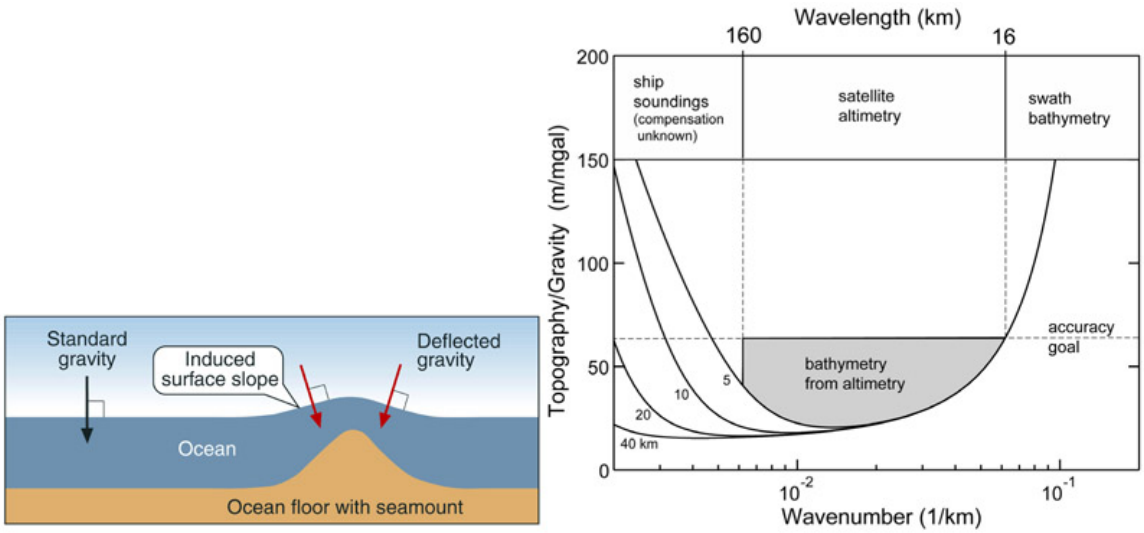

Figure 5.2-3. Satellite-derived bathymetry. (Left) A mountain on the ocean floor adds to the pull of Earth's gravity and changes its direction subtly, causing extra water to pile up around the mountain. The tilt in the direction of gravity, called a "deflection of the vertical," is equal to the slope of the sea surface, and is measured in microradians. One microradian of deflection appears as a 1 mm change in sea surface height per 1 km of horizontal distance. Laplace's equation allows the exact transformation of sea surface slope into gravity anomaly. One microradian error in slope translates into approximately 1 milligal (mgal) error in gravity. (Right) Over areas of thin sediment cover, the ratio of topography to gravity is primarily a function of topographic wavelength. A gravity field that is accurate to 1 milligal can recover topography between wavelengths of 16 km and 160 km to an accuracy of better than 70 m. The short-wavelength part of the transfer becomes singular because of the smoothing of gravity by upward continuation. The long-wavelength part of the transfer becomes singular because isostatic compensation cancels the long-wavelength gravity due to seafloor topography. For wavelengths of 160 km, the topography/gravity ratio is highly dependent on the elastic thickness of the lithosphere, so gravity cannot be uniquely inverted for topography. Both ship soundings and satellite altimeter data are needed to provide a global mapping of the seafloor topography. Existing sparse ship soundings are sufficient to constrain the long-wavelength (160 km) shape of the oceans. Ship soundings are also used to calibrate the topography to gravity ratio over the intermediate wavelength band (160–16 km). Shorter wavelength topography (<16 km) can only be recovered by swath bathymetry surveys. The resolution of seafloor structure within the achievable band of spatial resolution is a strong function of the signal-to-noise ratio in the altimeter data, and a new mission with a more precise altimeter would make improvements of a factor of 5 in vertical precision, 2–3 in horizontal length, and 4–9 in horizontal area.

ionosphere and troposphere delays, and deep ocean tides have slopes less than 1 microradian, which corresponds to a 1-milligal gravity accuracy. Besides having less stringent accuracy requirements, an altimeter optimized for gravity field recovery must have dense coverage. Current altimeters optimized for physical oceanography all have repeating orbits with sparse track coverage and thus do not contribute to the recovery of high-resolution gravity and bathymetry. The SWOT altimeter offers the possibility of dramatically increasing the resolution of the gravity field and ocean bathymetry if a

0.5-microradian precision can be achieved with 100% ocean coverage. Current altimeters have achieved 3-microradian precision, so achievement of a 0.5-microradian precision requires nearly an order of magnitude improvement in slope precision. Note that the 100% ocean coverage is not required for every 10-day repeat cycle. A swath altimeter mission having a drifting subcycle could achieve all the science goals related to bathymetry, while an exact repeat cycle mission would provide a mapping with spatial variations in gravity field accuracy that would need to be measured in a subsequent mission.

5.2.2 New Science

A new space bathymetry mission with 100% coverage would furnish—for the first time—a global view of the ocean floor at the proper scale to enable important progress in basic and applied science (Sandwell et al., 2006). This resolution threshold is critical for a large number of basic science and practical applications, including:

(1) Determining the effects of bathymetry and seafloor roughness on ocean circulation, mixing, climate, and biological communities, habitats, and mobility.

(2) Understanding the geologic processes responsible for ocean floor features unexplained by simple plate tectonics, such as abyssal hills, seamounts, microplates, and propagating rifts. Improving tsunami hazard forecast accuracy by mapping the deep ocean topography that steers tsunami wave energy.

(3) Mapping the marine gravity field to improve inertial navigation and provide homogeneous coverage of continental margins.

(4) Providing bathymetric maps for numerous other practical applications, including reconnaissance for submarine cable and pipeline routes, improving tide models, and assessing potential territorial claims to the seabed under the United Nations Convention on the Law of the Sea.

Because ocean bathymetry is a fundamental measurement of our planet, there is a broad spectrum of interest from government, the research community, industry, and the general public (e.g., Google Earth).

References

Baudry, N., and S. Calmant, 1991: 3-D Modelling of seamount topography from satellite altimetry. Geophys. Res. Lett., **18**, 1143–1146.

Brown, J., et al., 1998: The ocean basins: Their structure and evolution. Pergamon Press, Oxford.

Carron, M. J., et al., 2001: A proposed international long-term project to systematically map the world's ocean floors from beach to trench: GOMaP (Global Ocean Mapping Program). Inter. Hydr. Rev., **2**, 49–50.

Cazenave, A., et al., 1996: High-resolution mean sea surface computed with altimeter data of ERS-1 (Geodetic Mission) and TOPEX/Poseidon. Geophys. J. Int., **125**, 696–704.

Dixon, T. H., et al., 1983: Bathymetric prediction from Seasat altimeter data. J. Geophys. Res., **88**, 1563–1571.

Fairhead, J. D., et al., 2001: Satellite-derived gravity having an impact on marine exploration. In The Leading Edge, edited, 873–876.

Haxby, W. F., et al., 1983: Digital images of combined oceanic and continental data sets and their use in tectonic studies. EOS (AGU), **64**, 995–1004.

Jung, W. Y., and P. R. Vogt, 1992: Predicting bathymetry from Geosat-ERM and shipborne profiles in the South Atlantic Ocean. Tectonophysics, **210**, 235–253.

Kunze, E., and S. G. Llewellyn Smith, 2004: The role of small-scale topography in turbulent mixing of the global ocean. Oceanography, **17**, 55–64.

Mofjeld, H. O., et al., 2004: Tsunami scattering and earthquake faults in the deep Pacific Ocean. Oceanography, **17**, 38–46.

Mueller, R. D., et al., 1997: Digital isochrons of the world's ocean floor. J. Geophys. Res., **102**, 3211–3214.

Munk, W., and C. Wunch, 1998: Abyssal recipes II: Energetics of today and wind mixing. Deep-Sea Res. I, **45**, 1977–2010.

Ramillien, G., and A. Cazenave, 1997: Global bathymetry derived from altimeter data of the ERS-1 Geodetic Mission. J. Geodynamics, **23**, 129–149.

Sandwell, D. T., and W. H. F. Smith, 1997: Marine gravity anomaly from Geosat and ERS-1 satellite altimetry. J. Geophys. Res., **102**, 10039–10054.

Sandwell, D. T., W. H. F. Smith, S. Gille, E. Kappel, S. Jayne, K. Soofi, B. Coakley, and L. Geli, 2006: Bathymetry from space: Rationale and requirements for a new, high-resolution altimetric mission. Comptes Rendus Geoscience, **338**(14-15), 1049–1062.

Smith, W. H. F., and D. T. Sandwell, 1994: Bathymetric prediction fron dense satellite altimetry and sparse shipboard bathymetry. J. Geophys. Res., **99**, 21803–21824.

Smith, W. H. F., and D. T. Sandwell, 1997: Global sea floor topography from satellite altimetry and ship depth soundings. Science, **277**, 1956–1961.

Tapley, B. D., and M. C. Kim, 2001: Applications to Geodesy. In Satellite Altimetry and Earth Sciences, edited by L.-L. Fu and A. Cazenave, Academic Press, New York, 371–403.

5.3 Ice Sheets

The Earth's polar ice cover is one of the most rapidly changing components of the Earth System. In particular, changes in the Greenland and Antarctic ice sheets, which contain the equivalent of 7 and 60 m of sea level, respectively, pose a substantial threat for large and rapid sea level rise. Ice sheet contributions to sea level rise are controlled by the balance between growth processes—mainly accumulation—and loss processes—mainly surface ablation, discharge, and melting beneath the floating ice shelves and ice tongues (Figure 5.3-1).

Recent observations of the Greenland and Antarctic ice sheets have revealed that (a) these ice sheets are shrinking, and they are shrinking at a faster rate now than they were a decade ago (Rignot and Kanagaratnam, 2006; Rignot et al., 2008; Thomas et al., 2006; Rignot et al., 2008), (b) melt on the Greenland ice sheet has increased substantially to the point where about 30% more of the surface melts now than it did 30 years ago (Mote, 2007), and (c) many of Greenland and Antarctica's outlet glaciers are accelerating, hastening their delivery of ice to the surrounding seas (Rignot and Kanagaratnam, 2006; Rignot et al., 2008a).

The ice sheets are changing significantly in ways that matter to people all over the world. Yet the likely future behavior of the Greenland and Antarctic ice sheets is not well understood, as it is complicated by complex interactions between the ice sheet outlet glaciers and ice streams, and the surrounding seas.

The floating ice shelves and ice tongues that surround much of these ice sheets buttress the glaciers that discharge into the surrounding bodies of water. As a result, these

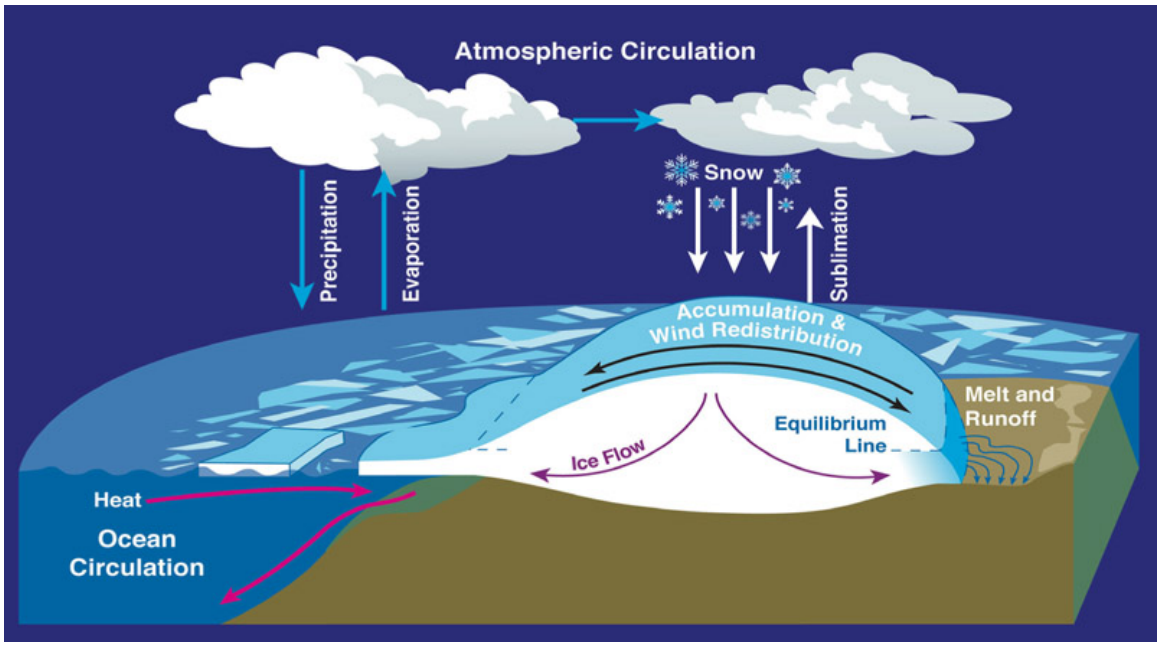

Figure 5.3-1. Schematic diagram of an ice sheet with its individual mass balance components.

glaciers are not flowing toward the sea as rapidly as they might in the absence of this floating ice (Mercer, 1978). As climate has warmed, these floating ice shelves have retreated, thinned and weakened in some areas, or in some instances, they have failed spectacularly (Figure 5.3-2). Without the ice shelf buttressing the outlet glaciers, their movement toward the sea can accelerate, in some cases two-fold or greater (Scambos et al., 2004; Rignot et al., 2004; Joughin et al., 2004). This phenomenon—an immediate response to present-day warming conditions—has been strikingly visible in Greenland with widespread glacier acceleration in the last decade (Rignot and Kanagaratnam, 2006; Rignot et al., 2008b). However, it is particularly significant in West Antarctica, where ice shelves are enormous, and where much of the ice rests on a soft deformable bed that lies below sea level. The disappearance of Antarctic ice shelves and the retreat of the ice sheet at its margins would allow the surrounding seawater to flow beneath the ice, eroding the ice further from underneath and enhancing its discharge. The time scales of these processes are not well known, but with the equivalent of 3.3 m sea level stored in the West Antarctic Ice Sheet (Bamber et al., 2009), this potential instability is of great importance to future sea level rise.

For the Greenland ice sheet there is an additional vulnerability associated with increased surface melting observed over the last several decades (Mote, 2007). Melt water from the ice sheet surface can penetrate through crevasses or tunnels in the ice (moulins) to the bed, where it lubricates the ice/bedrock interface, causing a summertime acceleration of glacier flow (Zwally et al., 2002; Joughin et al., 2008). This summer acceleration hastens the flow of ice toward the edges of the ice sheet, where it is either discharged to the sea or melts at the surface, directly contributing to sea level rise.

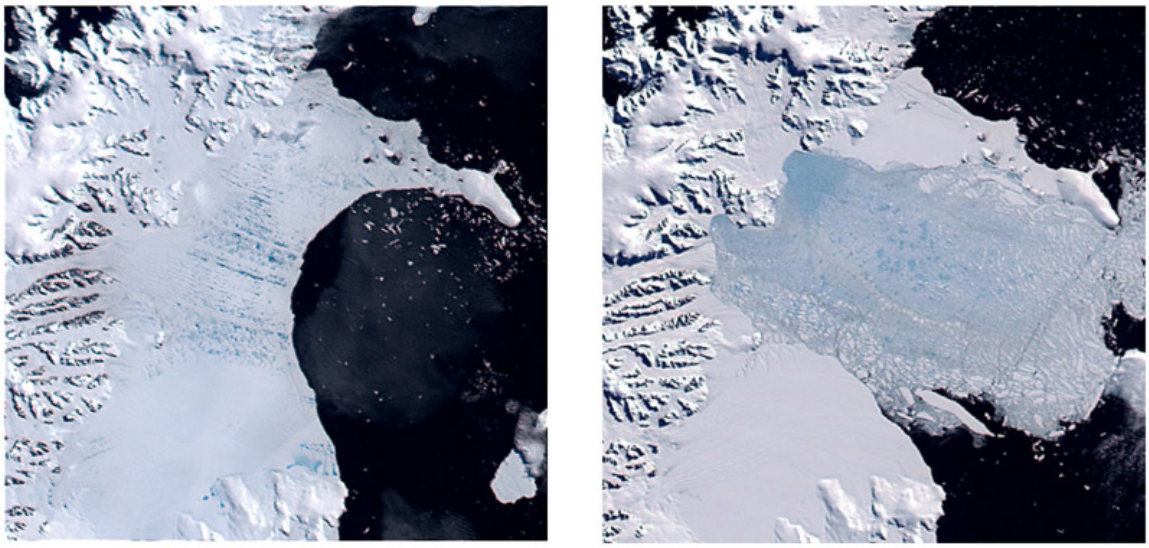

Figure 5.3-2. Larsen-B Ice Shelf on January 31, 2002 (left) and March 17, 2002. The 3,250-km section of ice shelf, estimated to be over 10,000 years old and 200-m thick, disintegrated in 6 weeks. Some of the glaciers that fed the ice shelf accelerated by eight-fold within months of the collapse. MODIS imagery courtesy of NASA and the National Snow and Ice Data Center.

Ice loss from these “dynamic vulnerabilities” is not limited only to the outlet glaciers or ice shelves. The ice in these regions is mechanically coupled to the rest of the ice sheets, so in time these losses propagate inward; thus the outlet glaciers and ice streams serve as conduits through which large amounts of ice from the ice sheet interior can flow.

The processes that govern ice sheet losses, in particular the flow of ice seaward, can be strongly nonlinear, causing such losses to be rapid. The growth processes, mainly snow accumulation, by contrast are more stable and change only slowly. As a result, there is a real potential for ice sheets to shrink rapidly, while growth (or recovery from ice loss) can only occur slowly. The processes that control the flow rates, and subsequently the potential for rapid loss, are not well understood. This prevented the IPCC from providing a comprehensive estimate of how much the ice sheets will contribute to sea level rise in the coming century.

Ice altimetry provides both an integrated assessment of ice sheet mass balance, by measuring elevation change rates, from which volume change rates, and subsequently ice sheet mass balance can be determined. In this way altimetry enables estimates of ice sheet contributions to sea level rise. Altimetry also provides important insights into the mechanisms that drive changes, as these mechanisms have distinct elevation-change signatures. Accumulation- and melt-driven imbalances, which are typically under a meter in height, tend to lower or raise surfaces in a manner that varies slowly over large distances; and that is not significantly different between adjacent areas of fast-moving ice streams and the slow-moving ice sheet. Dynamic imbalances, which can be many meters in magnitude, begin and are usually most extreme near outlet glacier termini, propagate inward with time, and vary significantly over small scales in transition regions between ice stream flow and sheet flow. Thus, with reasonable high-resolution observations, not only can the mass balance of large regions of the ice sheets be determined, but their underlying mechanisms can be assessed as well.

The SWOT mission is intended to have an inclination of 78°, covering most of the Greenland ice sheet (which extends northward to ~82°) and much of the Antarctic ice sheet (Figure 5.3-3). In the case of Antarctica, even though large areas will be omitted, the coastal regions will experience full coverage, with much higher density than conventional altimetry. The 120-km swath will provide several observations of any location on the ice sheet below 78° latitude several times during every 22-day orbit cycle. This will enable monitoring of seasonal evolution of the ice sheet surface, and will enable a spatially continuous high-resolution digital elevation model for the regions covered. As a result, the SWOT coverage will offer unprecedented opportunities to study ice sheet behavior. SWOT is expected to provide:

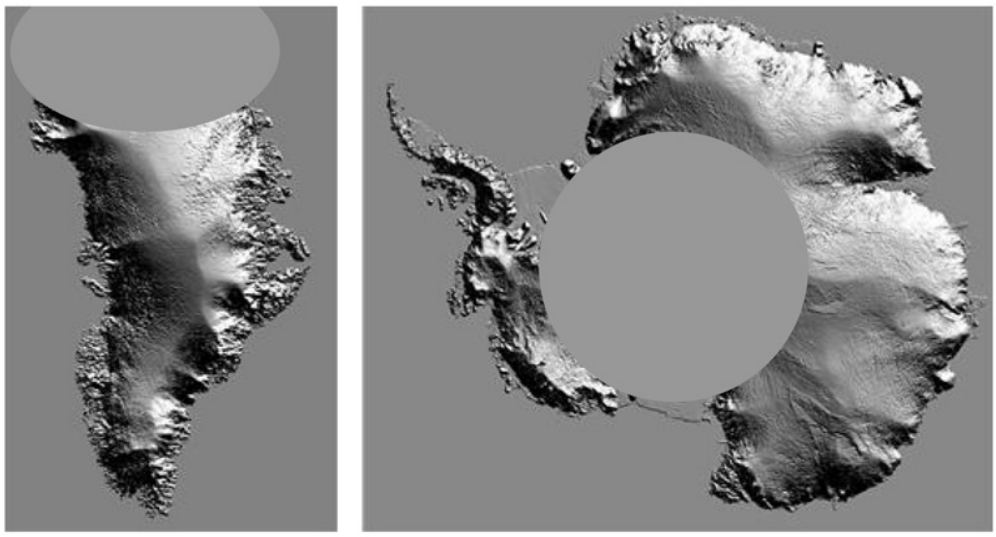

Figure 5.3-3. Shaded relief images of Greenland (left) and Antarctica (right) showing the areas expected to be covered by SWOT's 78° inclination (Dimarzio et al., 2007a and 2007b). The poleward most sections of the ice sheets that will omitted by the SWOT orbit are shaded gray.

- Important topographic information to aid in ice sheet modeling efforts
- Elevation change information to enable mass balance assessments of the most active areas of Greenland and Antarctica
- High spatial and temporal resolution of ice sheet changes to facilitate ice sheet modeling efforts and to provide critical insights into the mechanisms driving change.

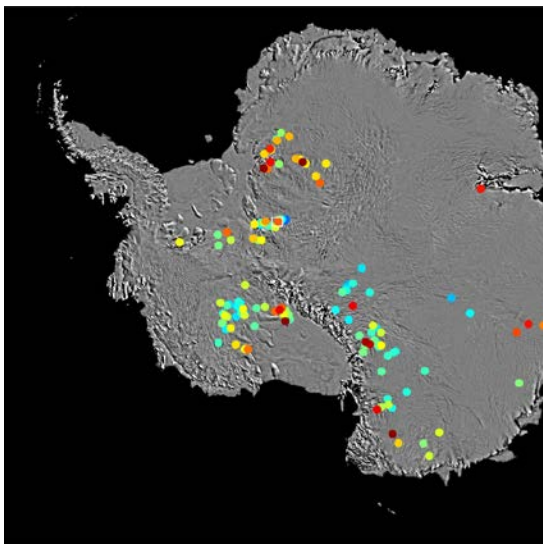

Figure 5.3-4. Locations and volume-range estimates for 124 active lakes under the Antarctic ice sheet found in Smith et al., 2009, shown as points color-coded by the volume range.

In addition, a newly emerging contribution of altimetry to our understanding of ice sheets is the insights it is providing into the hydrologic linkages among subglacial lakes (Figure 5.3-4). Some of these lakes drain and fill periodically as water flows from one to another beneath kilometers-thick of ice. (Wingham et al., 2006; Fricker et al., 2007). This sublglacial transport is expressed by increases and decreases of ice sheet surface height of several meters directly above the subglacial lakes. The frequent wide-swath characteristics of the SWOT mission will offer an

opportunity to observe this surface emergence and subsidence associated with lake filling and drainage, providing new insights into this little understood phenomenon. Additional contributions will include grounding line detection and movement, based on the topographic gradients where outlet glacier ice becomes a float, and improvements in our understanding of tidal characteristics in the vicinity of floating ice, as the vertical movement of this ice is monitored.

The ice sheets are shrinking, and they are shrinking at an increasing rate, raising questions about ice sheet stability, and the potential for rapid contributions to sea level rise. SWOT can provide an important complement to ICESat, ICESat-2, DESDynI, GRACE-2, and other NASA and international missions to help unlock the secrets to one of the most significant threats of global climate change: large and rapid increases in sea level.

References

Bamber, J. L., R. E. M. Riva, B. L. A. Vermeersen, and A. M. LeBrocqu, 2009: Reassessment of the potential sea-level rise from a collapse of the West Antarctic Ice Sheet. Science, **324**, doi: 10.1126/science.1169335, 901–903.

DiMarzio, J., A. Brenner, R. Schutz, C. A. Shuman, and H. J. Zwally, 2007a: GLAS/ICESat 500 m laser altimetry digital elevation model of Antarctica. National Snow and Ice Data Center, Boulder, Colorado, digital media.

DiMarzio, J., A. Brenner, R. Schutz, C. A. Shuman, and H. J. Zwally, 2007b: GLAS/ICESat 1 km laser altimetry digital elevation model of Greenland. National Snow and Ice Data Center, Boulder, Colorado, digital media.

Fricker, H. A., and T. Scambos, 2009: Connected subglacial lake activity on lower Mercer and Whillans ice streams. West Antarctica, 2003–2008. J. Glaciol, **55**(190), 303–315.

Fricker, H. A., T. A. Scambos, R. Bindschadler, and L. Padman, 2007: An active subglacial water system in West Antarctica mapped from space. Science, **315**(5818), 1544–1548.

Joughin, I., W. Abdalati, and M. Fahenstock, 2004: Large fluctuations in speed on Greenland's Jakobshavn Isbrae glacier. Nature, **432**, 608–610.

Joughin, I., S. B. Das, M. A. King, B. E. Smith, I. M. Howat, and T. Moon, 2008: Seasonal speedup along the western flank of the Greenland Ice Sheet. Science, **320**, 781–783; published online 16 April 2008, doi: 10.1126/science.1153288, in Reports.

Mercer, J. H., 1978: West Antarctic Ice Sheet and CO2 greenhouse effect: A threat of disaster. Nature, **271**, 321–325.

Mote, T. L., 2007: Greenland surface melt trends 1973–2007: Evidence of a large increase in 2007. Geophys. Res. Lett., **34**(22), L22507.

Rignot, E., G. Casassa, P. Gogineni, W. Krabill, A. Rivera, and R. Thomas, 2004: Accelerated ice discharge from the Antarctic Peninsula following the collapse of Larsen B ice shelf. Geophys. Res. Lett., **31**, L18401, doi:10.1029/2004GL020697.

Rignot, E., and P. Kanagaratnam, 2006: Changes in the velocity structure of the Greenland Ice Sheet. Science, **311**(5763), 986–990.

Rignot, E., J. L. Bamber, M. R. Van den Broeke, C. Davis, Y. H. Li, W. J. Van de Berg, and E. Van Meijgaard, 2008a: Recent Antarctic ice mass loss from radar interferometry and regional climate modeling. Nature Geosci., **1**(2), 106–110.

Rignot, E., J. E. Box, and E. Burgess, et al., 2008b: Mass balance of the Greenland Ice Sheet from 1958 to 2007. Geophys. Res. Lett., **35**(20), L20502.

Scambos, T. A., J. A. Bohlander, C. A. Shuman, and P. Skvarca, 2004: Glacier acceleration and thinning after ice shelf collapse in the Larsen B embayment, Antarctica. Geophys. Res. Lett., **31**, L18402, doi:10.1029/2004GL020670.

Smith, B., H. A. Fricker, I. Joughin, and S. Tulaczyk, 2009: An inventory of active subglacial lakes in Antarctica detected by ICESat (2003–2008). J. Glaciol, **55**(192), 573–595.

Thomas, R., E. Frederick, W. Krabill, S. Manizade, and C. Martin, 2006: Progressive increase in ice loss from Greenland. Geophys. Res. Lett., **33**(10), L10503 (10.1029/2006GL026075.)

Wingham, D. J., M. J. Siegert, A. Shepherd, and A. S. Muir, 2006: Rapid discharge connects Antarctic subglacial lakes. Nature, **440**, 1033.

Zwally, H. J., W. Abdalati, T. Herring, K. Larson, J. Saba, and K. Steffen, 2002: Surface melt acceleration of Greenland Ice Sheet flow. Science, **297**(5579), 218–222.

5.4 Sea Ice

The thickness distribution of sea ice controls the energy and mass exchanges between the ocean and atmosphere at the surface. The growth, movement, and decay of sea ice shape this time-varying field of ice thickness of the Arctic and Southern Oceans. Ice production and melt have broad consequences. The ice-covered ocean reflects a large fraction of the incident solar radiation back into space, while fresh water fluxes associated with melting Arctic ice may serve as stabilizing elements in the circulation of the North Atlantic waters. Furthermore, sea ice processes along the ice margin and coastlines participate in water-mass formation, upwelling, and sediment transport. Thus, monitoring the changes sea-ice thickness distribution is crucial for understanding its role in regional and global climate.

The Northern Hemisphere ice extent has been declining at an average rate of ~3% per decade over the satellite record, and the summer decline seems to be accelerating (Comiso et al., 2008). In September 2007, the summer ice extent reached a record minimum of 4.2×106 km^2, which was 1.6×106 km^2, or 23% less than the previous record set in September 2005 (Stroeve et al., 2008). Prior to ICESat, there has been a lack of ice thickness data to provide a basin-scale picture of the response of the ice cover to warming trends in the Arctic associated with changes in the atmosphere (Rigor and Wallace, 2004) and the ocean (Woodgate et al, 2006; Polyakov et al., 2007). The longest record documenting the decline in Arctic sea ice thickness over a sizable portion of the Arctic Ocean (Rothrock et al., 2008) is based on submarine ice draft from 1975 to 2000. However, few ice draft data sets are available from submarine cruises for the period after the concerted Science Ice Exercise (SCICEX) efforts of the 1990s. Compared to the data available for the Arctic Ocean, accurate and extensive measurements of the sea ice thickness of the Southern Ocean are virtually nonexistent (Worby et al., 2008).

Recent work demonstrated the efficacy of obtaining thickness using the retrieved freeboard from the profiling lidar on ICESat (Kwok et al., 2009). Ice thickness is estimated using altimeter-derived freeboards (the difference in elevation between the air/snow interface and the local sea surface; see Figure 5.4-1), along with estimates of snow loading. Figure 5.4-2 shows the winter ice thickness fields from five ICESat campaigns. Results from the ICESat thickness record show

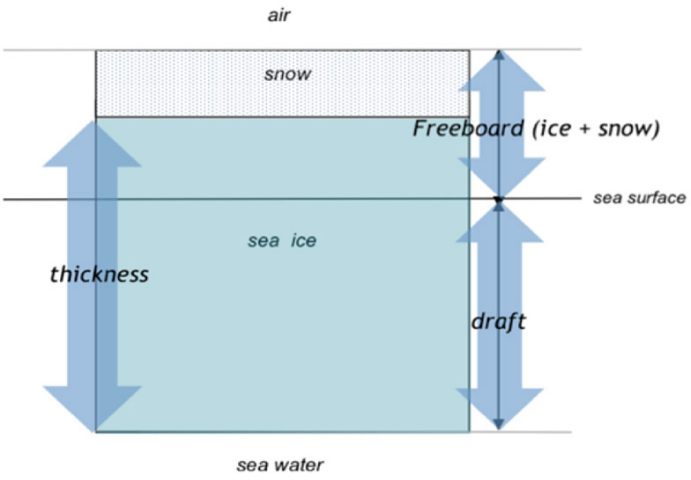

Figure 5.4-1. Schematic showing the geometric relationships between sea ice freeboard, thickness, and draft.

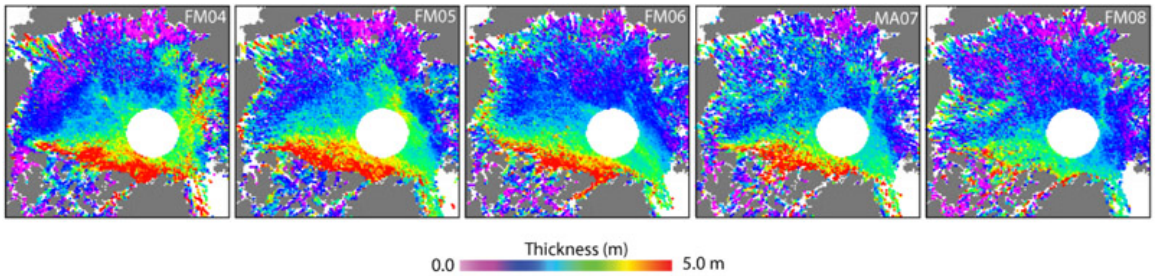

Figure 5.4-2. Sea ice thickness fields from five ICESat campaigns (2004–2008. http://rkwok.jpl.nasa.gov/icesat/index.html).

that between 2005 and 2008, there was a remarkable thinning of ~0.6 m in multiyear (MY—ice that has survived one summer) ice thickness (Figure 5.4-3). In contrast, the average thickness of the first-year (FY) ice in mid-winter (~2 m), which covered more than two-thirds of the Arctic Ocean in 2007, exhibited a negligible trend. Average winter sea ice volume from 2003 to 2008 was ~14000 km^3. Overall, the total MY ice volume in the winter has experienced a net loss of 6300 km^3 (>40%) in the years since 2005, while the FY ice cover gained volume due to increased overall area coverage. Together with a large decline in MY ice coverage over this short ICESat record, there is a reversal in the volumetric and areal contributions of the two ice types to the total volume and area of the Arctic Ocean ice cover. Seasonal ice surpassed MY ice in winter area coverage and volume. These recent changes have been dramatic.

Given the rapid changes of the ice extent during the past five years, there is a compelling need for up-to-date spatial patterns of Arctic sea ice thickness in order to understand the consequences of the large declines in summer ice coverage and likelihood of an ice-free Arctic during summer. Satellite estimates of sea ice thickness from ICESat elevation profiles have been shown to be useful for addressing this need. However, the ICESat data collection terminated in 2009. A lidar system on ICESat-2, to be launched in 2016, will continue this record. A nadir-looking radar altimeter on the CryoSat-2, launched in 2010, has been providing elevation profiles of the Arctic ice cover, and thickness estimates from this mission are anticipated.

However, cloud cover limits lidar coverage of the ice-covered oceans. This is especially acute during the summer and near the ice edge where there are strong atmosphere-ice-ocean interactions. SWOT's synthetic aperture radar interferometry offers advancements over the lidar altimetry in two respects: (1) the imaging technique is relatively unaffected by cloud cover and (2) its swath width is significantly larger (about 120 km). Due to clouds, lidar coverage of the polar oceans is reduced to ~40% after the onset of spring melt (from almost 90% during the winter), and there is significantly reduced coverage near the ice edge. With SWOT, the uninterrupted all-season coverage of the polar oceans represents a significant contribution to the understanding of changes in ice thickness–associated summer and fall processes that are not observed by the lidar. In addition, the fine spatial resolution of the instrument (10 m–70 m) is an advancement

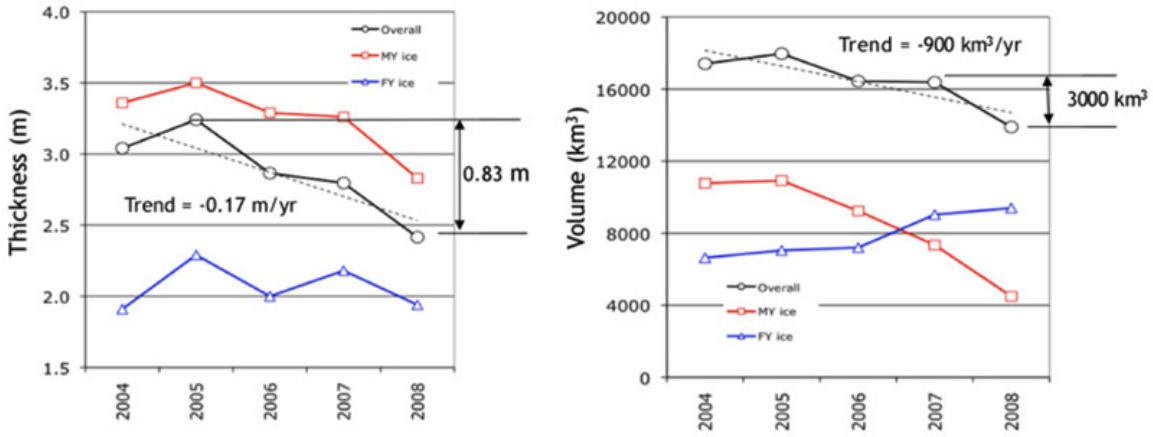

Figure 5.4-3. Decline in Arctic Ocean sea ice thickness and volume from ICESat (2004–2008). Plots show the mean multiyear ice (red) and first-year ice (blue), and overall ice thicknesses (black).

over the synthetic aperture radar mode of the CryoSat-2 altimeter (resolution: 1 km by 250 m) (Wingham et al., 2006). Fine resolution in radar altimetry is important for resolving the small areas of open water (leads, melt ponds) within the sea ice cover. Furthermore, the total swath width of 120 km—achieved by looking at both sides of the nadir track—would allow two-dimensional depictions of spatial variability of the freeboard/thickness of the ice cover that are important for quantifying exchanges of momentum between sea ice and the atmosphere and ocean.

The selected SWOT orbit provides coverage from 78° S to 78 °N with a 22-day repeat period. Even though this provides only partial coverage of the Arctic Ocean, the instrument covers the entire Southern Ocean sea ice cover. With the scientific benefits discussed above, the SWOT instrument is poised to provide unique contributions to polar science.

References

Comiso, J. C., C. L. Parkinson, R. Gersten, and L. Stock, 2008: Accelerated decline in the Arctic sea ice cover. Geophys. Res. Lett., **35**, L01703, doi:10.1029/2007GL031972.

Kwok, R., M. Wensnahan, I. Rigor, H. J. Zwally, and D. Yi, 2009: Thinning and volume loss of Arctic sea ice: 2003-2008. J. Geophys. Res., **114**, C07005, doi:10.1029/2009JC005312.

Polyakov, I., et al., 2007: Observational program tracks Arctic Ocean transition to a warmer state. EOS (AGU), **88**, 398–399.

Rigor, I. G., and J. M. Wallace, 2004: Variations in the age of Arctic sea ice and summer sea-ice extent. Geophys. Res. Lett., **31**, L09401, doi:10.1029/2004GL019492.

Rothrock, D. A., D. B. Percival, and M. Wensnahan, 2008: The decline in Arctic sea-ice thickness: Separating the spatial, annual, and interannual variability in a quarter

century of submarine data. J. Geophys. Res., **113**, C05003, doi:10.1029/2007JC004252.

Stroeve, J., et al., 2008: Arctic sea ice extent plummets in 2007. EOS(AGU), **89**, 13.

Wingham, D. J. et al., 2006: CryoSat: A mission to determine the fluctuations in Earth's land and marine ice fields. Adv. Space Res., **37**, 841–871.

Woodgate, R. A., K. Aagaard, and T. J. Weingartner, 2006: Interannual changes in the Bering Strait fluxes of volume, heat and freshwater between 1991 and 2004. Geophys. Res. Lett., **33**, L15609, doi:10.1029/2006GL026931.

Worby, A. P., C. A. Geiger, M. J. Paget, M. L. Van Woert, S. F. Ackley, and T. L. DeLiberty, 2008: Thickness distribution of Antarctic sea ice. J. Geophys. Res., **113**, C05S92, doi:10.1029/2007JC004254.

5.5 Tropical Cyclone Intensification Studies and Forecasts

Tropical cyclones (TCs) occur in seven ocean basins: tropical Atlantic, northeast Pacific, northwest Pacific, southwest Indian, north Indian, southeast Indian, and south Pacific (Figure 5.5-1). In general, the forecast of TC intensity has lagged behind the TC track because of the complexity of the problem and because many of the errors introduced in the track forecast are translated into the intensity forecast (DeMaria et al., 2005). While sea surface temperature (SST) plays a role in the genesis of tropical cyclones (TCs), the thermal structure of the upper ocean has been shown to also play an important role in TC intensity changes (Leipper and Volgenau, 1972; Shay et al., 2000), provided that atmospheric conditions are also favorable. However, studies geared towards the investigation of the role of the ocean on TC intensification have been limited due to the lack of in situ hydrographic observations that are able to resolve oceanic mesoscale features. Recent efforts to supplement the backbone observing system have focused on efficiently targeted observations ahead of major hurricanes such as Rita (2005), Dean (2007), Gustav and Ike (2008). These studies have confirmed that the upper ocean thermal structure from the sea surface to depths up to a few hundreds of meters can be linked to TC intensification. It is now accepted that resolving, understanding, and monitoring the upper ocean mesoscale field and its vertical thermal structure may be critical for TC intensification studies and forecasts.

The current sustained ocean observing system was not designed for these types of studies. In fact, sustained in situ hydrographic observations alone cannot completely

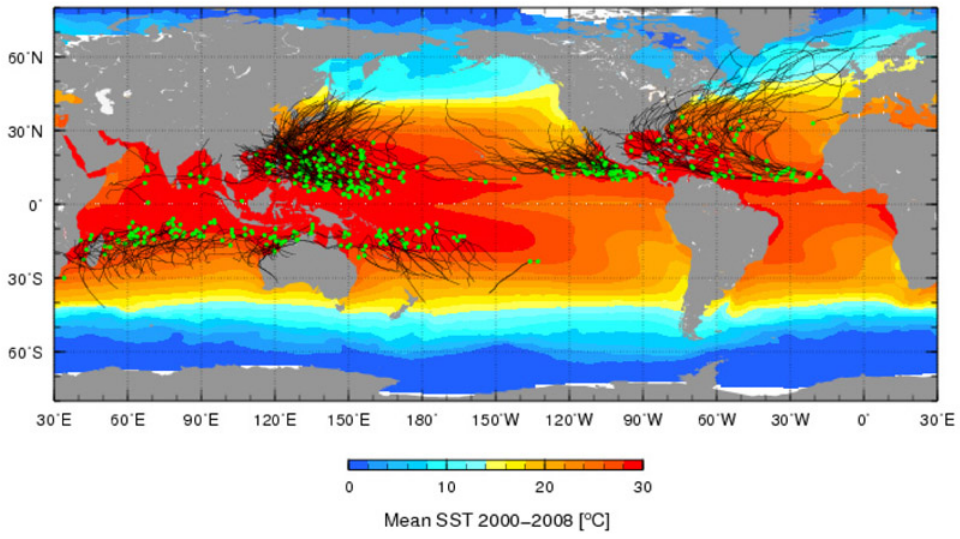

Figure 5.5-1. Global map showing the tracks of tropical cyclones (category 1 and above) during the period 2000–2008, with the green circles indicating the location of their formation. The background color is the satellite-derived mean sea surface temperature during the same years, for June through November in the Northern hemisphere and November through April in the Southern hemisphere.

resolve mesoscale features and their vertical thermal structure with a spatial and temporal resolution sufficient for TC intensification research. The number of global vertical temperature profile observations are dominated by observations from profiling floats that are somewhat evenly spaced and by eXpendable BathyThermograph (XBT) transects that provide better spatial resolution but only along fixed tracks. In the Gulf of Mexico and the Caribbean Sea, two regions where TC activity is large, the observations are even sparser, because there are no XBT transects and because profiling floats were not originally designed for enclosed seas. Therefore, different indirect approaches and techniques are needed to estimate the upper ocean heat content. One such technique includes sea surface height observations derived from satellite altimetry, which provides information on the upper ocean dynamics and vertical thermal structure, at a spatial and temporal resolution that allows resolving ocean mesoscale features. This article presents evidence that more detailed information on the location of mesoscale features and on their vertical thermal structure, such as that provided by a wide-swath high-resolution altimetry mission, may help us better understand the processes involved in air-sea interaction during TC events and may ultimately reduce the error in TC intensification forecasts.

The operational satellite altimetry-based upper ocean heat content or tropical cyclone heat potential (TCHP) analysis was implemented at the National Oceanic and Atmospheric Administration National Hurricane Center in 2004 (Mainelli et al., 2008). This approach uses alongtrack altimetry-derived sea height anomaly (SHA) fields derived from altimetry and historical hydrographic observations in a statistical analysis to determine the depth of the main thermocline, usually the 20°C isotherm in tropical regions (Goni et al., 1996); and climatological relationships are used to determine the depth of the 26°C isotherm (D26) from the depth of the 20°C isotherm (Shay et al., 2000). These TCHP fields are used qualitatively by the National Hurricane Center forecasters for their subjective TC intensity forecasts and quantitatively in the Statistical Hurricane Intensity Prediction Scheme (SHIPS, DeMaria and Kaplan, 1994). SHIPS is an empirical model that uses a multiple regression method to forecast intensity changes out to 120 h. The 2008 version of SHIPS includes 21 predictors, mostly related to atmospheric conditions. The ocean predictors are the SST and the TCHP. Despite the model's simplicity, the SHIPS forecasts are comparable to or more accurate than those from much more general models. For recent category 5 hurricanes, the TCHP input improved the SHIPS forecasts by about 5% (Figure 5.5-2), with larger improvements for individual storms (Mainelli et al., 2008). A validation performed on 685 Atlantic SHIPS forecasts from 2004–2007 shows that SHIPS improved, on the average, 3% for the 96 h forecast due to the inclusion of the TCHP and Geostationary Operational Environmental Satellite (GOES) SST data.. Nearly all of the improvements at the longer forecast intervals are due to the TCHP because the input is averaged along the storm track. Although not as large as the sample of the category 5 hurricanes alone, this result indicates that the TCHP input improved the operational SHIPS forecasts, especially at the longer forecast intervals.

The importance of resolving mesoscale features accurately in the ocean has been reported with the use of near–real time fields of sea surface height and/or D26 derived from gridded altimetry fields derived from alongtrack satellite altimetry observations. These fields are used to adjust the position of the Loop Current (LC) in the Gulf of Mexico and insert these eddies into the background climatological ocean temperature field prior to the passage of a hurricane. For hurricane Katrina (2005), the presence of the LC and of a warm ring, as given by the assimilated altimeter data, reduced the SST cooling along the hurricane track and allowed the storm to become more intense (Figure 5.5-3). This assimilation improved the intensity forecast of the actual storm with respect to that obtained without assimilating the altimetry fields. In this specific case, the inclusion of the LC and anticyclonic ring data collaborated to reduce the error of the forecast of minimum pressure by approximately 50%.

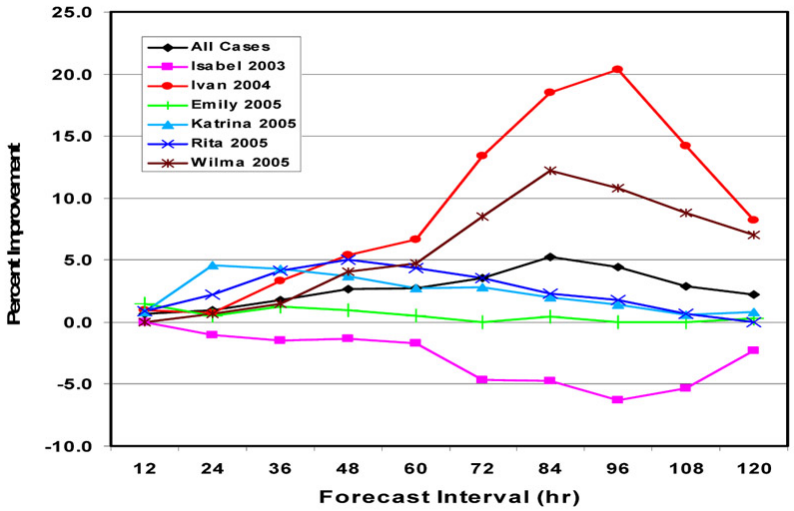

Figure 5.5-2. Reduction of error in TC intensity forecast by incorporating upper ocean thermal structure information. The percentage of SHIPS model forecast improvement, for six category 5 Atlantic hurricanes and collectively, with the incorporation of the TCHP fields, created at the NOAA National Hurricane Center (adapted from Mainelli et al, 2008).

In order to investigate the effect of using upper ocean heat content fields with different spatial resolutions, the upper ocean thermal conditions are simulated using the following resolutions: (a) An 0.08° resolution 32-vertical layer HYCOM simulation configured for the global ocean (Chassignet et al., 2009): This field approximately represents the spatial resolution that will be provided by missions such as SWOT. (b) A 0.25° resolution obtained by subsampling the original 0.08° field along the Jason-1, TOPEX/Poseidon, and Envisat groundtracks. In both cases, surface forcing is from U.S. Navy Operational Global Atmospheric Prediction System (NOGAPS), which includes wind stress, wind speed, heat flux (using bulk formula), and precipitation. Data assimilation into the model is based on the U.S. Navy Coupled Ocean Data Assimilation (NCODA) system (Cummings, 2005).

These two test cases are run for the upper ocean conditions prior to the passage of hurricanes Katrina (2005) and Wilma (2005). Differences obtained between the full-resolution fields that reproduce results from a SWOT mission and those from a resolution-simulating results from a coarse gridded field as obtained from alongtrack observations show high positive and negative values (Figure 5.5-4). In the case of the ocean conditions during these two TCs, the main features, including the Loop Current and rings, are identified in both fields. However, the fields constructed with alongtrack altimetry appear to underestimate the values of TCHP in these features, which are considered critical for TC intensification studies. As indicated, the accurate position of mesoscale features and their values are critical for reducing error in intensity forecasting. However, the full extent to which higher-resolution altimetry-derived data can help reduce intensity forecast errors still needs to be adequately evaluated.

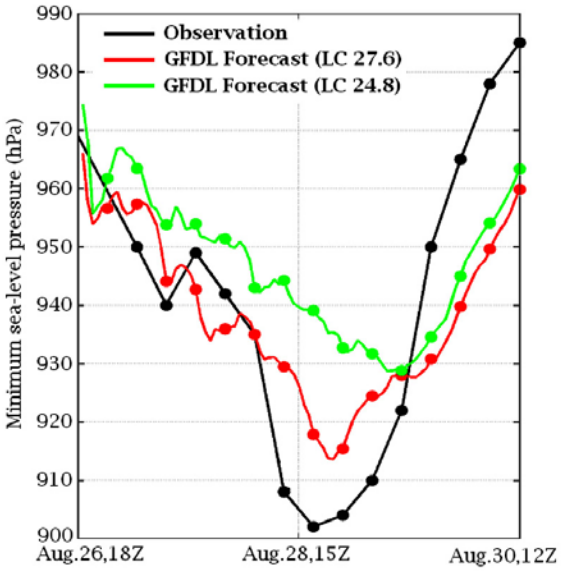

Figure 5.5-3. Reduction of intensity forecast error by incorporating mesoscale features in the ocean. Effect of including the correct mesoscale features in a Geophysical Fluid Dynamics Laboratory (GFDL) intensity model. The graph tracks the minimum atmospheric pressure at sea level during the passage of hurricane Katrina in the Gulf of Mexico in 2005 and depicts the actual observations (black), as well as the reduction of error in the GFDL model output with (red) and without (green) initializing the model with the TCHP produced at NOAA National Hurricane Center. (Figure courtesy of Isaac Ginis).

References

Chassignet, E. P., H. E. Hurlburt, E. J. Metzger, O. M. Smedstad, J. Cummings, G. R. Halliwell, R. Bleck, R. Baraille, A. J. Wallcraft, C. Lozano, H. L. Tolman, A. Srinivasan, S. Hankin, P. Cornillon, R. Weisberg, A. Barth, R. He, F. Werner, and J. Wilkin, 2009: U.S. GODAE: Global ocean prediction with the HYbrid coordinate ocean model (HYCOM). Oceanography, **22**(2), 48–59.

Cummings, J. A., 2005: Operational multivariate ocean data assimilation. Q. J. Royal Meteorol. Soc., **131**, 3583–3604.

DeMaria , M., M. Mainelli, L. K. Shay, J. Knaff, and J. Kaplan, 2005: Further improvements to the Statistical Hurricane Intensity Forecasting Scheme (SHIPS). Wea. Forecasting, **20**, 531–543.

Goni, G., S. Kamholz, S. Garzoli, and D. Olson, 1996: Dynamics of the Brazil-Malvinas confluence based on inverted echo sounders and altimetry. J. Geophys. Res., **101**, 16273–16289.

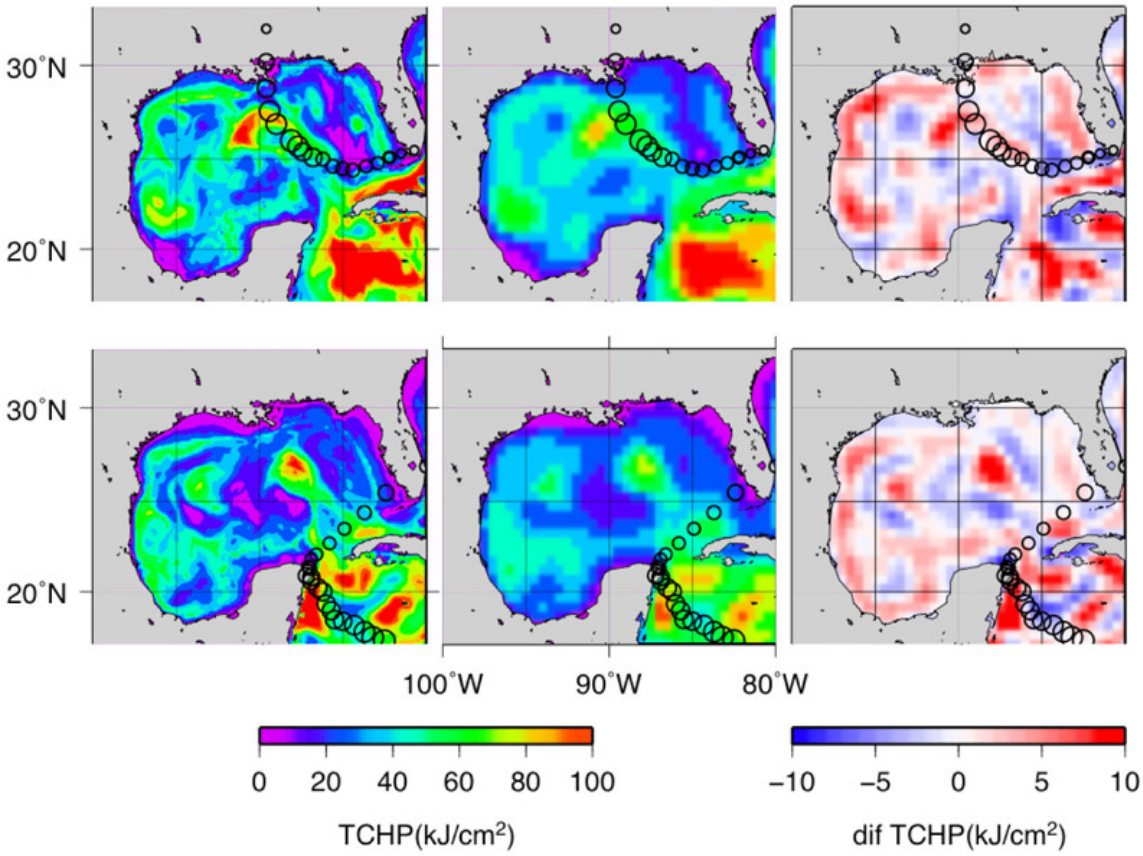

Figure 5.5-4. TCHP fields during the passage of hurricane (top) Katrina and (bottom) Wilma obtained using (left) the full-resolution HYCOM-derived fields and (center) the 0.25° resolution, and (right) their differences. The circles indicate the trajectories of these to TCs with their intensity proportional to their sizes.

Goni, G. J., 2008: Tropical cyclone heat potential. In State of the Climate in 2007, Special Supplement to the Bull. Am. Met. Soc., **89**, 43–45. Eds. D. H. Levinson and J. H. Lawrimore.

Leipper, D., and D. Volgenau, 1972: Hurricane heat potentical in the Gulf of Mexico. J. Phys. Ocean., **2**, 218–224.

Mainelli, M., M. DeMaria, L. K. Shay and G. Goni, 2008: Application of oceanic heat content estimation to operational forecasting of recent Atlantic category 5 hurricanes. Wea. Forecasting, **23**, 3–16.

Shay, L. K., G. J. Goni, and P. G. Black, 2000: Effects of a warm oceanic feature on Hurricane Opal. Mon. Wea. Rev., **128**, 1366–1383.

5.6 Sea-Level Change

5.6.1 Scientific Background

The 2007 Intergovernmental Panel for Climate Change (IPCC) Fourth Assessment Report (AR4), Working Group (WG) I, The Physical Science Basis, concluded that the warming of the climate system is unequivocal, and with high certainty that the effect of human activities since 1750 has largely been responsible for the observed warming of Earth's surface (IPCC, 2007). Observational evidence confirms the anthropogenic increase of average air, land, and ocean temperature; melting of snow and ice; and global average sea level rise. Sea level rise has been widely recognized as a measurable signal (Wilson et al., 2010) as one of the consequences of anthropogenic global climate change (e.g., Church et al., 2011), and has a substantial societal and economic impact (Nicholls, 2010).

The sea level reconstruction during 100BC~1865AD, based on geological methods and salt-marsh sediment sequences, is estimated at 0.0–0.6 mm/yr (Kemp et al., 2011); the observed sea level rise using tide gauge data (1900–2006) is estimated at 1.7–1.8 mm/yr (Shum and Kuo, 2011); and the sea level rise observed using satellite altimetry (1993–2011) is ~3 mm/yr (Nerem et al., 2010; Cazenave et al., 2010; Willis et al., 2010; Shum and Kuo, 2011). The observation evidence indicates that sea level rise has accelerated since ~1900 (Kemp et al., 2011). The hindcast and predicted sea level rise based on 'natural' forcing and 'natural' plus greenhouse gases scenario using the Hadley Centre Coupled Model, version 3 (HadCM3) climate model (Gregory et al., 2006), indicated that the worst-case scenario (2005–2100) could raise global mean sea level by ~60 cm by the end of the next century (IPCC, 2007). Recent studies provide significantly higher 21st century predicted sea level using empirical correlations between temperature and sea level rise—at ~120 cm and even higher (Rahmstorf et al., 2011)—than the IPCC AR4 predicted sea level rise, and thus this subject remains controversial.

Quantifying, understanding, and predicting the small rate of sea level rise at 1–2 mm/yr remains challenging: the sea level signal has a wide range of temporal and spatial scales resulting from complex interactions between various Earth-atmosphere-ocean-cryosphere-hydrosphere processes. Extending the high-quality satellite altimetry observations of global sea level measurements, and commencing high-resolution surface water level measurements over hydrologic basins and land-ice regions, will enable us to improve the determination of sea level rise, and enhance our understanding of its geophysical causes.

5.6.2 Sea Level Rise Is Not Uniform

Tide gauges and satellite altimetry data are available for the 20th century and since the early 1990s, respectively. Tide gauge records (Woodworth and Player, 2003) observed a mean rate of global sea level rise of 1.7–1.8 mm/yr over 1900–2000 (Church

and White, 2011); however the gauges are sparsely distributed (Figure 5.6-1; gauge locations also denote individual color-coded sea-level trends). Satellite altimeter data from TOPEX/Poseidon and Jason-1/-2 show that sea level has been going up at 3.2 ± 0.4 mm/yr since 1993 (Nerem et al., 2010; Mitchum et al., 2010). Figure 5.6-1 shows the geographical variations of the rate of sea level change from satellite radar altimetry, 1985–2008, with some of the altimetry data [Geosat, Geosat Follow-on (GFO), ERS-1/-2, Envisat] covering the polar ocean as far as ±81.5° latitude. As a point of comparison, TOPEX/Poseidon, Jason-1/-2 observe up to ±66° latitude. Owing to its quasi-global coverage of the oceanic domain, satellite altimetry has revealed that sea level is not rising uniformly (Figure 5.6-1). In some regions (e.g., western Pacific), rates of sea level rise are faster than the global mean rate by as much as a factor of 3. In other regions, rates are slower than the global mean (e.g., eastern Pacific).

Regional variability in the rates of sea level change result from various factors (e.g, Milne et al., 2009): (1) temperature and salinity changes; (2) exchange of fresh water with the atmosphere and land through changes in evaporation, precipitation and runoff; and (3) redistribution of water mass by advection within the ocean. As shown by Wunsch et al. (2007), observed sea level trend patterns result from a complex dynamical response of the ocean, involving not only the forcing terms but also water movements associated with wind stress. Additional processes are expected to also give rise to regional variations in sea level rates. For example, the response of the solid Earth to last deglaciation (the glacial isostatic adjustment, or GIA process) and to the ongoing melting of land ice in response to global warming has led to the secular change of the geoid (an equipotential surface of the Earth gravity field that coincides with the mean surface of the oceans at

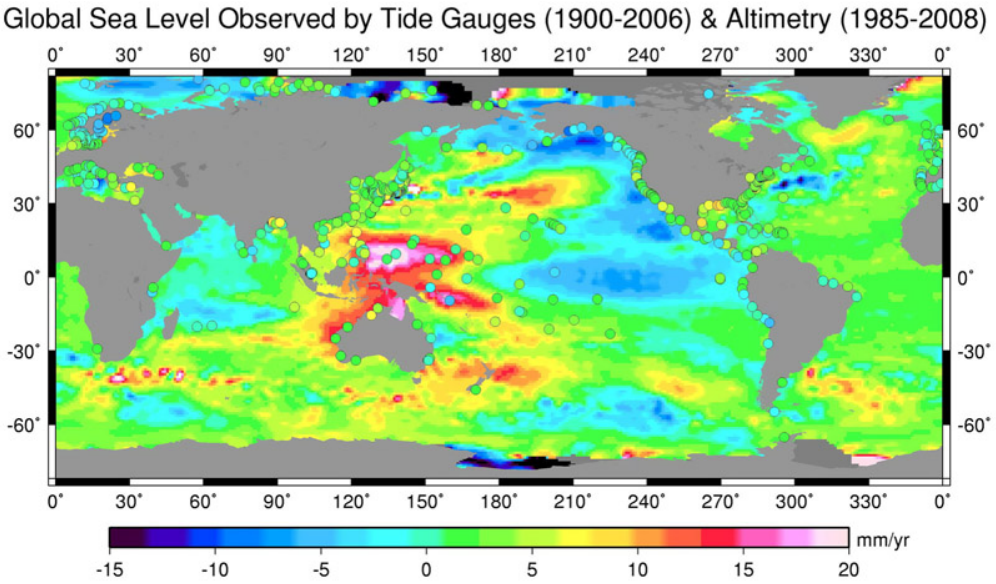

Figure 5.6-1. Multiple satellite altimetry estimated sea-level trend (1985–2008, with 4 year data gap between 1988–1992). Circles are color-coded sea level trend observed by global tide gauges (1900–2006); these data represent a much longer (>30 years) data span than is available from altimetry. Figure updated from Shum and Kuo (2011).

rest) and gravitational deformations of ocean basins and of the sea surface (e.g., Tamisiea and Mitrovica, 2011). Mitrovica et al. (2009) showed that rapid melting of the West Antarctic ice sheet will lead to nonuniform sea level rise because of the changing mutual gravitational attraction between the ice sheet and the nearby ocean as well as the elastic deformation of the solid Earth in response to the load redistribution. Such regional sea level changes are broad-scale but different for each melting source (Greenland, Antarctica, glaciers). The regional variation due to these effects can reach up to 30% of the melt contribution to sea level rise. In the vicinity of the melt sources, large regional sea-level decrease is expected (e.g., Tamisiea and Mitrovica, 2011).

The SWOT mission will provide high–spatial resolution sea level measurements. Improved spatial mapping of the regional variability should allow scientists to discriminate between the various physical processes causing nonuniform sea level rise.

While the sea level trend estimated using sparsely located tide gauges agrees with the value determined by satellite altimetry over the same data span (i.e., 1990s–present) (Bindoff et al., 2007), the significantly different trend estimates from the tide gauges (~1.8 mm/yr) and from the altimetry (~3.2 mm/yr) suggest that either the sea level rise is accelerating since the 1990s (Merrifield et al., 2009; Woodworth et al., 2011), or the sea level trend estimate is influenced by interannual or longer variations, or both. SWOT will extend accurate sea level measurements within a well-realized International Terrestrial Reference Frame (ITRF) (Blewitt et al., 2010), and along with other space geodetic and in situ observations (e.g., Casenave et al., 2010) will help address the contemporary scientific question: Is the present-day sea level rise accelerating?

5.6.3 Mapping the Sea level rise in High-Latitude Regions

SWOT will be able to continue and enhance the geophysical record of sea-level time series started by TOPEX/Poseidon and the Jason-series satellite missions. SWOT will be in a non–sun synchronous orbit with a higher inclination (~78°) than the TOPEX/Poseidon and Jason-series satellites, thus enabling the measurement of sea level variations in high-latitude oceans. Polar oceans have significantly fewer long-term tide gauge sites than the rest of the ocean; and where they do have long-term tide gauge sites (e.g., in Alaska and Greenland), they are more influenced than other tide gauge sites by vertical land motions, due to glacial isostatic adjustment (GIA) and to elastic crustal loading as a result of accelerated glacier or ice-sheet melting. Current observations indicate that Arctic climate is changing faster than the climate in the rest of the world (IPCC, 2007). The change has already had considerable impact on sea level through ice mass loss from the margins of the Greenland ice sheet, melting of Alaska and Svalbard glaciers, warming of the Arctic Ocean, melting of the permafrost in Siberia, and change of water storage in Arctic river basins.

SWOT will be able to address three important scientific questions: (1) Is sea level rising faster in the Arctic Ocean in response to higher ocean warming? (2) What is the

contribution of polar ocean to global sea level rise? (3) Can we detect or quantify the sea level rise signal resulting from accelerated ice-sheet melt?

5.6.4 Hydrologic and Anthropogenic Contributions to Sea Level Rise

The two main causes of contemporary global mean sea level change are (1) the addition of freshwater to the oceans as a result of land ice loss and water exchange with terrestrial reservoirs (soil and groundwater, lakes, snowpack, etc.) and (2) thermal expansion of the sea-water in response to ocean warming (Bindoff et al., 2007; Cazenave and Remy, 2011). Until recently, only contributions of ocean thermal expansion and land ice melt could be estimated. Over 1993–2003, the altimetry-based global mean sea level increase is 50% due to ocean thermal expansion and 50% to land ice loss (Bindoff et al., 2007). Since 2003, land ice loss appears to be the main contributor to sea level rise (e.g., Shum et al., 2008). While the sea level budget is arguably closed for the recent years, this is not the case for the previous decades (Bindoff et al., 2007), leaving room for an additional contribution: exchange of water with terrestrial stores. Change in land water storage due to natural climate variability and human activities (i.e., anthropogenic changes in the amount of water stored in soils, reservoirs and aquifers as a result from dam building, underground water mining, irrigation, urbanization, deforestation, etc.) is indeed another potential contribution to sea level change. Model-based estimates of land water storage change caused by natural climate variability suggest no long-term contribution to sea level for the past few decades, although interannual/decadal fluctuations may have been significant (e.g., Milly et al., 2010). Estimated anthropogenic groundwater depletion and water impoundment behind dams can significantly impact sea level change but more or less cancel each other out (Milly et al., 2010 and Church et al., 2011). Since 2002, space gravimetry observations from GRACE allow us to determine the total (i.e., due to climate variability and human activities) land water contribution (e.g., Cazenave and Remy, 2011) to sea level (e.g., Leuliette and Willis, 2011). The land water signal is dominated by interannual variability with only a modest contribution (<10%) to sea level trend (Ramillien et al., 2008). However, GRACE cannot separate the contribution from surface and ground waters. SWOT, with its swath instrument, will be able to provide an accurate measurement of the storage changes in lakes and artificial dams/reservoirs on land (see section 4.3). In particular, SWOT should also be able to facilitate better quantification of the sources of negative impact to global sea level rise, starting from the first SWOT data records. In addition, SWOT also provides additional measurements that will help reduce the uncertainty in the estimate of anthropogenic contributions to reduction of global sea level rise. During the SWOT observational time period, SWOT will (1) provide more accurate measurements of areas of the world's large reservoirs, and (2) conduct possible validations of reservoir absolute water storage volume estimated, e.g., by Chao et al. (2008). SWOT will be able to constrain the total terrestrial water contribution to sea level, and will potentially reduce the uncertainty for the estimate of the effect of human impoundment of water in reservoirs and its resulting impact on global sea level rise.

5.6.5 Coastal Impacts of Sea Level Rise

Sea level rise is a major threat for many low-lying, highly populated coastal regions of the world (about 600 million people live presently in coastal areas lower than 10 m above sea level) (Nicholls, 2010). Negative effects of sea level rise include: (1) inundation and recurrent flooding in association with storm surges, (2) wetland loss, (3) shoreline erosion, (4) saltwater intrusion in surface water bodies and aquifers, and (5) rising water tables (Nicholls, 2010). In such regions, climate-induced sea level rise (uniform trend plus regional variability) amplifies other stresses due to natural phenomena (e.g., sediment load-induced ground subsidence in deltaic areas; vertical ground motions due to tectonics, volcanism, and glacial isostatic adjustment; increased frequency of extreme events like storm surges) or human activities (e.g., ground subsidence due to ground water pumping and/or oil extraction, urbanization).

Relative sea level rise (i.e., absolute sea level rise plus ground motions) acts as an additional stress on coastal systems as it interacts with other phenomena such as storms, waves, currents, and winds. In response to sea level changes, these phenomena give rise to change in shoreline morphology. Moreover, the sediment budget is affected by human coastal activities such as coastal infrastructures (harbour, dikes, artificial beaches, dam building along rivers, etc.) and land use practices that today generally prevent in-land sediments from migrating to the coast. Thus, the response to sea level rise must be part of an integrated management of coastal and estuary zones. Yet, the multidisciplinary nature of the underlying science as well as associated uncertainties of future sea level projections largely prevents coastal communities and decision makers from taking appropriate adaptation measures. The fact that sea level rise varies regionally (Figure 5.6-1) is an additional source of uncertainty that makes adaptation measures difficult to take.

Unlike conventional altimetry, SWOT will provide accurate and high-resolution sea level measurements at the ocean-land interface, as well as land topography in the coastal zones, to enable (1) a direct link between land and sea with refined vertical datum, (2) quantification of sea level rise hazards in the estuary and coastal regions, and (3) contributions to improved storm surge prediction/modelling in low-lying coastal regions.

5.6.6 Atlantic Meridional Overturning Circulation

A number of studies have suggested the susceptibility of the Atlantic meridional overturning circulation (AMOC) to past abrupt climate change during the Pleistocene, and to a lesser extent, during the Holocene. Studies using circulation and climate model simulations indicate potential recent (the last few decades) rapid weakening or shutdown of the AMOC due to accelerated freshening of north Atlantic surface waters (Curry and Mauritzen, 2005). Hakkinen and Rhines (2004) applied an empirical orthogonal function (EOF) analysis to TOPEX/Poseidon altimetry sea level data to infer geostrophic current

velocity changes in the north Atlantic and to conclude that the sea level increased and the subpolar north Atlantic gyre declined during the 1990s. Hatun et al. (2005) reported that the record-high salinities in the Atlantic subpolar gyre, which inflows to the Nordic seas and the Arctic ocean, may counteract the observed increased freshening of the north Atlantic surface water, and thus stabilize the AMOC evolution.

In addition to the direct estimates of river runoff at a global scale and covering extreme polar oceans, SWOT with its higher orbital inclinations (78°) will provide an accurate estimate of the total surface fresh water input to the ocean—thus quantifying the discharge of Arctic River—and the total water cycle freshening the North Atlantic Ocean. SWOT's high-spatial resolution measurement of the Arctic sea level and the North Atlantic (including the Labrador Sea) ocean circulation contributes to the potential monitoring of the contemporary evolution of the AMOC towards addressing the science question: Is there a link between sea level rise and the evolution of the Atlantic meridional overturning circulation?

References

Bindoff, N., J. Willebrand (Coordinating Lead Authors), V. Artable, A. Cazenave, J. Gregory, S. Gulev, K. Hanawa, C. Le Quere, S. Levitus, Y. Nojiri, C.K. Shum, L. Talley, A. Unnikrishnan (Lead Authors), and 50 contributing authors, 2007: Chapter 5: Observations: Oceanic climate change and sea level. Intergovernmental Panel Climate Committee Working Group 1 Fourth Assessment Report.

Blewitt, G., Z. Altamimi, J. Davis, R. Gross, C. Kuo, F. Lemoine, A. Moore, R. Neilan, H.-P. Plag, M. Rothacher, C. Shum, M. Sideris, T. Schöne, P. Tregoning, and S. Zerbini, 2010: Geodetic observations and global reference frame contributions to understanding sea-level rise and variability. In Understanding Sea-Level Rise and Variability, 256–284. Eds. J. Church, P.L. Woodworth, T. Aarup, and S. Wilson, Wiley-Blackwell, ISBN: 978-1-443-3451-7.

Cazenave, A., D. Chambers, P. Cipollini, L. Fu, J. Hurell, M. Merrifield, R. Nerem, H. Plag, C. Shum, J. Willis, 2010: The challenge of measuring sea level rise and regional and global trends, geodetic observations of ocean surface topography, ocean currents, ocean mass, and ocean volume changes. Proc. OceanObs09: Sustained Ocean Observations and Information for Society, **2**, Venice, Italy, 21-25 Sept. 2009. Eds. J. Hall, D. E. Harrison, and D. Stammer, ESA Publication WPP-306, 2010.

Cazenave, A., F. Remy, 2011: Sea level and climate: measurements and causes of changes. Interdisciplinary Reviews: Climate Change, **2**(5), 647–662, doi:10.1002/wcc.139, 2011.

Chao, B., Y. Wu, and Y. Li, 2008: Impact of artificial reservoir water impoundment on global sea level. Science, 10.1126/science.1154580.

Church, J., A., and N. J. White, 2011: Sea-level rise from the late 19th to the early 21st century. Surv. Geophys., doi10.1007/s10712-011-9119-1.

Church, J. A., N. J. White, L. F. Konikow, C. M. Domingues, J. G. Cogley, E. Rignot, J. M. Gregory, M. R. van den Broeke, A. J. Monaghan, and I. Velicogna, 2011: Revisiting the Earth's sea-level and energy budgets from 1961 to 2008. Geophys. Res. Lett., **38**, L18601, doi:10.1029/2011GL048794.

Curry, R., and C. Mauritzen, 2005: Dilution of the Northern North Atlantic Ocean in recent decades. Science, **308**, 1772–1774.

Gregory, J., J. Lowe, and S. Tett, 2006: Simulated global-mean sea-level changes over the last half-millennium. J. Climate, **19**, 4,576–4,591, doi: 10.1175/JCLI3881.1.

Hakkinen, S., and P. Rhines, 2004: Decline of subpolar north Atlantic circulation during the 1990s. Science, **304**, 555–559.

Hatun, H., A. Sando, H. Drange, B. Hansen, and H. Valdimarsson, 2005: Influence of the Atlantic subpolar gyre on thermohaline circulation. Science, **309**, 1841–1845.

IPCC, Intergovernmental Panel on Climate Change, 2007: Climate Change 2007: The Physical Science Basis, Summary for Policymakers.

Kemp A. C., B. Horton, J. P. Donnelly, M. E. Mann, M. Vermeer, and S. Rahmstorf, 2011: Climate related sea-level variations over the past two millennia. PNAS, doi/10.1073/pnas.1015619108.

Leuliette, E. W., and J. K. Willis, 2011: Balancing the sea level budget. Oceanography, **24(**2), 122–129, doi:10.5670/oceanog.2011.32.

Milly, P., A. Cazenave, J. Famiglietti, V. Gornitz, K. Laval, D. Lettenmaier, D. Sahagian, J. Wahr and C. Wilson, 2010: Terrestrial water storage contributions to sea level rise and variability.In Understanding Sea-Level Rise and Variability. Eds. J. Church, P. Woodworth, T. Aarup, and S. Wilson, Wiley-Blackwell, London.

Merrifield, M., S. Merrifield, and G. Mitchum, 2009: An anomalous recent acceleration of global sea level rise. J. Climate, doi: 10.1175/2009JCLI2985.1.

Milne G., W. R. Gehrels, C. Hughes, and M. Tamisiea, 2009: Identifying the causes of sea level changes. Nature Geoscience, **2**, 471–478, doi:10.1038/ngeo544.

Mitchum, G. T., R. S. Nerem, M. A. Merrifield, and W. R. Gehrels, 2010: Modern sea level changes estimates. In Understanding Sea-Level Rise and Variability. Eds. J. A. Church, P. L. Woodworth, T. Aarup, and W. S. Wilson. Wiley-Blackwell, London.

Mitrovica, J. X., N. Gomez, and P. U. Clark, 2009: The sea-level fingerprint of West Antarctic collapse. Science, **323**, 753, doi:10.1126/science.1166510.

Nerem, R. S., D. P. Chambers, C. Choe, and G.T. Mitchum, 2010: Estimating mean sea level change from the TOPEX and Jason altimeter missions. Marine Geodesy, **33**, 435–446.

Nicholls, R .J., 2010: Impacts of and responses to sea level rise. In Understanding Sea-Level Rise and Variability. Eds. J. A. Church, P .L. Woodworth, T. Aarup, and W. S. Wilson. Wiley-Blackwell, London.

Rahmstorf, S., M. Perrette, and M. Vermeer, 2011: Testing the robustness of semi-empirical sea level projections. Climate Dynamics, doi:10.1007/s00382-011-1226-7.

Ramillien, G., S. Bouhours, A. Lombard, A. Cazenave, F. Flechtner, and R. Schmidt, 2008: Land water contributions from GRACE to sea level rise over 2002–2006. Global and Planetary Change, **60**, 381–392.

Shum, C., C. Kuo, and J. Guo, 2008: Role of Antarctic ice mass balances in present-day sea level change. Polar Science, **2**, 149–161.

Shum, C., and C. Kuo, 2011: Observation and geophysical causes of present-day sea level rise. In Climate Change and Food Security in South Asia. Eds. R. Lal, M. Sivakumar, S. Faiz, A. Rahman, and K. Islam, Part 2, Chapter 7, 85–104, doi: 10.1007/978-90-481-9516-9_7.

Tamisiea, M. E., and J. X. Mitrovica, 2011: The moving boundaries of sea level change: Understanding the origins of geographic variability. Oceanography, **24**(2), 24–39, doi:10.5670/oceanog.2011.25.

Willis, J. K., D. P. Chambers, C.-Y. Kuo, and C. K. Shum, 2010: Global sea level rise. Oceanography, **23**(4), 26–35, doi:10.5670/ oceanog.2010.03, 2010.

Wilson, W. S., W. Abdalati, D. Alsdorf, J. Benveniste, H. Bonekamp, J. G. Cogley, M. R. Drinkwater, L.-L. Fu, R. Gross, B. J. Haines, et al., 2010: Observing systems needed to address sea-level rise and variability, Chapter 12. In Understanding Sea-Level Rise and Variability. Eds. J. A. Church, P. L. Woodworth, T. Aarup, and W. S. Wilson, Wiley-Blackwell, London.

Woodworth, P. L., and R. Player, 2003: The permanent service for mean sea level: An update to the 21st century. J. Coastal Research, **19**, 287–295.

Woodworth, P. L., W. R. Gehrels, and R. S. Nerem, 2011: Nineteenth and twentieth century changes in sea level. Oceanography, **24**(2), 80–93, doi:10.5670/oceanog.2011.29.

Wunsch, C., R. M. Ponte, and P. Heimbach, 2007: Decadal trends in sea level patterns: 1993–2004. J Climate, **20**(24), doi: 10.1175/2007JCLI1840.1.

6 MEASUREMENT OF WATER ELEVATION

The principle of radar interferometry for measuring the elevation of water on land and in the ocean is described in the section. Also discussed are the various factors affecting the measurement: the effects of the intervening atmosphere on the delay of radar signals and the effects of ocean tides and waves, as well as the target layover on land. The detection of the various water bodies on land is also a challenge to be addressed.

6.1 Radar Interferometry

Conventional altimeters use pulse-limited ranging technique to measure the range of the instrument above sea surface. A finite foot-print of the radar is determined by the radar pulse width and the altitude of the spacecraft. For TOPEX/Poseidon, the footprint diameter varies from 2 km over calm seas to 10 km over rough seas of 10 m waves. The radar must maintain precise nadir pointing to obtain the range measurement between the radar and its nadir on the surface. The major limitations of the technique include errors in radar waveform analysis, land contamination near coasts and islands, and the one-dimensional nature of the measurement. These limitations can be overcome by the technique of radar interferometry.

The range of a target can be precisely determined by the round-trip travel time measured by the radar's timing system. The missing information is the location of the target on Earth. Nadir-looking conventional altimeters are designed for tracking the leading edge of the radar return signals coming from the nadir. Radar interferometry determines the location of the target by measuring the relative delay (or phase shift) between the signals from two antennas that are separated by a baseline distance. Using geometry, the location of the range measurements in the plane of the observation can be determined (Figure 6.1-1).

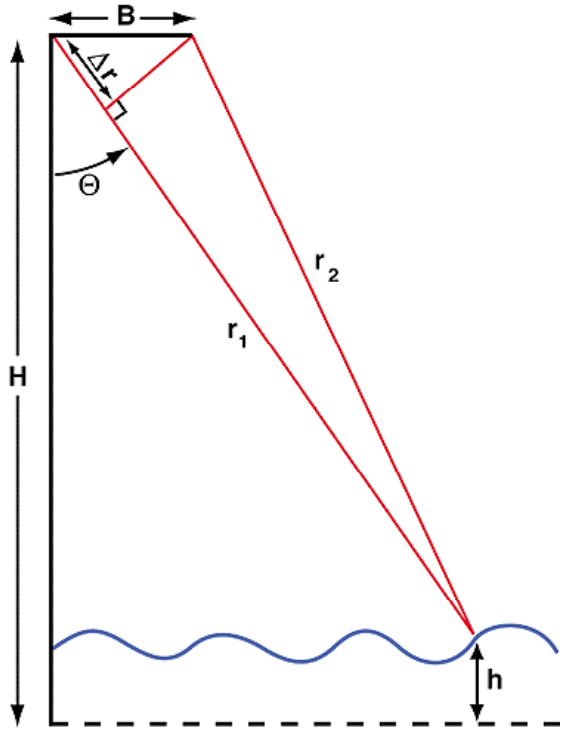

Figure 6.1-1. Geometric concept used for interferometric measurements.

The measurement triangle is made up of the baseline B, and the range to the two antennas, r_1 and r_2. The baseline is known by construction and knowledge of the spacecraft attitude. The range r_1 is determined by the system timing measurements. The range difference between r_1 and r_2 is determined by measuring the relative phase shift Φ between the two signals. The phase shift is related to the range difference Δr by the equation $\Phi=2\pi\Delta r/\lambda$, where λ is the radar wavelength. The additional information required for determining the measurement location, the incidence angle θ, can be obtained from the range difference by means of the relationship $\Phi=2\pi$ B $\sin(\theta)/\lambda$. Given these measurements, the height h above a reference plane can be obtained using the equation $h=H-r_1 \cos(\theta)$. The formulas given here are appropriate for mapping heights relative to a reference plane. A detailed treatment of mapping heights relative to the curved surface of the Earth is given in Rosen et al. (2000).

If both antennas are synthetic-aperture radars (SAR), the interferometry system is then able to provide two swaths of measurement of sea surface height parallel to the flight direction (Figure 6.1-2). The spatial resolution of the measurement is dependent on the bandwidth (the range resolution in the cross-track direction) and antenna size (the azimuth resolution in the alongtrack direction). A major difference between conventional altimetry and interferometry is that the interferometric measurement of the range relies on the complex phase information, which is available for each imaged pixel in the scene. In contrast, the altimeter measurement relies on the power and the specific shape of the leading edge of the return waveform, which is only available for the nadir point. Thus, the interferometric measurement of the range is intrinsically more accurate than the altimeter measurement (since it relies on the phase, which can be determined to a fraction of a wavelength), and is available for all imaged points in the scene. Furthermore, the pixel size, on the order of tens of meters, is much smaller than the pulse-limited footprint of the conventional altimeter and thus much less prone to land (or sea ice) contamination.

The technique of interferometry SAR (IFSAR) is quite mature and has been demonstrated from airborne platforms—most notably from space by the Shuttle Radar Topography Mission (SRTM), which, with two IFSARs (at C and X bands), produced global data with an accuracy of a few meters. In order to achieve centimeter accuracies, a few changes to the SRTM design are required.

A Ka-Band Radar Interferometer (KaRIn)

Random errors in the interferometric measurements are introduced through measurement noise of the interferometric phase difference. This noise has two sources: thermal noise in the two interferometric channels, and differences in the return signal speckle from distributed targets. The first source of noise decreases with increasing signal brightness, while the second is independent of brightness, but depends on the geometry.

Given a phase error, $\delta\Phi$, the resulting height error is given by $\delta h=\lambda r \tan(\theta)/(2\pi B)\delta\Phi$, where r is the range from the platform to the imaged point on the ground, θ is the look

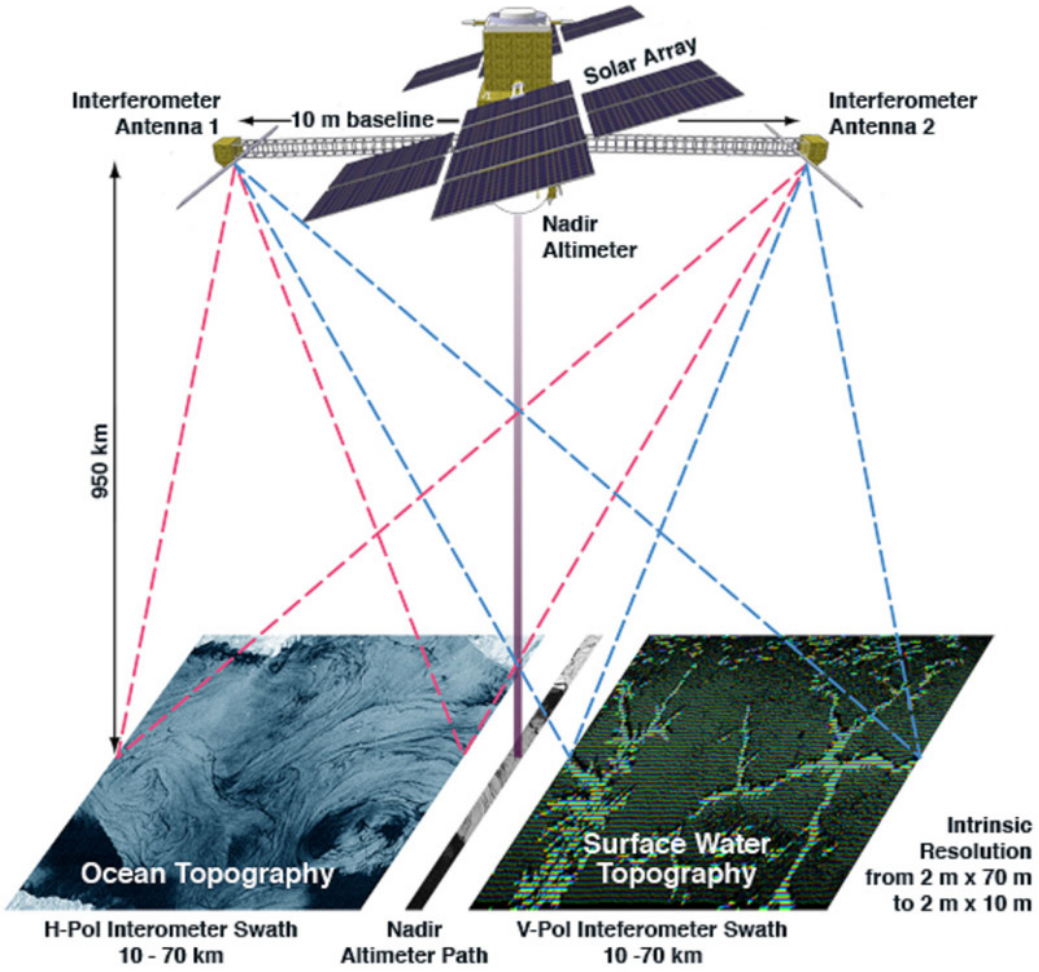

Figure 6.1-2. SWOT mission configuration.

angle, λ is the wavelength, and B is the baseline length. The geometry behind the effect of phase errors on height errors is illustrated in Figure 6.1-3. For small look angles, this can be written as $\delta h=\lambda x/(2\pi B)\delta\Phi$, where x is the cross-track distance. For SRTM, a 63 m baseline was required to achieve the desired height accuracy using a wavelength of 5.6 cm (C band; $\lambda/B\sim8.9\times10^{-4}$). Such a large structure entails large costs. In order to reduce the instrument size, we will use a smaller wavelength (Ka-band, $\lambda=0.86$ cm), and reduces the interferometric mast size to 10 m ($\lambda/B\sim8.6\times10^{-4}$), leading to the design of a Ka-band radar interfermeter, dubbed KaRIn. The technology for a 10 m interferometric mast capable of meeting the stringent mechanical stability required for centimetric measurements has been developed by Able Engineering (SRTM mast manufacturer) in support of the WSOA technology development.

The errors increase linearly with cross track distance and, when generated by random sources such as thermal noise, are independent from pixel to pixel. Spatial averaging will reduce the random errors by the square root of the number of pixels averaged. SRTM averaged about two pixels in order to achieve a 30-m spatial resolution with a meter-level

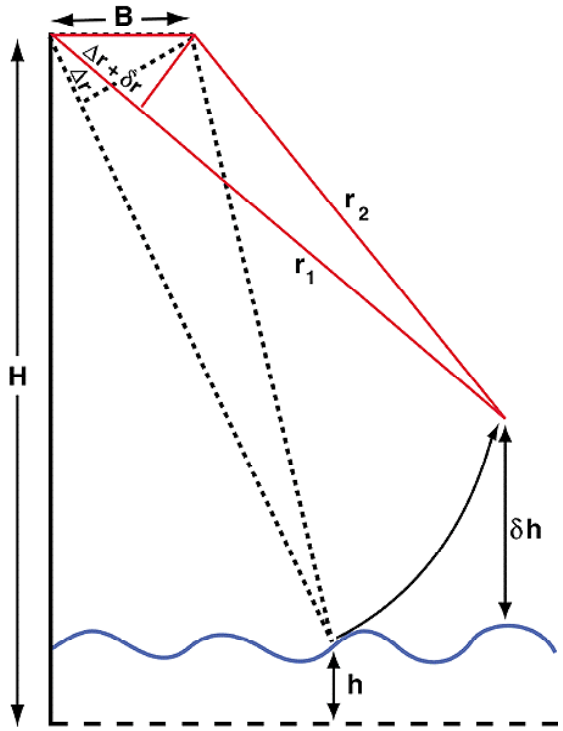

Figure 6.1-3. Illustration of the impact of a phase error, $\delta\Phi=2\pi\Delta\, r/\lambda$, on the measured height, δh.

height noise. To achieve centimetric height noise, and also to produce images of the water bodies, an increase in the intrinsic range resolution of the instrument is required. Using a 200 MHz bandwidth system (0.75-m range resolution) achieves ground resolutions varying from about 10 m in the far swath to about 70 m in the near swath. A resolution of about 5 m (after onboard data reduction) in the along track direction is derived by means of synthetic aperture processing. Noise reduction is achieved by averaging over the water body. The increase in bandwidth requires an appropriate amount of power to be available: building on heritage from the CloudSat mission EIK technology achieves an appropriate SNR for centimetric accuracies.

The required noise level for resolving oceanic submesoscales is illustrated in Figure 3-7a. The noise power density must be less than 1 cm^2/cycles/km in order to have the signal-to-noise ratio at 10 km wavelength larger than one. The Nyquist posting for resolving 10 km wavelength is every 5 km. The rms noise at the 5 km×5 km grids is then the square root of (1 cm^2/cycles/km×0.1 cyces/km), or 0.316 cm. This can be achieved by rms noise level of 1.58 cm at the sampling 1 km×1 km grids.

Anotherr major contributor to height errors is the lack of knowledge of the interferometric baseline roll angle: an estimation error of $\delta\theta$ will result in a height error $\delta h=x\delta\theta$, where x is the cross track distance. Clearly, the error will be reduced if the swath cross-track distance, or, equivalently, the radar look angles are reduced. In SRTM, the look angle varied from about 20º to about 60º. We propose to limit KaRIn's maximum

look angle to about 4.5º, which will reduce the outer swath error by about 14 times, compared to the SRTM outer swath attitude error. A similar reduction applies to errors due to phase, since the two errors have similar angular signatures (Rodriguez and Martin, 1992). The reduction in look angles entails a reduction in swath, from 220 km for SRTM, to about 60 km (from 10 km to 70 km in cross-track distance) for the KaRIn instrument. In order to mitigate this loss in coverage, the instrument looks to both sides of the nadir track to achieve a total swath of 120 km. The isolation between the two swaths is accomplished by means of offset feed reflect array antennas which produce beams of orthogonal polarizations for each swath. This technology was developed for WSOA, and the antennas have been prototyped and their performance demonstrated.

Note that to achieve the desired resolution, SAR processing must be performed. On board processing to 1 km×1 km pixels for ocean applications is achievable. However, the large volume of the high-resolution data for hydrological applications must be downlinked for ground processing. Therefore, after passing through a data reduction presuming filter, the raw data are stored and subsequently downlinked to the ground. The data downlink requirements can be met with four 300Mbit/s X-band receiving stations.

Table 6.1-1 summarizes the design parameters for KaRIn.

Table 6.1-1. SWOT Design Parameters

Parameter	Units	Value
Mass	kg	150
Frequency	GHz	35
Peak Transmit Power	W	1500
Duty Cycle	%	2.65
RF Operating Power	W	790
Operating Time/Orbit	%	40
Average Power/Orbit	W	316
Raw Data Rate	Mbits/s	504
Data Volume/Orbit	Gbytes	76
Antenna Length	m	4
Antenna Width	m	0.2
Boresight Look angle	deg	3.5
Baseline Length	m	10
Orbit Height	km	800
One-Sided Swath	km	50
Number of Swaths		2
Range Resolution	m	0.75
Azimuth Resolution	m	5

6.2 Media Effects

The propagation of radar signals is delayed in the ionosphere by free electrons and in the atmosphere by both dry gas and water vapor, causing errors in the radar range measurement, denoted by δr. The resulting error in sea surface height is given by $\delta h = -\delta r/\cos(\theta)$, which, for the angles of incidence <4°, can be approximated by $\delta h = -\delta r$. These errors have been extensively discussed for analyzing conventional altimeter data for oceanographic applications (Chelton et al., 2001). Their spatial scales are large compared to the mesoscale and submesoscale foci of SWOT. To illustrate this point, shown in Figure 6.2-1 are the wavenumber spectra of SSH, the wet and dry tropospheric corrections, and the ionospheric corrections. All of them were computed from 7 years' worth of data from a pass (#132) of Jason-1 satellite. The pass traverses from the central north Pacific to the southeastern Pacific over regions of low SSH variability. The ionospheric corrections were scaled from the Ku band observations to a level corresponding to the Ka band SWOT observations, which are a factor of 6.6 smaller than the Ku band values.

At wavelengths shorter than 300 km, which are the oceanographic objectives of SWOT, the errors from these media effects are negligible except for wet tropospheric correction. This is also true for land hydrological applications.

6.2.1 Wet Tropospheric Effects over the Ocean

A conventional water-vapor radiometer like the Advanced Microwave Radiometer (AMR) flying on Ocean Surface Topography Mission (OSTM)/Jason-2 is able to provide appropriate path delay correction along the nadir path of SWOT. However, it is also important to consider the two-dimensional variability of water vapor over the 120-km swath. Displayed in Figure 6.2-2 is a map showing the rms difference in path delay over a distance of 60 km based on AMSR-E data. This information provides an estimate of the errors in using the alongtrack nadir measurements for making corrections across the swath. This error, however, has contributions from all wavelengths and is dominated by long-wavelength components as indicated by the spectrum shown

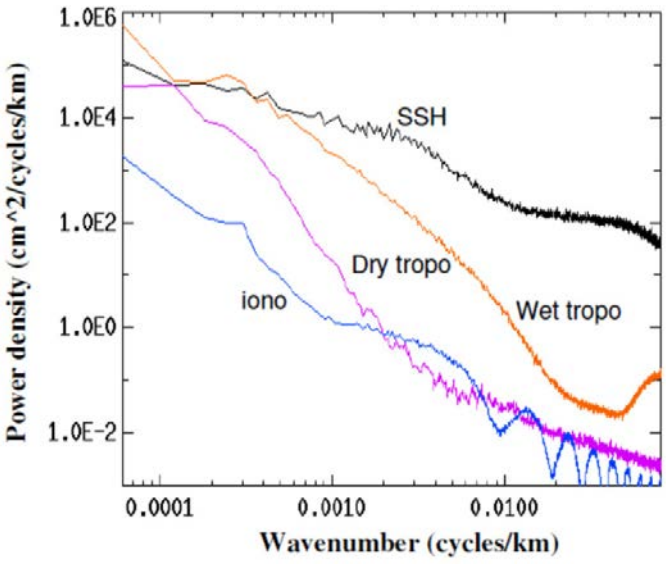

Figure 6.2-1. Wavenumber spectrum of the various media effects on the SSH measurement.

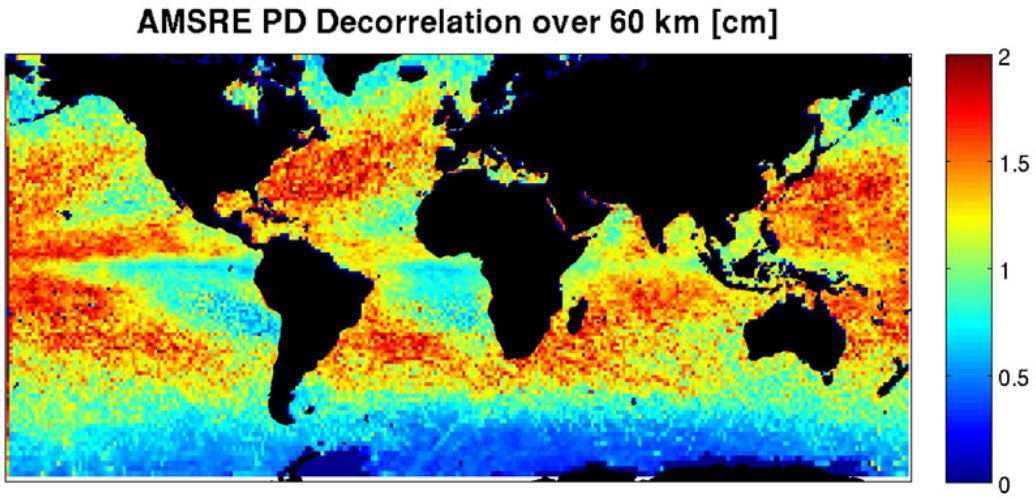

Figure 6.2-2. The rms difference in path delay over a distance of 60 km based on the AMSR-E data.

in Figure 6.2-1. To assess the errors from wavelengths shorter than 300 km, we need to perform high-pass filtering. To illustrate the high end of the error magnitude, we analyzed the wet tropospheric corrections from Jason-1 in the western North Atlantic near the Gulf Stream, where the rms path delay errors shown in Figure 6.2-2 are relatively high. Displayed in Figure 6.2-3 are profiles of the corrections along two passes. The sharp rise of the water-vapor effects associated with the warm water over the Gulf Stream region is clearly shown. The pink curves represent the variability at wavelengths shorter than 300 km that would affect the SWOT objectives. The rms variability is 0.7–0.8 cm, which cannot be corrected for by a single profile of water vapor measurement.

The variability over the swath will manifest as coherent error structures in the SWOT imagery. To illustrate, the SWOT orbit was overlaid on a plot description (PD) field produced from AMSR-E data. This is shown in Figure 6.2-4 (left). Most of the structures in this image are from synoptic-scale (>100 km) water vapor features. Figure 6.2-5 (right) shows the residual PD error structures across the swath for a nadir-only radiometer correction. The errors can reach 6 cm toward the edge of the swath, but are on average ~2 cm, 1σ, consistent with Figure 6.2-2. Figure 6.2-5 shows the residual path delay error spectrum averaged across the SWOT swath for a nadir-only path delay correction computed using many realizations of the swath errors computed from AMSR-E data.

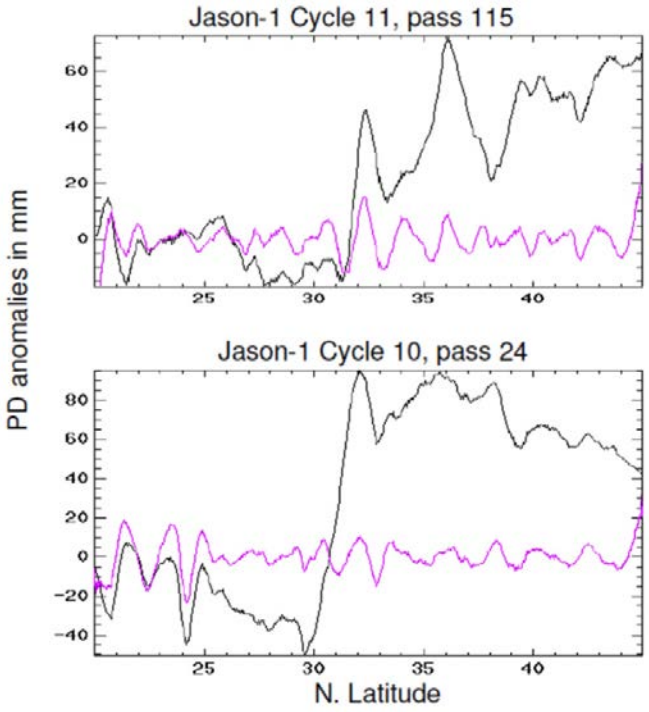

Figure 6.2-3. Jason Microwave Radiometer path delays (black lines) along two Jason-1 ascending passes crossing the Gulf Stream region. The pink lines show high-passed part of the path delays at wavelengths shorter than 300 km.

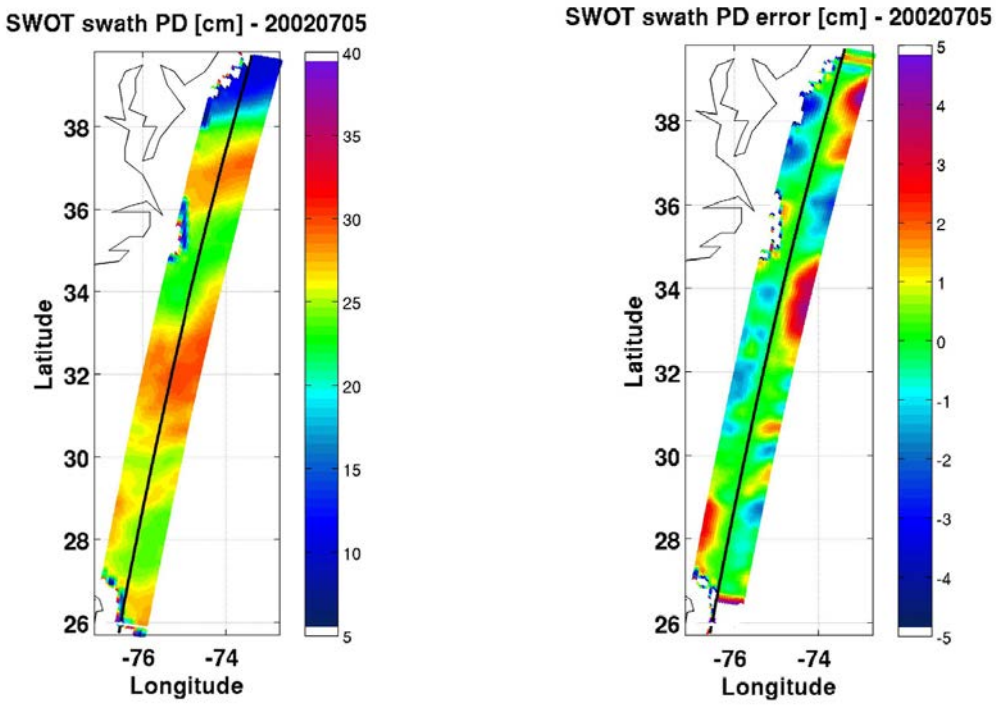

Figure 6.2-4. (Left) Path delay across the SWOT swath derived from AMSR-E fields. (Right) Residual path delay error structures across the SWOT swath from a nadir-only correction.

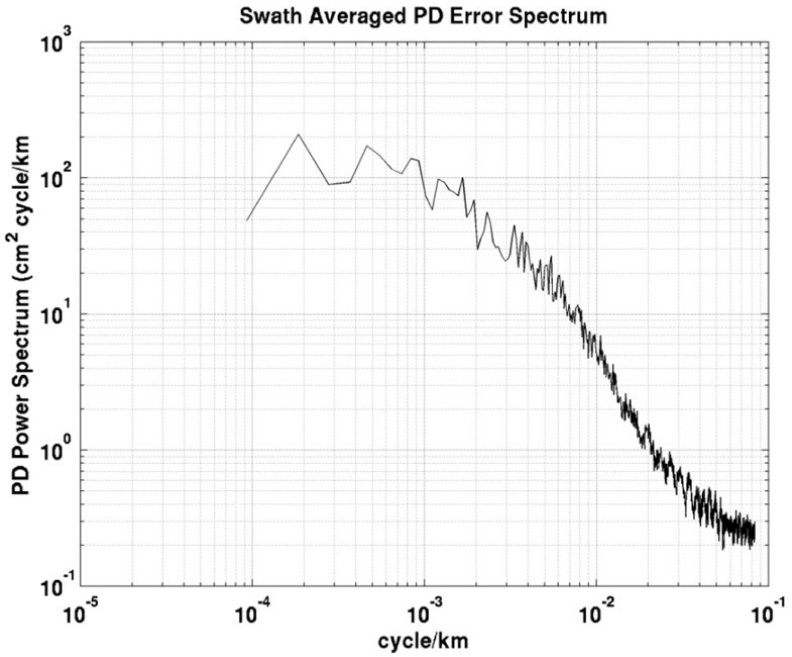

Figure 6.2-5. Residual path delay error spectrum averaged across the SWOT swath for a nadir-only path delay correction.

6.2.2 Wet Tropospheric Effects over Land

An analysis was conducted to assess path delay variability over land. Path delay was computed from a large set of globally distributed radiosonde (RaOb) soundings from 1980–2010. The RaOb data were acquired from the quality controlled Integrated Global Radiosonde Archive (IGRA) database. The database included 981 stations, shown in Figure 6.2-6. The color of each point represents the average path delay at that station. These data were used to assess the pass-to-pass variability by computing the standard deviation of the path delay over time at each station from 1980–2010. The variability is dominated by an annual signal, and the total variability can reach 12 cm, 1σ. With the annual signal removed, the worst-case variability is 7 cm, 1-sigma. Figure 6.2-7 shows a map of the total variability and the variability with the annual harmonic removed. Also shown is the histogram of the variability and the cumulative distribution function.

An assessment of upward-looking ground-based radiometer measurements was used to estimate the expected variability across the swath over land. The radiometer data were acquired from the Department of Energy Atmospheric Radiation Measurement (DOE ARM) sites, which have a long time series of derived precipitable water vapor (PWV). The PWV data were converted to path delay using a simple scaling factor of 6.7 cm/cm. The path delay variability at each station with respect to time is the sum of the local time variability and the variability due to advection over the station from all other directions,

$$\frac{DPD}{Dt} = \frac{\partial PD}{\partial t} + \vec{V} \bullet \nabla PD \quad . \tag{6.2-1}$$

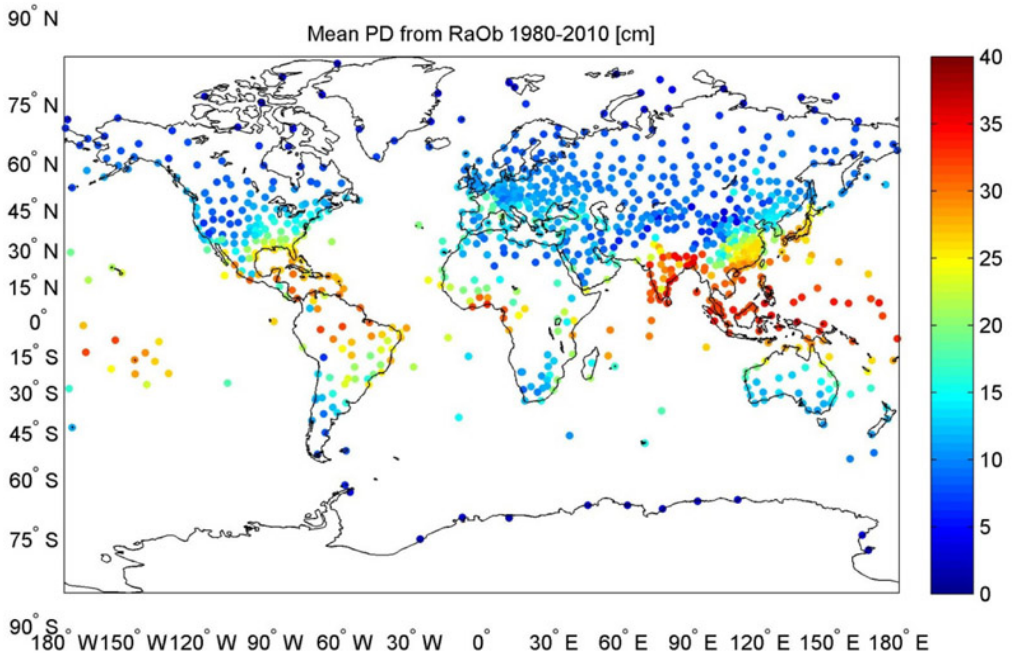

Figure 6.2-6. IGRA stations used in land variability analysis. The color of each station indicates the mean path delay at that station.

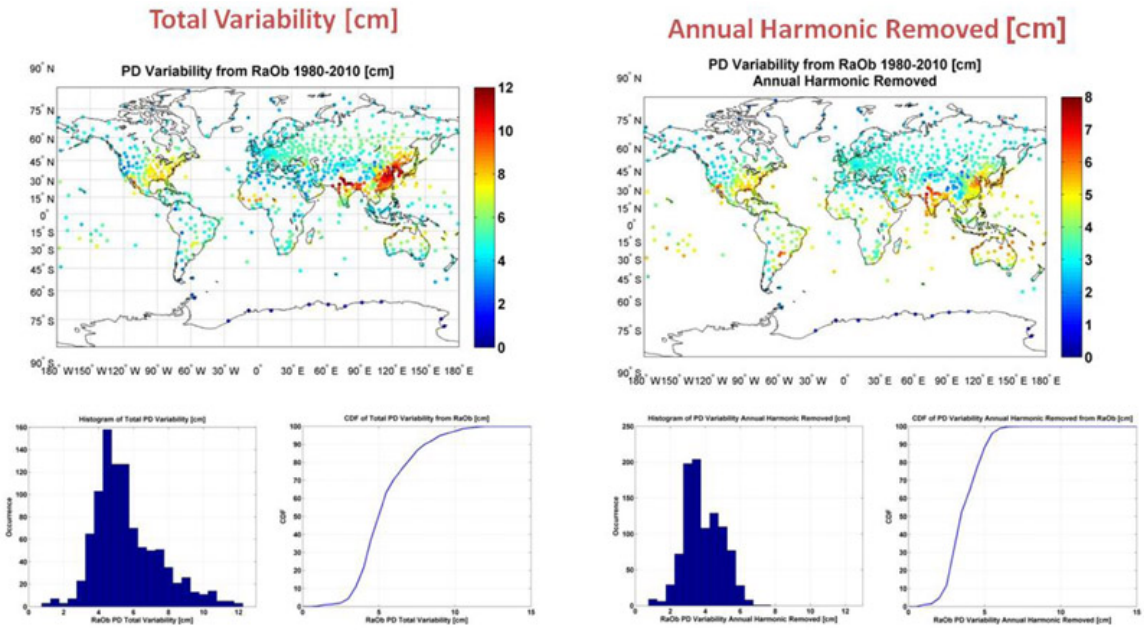

Figure 6.2-7. Pass-to-pass variability of path delay at the IGRA station locations (top left) and with the annual signal removed (top right). The bottom panels show the distribution of the errors in the maps.

If local time variability is assumed to be zero (first term on the right hand side), then variability over time at each station is equal to the product of the spatial PD gradient and mean flow velocity. Therefore, we can use the ARM radiometer time series as a proxy to estimate variability over SWOT swath, making an assumption about the mean flow velocity (V) of the atmosphere. In the lower troposphere, a typical mean flow velocity is 10 m/s, which means that the temporal variability over 2 hours is equivalent to spatial variability over about 70 km, or from the center to the edge of the SWOT swath. Figure 6.2-8 shows a representative time series from one of the AMR sites in Black Forest Germany for July 2007. The left panel shows the entire month, and the middle and right panels show the variation over a few days and a few hours, respectively. The time series data for the five ARM stations were analyzed to determine the temporal decorrelation over 2 hours. The locations of the ARM stations are shown in Figure 6.2-9 along with the temporal decorrelation curves over 2 hours. Although these data only represent five points globally, it can be estimated that the variability over the swath likely will not exceed 2 cm, but it should be noted that the variability can be several centimeters near fronts.

A recent set of measurements made by the JPL High Altitude MMIC (Monolithic Microwave Integrated Circuit) Sounding Radiometer (HAMSR) was used to estimate the path delay along a scan arc across the sky over JPL on 2 February 2010. These data represent the most sensitive measurements ever made of water vapor variability and reveal structures on time scales of seconds. Figure 6.2-10 shows a 15 minute time series of data scanning across the sky. The approximate dimensions of the image are 3 km across track and 9 km along track. These data reveal significant PD structures, approaching 1 cm, on kilometer spatial scales.

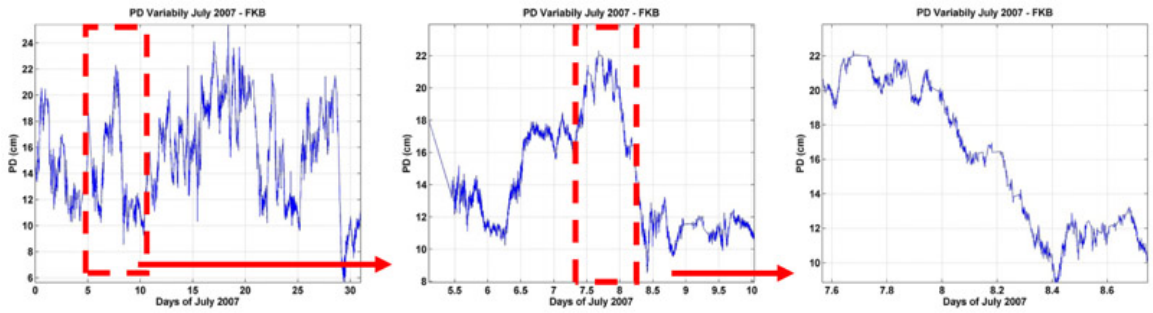

Figure 6.2-8. Path delay time series at the ARM site in Black Forest, Germany, for July 2007. The left panel shows the entire month and the middle and right panels show the variation over a few days and a few hours, respectively.

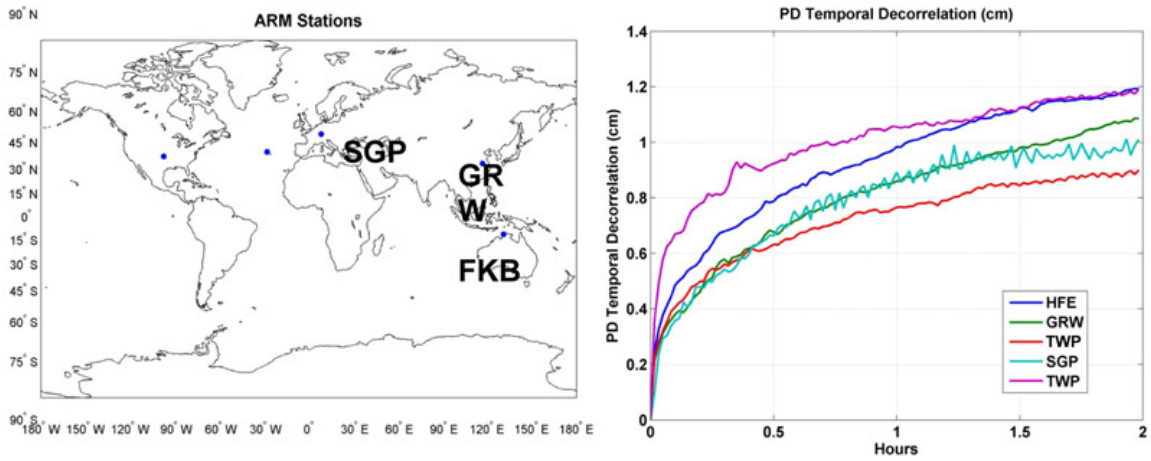

Figure 6.2-9. Location of ARM stations (left). Path delay temporal decorrelation at each ARM station (right).

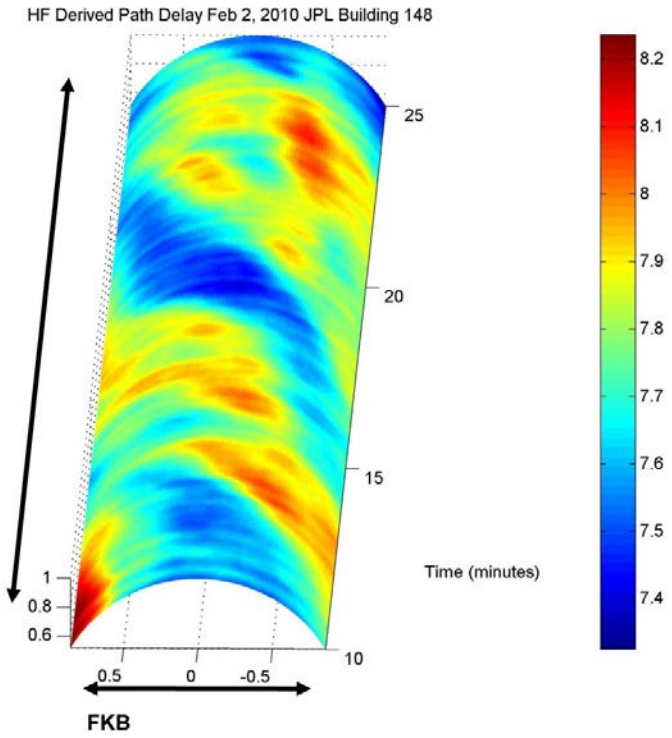

Figure 6.2-10. Small-scale path delay variability estimated using the JPL HAMSR instrument over JPL on February 2, 2010. The approximate cross track dimension is 3 km and the approximate along track direction is 9 km.

References

Chelton D .B., J. Ries, B. Haines, L.-L. Fu, and P. Callahan, 2001: Satellite altimetry. In "Satellite Altimetry and Earth Sciences: A Handbook for Techniques and Applications," edited by L.-L. Fu and A. Cazenave, pp. 1-131. Academic Press, San Diego.

6.3 Ocean Tides

The success in using data from TOPEX/Poseidon and subsequent nadir altimeter missions for studying nontidal motions hinged upon the accurate removal of tidal elevations, which account for approximately 80% of the sea surface height variance measured by these altimeters. The models used to detide present-day nadir altimetry are extremely accurate in the deep ocean, because they were tightly constrained by the tidal signals in the multiyear TOPEX/Poseidon and Jason data sets. While SWOT will clearly benefit from this heritage, its requirements for high horizontal resolution imply that current tide-correction procedures must be improved or supplemented in several ways.

In light of SWOT's primary oceanographic objective of submesoscale variability, correcting the sea-surface elevation data for internal-tide signals is critical. Examples of such signals are shown in Figures 5.1-4 and 5.1-5 (section 5.1.3). For typical wavelengths of 100 km, an error of 1 cm in the internal-tide correction could lead to falsely inferring a geostrophic velocity of order 1 cm/s. Therefore, the SWOT mission should aim toward internal-tide corrections accurate to the sub-centimeter level. As Figure 5.1-5 and the discussion in section 5.1.3 suggests, current state-of-the-art global models of baroclinic tides cannot yet provide such accurate predictions. These models are nonetheless improving (Arbic et al., 2009), and initial assimilation work also holds much promise; but ultimately the best corrections are likely to rely heavily on the SWOT measurements themselves. This has two important implications: (a) initial SWOT data during the beginning of the mission will have inadequate corrections as we await buildup of a sufficiently long time series to allow tidal inversion; and (b) the orbit for SWOT must be designed to allow successful tidal analysis—i.e., due consideration must be given to tidal aliasing characteristics of the SWOT orbit and its data-sampling scheme. This sets limits on the precession rate of the satellite orbit plane, and thus on the satellite inclination and altitude. Similarly, use of SWOT to improve tidal charts in high latitudes and in near-coastal regions (see section 5.1) also requires an orbit designed for tidal analysis.

Furthermore, point (a), combined with the fact that tidal models will never be perfect, argues for selecting an orbit for which tidal alias frequencies are easily separable from major frequencies of oceanographic interest (e.g., annual, semi-annual, and very low frequencies). Any remaining errors in tide corrections can then be more readily recognized as such.

6.3.1 Tidal Aliasing

Nominal SWOT orbit parameters are discussed in section 7.2. Tidal aliasing issues were considered in the selection of these parameters. Although small adjustments to these parameters may occur, the aliasing characteristics of the solar tides are unlikely to change significantly; lunar tides are more flexible and less worrisome. Adopting an inclination of 78°, an altitude of 971 km, and a repeat period of 21.8637 days, we find the following

alias periods for the major (plus two compound) tidal constituents, based on a classical analysis of one observation per repeat period:

Q_1	46 d	N_2	48 d	M_4	44 d
O_1	68 d	M_2	89 d	MS_4	843 d
S_1	160 d	S_2	80 d		
K_1	286 d	K_2	143 d		

The alias period for K_1 is somewhat long, but this is an unavoidable compromise for a relatively high-inclination orbit—unless the altitude is very low, at least one solar diurnal tide must be aliased to periods longer than 200 days. By design, the K_1 alias is well away from the annual and semi-annual cycles. All the other tabulated periods appear acceptable, except for the small compound constituent MS_4. The period for MS_4—843 days—is rather unsatisfactory; unfortunately it was also unsatisfactory for TOPEX/Poseidon with an even longer alias period of 1084 days. A small reduction in the SWOT inclination to 77.2° would yield a period of 478 days for MS_4, so it is possible some small adjustments in this regard may be made before the final orbit selection.

6.4 Ocean Waves

The presence of surface gravity waves can introduce an additional source of height noise error, since the average of the wave height over a 1×1 km^2 pixel will not be exactly zero. We will show that this error can be greatly mitigated by using an adequate weighted averaging. Assume a two-dimensional monochromatic wave train, which can be written as:

$$h(x, y) = a(k)\cos(k_x x + k_y y + \varphi)$$

Using an averaging window w(x,y), the weighted average height would be:

$$< h(x_0, y_0 >= \frac{1}{A}\int dx \int dy\, w(x - x_0, y - y_0)h(x, y)$$

with

$$A = \int dx \int dy\, w(x - x_0, y - y_0)$$

A rectangular-product window of the form results in a height error over a given resolution cell of characteristic dimension L_x and L_y:

$$\sigma_{hR} = \frac{a(k)}{\sqrt{2}} \frac{|W_x(k_x)|}{L_x} \frac{|W_y(k_y)|}{L_y}$$

Here we show that the effect of a wave with amplitude of 1-m and 230-m wavelength (2.8-m significant wave height) on 1×1 km^2 pixels can be greatly reduced if weighting is used. The following weighting windows are considered: Uniform, Hamming and Gaussian.

$$w_U(x) = \begin{cases} 0 & |x| > L/2 \\ 1 & |x| \le L/2 \end{cases}$$

$$w_H(x) = \frac{0.54 + 0.46\cos(\pi x/(L/2))}{(1.08/2)}$$

$$w_G(x) = \frac{1}{\sqrt{2\pi}} \exp\left[-\frac{x^2}{2L^2}\right]$$

Figure 6.4-1 shows the rms height error as a function of the direction of travel of the wave relative to the averaging direction. The errors for a Gaussian window are too small to show in this scale. Therefore, this is a requirement on the onboard processor to perform weighted averaging.

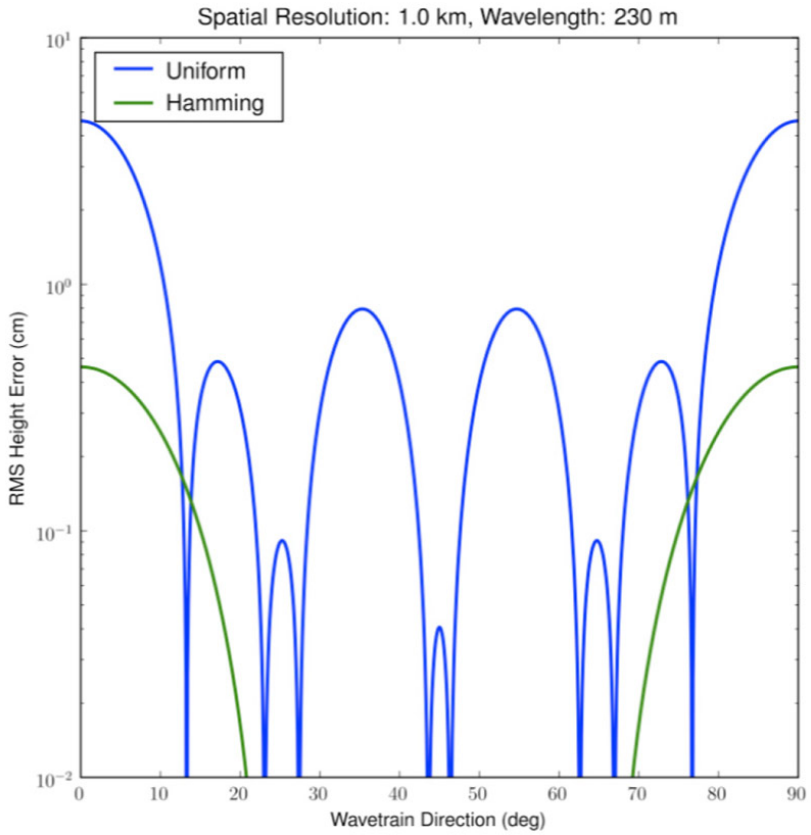

Figure 6.4-1. The effects of weighting windows on the errors resulting from waves.

6.5 Layover and Vegetation Effects

6.5.1 What is Layover?

The interferogram from a scene containing topography and volume scatterers, such as vegetation, can be written (Rodríguez and Martin, 1992) as a sum of the interferometric phase contributions from all the scatterers in a scene, weighted by the radar antenna gain and range resolution response and by the intrinsic brightness of each scatterer:

$$\langle v_1 v_2^* \rangle (t) \approx A \int dx dz \, G^2(x) \chi^2(t - 2r(x,z)/c) \exp\left[-i\Phi(x,z)\right] \sigma_0(x,z)$$

In this formula, the expression on the left-hand side is the interferogram at a range corresponding to the time of arrival; t; x, and z are the cross-track and vertical coordinates, respectively; A is a constant containing system and geometry parameters; G is the antenna gain pattern; χ is the system range point target response, which has a peak for all points at a range r from the radar arriving at the same time $t=2r/c$, and a width, Δr, corresponding system range resolution; $\Phi(x,z)$ is the interferometric phase for a pixel located at (x,z); and, finally, σ_0 is the radar cross section of the scatterer per unit volume. (Note that in the previous equation, we have assumed that the azimuth resolution is small, and phase variations over azimuth can be ignored.)

If the scattering surface is sufficiently smooth, a given range will intersect the surface at a single point, whose cross-track distance will be denoted x_0. The range point target response will then isolate an area on the ground, nominally centered at x_0 and having a width $\Delta x = \Delta r/\sin\theta$, where θ is the incidence angle, as being the only one contributing to the integral in the previous equation. If the surface is sufficiently rough, however, the iso-range line may intersect the surface at multiple points, and all of their phases will contribute to the final phase of the interferogram at a given range. This situation is illustrated in Figure 6.5-1, where it is shown how an iso-range line can simultaneously intersect the desired water surface, vegetation along the riverbank, and topography further away. All of these points will have the same range, but different look angles, and therefore, different interferometric phase, since phase is proportional to the look angle. In general, all points on a line having a slope equal to the angle incidence will arrive at the same time at the radar. For near-nadir incidence, this slope is small, and the likelihood of having layover increases.

The interferogram in the previous equation can be decomposed into contributions from the nominal cross-track pixel, and contributions from other scatterers that have the same range.

$$\langle v_1 v_2^* \rangle (t) = P_w \gamma_w \exp\left[-i\Phi_w\right] + P_L \gamma_L \exp\left[-i\Phi_L\right.$$

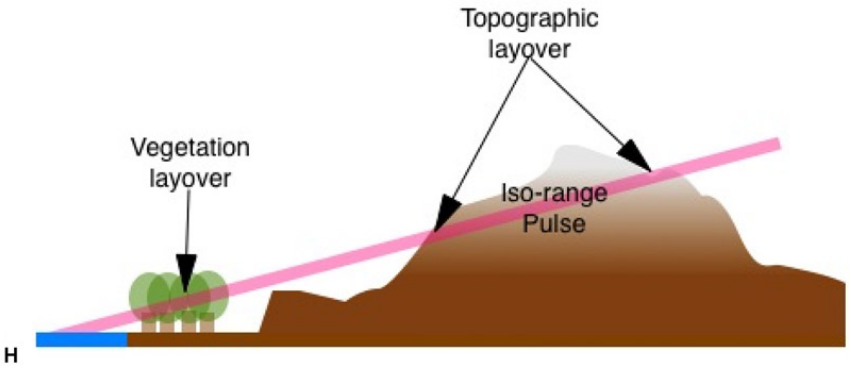

Figure 6.5-1. Cartoon illustrating how a radar interferogram can have contributions from the desired water body (shown in blue), streamside vegetation, and topography, since the scatterers at each of these locations have the same range relative to the radar (located to the left and up from the edge of the image).

where the power, correlation and phase contributions from water and layover have been explicitly separated, as follows:

$$P_w \gamma_w \exp\left[-i\Phi_w\right] = A \int_W dx\, G^2(x)\chi^2(t - 2r(x)/c) \exp\left[-i\Phi(x)\right] \sigma_{0w}(x)$$

$$P_w = A \int_W dx\, G^2(x)\chi^2(t - 2r(x)/c)\sigma_{0w}(x)$$

$$P_L \gamma_L \exp\left[-i\Phi_L\right] = A \int_L dxdz\, G^2(x)\chi^2(t - 2r(x,z)/c) \exp\left[-i\Phi(x,z)\right] \sigma_{0L}(x)$$

$$P_L = A \int_L dxdz\, G^2(x)\chi^2(t - 2r(x,z)/c)\sigma_{0L}(x)$$

The first two integrals are taken over the water areas, while the last two are taken over all space *excluding* the surface contribution from the water. We identify P_w and P_L with the return power from water and layover, respectively; the real quantities γ_w and γ_L with the interferometric correlation from water and land; finally, Φ_w and Φ_L are the effective interferometric phases from water and land, respectively. One can then separate the total interferogram into two multiplying factors

$$\langle v_1 v_2^* \rangle = P_w \gamma_w \exp\left[-i\Phi_w\right] \left[1 + \frac{P_L \gamma_L}{P_w \gamma_w} \exp\left[-i\left(\Phi_L - \Phi_W\right)\right]\right]$$

The term inside the square brackets is the contribution due to the layover, while the factors outside represent the return from the water surface, in the absence of layover.

When we are in the near-nadir regime, water will be significantly brighter than land, and due to the greater angular extent of the layover, the water correlation will be greater than the land correlation. In this case, we can bound the difference between the expected interferometric phase difference in the absence of layover and the phase in the presence of layover as

$$\delta\Phi = \arg\left[1 + \frac{P_L\gamma_L}{P_w\gamma_w}\exp\left[-i\left(\Phi_L - \Phi_W\right)\right]\right] \leq \frac{P_L\gamma_L}{P_w\gamma_w}$$

and the associated height error will be bounded by

$$\delta h \leq \frac{x_0}{2kB}\frac{P_L\gamma_L}{P_w\gamma_w}$$

$$\leq 6.4x_0\frac{P_L\gamma_L}{P_w\gamma_w}$$

In the last equation, applicable to the SWOT parameters, the error δh will be in centimeters when x_0 is given in kilometers. As a bound for the power ratio, we can use the fact that for the Ka-band, the water normalized radar cross section is at least a factor of 10 greater than that for land. However, as we will see below, the scattering areas for the layover, as well as the greater decorrelation exhibited by the layover, will cause a significant decrease in the error associated with the layover.

6.5.2 Topographic Layover

To get a first assessment of the probability of layover, we look at large-scale topography. The probability of layover due to topography is related to the probability of the slope of the line connecting two points being equal to the incidence angle. Due to the small incidence angles for KaRIn observations, relatively small height differences can result in layover. To quantify the layover problem, we separate the layover due to topographic variations from that due to the presence of vegetation surrounding the water body. Given typical tree heights between 15 m and 20 m, the layover due to vegetation will dominate for small distances from the water's edge, while topographic variations will dominate for larger distances. We choose 500 m to 1 km as the separation scale between these two contributions, since we have reliable topographic statistics for these distances, although the answer is not highly dependent on the actual number. The probability of layover due to topography depends on the probability for surface slopes as a function of point-to-point separation distance. Kreslavsky and Head (1999) have used the Global 30 Arc-Second Elevation Data Set (GTOPO30) digital elevation model of the Earth to derive the probability density function (pdf) for slopes as a function of separation for the continents. They note that the slope pdf is nearly exponential, and that the median slope value has a linear relationship in log-log space with the separation. Continental values for the median slope vary from approximately 0.6° (1 km separation) to about 0.2° (10 km separation). Given these statistics, it is possible to estimate that layover will occur on a global basis. The results, shown in Figure 6.5-2, depend somewhat on the topography correlation distance, but generally show that the probability of layover is smaller than 10% as a worst case, and generally significantly smaller. Although these numbers are small, they can become significantly worse in areas of high relief, as the median slope increases, and this limits the regions where KaRIn can produce useful measurements to areas of relatively low relief. Fortunately, these areas are generally coincident with the location of large rivers, lakes, and wetlands.

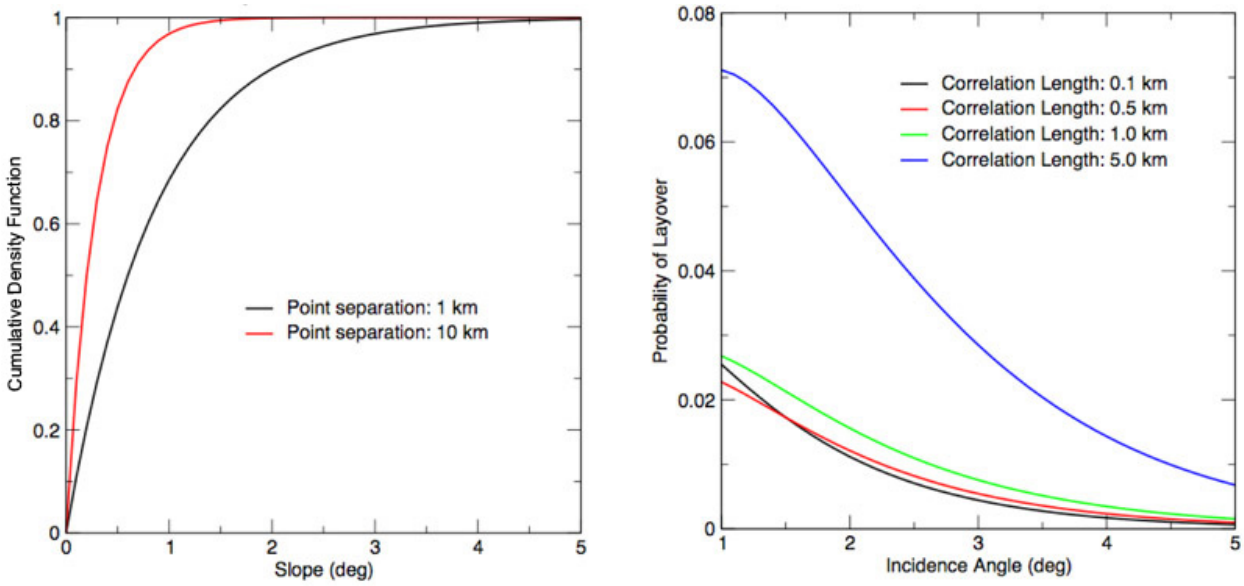

Figure 6.5-2. (Left panel) cumulative density function for slopes for points separated by 1 km (black line) or 10 km (red line) derived from global GTOPO30 topography, as derived by Kreslavsky and Head (1999). (Right panel) Probability of topographic layover, as a function of incidence angle and surface topography correlation length.

To assess the effect of topographic layover in greater detail, one must use a high-resolution Digital Elevation Model (DEM) to integrate numerically the equations for the interferogram presented in section 6.5.1. We have conducted such a simulation over different river basins, and present an example of the results for the simulated interferogram showing the effect of layover in Figure 6.5-3 for the Ohio River using the SRTM (Farr et al, 2007) DEM. In this simulation, we assume, conservatively, that the water normalized cross section is only 10 dB brighter than the land cross section.

To study quantitatively the layover effects, we geolocate the pixels in the interferogram using the phase and range and estimate the elevation errors relative to the known water surface. We also associate a color to each point, depending on whether it has no layover (blue), or is contaminated by layover (red). The results for sections of the river in the mid-range (~4° incidence angle) and near-range (<1° incidence angle) are shown in Figure 6.5-4. This figure shows that while the layover covers a relatively minor part of the mid-swath, it can be very common in the near swath. However, this classification does not take into account the fact that the elevation error due to layover may be relatively small. If we assume that errors smaller than 5 cm are acceptable (compatible with the SWOT 10 cm elevation error budget), a significant number of points in the near swath become useful, as shown in Figure 6.5-5.

In summary, topographic layover may be present in a substantial part of the SWOT swath. By using DEMs and interferogram simulation, the location of the areas affected by layover can be identified. Furthermore, the interferogram simulation allows the identification of points that, while affected by layover, are still useful for hydrologic studies. These conclusions are based on simulation, and should be refined with the aid of real interferometric data, such as will be collected with the AirSWOT instrument described in Section 7.6.

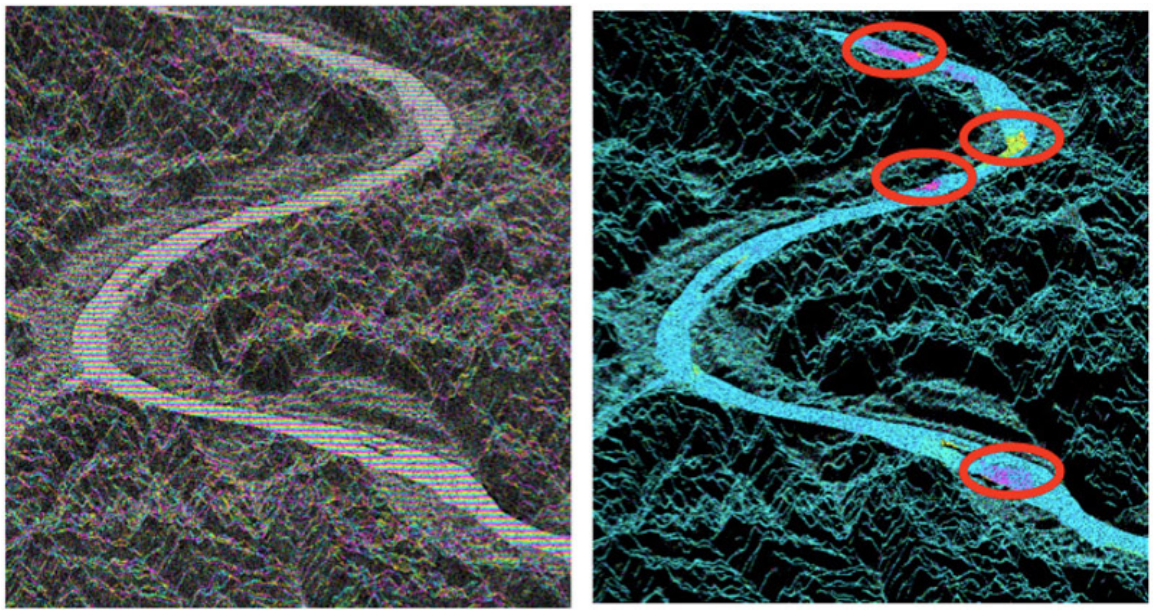

Figure 6.5-3. (Left panel) Simulated interferogram of the Ohio River observed by SWOT. Colors represent interferometric phase, which wraps between 0 and 2π, while intensity represents the returned power. (Right panel) Interferometric phase after subtracting an interferogram containing no layover over water. The circled regions indicate locations where the interferometric phase is substantially affected by layover.

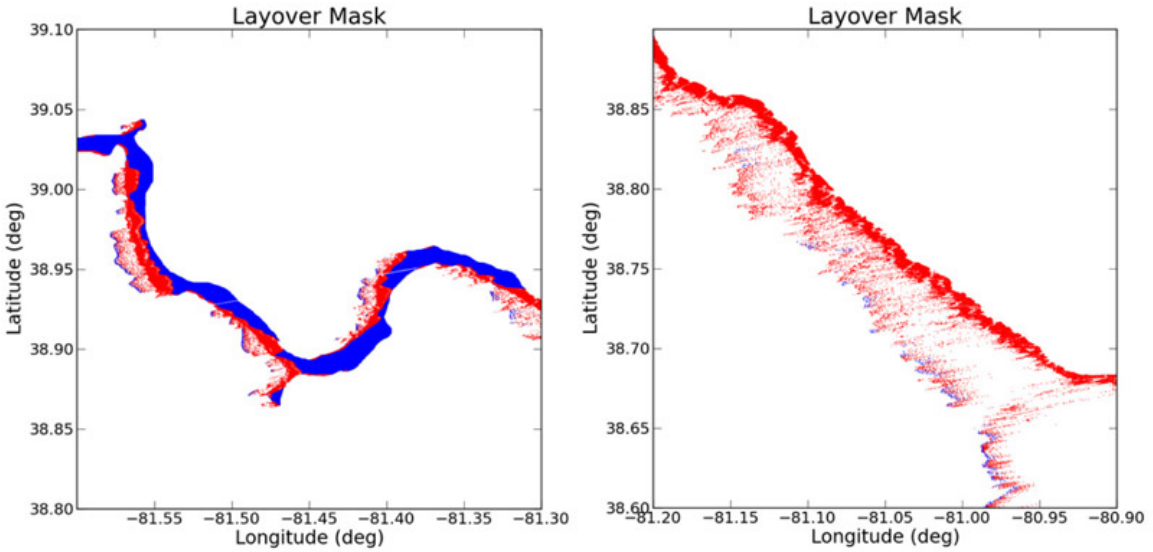

Figure 6.5-4. (Left panel) Mid-swath mask of all points containing some water return from the Ohio River simulation. Blue points are pure water, while red points are a combination of water and layover. The points have been geolocated according to their interferometric phase, so points with large phase errors will lie outside the river. (Right panel) Same as left panel, but for a portion of the river in the near range, where layover is prevalent.

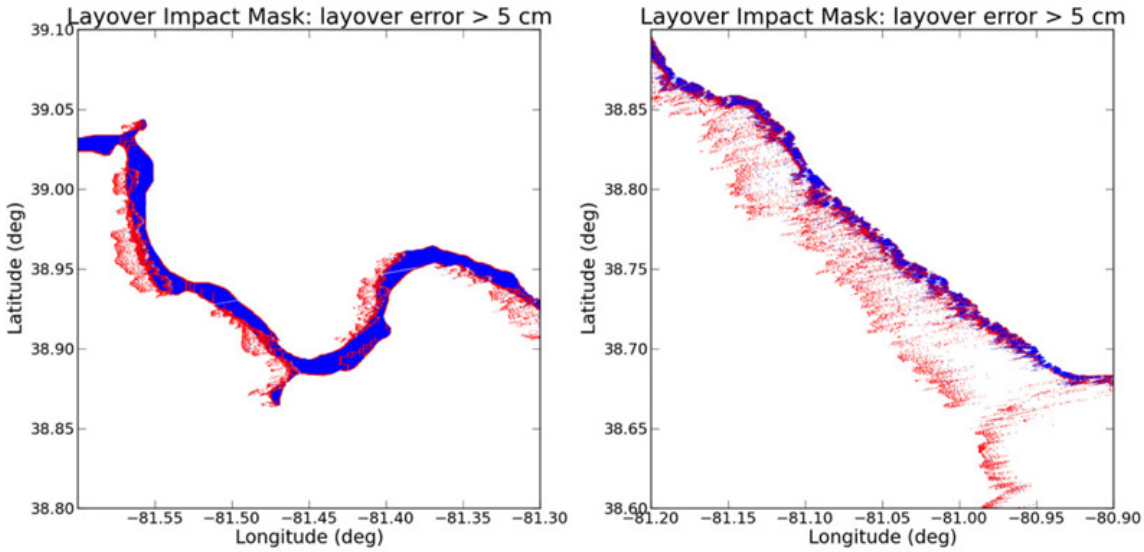

Figure 6.5-5. Same as Figure 6.5-4, but all the layover points that have an error smaller than 5 cm have also been colored blue. Notice that a significant number of points in the near range have become valid water points.

6.5.3 Vegetation Layover and Attenuation

Vegetation present either at the fringes of a river, lake, or wetland—or, for flooded areas, contained within the water body—can distort the signal from the water surface in two ways: first, if the vegetation happens to lie in the path between the antenna and the water surface, it will attenuate the return from the desired target. The attenuated signal will have a lower signal-to-noise ratio and will therefore present a higher level of random noise. However, this random noise will be unbiased, and will not distort the estimation of the mean water level. Due to the fact that the return is darker, water that lies below trees may be misclassified as land. If μ is the intrinsic ratio between the vegetation return and the water return, there will be confusion if the attenuation term—which we assume to be the exponential term $\exp[-\beta(T-z)/T]$ (where z is the height above the surface, and T is the tree height)—is approximately equal to μ. Experimental evidence suggests that μ ranges between –20 dB and –10 dB, with a likely value of about –15 dB. This implies that β must range from 4.6 to 2.3, with a most likely value of 3.5 for water to be separable from land.

The second distortion due to vegetation is the fact that signals from the vegetation may arrive at the same time as signals from the water, an effect called layover in radar remote sensing. Layover can occur when the vegetation is present further from the water point along the range direction and in a locus of heights z obeying the equation $z=x\sin\theta$, where x is the distance along the ground between the water under observation and the patch of vegetation, and θ is the local incidence angle. Typically, when layover from a vegetation patch occurs, there will be a range of distances $[x_1,x_2]$ that will be laid-over. The corresponding set of heights will be denoted by $[z_1, z_2]$; notice that $0<z_1<z_2<T$. For

each layover height, the vegetation will introduce a phase error that is proportional to the vegetation brightness at that height (including attenuation) and the intercepted volume. When a range of layover is present, one can show by integrating the interferogram models presented in the first section that the total phase error will be

$$\delta\Phi = \arg\left[1 + \frac{\mu\nu}{\beta + i\kappa_z T}\left(\exp\left[i\kappa_z(T - z_1)\right]e^{-\beta z_1/T} - \exp\left[i\kappa_z(T - z_2)\right]e^{-\beta z_2/T}\right)\right]$$

$$\kappa_z = \frac{kBT}{H\sin\theta}$$

$$\nu = \frac{\beta}{1 - e^{-\beta}}$$

where B is the interferometric baseline and H is the platform height. In Figure 6.5-6, we plot the associated height bias as a function of the distance along the range direction between the water pixel and 10 km-wide stand of vegetation. Notice that distance to the stand is along the range direction, and not the distance from the water to the nearest stand. This means that the distance to the stand will depend on the orientation of the river to the direction of observation. In the worst case, the river is perpendicular to the observer, and the distance to the tree stand will be the distance from the water pixel to the far bank (assuming the tree stand starts at the river's edge). In general, the distance to the tree line will be the worst-case distance divided by the cosine of the river angle relative to the worst case. Figure 6.5-7 shows similar results when the tree stand is only 50 m wide, which is more typical of the distortion expected due to trees in flooded areas. We conclude from these figures that the effects of vegetation will get worse with increasing cross-track distance and decreasing vegetation/water contrast. In the worst cases, the height distortions may be unacceptable, and these areas may need to be masked out from the river stage estimation.

To further quantify this effect for more realistic vegetation distributions, we have conducted a detailed simulation of the interferometric errors for the water bodies in the Amazon basin. Our simulation is based on a 90 m vegetation/water mask provided by L. Hess (Hess et al., 2003), and oversampled to 30 m spacing. We assume that the vegetation is present everywhere with a height of 20 m, and that penetration into the canopy occurs with the observed penetration of other radar interferometric data that typically reports a tree height that is about 60%–70% of the true height (Rosen et al., 2000). We simulated three swaths of data covering a total area of about 390,000 km^2. The root mean squared height error for the entire data set was about 2.8 cm. The error was more pronounced for the smaller water bodies and for the larger incidence angles. Figure 6.5-8 shows the simulation extent, together with a few examples of vegetation-induced errors for small water bodies of different morphology. Figure 6.5-9 is a detailed histogram of the errors, given different contrasts between water and land. Although in a few extreme cases the errors can be as large as 30 cm, the performance over the scene meets the desired accuracy for the KaRIn instrument. Errors can be reduced by excluding

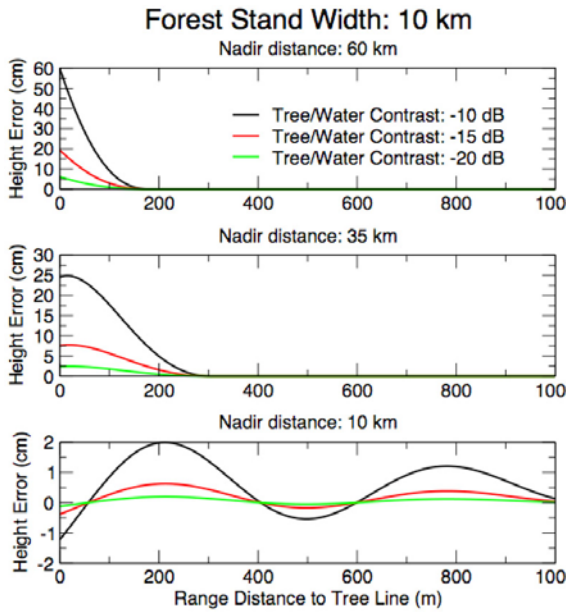

Figure 6.5-6. Height errors as a function of cross-track distance [from near swath (bottom) to far swath (top)], tree/water brightness contrast, and distance between the water pixel and the start of the vegetation patch along the range direction. The tree stand has a range extent of 10 km and was assumed to be 15 m tall.

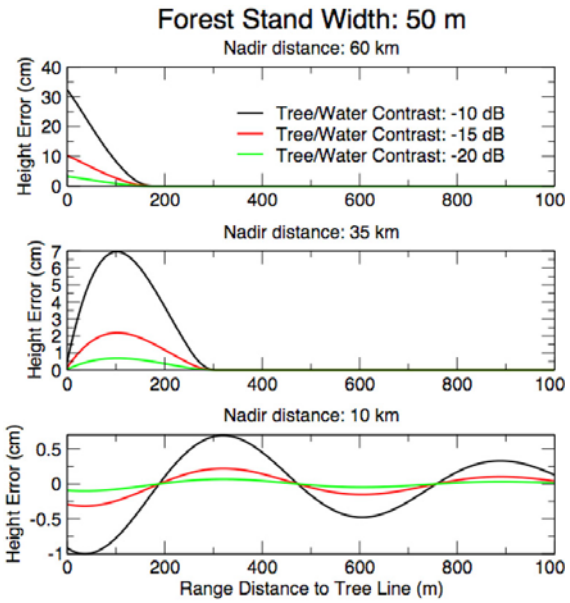

Figure 6.5-7. Height errors as a function of cross-track distance [from near swath (bottom) to far swath (top)], tree/water brightness contrast, and distance between the water pixel and the start of the vegetation patch along the range direction. The tree stand has a range extent of 50 m and was assumed to be 50 m tall.

the areas on the affected banks, at the expense of reducing coverage. As a final comment we note that the effect of vegetation on top of water is to attenuate the signal, leading to a noisier return, but no systematic height bias is introduced, unlike the vegetation layover contamination. The amount of penetration into vegetation canopies in the near-nadir direction will be no worse than that of optical instruments, such as the ICESat altimeter, which have demonstrated penetration even for tropical canopies (Harding et al., 2004). The main impact of vegetation over water will be to decrease the ability to distinguish between the two by looking at the radar brightness. Since water is much brighter than vegetation, the requirement that inundation extent be detectable will be possible as long as the fraction of canopy gaps times the ratio of water to land brightness is greater than about 2. This leads to a requirement that the canopy have a fraction of gaps greater than about 20%, which is true for all but the heaviest canopies.

In summary, due to the phase variation inside the vegetation layer, and the associated decorrelation, vegetation effects tend to be significantly lower than the effects due to topographic layover. This conclusion applies to the simple models studied to date, but should be validated by means of direct measurements, such as the ones that will be collected by AirSWOT, and greater sophistication in the vegetation models.

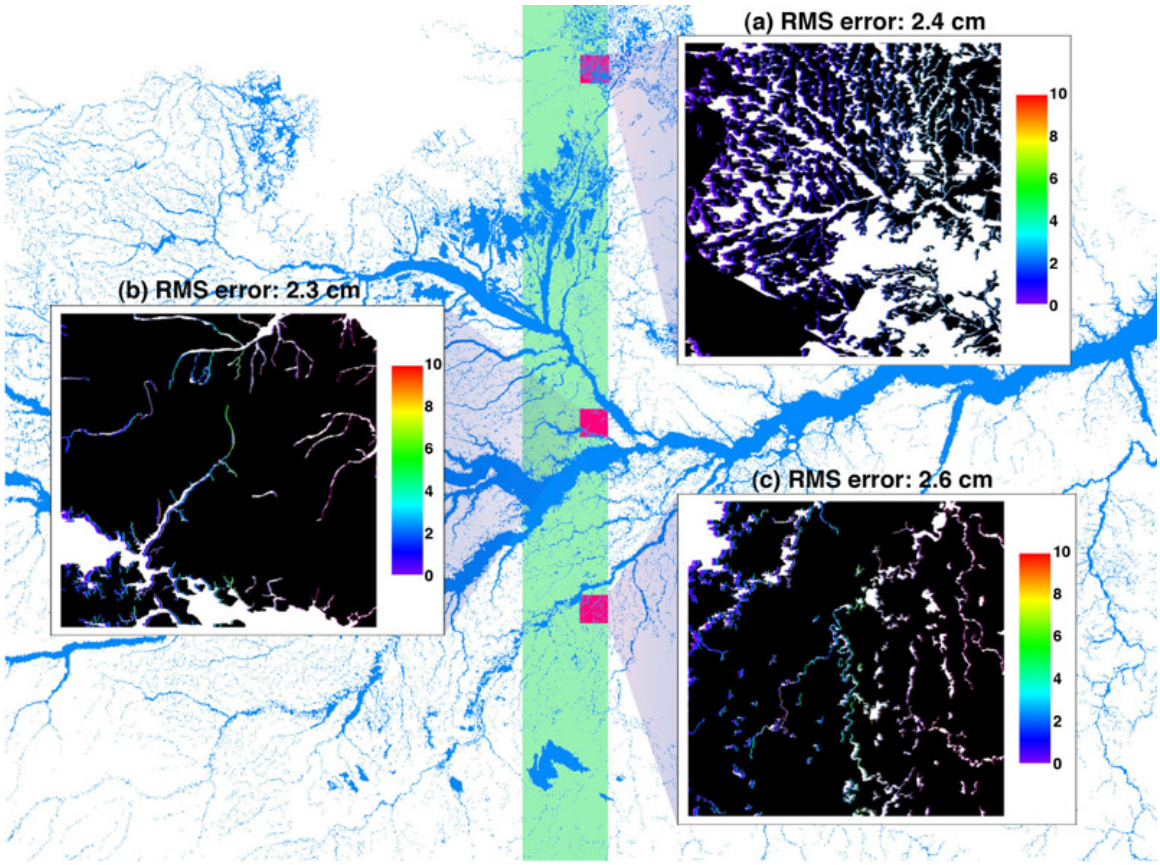

Figure 6.5-8. The area in green shows the region used to simulate the effect of vegetation on the interferometric heights for a region in the Amazon basin. The water mask used is shown in blue, and we magnify three 60 km square areas containing small rivers with different river and wetland morphology. The instrument was looking from the left (west), and one can see the effects of layover errors on the right (east) bank of the water bodies. In the far range (east side of the swath), the errors can be larger than in the near (west) side, due to higher volumetric correlation of the vegetation returns. The root mean squared error for the entire simulation is 2.8 cm, assuming that the water was 10 times brighter than the vegetation.

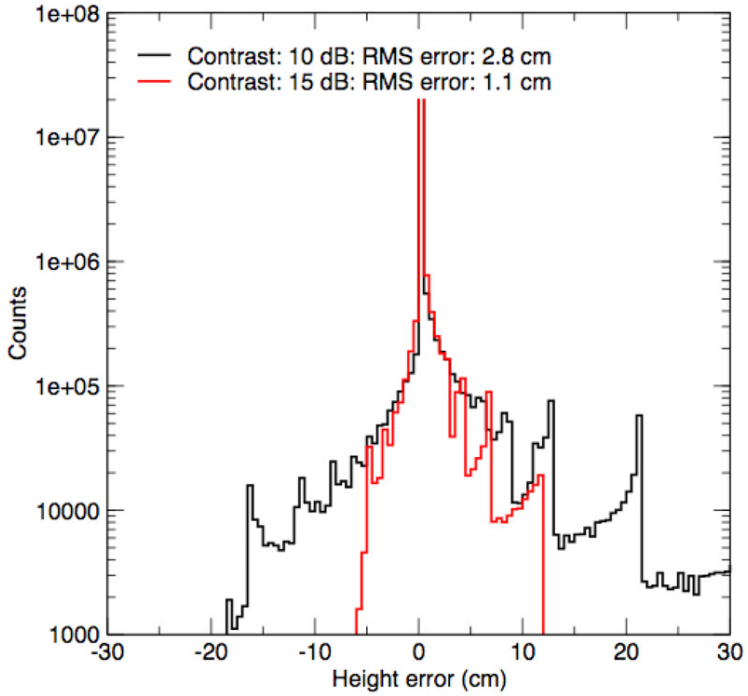

Figure 6.5-9. Distribution of height errors for the Amazon simulation for two different values of the tree-to-water contrast.

References

Farr, T., P. Rosen, E. Caro, R. Crippen, R. Duren, S. Hensley, M. Kobrick, M. Paller, E. Rodríguez, L. Roth, D. Seal, S. Shaffer, J. Shimada, J. Umland, M. Werner, M. Oskin, D. Burbank, and D. Alsdorf, 2007: The shuttle radar topography mission. Reviews of Geophysics, **45**, doi:10.1029/2005RG000183.

Harding, D. J., and M. F. Jasinski, 2004: ICESat observations of inland surface water stage, slope, and extent: a new method for hydrologic monitoring. AGU Fall meeting, C21B-05, abstract.

Hess, L. L., J. M. Melack, E. M. L. M. Novo, C. C. F. Barbosa, and M. Gastil, 2003: Dual-season mapping of wetland inundation and vegetation for the central Amazon basin. Remote Sensing of Environment, **87**(4), 404-428.

Kreslavsky, M., and J. Head, 1999: Kilometer-scale slopes on Mars and their correlation with geologic units: Initial results from mars orbiter laser altimeter (MOLA) data. Journal of Geophysical Research, **104**, 21,911-21,924.

Rodríguez, E., and J. M. Martin, 1992: Theory and design of interferometric synthetic aperture radars. IEE Proc.-F, **139**(2), 147–159.

Rosen, P., S. Hensley, I. Joughin, F. Li, S. Madsen, E. Rodriguez, and R. Goldstein, 2000: Synthetic aperture radar interferometry (invited paper). Proceedings of the IEEE, **88**(3), 333–382.

6.6 Waterbody Delineation

The scientific requirements state that SWOT should provide a global inventory of all terrestrial surface water bodies whose surface area exceeds 250 m^2 (lakes, reservoirs, wetlands) and rivers whose width exceeds 100m (requirement) or 50 m (goal). The lake, reservoir, and wetland areas estimated using the extracted water mask should have a relative error smaller than 20% (1σ) of the total water body area. The water mask will be represented by an irregular grid conformal to the shape of the water body, with an average post spacing of 50 m.

Several water masks that cover most of the globe already exist, such as the Central Intelligence Agency (CIA) World Data Bank, the SRTM Water Body Database, MOD44W based on MODIS data, the Global Lake and Wetland Database, and the Global Reservoir and Dams Database. By 2013–2014 there will also be a high-resolution TanDEM-X water mask (DLR's TerraSAR-X add-on for Digital Elevation Measurement). Even though a compilation of these water masks could marginally fulfill the above requirements in terms of coverage and accuracy, such a static mask would not reflect the variations of the extent of the water surfaces with the water level, which is an important part of the SWOT objectives. Moreover, flooding situations will create new water bodies temporarily. It is, therefore, necessary to derive an updated water mask based on the KaRIn high-resolution (HR) data for each satellite pass.

Extracting water masks from the SAR images produced by KaRIn in HR mode means that we have to detect the presence of water surfaces within the images, and to localize the boundaries between the water bodies and the surrounding land surfaces. The water mask obtained in the range/azimuth image geometry will ultimately be geolocated in ground coordinates (latitude, longitude) by using the interferometric phase in addition to the range and azimuth information.

6.6.1 Challenges and Opportunities

Several factors complicate the water mask extraction from SWOT data:

- Speckle is a phenomenon inherent to SAR imagery (and other imaging techniques based on coherent illumination), which can be modeled as a strong, multiplicative noise (variance equal to one at full resolution) for an individual high-resolution pixel, making all kinds of automatic interpretation difficult. In our case, the strong intensity variations due to speckle imply that water and land surfaces cannot be distinguished based on the intensity of individual pixels, even when the underlying radar reflectivity of the water and land surfaces are well separated: the decision must be based on the values of several neighboring pixels.
- Layover, described in a previous section, is a geometrical distortion that causes a mixture of land and water responses when there is significant topography around the water body. It will certainly complicate the delineation of the water surface

boundaries, but the scientific requirements state that only zones where layover is negligible should be used for height computations (to avoid biases in the height estimation due to land pollution). A DEM with relatively high resolution and accuracy is needed to foresee where layover will occur.

- Even though the water/land radar reflectivity contrast generally can be supposed to be high, it will be variable depending on the surface types and their states, and theoretical models indicate that there may be particular cases where the contrast is weak, making it difficult to distinguish water from land. The water/land contrast will also vary throughout the swath (as a function of incidence). Airborne acquisitions will teach us more about what contrasts can be expected and how each contrast depends on incidence angle and wind conditions.
- The range pixel size varies from 70 m in near range to 10 m in far range. The detection of narrow rivers, down to a width of 100 m or even 50 m, will therefore be particularly difficult for rivers in near range that are oriented alongtrack (roughly North-South), because these rivers will only be 1–2 pixels wide, and therefore hard to distinguish in the presence of speckle.
- Water movement during the SAR integration time (0.25 s) could, depending on the speed and the direction, cause blur or displacement of the water body in the image. Simulation results, however, indicate that the degradation will be very small for the velocities that will be encountered in practice.
- Given the data rate (almost 1 TB of raw HR data per day), the water extraction must be fully automated: after an initial calibration phase where parameters and algorithms are tuned, there can be no manual tuning for each image pair; all parameters must be fixed or estimated automatically from the images. Flags should be raised when algorithms fail.

There are also several factors that facilitate the water mask extraction:

- Even though there may be exceptions, both theoretical models and the first airborne acquisitions confirm that the water/land reflectivity will generally be quite high (several decibels).
- While the range pixel size varies between 70 m and 10 m, the azimuth pixel size is constant and equal to 5 m in HR mode. This allows for some multilooking (incoherent averaging) in the azimuth direction, to reduce the speckle and make it easier to distinguish water from land. Averaging groups of 4 consecutive rows of the full-resolution SAR images allows the researcher to reduce the variance due to speckle by 4, with an azimuth pixel size degraded to 20 m, which is of the same order as the range pixel size and still well below the average spacing of 50 m of the final water mask. For many image interpretation algorithms, it is an advantage to have isotropic images (about the same pixel size in both directions). It should be noted that water and land still cannot be distinguished accurately based on single pixels, even though the intensity variations due to speckle are then considerably reduced, as there will still be overlap between the histograms due to speckle.

- So far we have concentrated on the intensity of the SAR images and the reflectivity contrast between water and land. However, we also have the interferometric phase and coherence of the image pairs. The latter is a measure of phase quality, and airborne acquisitions indicate that it is higher over water than over land. Coherence could, therefore, be used as an additional indicator to distinguish water from land.
- Prior information is available and can be used to guide the automatic analysis. In particular, we will have an external water mask in the beginning of the mission, and after the first orbit, we will have the water mask derived from the first pass (22-days repeat pass orbit). Even though there may have been changes in the waterbody extent meanwhile, the mask of the previous pass can be used as a starting point or an additional indicator for the water extraction algorithm. A DEM of the floodplain and other surrounding areas can also be used to guide the algorithm. It should be noted that the geolocated prior information need to be projected into slant range SAR geometry, meaning that we will need at an approximate geolocation of the SAR data already at this stage in the processing chain. The accuracy of this preliminary geolocation has consequences for the weight that can be given to the prior data.

6.6.2 Approaches and Methods

Pixelwise Classification

Binary classification in its simplest form consists in establishing a threshold for the pixel values. In our case this would mean that pixels whose intensities above the threshold are attributed to the "water" class, and those with values below the threshold are attributed to "land." As already mentioned, classification of individual pixels will be inefficient for SWOT images due to speckle. An ad hoc approach to avoid this problem is to apply adaptive speckle filtering prior to establishing the threshold. This will reduce speckle within areas of homogeneous reflectivity, but the edges between regions (i.e., between water and land) will either remain noisy or accidentally be smoothed. Refined speckle filters, including local edge detection, could reduce this problem (Lopès et al., 1993), but there is a risk of introducing artifacts. This approach is, therefore, considered as suboptimal.

Region-Based Classification

The idea behind region-based classifications is to first perform a segmentation of the image (group neighboring pixels with similar properties into regions) and then classify entire regions rather than individual pixels. Methods based on edge detection only (Touzi et al., 1988; Oliver et al., 1996) and region merging only (Cook et al., 1994) have been developed for radar images, as well as hybrid methods combining edge detection and region merging (Fjørtoft et al., 1998). Pixelwise region growing, starting from seed points or a previous water mask, is another option, but this approach is likely to cause an over-adaptation to local speckle patterns.

While the basic active contour or “snake” algorithm (Kass et al., 1988) used in computer vision optimizes the boundary positions of only a single object, there are also segmentation methods based on the concept of active contours that are capable of managing multiple regions (Zhu et al., 1995, Germain and Réfrégier, 2001). Starting from a fine grid, they split and merge regions, and adjust the boundaries in an iterative manner. The MDL (minimum description length) principle (Rissanen, 1978; Barron et al., 1998) applied to SAR image segmentation (Galland et al., 2003) is very fast, and MDL automatically establishes a balance between over-segmentation (implying a unnecessarily long description of the segmentation) and under-segmentation (implying unnecessarily complex descriptions of the radiometry inside the regions). An example of a segmentation result obtained on a simulated KaRIn image with this method is shown in Figure 6.6-1.

Global Methods

Another way to mitigate the speckle problem is to introduce spatial regularization into the classification algorithm through hidden Markov models. As opposed to the region-based methods, Markov random field (MRF) methods (Geman and Geman, 1984) do not consider the values of the neighboring pixels directly; rather, MRF methods consider the pixels’ (preliminary) class attribution, in an iterative energy minimization process that relates the local and global scales of the image. The optimal solution relies on simulated annealing, which is extremely time consuming; there are faster (but suboptimal) ways to realize MRF methods. Classification methods based on MRF, as well as two-dimensional extensions of Markov chain methods, have been developed specifically for SAR imagery (e.g., Kelly et al., 1988; Fjørtoft et al., 2003).

While the methods described above are well adapted to large water bodies, they may not detect narrow rivers, whose widths are only a few pixels. For these narrow structures, special methods can be applied. A method for detecting road networks in SAR images has been adapted to the problem of detection of narrow rivers in SWOT images (Cao et al., 2011). It features a low-level step to detect bright, linear structures in the image, followed by a high-level step based on Markov models that connects isolated segments into a network of rivers. An example of a result obtained with this method is given in Figure 6.6-2.

We see that this method extracts precisely the narrow rivers, which constitute the most challenging part of the detection problem; but, as expected, it misses larger lakes or wetlands. However, the latter can be extracted by a more general segmentation and classification algorithms such as the MDL method (Figure 6.6-1). Data fusion is then required to combine the intermediate or final results of the complementary methods, and possibly prior information, to obtain the overall water mask. Post-processing can be applied to remove isolated points and other kinds of outliers. Additional processing steps concerning the water mask include the computation of a triangular network representation and precise geolocalization.

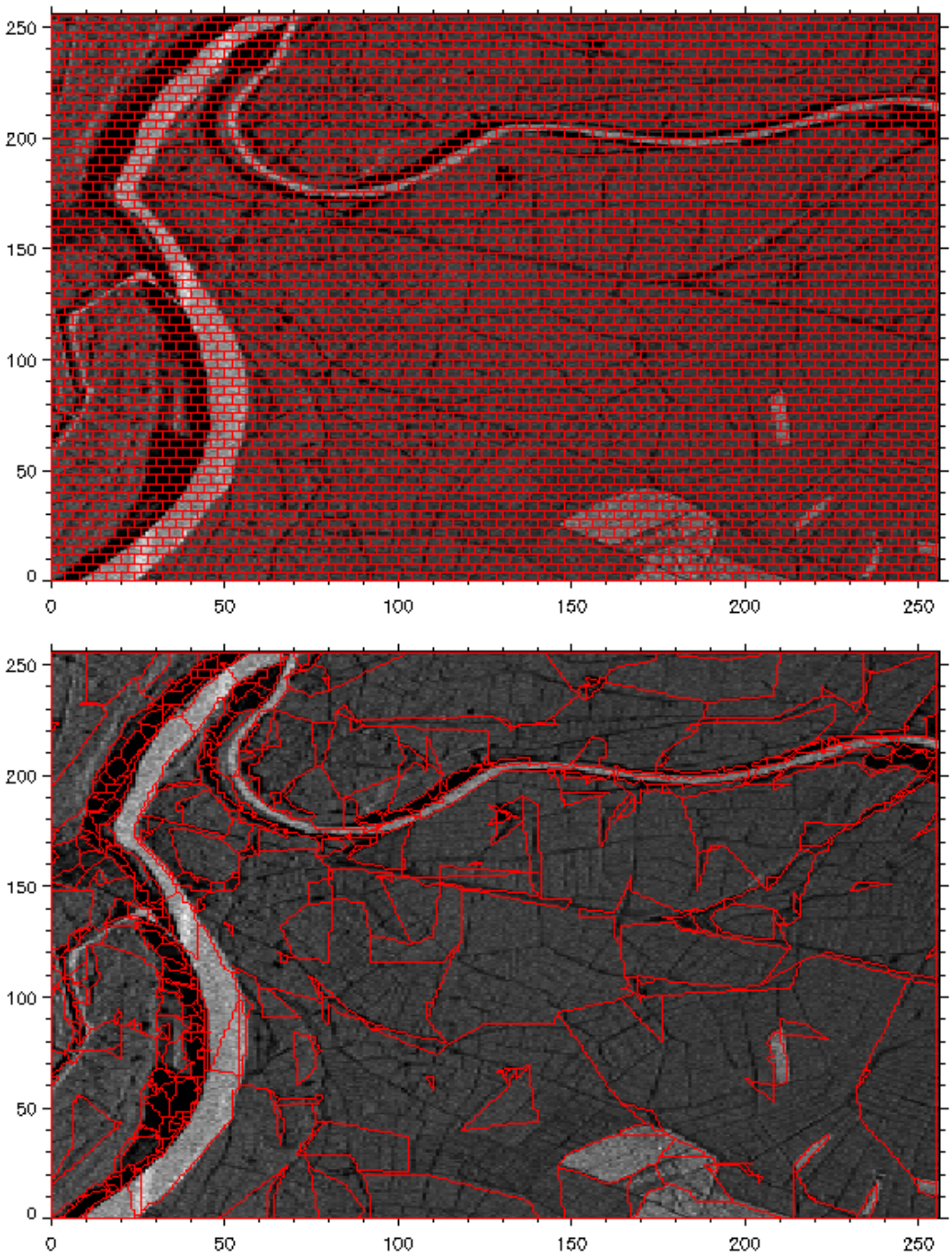

Figure 6.6-1. Example of result obtained with the MDL segmentation method (Galland et al., 2003) on an extract of a simulated KaRIn image (here shown multi-looked). Starting from an initial grid (upper panel), regions are merged and edge positions are refined in an iterative manner. The result (lower panel) is somewhat over-segmented, but the subsequent water/land classification will regroup regions belonging to the same class. This approach is not suited for the detection of narrow structures (small rivers).

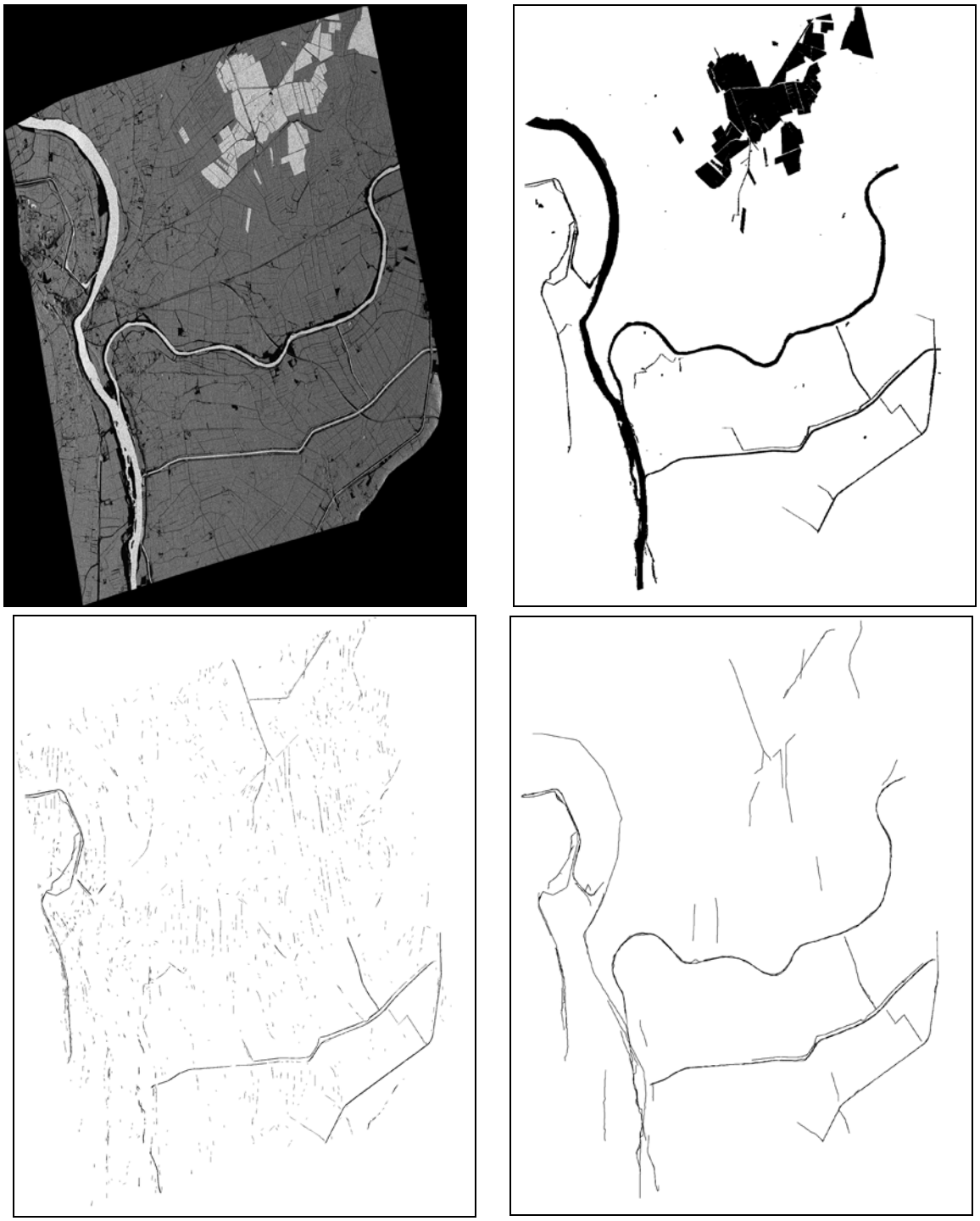

Figure 6.6-2. Example of result of detection of narrow water surfaces (Cao et al., 2011). Simulated KaRIn/SWOT amplitude image (upper panel, left), reference water mask (upper panel, right), result of low-level water detection step (lower panel, left), and result of high-level water detection step (lower panel, right).

6.6.3 Summary and Outlook

A wealth of image interpretation tools exists that can be used to optimize the detection and localization accuracy of the water mask derived from the KaRIn/SWOT images, within the limits of reasonable computational complexity and with the necessary robustness for fully automatic operation. Tests on simulated and airborne KaRIn images will allow us to identify the best combination of methods.

The scientific requirements also state that a flag should be provided for frozen surface water. This can be seen as an extension of the water/land classification problem (with an additional class), or it can be handled separately. The backscattering of frozen water surfaces is not well known, and experimental data are required.

References

Barron, A., J. Rissanen, and B. Yu, 1998: The Minimum Description Length Principle in Coding and Modeling. IEEE Trans. Information Theory, **44**(6).

Cao, F, F. Tupin, J.-M. Nicolas, R. Fjørtoft, and N. Pourthié, 2011: Extraction of water surfaces in simulated Ka-band SAR images of KaRIn on SWOT. Proc. IGARSS, Vancouver, Canada.

Cook, R., and I. Mc Connell, 1994: MUM (merge using moments) segmentation for SAR images. Proc. SAR Data Processing for Remote Sensing, Rome, Italy. SPIE, **2316**, 92-103.

Fjørtoft, R., A. Lopès, P. Marthon, and E. Cubero-Castan, 1998: An optimum multiedge detector for SAR image segmentation. IEEE Trans. Geosci. Remote Sensing, **36**(3), 793-802.

Fjørtoft, R., Y. Delignon, W. Pieczynski, M. Sigelle, and F. Tupin, 2003: Unsupervised Classification of Radar Images Using Hidden Markov Chains and Hidden Markov Random Fields. IEEE Trans. Geoscience and Remote Sensing, **41**(3), 675-686.

Galland, F., N. Bertaux, and P. Réfrégier, 2003: Minimum description length synthetic aperture radar image segmentation. IEEE Trans. Image Processing, **12**.

Geman, S., and D. Geman, 1984: Stochastic Relaxation, Gibbs Distribution, and the Bayesian Restoration of Images. IEEE Trans. Pattern Anal. Machine Intelligence, **6**, 721-741.

Germain, O., and P. Réfrégier, 2001: Statistical active grid for segmentation refinement. Pattern Recognition Letters, **22**, 1125-1132.

Kass, M., A. Witkin, and D. Terzopoulos, 1988: Snakes: Active contour models. Int. J. Computer Vision, **1**, 321-331.

Kelly, P. A., H. Derin, and K. D. Hartt, 1988: Adaptive Segmentation of Speckled Images Using a Hierarchical Random Field Model. IEEE Trans. Accoust. Speech Signal Proc., **36**(10).

Lopès A., R. Touzi, and E. Nezry, 1993: Structure detection and statistical adaptive speckle filtering, Int. J. of Remote Sensing, **14**(9), 1735-1758.

Oliver, C. J., I. Mc Connell, D. Blacknell, and R. G. White, 1996: Optimum edge detection in SAR. IEE Proc. Radar, Sonar and Navigation, **143**(1), 31–40.

Rissanen, J., 1978: Modeling by shortest data description. Automatica, **1,** 465-471.

Touzi, R., A. Lopès, and P. Bousquet, 1988: A statistical and geometrical edge detector for SAR images. IEEE Trans. Geosci. Remote Sensing, **26**(6), 764-773.

Zhu, S., T. Lee, and A. Yuille, 1995: Region competition: unifying snakes, region growing, and Bayes/MDL for multiband image segmentation. Proc. Int. Conf. Computer Vision, 416-423.

7 THE SWOT MISSION

The Surface Water and Ocean Topography (SWOT) mission has been recommended by the U.S. National Research Council decadal survey *Earth Science and Applications from Space: National Imperatives for the Next Decade and Beyond* for implementation by NASA. A partnership has been reached between NASA and CNES in developing the mission, based on the successful collaboration between the two agencies for more than two decades. Joint working groups in both science and engineering have been working on a preliminary design of the mission since 2007. A set of science goals and requirements has been established, leading to a preliminary configuration of the mission. The science goals are available in the SWOT Science Requirements Document at: http://swot.jpl.nasa.gov/files/SWOT_science_reqs_release2_v1.14.pdf.

7.1 Orbit and Sampling Issues

The orbit design of the SWOT mission is primarily driven by a trade-off between spatial and temporal sampling. As a starting point, we looked at orbits with a 15–25 day repeating ground track, an altitude of 800–1000 km, and an inclination of 70°–80°. We are choosing a lower altitude than TOPEX/Poseidon because we want to reduce mission costs. Sun-synchronous orbits were not considered due to the fact that all observations would occur at the same local solar time, and solar tide cycles would be heavily aliased. Requirements such as spatial coverage revisit times, tidal aliasing, and subcycle length (to enable multiple orbit mission phases) drove the selection of a 22-day repeat, 78° orbit.

7.1.1 Spatial Coverage

The orbital inclination determines and is equivalent to the maximum latitude sampled by the spacecraft. In order to cover the Arctic rivers, an inclination of greater than 70° is required. However, inclinations above 80° begin to have problems with tidal aliasing (see Section 6.3) and are above the region of greatest interest. A 78° orbit was chosen as a good compromise of coverage and aliasing qualities.

It is desired to cover as much of the surface of the globe as possible between the maximum latitudes. The longer the repeat period, the tighter the ground track spacing. At the equator, the ground tracks are at their greatest separation. The nominal SWOT swath width is approximately 120 km. Figure 7.1-1 illustrates how the equatorial coverage gaps diminish as the repeat length increases (blue line). At 22 days, the diamond-shaped gaps disappear for the nominal swath width. The magenta line shows the latitude above which there are no coverage gaps (up to the maximum latitude).

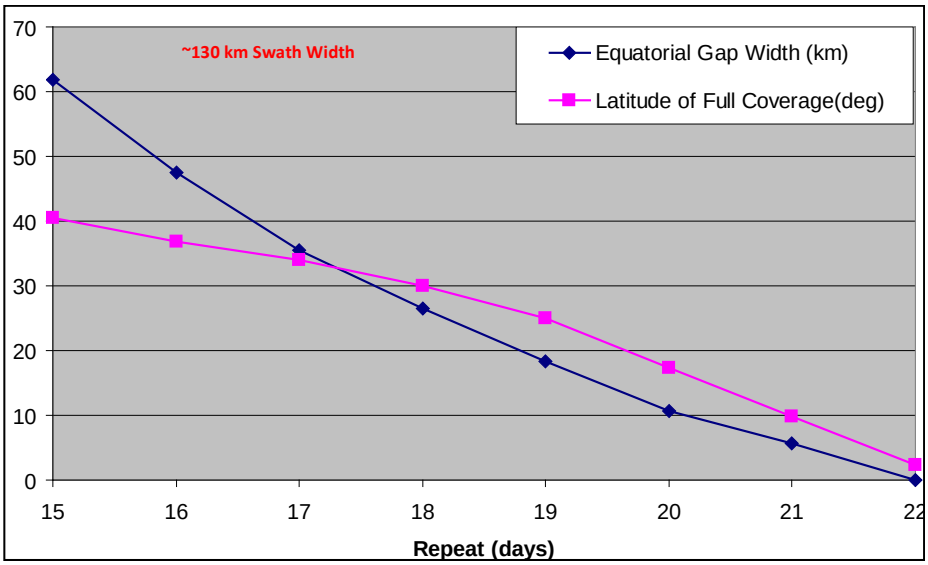

Figure 7.1-1. Equatorial coverage gaps versus orbit repeat period.

7.1.2 Temporal Sampling

The disadvantage of increasing the repeat period is the longer revisit time for a given location. For most areas near the equator, each specific point is observed twice per repeat cycle, once on the ascending pass and once on the descending pass. These passes are not spaced evenly, e.g. they can occur on days 1 and 12, 14 and 18, etc. For areas where the swath overlaps with a neighboring swath path (more and more likely as latitude increases), it is possible to have from 3 to 10+ observations per cycle. Again, the temporal separation of these observations is a statistical distribution depending on the specific location being observed.

In general, the number of observations per repeat cycle ranges from 2 to 4 near the equator, 3 to 6 for mid-latitudes, and 5 to 10+ for high latitudes. Figure 7.1-2 shows the Lena River region (high latitude), which is color-coded to show the number of observations/cycle. The diamond structures are created by the numerous orbit passes and illustrate the statistical distribution of revisit times.

7.1.3 Tidal Aliasing

Nonsynchronous repeating orbits do not repeat in an integer number of days, e.g., a "22-day" orbit actually repeats in 21.8635 solar days. The exact repeat length is determined by the altitude and inclination. This repeat length is what determines the tidal aliasing frequencies. Figure 7.1-3 shows the aliased frequencies of various tides versus the repeat period for a 78° orbit. The Xs show where the constituents do not have sufficient separation to be distinguished, or when they are aliased to long periods (<1 cpy). The result is that only the orbits with 15, 21, and 22 days were considered.

7.1.4 Subcycles and Mission Phases

Repeating orbits also have subcycles, which are determined by the way in which the ground tracks fill in. The length of the subcycle is the duration between neighboring passes in the ground track grid. It can be up to half the repeat period and must be coprime, i.e. it cannot be a factor of the repeat period.

The subcycle is important at higher latitudes where the swaths begin to overlap in that it sets a maximum for revisit time for most locations. This is illustrated in Figure 7.1-4. The upper plot shows a histogram of revisit times for the Lena River region shown in Figure 7.1-2. The orbit has a 3-day subcycle that is apparent by the spike at 72 hours. The lower plot is a cumulative distribution function of the revisit times in the first plot.

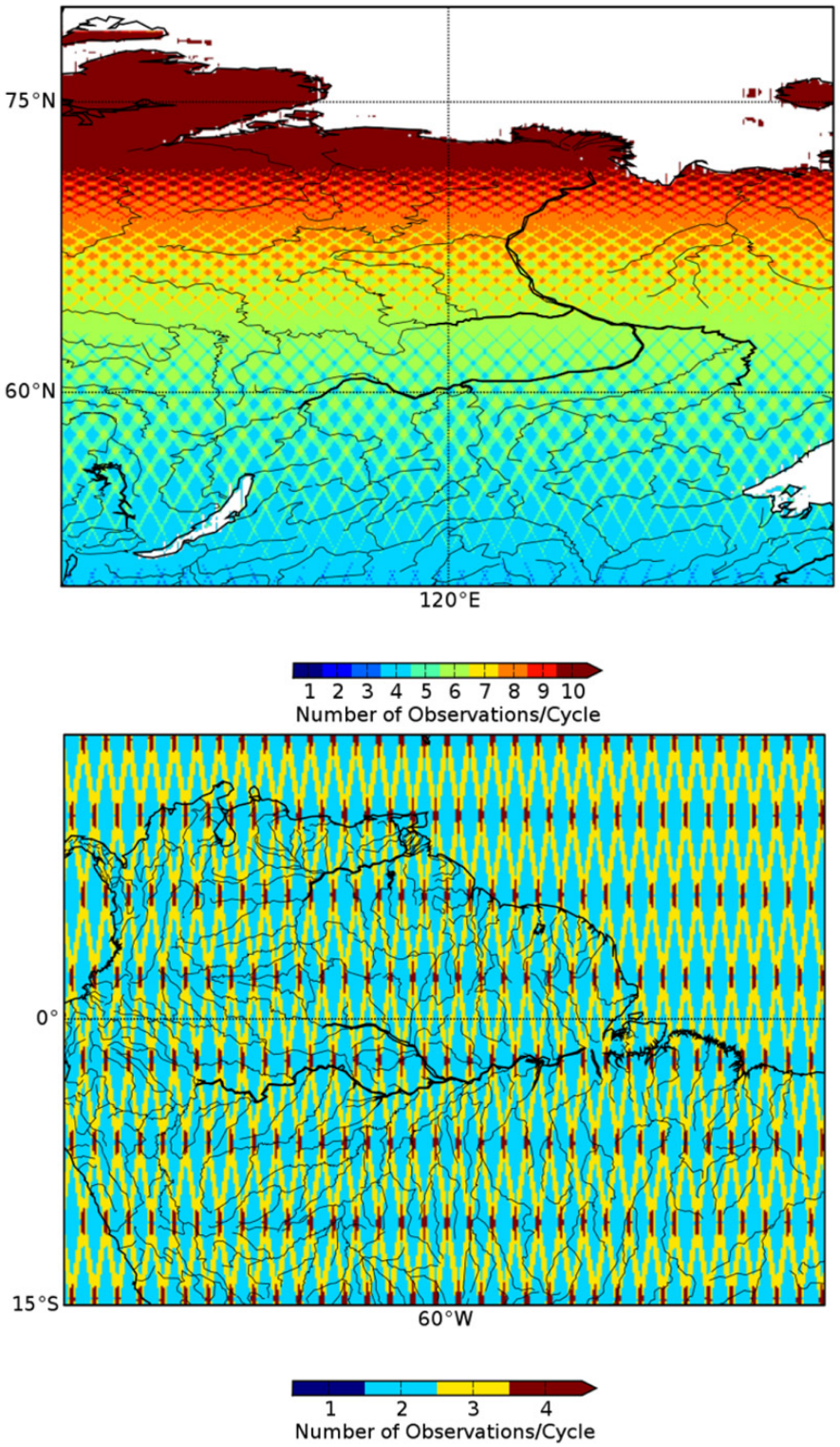

Figure 7.1-2. Number of observations versus locations for the 78° 22-day repeat nominal repeat orbit in the Lena River region (top) and in the Amazon region (bottom).

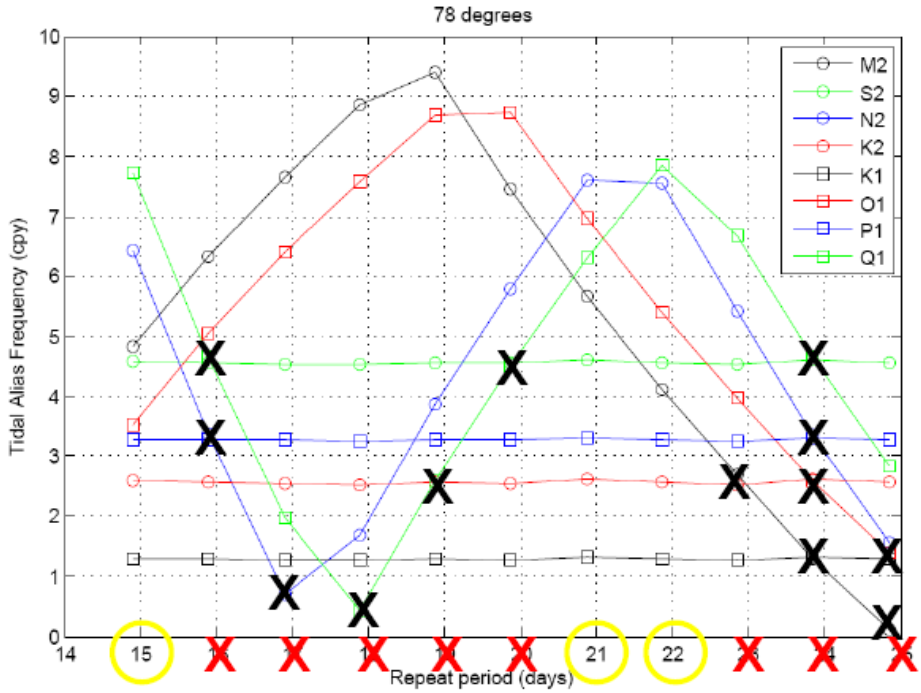

Figure 7.1-3. Orbit repeat period versus tidal aliasing frequency for the major ocean tides (78° inclination).

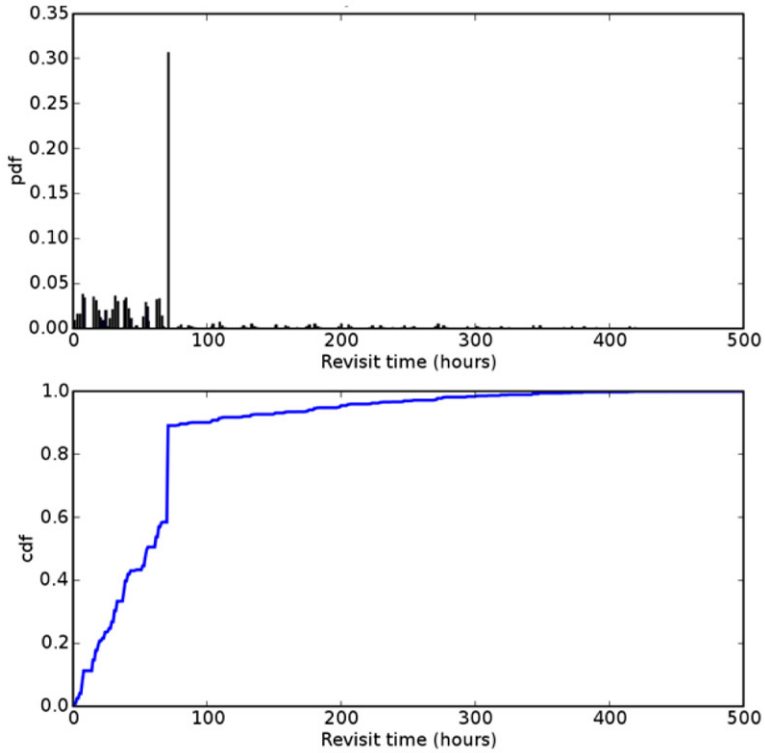

Figure 7.1-4**.** (Top) Histogram of revisit times for the Lena River region shown in Figure 7.1-2. (Bottom) Cumulative distribution function for the same data (bottom).

Another feature of an orbit with a given subcycle is that it is very close in altitude to the repeating orbit of the same length. This means that an orbit with a 3-day subcycle can maneuver to a 3-day repeat orbit with very little fuel (a few meters per second ΔV). The SWOT mission could have one phase with a fast revisit and poorer spatial coverage, then later move into another orbit with a longer repeat and full coverage with minimal fuel expenditure. With the same 78° inclination, it is also possible to select a 22-day repeat orbit that has a 1-day subcycle. There are two such possible orbits—one at 873 km and one at 842 km. Both have similar tidal aliasing characteristics to the 970-km orbit. These orbits provide the opportunity to maneuver into a very rapid sampling 1-day repeat, and the lower altitude would reduce the mission costs. Figure 7.1-5 compares the groundtrack coverage for the 3-day and 1-day repeat orbits.

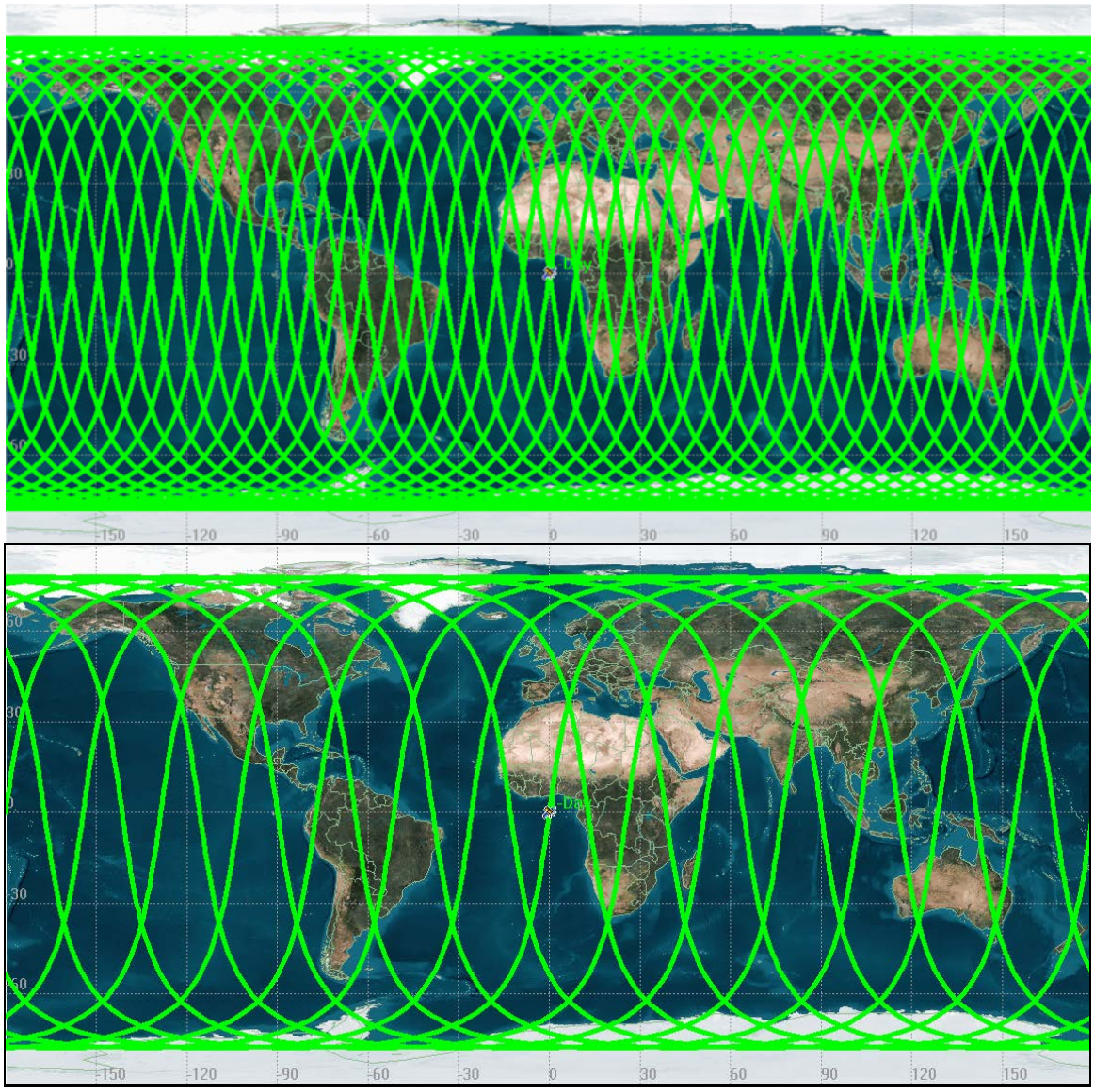

Figure 7.1-5. (Top) Groundtrack coverage for the 3-day repeat orbit and (bottom) the 1-day repeat orbit.

Due to the global coverage of the 22-day repeat orbit and the availability of a 3-day subcycle (as opposed to the 15- and 21-day orbits, which have 4-day subcycles), the 22-day orbit with a 78° inclination was selected as the nominal orbit. Orbits were generated using an oblate Earth model (J_2=1.0826E−3). A full-gravity model would change the altitudes by as much as to tens of meters. The computed mean orbital elements are shown in Table 7.1-1.

Table 7.1-1. Computed meal orbital elements for the nominal 22-day orbit with 78° inclination

a	i	e	ω	Ω	h
7348.7064 km	78°	0	0	0	970.5704 km

Repeat	Subcycle	Eq. Spacing	Eq. Spacing	rev./cyc.	Period
21.8635 d	3 days	133.1 km	1.20°	301	104.49 min

7.2 Precise Orbit Determination

The SWOT mission carries a requirement of 1.5 cm (rms) for the radial accuracy of the computed orbit (SWOT, 2009). This figure is based on current performance of the Jason-class missions (traditional nadir-pointing altimeter measurement systems). In fact, the best orbit solutions for Jason-2 are probably accurate to better than 1 cm in an rms radial sense (Bertiger et al., 2010; Cerri et al., 2010). The SWOT mission will carry similar payloads to support Precise Orbit Determination (POD): (1) a geodetic-quality Global Navigation Satellite Systems (GNSS) receiver, (2) a passive Laser Retro-reflector Array (LRA) to support precise ranging from ground-based laser observatories, and (3) a Doppler Orbitography and Radiopositioning Integrated by Satellite (DORIS) receiver to collect data from the French Doppler tracking system.

In view of the estimated 2019 launch date, the POD systems will have advanced significantly from the versions on Jason-2 (launched in 2008). Of particular note is the GNSS receiver, which is slated to be a Tri-GNSS (TriG)—the next-generation spaceborne receiver from JPL. While the legacy (BlackJack) receivers on the Jason satellites tracked only GPS signals, the TriG will also track transmissions from the European Galileo system and Russian Global Navigation Satellite System (GLONASS). The TriG is also designed to fully exploit the gradual emergence of modernized GPS signals (L5 and L2C) as the constellation is replenished. The ability to track multiple GNSS satellite signals—including the modernized GPS signals—will enable accurate and seamless POD throughout the transition to GPS-III and past the 2020 retirement of the legacy signals (Tien et al., 2010).

Even if the tracking capability of the SWOT GNSS receiver is equal to or better than the BlackJack receivers on the Jason missions, meeting the POD requirement of 1.5 cm cannot be ensured without first considering the impact of the spacecraft and orbit selections. While the Jason missions flew in a 1300-km altitude orbit, SWOT will be lower (970 km), which can exacerbate POD errors due to the higher air drag. In addition, the SWOT spacecraft form (Figure 7.2-1) is significantly more complex than its Jason counterparts. This is due to the accommodation of the KaRIn system, which employs a large reflect-array antenna assembly and which also necessitates larger solar panels for increased power needs. The greater complexity of the spacecraft implies a greater difficulty in modeling surface forces (such as air drag and solar radiation pressure), which depend on the size and properties of the various spacecraft surfaces exposed to the forcing mechanisms (e.g., sunlight, albedo, air particles). To address this, a simulation was performed using the JPL GNSS-Inferred Positioning System and Orbit Analysis Simulation Software (GIPSY) software (http://gipsy.jpl.nasa.gov) the same POD package that supports state-of-the-art (1-cm quality) GPS-based orbits for Jason-2 (Bertiger et al., 2010).

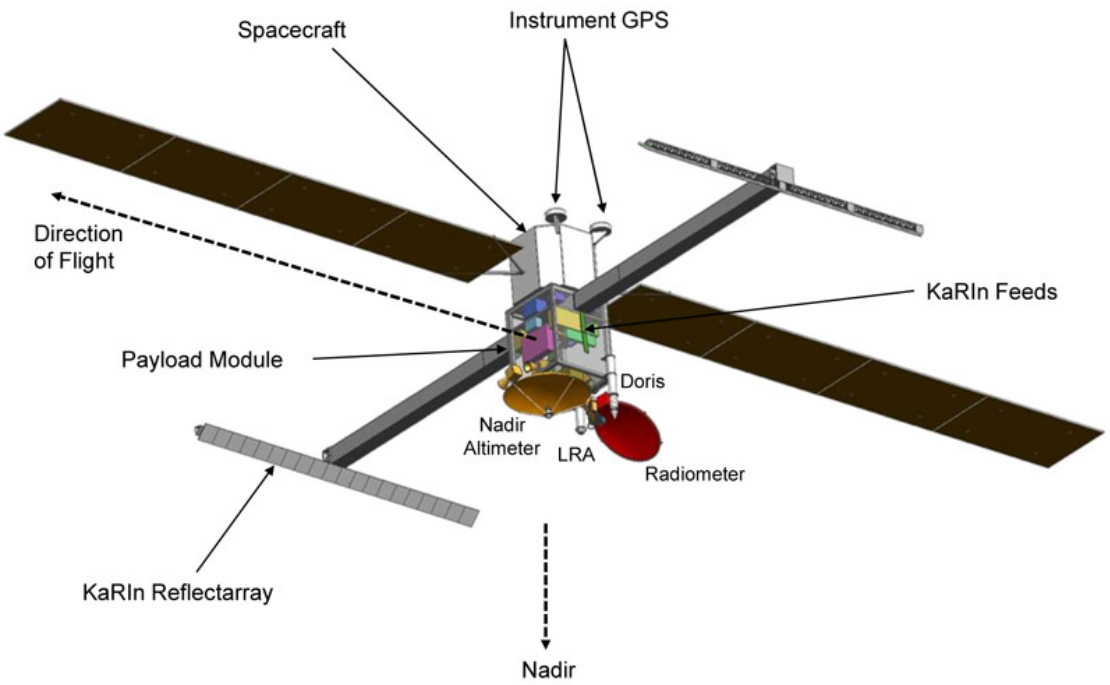

Figure 7.2-1. SWOT spacecraft: current design.

Compiled in Table 7.2-1 are the assumptions, including the SWOT orbit characteristics, used in the simulation study. For this exercise, a truth SWOT orbit is first generated using high-fidelity models of the forces underlying the satellite motion. A realistic custom model of the SWOT spacecraft is oriented using the Jason attitude model in order to integrate the surface forces (solar radiation pressure, drag, albedo). To ensure the assumptions for air drag are conservative, the atmospheric density was modeled using a highly active period (2001) for the 11-year solar cycle. (From the trough to peak of the solar cycle, air density at high altitudes can increase by orders of magnitude due primarily to heating from increased absorption of extreme ultraviolet radiation.) Additional (high-frequency) drag signal was added using information from the GRACE accelerometer. In particular, differences of the GRACE accelerometer data were taken with respect to accelerations from an atmospheric density model (DTM2000), and the residuals were scaled appropriately for the altitude of the satellite. Reference values for the GPS constellation (orbit ephemerides and clock offsets) were provided by (actual) definitive estimates from JPL, which are accurate to a few centimeters (Desai et al., 2009).

These truth models provide the framework for simulating GPS tracking observations. Both random (white) and systematic errors are added to the simulated data. The latter are intended to represent multipath errors, and are derived from actual pre-launch measurements of the antenna phase variations on the OSTM/Jason-2 flight antennas. The simulated tracking measurements are then filtered and smoothed in the presence of perturbed force and measurement models (Table 7.2-1); which correspond to a degraded set of assumptions. The perturbed models are selected so that the differences with their "truth" counterparts are proxies for the actual expected errors.

Table 7.2-1. Simulation assumptions for SWOT POD

SWOT Orbit Elements

a = 7348.137 km
e = 0.001 (near circular)
i = 78.0°
Ω = 51.123127°
ω = 68.70692°
M = 291.43694

Error Source	Truth Model	Perturbed Model
Custom spacecraft model	February 2010 Version of SWOT	—
Spacecraft mass	1278.5 kg	—
Atmospheric density	DTM94 driven by peak solar activity (2001)	DTM94 Shifted by 3 Days
Additional drag force	10% of GRACE accelerometer data residuals	None
Solar radiation pressure	GIPSY with custom spacecraft model	Estimate CR
Albedo	GIPSY with custom spacecraft model	None
Gravity	GRACE 120×120	GRACE 70×70
GPS spacecraft orbits and clock	Definitive JPL (Flinn)	Quick look JPL (next-day)
Spacecraft Attitude Law	Jason-2/OSTM	SA offset by 5°
Phase Multipath	OSTM pre-launch (anechoic) estimate	—
Phase Noise	1 cm (white)	—
Pseudorange Noise	1 m (white)	—

The results of the simulation indicate that radial orbit accuracies of 0.8 to 1.1 cm (rms) can be achieved, depending on the level of multipath. It should be noted that a significant fraction of the multipath can be estimated and removed using in-flight data (Haines et al., 2004). Of particular interest for SWOT—which is focused on the characterization of the ocean mesoscale—is the frequency content of the radial orbit error. Errors in POD tend to manifest at the satellite orbital harmonic (frequency of one cycle-per-revolution, or "1 cpr"), and the errors diminish substantially at higher frequencies. Figure 7.2-2 provides the frequency spectra of the errors in the simulated SWOT orbit, and confirms that errors at wavelengths of 1000–10000 km are very small (<<1 cm). A more robust simulation—incorporating, for example, time-variable gravity and short-wavelength multipath—could alter this conclusion somewhat. Orbit errors, however, are not expected to be limiting error sources for mesoscale monitoring. Future studies should also consider the impact of other modernized tracking data types [e.g., other GNSS constellations, DORIS, satellite laser ranging (SLR)], and should address the impact of station-keeping maneuvers that will be required to keep the satellite in its repeating orbit.

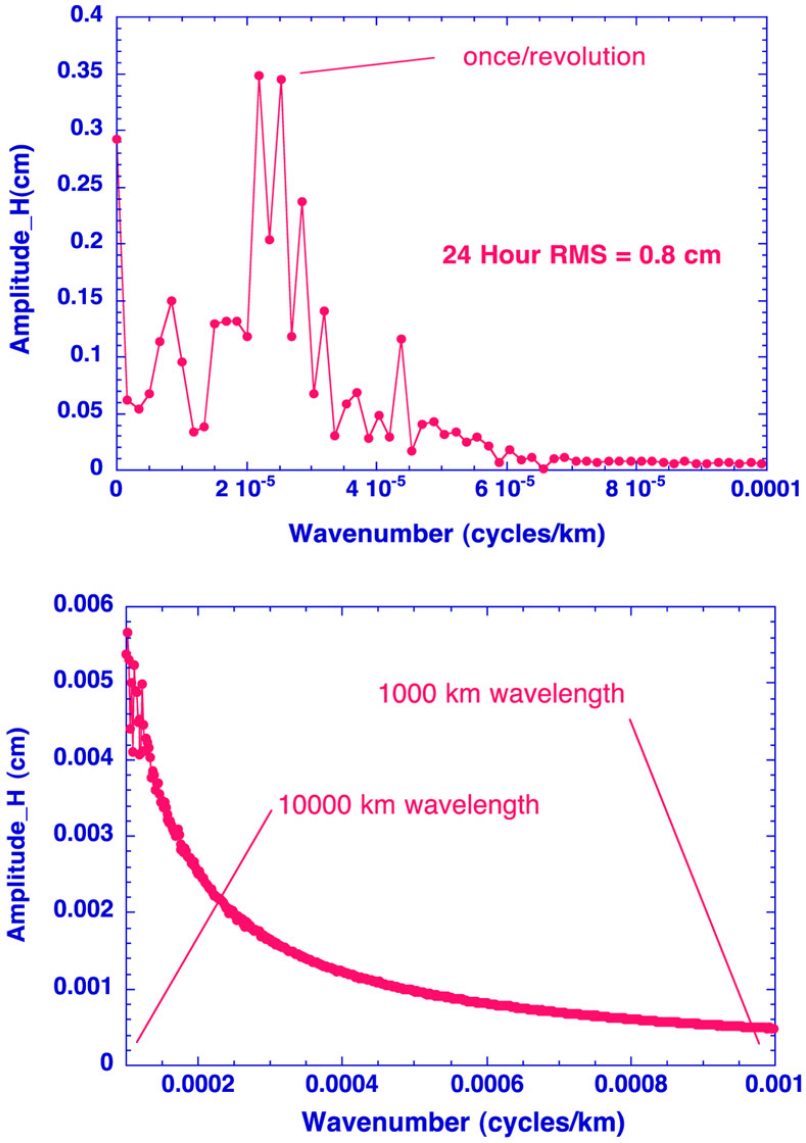

Figure 7.2-2. SWOT simulated radial orbit error spectra for long (>10000 km) and short (<10,000 km) wavelengths.

References

Bertiger, W., D. Desai, A. Dorsey, B. Haines, N. Harvey, D. Kuang, A. Sibthorpe, and J. Weiss, 2010: Sub-centimeter precision orbit determination with GPS for ocean altimetry. Marine Geodesy, **33**(1), 363–378.

Cerri, L., J. P. Berthias, W. I. Bertiger, B. J. Haines, F. G. Lemoine, F. Mercier, J. C. Ries, P. Willis, N. P. Zelensky, and M. Ziebart, 2010: Precision orbit determination standards for the Jason series of altimeter missions. Marine Geodesy, **33**(1), 379–418.

Desai, S., W. Bertiger, B. Haines, N. Harvey, D. Kuang, C. Lane, A. Sibthorpe, F. Webb, and J. Weiss, 2009: The JPL IGS Analysis Center: Results from the reanalysis of the

global GPS network. Eos Trans. AGU, **90**(52), Fall Meet. Suppl. Abstract G11B-0630.

Haines, B., Y. Bar-Sever, W. Bertiger, S. Desai, and P. Willis, 2004: One-centimeter orbit determination for Jason-1: New GPS-based strategies. Marine Geodesy, **27**(1–2), 299–318.

SWOT, 2009: Surface Water and Ocean Topography Mission Science Requirements Document. Initial Release (E. Rodriquez, Document Custodian). Also at http://swot.jpl.nasa.gov/files/SWOT_science_reqs_final.pdf. Last accessed December 31, 2011.

Tien, J., L. Young, T. Meehan, G. Franklin, K. Hurst, and S. Esterhuizen, 2010: Next Generation of Spaceborne GNSS Receiver for Radio Occultation Science and Precision Orbit Determination. Eos Trans. AGU, **91**(52), Fall Meet. Suppl. Abstract G51A-0661.

7.3 Science Payload

The SWOT satellite and payload configuration are shown in Figure 7.3-1.

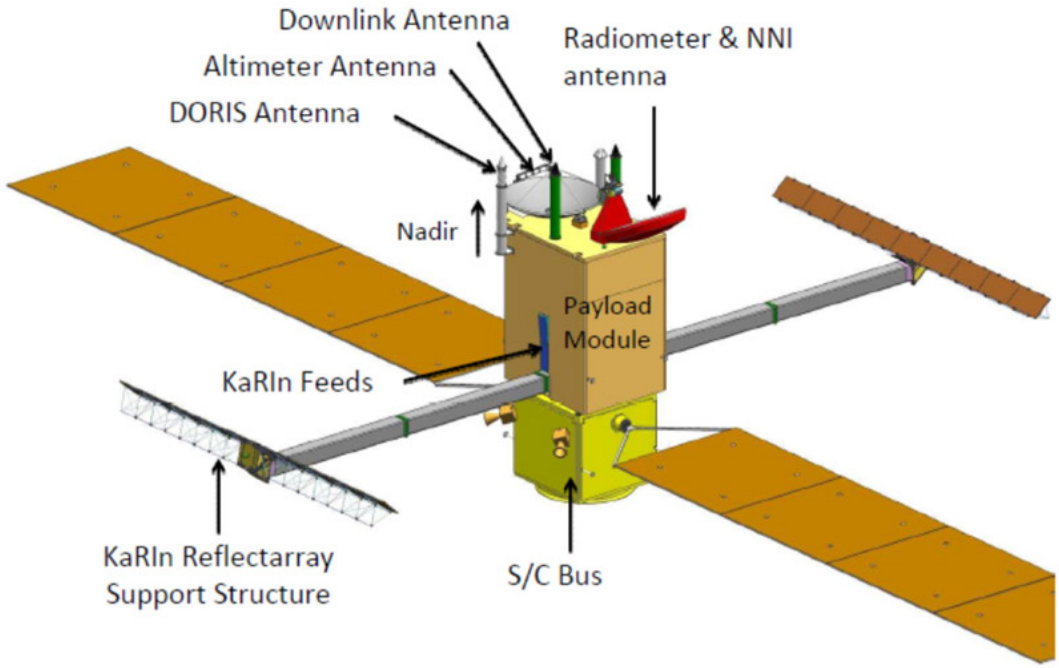

Figure 7.3-1. SWOT satellite and payload configuration.

7.3.1 Primary Payload

As dictated by the science requirements given in the SWOT Science Requirements Document http://swot.jpl.nasa.gov/files/SWOT_science_reqs_release2_v1.14.pdf, the mission's primary science payload consists of the following components:

- Ka-Band Interferometer (KaRIn): This is the primary instrument for measuring the elevation of water surface over two swaths; described in section 6.1.
- Dual-frequency radar altimeter: This is a conventional radar altimeter with performance similar to the Jason-class missions. It will operate at the Ku-band and C-band to retrieve signal delays in the ionosphere.
- Advanced microwave radiometer: This is based on the microwave radiometer flown on the Jason-class missions. It operates at 3 frequncies (18, 23, 34 GHz) for retrieving signal delays caused by the tropospheric water vapor along the nadir path.
- Precision orbit determination system: The system is similar to those flown on the Jason-class missions, consisting of a laser retroreflector, a DORIS receiver, and a GPS receiver.

7.3.2 Experimental Payload

To mitigate the data-void gaps between the nadir altimeter coverage and the KaRIn swath coverage, the science payload will include an experimental component to perform near-nadir interferometry (NNI) measurement. This measurement will be achieved by adding a Ka-band receiver for receiving KaRIn signals reflected from the near-nadir surface and performing interferometry between the nadir receiver and the KaRIn antennas.

To mitigate the errors from wet tropospheric range delays resulting from the cross-swath variability of water vapor, the science payload will evaluate the feasibility of adding additional feeds and receivers to the microwave radiometer system for measuring off-nadir water vapor signals.

7.4 Mission Operation and Data Products

The Mission System consists of the Ground System and Mission Operations System (MOS)—the systems, people, and procedures needed to operate the mission—and the Science Data System (SDS)—the development of the system for processing science data by MOS personnel. Following the commissioning phase (Launch + 30 days), remaining development personnel will be absorbed into the MOS to update and maintain the systems and procedures through calibration and validation (cal/val) and the remainder of the operations phase.

7.4.1 Mission Phases

The main Mission Phases with approximate durations are identified in Table 7.4-1. Note that cal/val and the Fast Repeat phase are not necessarily identical. The duration of these phases and their relationship will be worked out with the Science Team.

Table 7.4-1. Mission Phases and Durations

Phase	Duration	Comments
Launch and Early Orbit Operations	~3 days	Launch planned for late 2019
Checkout / Commissioning	~30 days	
Fast repeat orbit at 3 (or 1) days	for ~90 (or 30) days	For ocean submesoscale
Calibration (Cal)	~1 month, mainly during Fast Repeat orbit	Determine instrument parameters
Transition to Science Orbit, Operations	~15 days from the Fast Repeat orbit	
Validation (Val)	~8 months, covering Fast Repeat and early Science Operations	Determine geophysical parameters, update algorithms, validate data products
Science Observations	Requirement = 3 years; starts ~4.5 months after launch	
Disposal and Ground System Closeout	3 months	

7.4.2 Ground System

Figure 7.4-1 shows an overview of the Ground System during operations. The seven elements of the Ground System are described in the following sections. The elements are identified in Table 7.4-2.

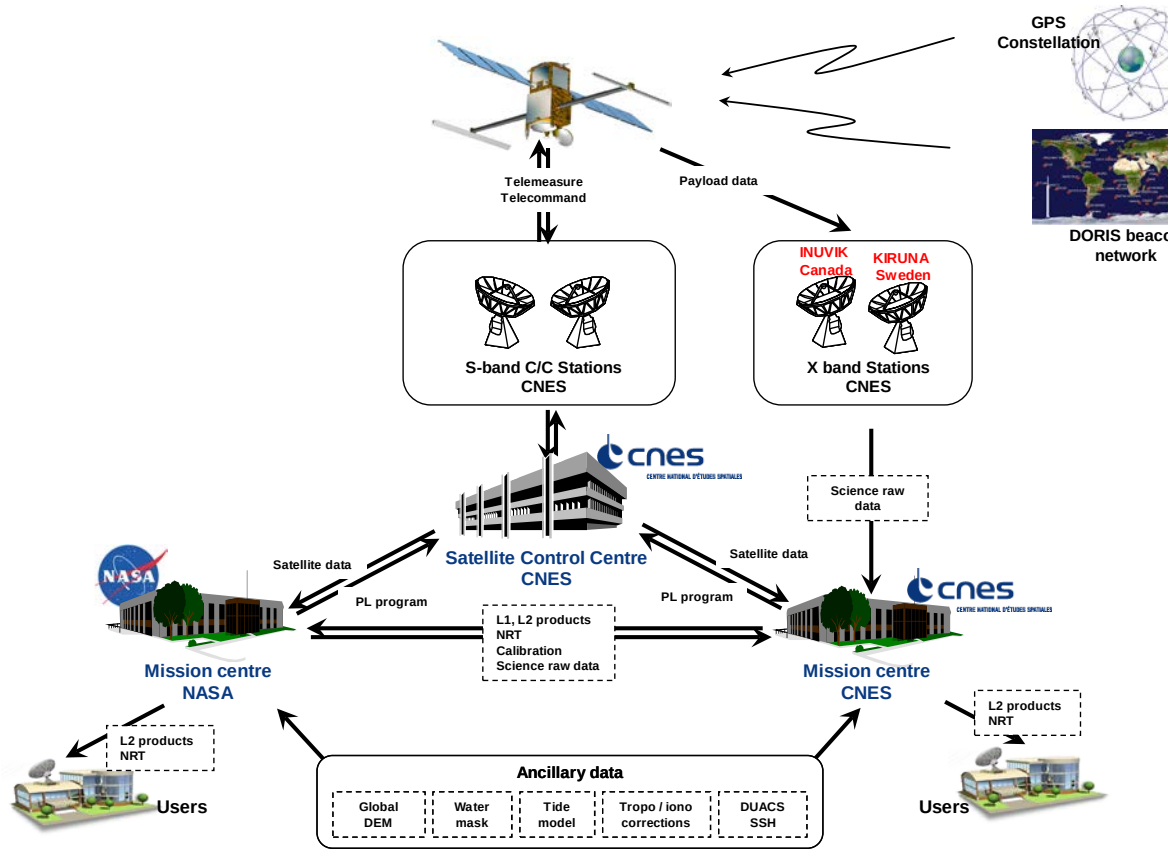

Figure 7.4-1. Overall Ground System architecture, including links to spacecraft.

7.4.2.1 Tracking Stations

CNES will provide the tracking assets with two of their stations: Kiruna, Sweden, and Inuvik, Canada. These CNES stations are co-located with facilities of the Swedish Space Corporation (SSC). A third station from the CNES X-band network will also be used to supply 2–3 passes per day to handle the full data volume.

All science data and related payload engineering (e.g., payload gyro) data downlink will be via X-band at 620 Mbps. Data will flow from CNES stations to the CNES Network Operations Center (in French named COR, Centre d'Operations du Reseau). The expected delivery time is within 24 hours of the completion of each pass. This requires a line rate from each station to the COR of >~45 Mbps.

Table 7.4-2. SWOT Ground System Elements

Element	Description
Tracking Stations	▪ CNES S-band stations: Downlink for spacecraft engineering. Uplink commanding. ▪ X-band stations (620 Mbps net data rate): Downlink for science and associated engineering data
Front End Networks	▪ Networks to/from CNES S-band stations to CNES (contractor) spacecraft operations center ▪ Networks from CNES X-band stations to X-band network center ▪ Network from CNES to/from JPL for S-band engineering data, payload commands ▪ Network from CNES X-band Data Center to JPL and CNES operation centers
Spacecraft Control Center (SCC, CNES spacecraft contractor)	▪ Real time monitoring of spacecraft and payload via S-band housekeeping telemetry
Payload Operations Centers (POC)	▪ JPL: Near Real Time health monitoring of KaRIn, GPS, Radiometer ▪ CNES: Near Real Time health monitoring of Jason Altimeter Suite
Science Processing Centers	▪ JPL: Processing of KaRIn and associated data, POD ▪ CNES: Processing of Jason Suite, POD
Data Archiving and Distribution Centers	▪ JPL: NASA-specified archive center (PO.DAAC) ▪ CNES: Aviso
Project Data Distribution Networks	▪ JPL-CNES link ▪ Science Processing Centers to Archiving/Distribution Centers

The KaRIn instrument acquires data at a very high rate for hydrology and other targets requiring fine resolution. In the high-rate mode, data are written to the payload solid state record (SSR) at a rate of 268 Mbps. The onboard-processed data that are used for the sea surface height of the ocean are written to the SSR at about 200 kbps. In order to get the data to the ground, a telemetry link of 620 Mbps is needed with at least one pass per revolution (rev). Analysis of coverage from available stations has been done and is summarized in Figure 7.4-2. The x-axis shows the percentage of high-rate data taking ("land") on average during a cycle. The y-axis shows the available margin for the downlink. A margin of zero means that data will begin to accumulate and quickly overfill the SSR. Using the longer pass on each rev over one of the two northern high-latitude

stations at Kiruna and Inuvik (Canada) allows high-rate data taking about 28% of the time, approximately equal to the land that the swath will cover in a cycle. The project needs to maintain a margin of 30% during the design phase; this limits high-rate data taking to about 22% of the time. This would not provide full coverage of the land, so a third station is needed. The CNES X-band network will have stations at Aussaguel (France) and Hartebeesthoek (South Africa) that will see the spacecraft several times a day. If the available passes from either of these stations are included, the 30% design margin can be obtained while taking about 25% (Aussaguel) or 27% (Hartebeesthoek) high-rate data, thus providing acceptable coverage of land in the swath.

As the project design matures, the remaining data margin (initially 30%) will be released to allow high-rate data taking the additional targets of interest ("synergistic science"). These targets may include coastal ocean and ice areas. The targets can be changed seasonally as the KaRIn data taking mask can be updated by ground command. The Science Team will choose the additional targets during the year or two before launch.

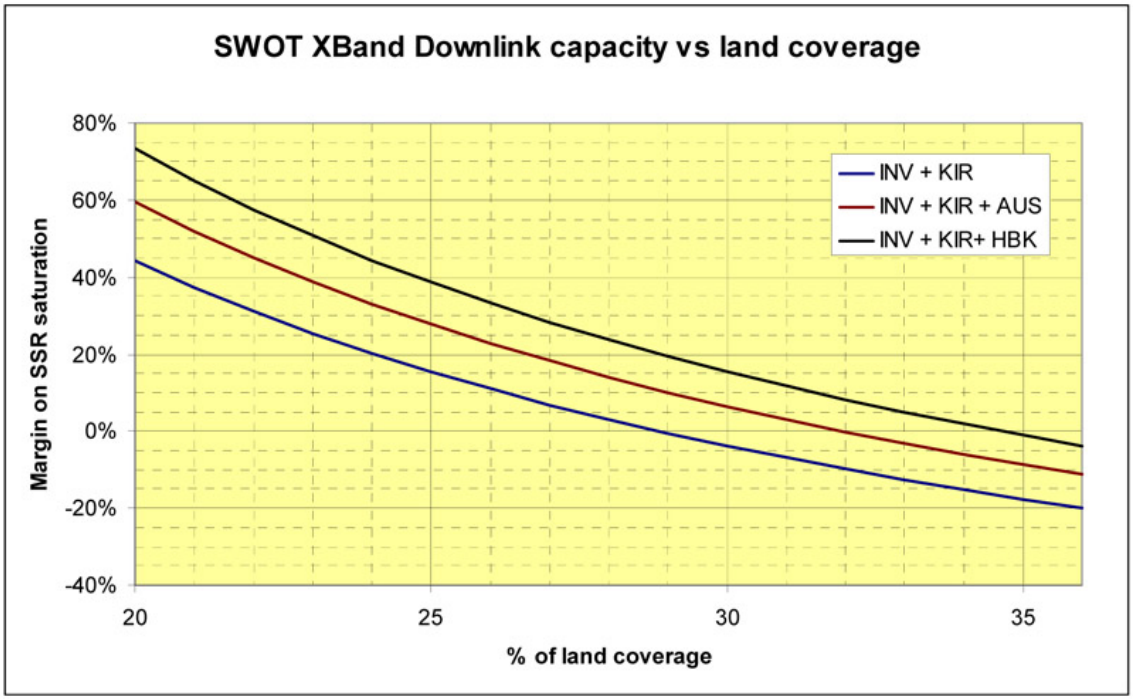

Figure 7.4-2. Downlink data margin as a function of high-rate data taking ("land") for three station configurations. INV = Inuvik, KIR = Kiruna, AUS = Aussaguel, HBK = Hartebeesthoek. A margin of 0% indicates that the SSR will overfill in a short time. Initially, the project will retain a 30% margin requiring three stations to acquire all the land data.

7.4.2.2 Front End Networks

See Figure 7.4-1.

- CNES S-band stations to CNES SCC
- CNES X-band telemetry to CNES COR
- Network from X-band Data Center(COR) to JPL
- CNES POC to JPL POC
    - To JPL: Jason Altimeter Suite; Engineering data
    - To CNES: JPL instrument commands for KaRIn, Radiometer, GPS

These networks will use a combination of private lines for sensitive data such as commands and low-rate engineering data and commercial services for high rate science (e.g., KaRIn) and processed data.

7.4.2.3 Spacecraft Operations Center

The SOC will be developed and operated for CNES by the spacecraft contractor.

7.4.2.4 Payload Operations Center

The Payload Operations Center (POC) will be the primary interface for information transfer between JPL and other parts of the project. All data transfers to/from CNES systems will go through the POC.

Tools and procedures to accept, ingest, and acknowledge data from external networks, e.g., telemetry data from CNES operations center, will be developed. These tools will be based on existing infrastructure and COTS (commercial off-the-shelf) software. The tools will be automated to provide 24/7 functionality with minimal operator intervention.

Tools and procedures to assess instrument performance from both housekeeping (HK) and science data will be developed based on instrument engineering tools. Out-of-limits conditions will be categorized as to the level of alarm, including at least two warning levels: yellow (moderate) and red (severe). Red alarms will automatically generate messages to operations personnel.

Tools and procedures to command the instrument will be developed based on instrument engineering tools.

7.4.2.5 Science Processing Center

Figure 7.4-3 shows the main processing elements in the Science Data System (SDS). Figure 7.4-4 shows an expanded view of the architecture of each of the processors within SDS using infrastructure like that used for other JPL Earth-orbiting missions.

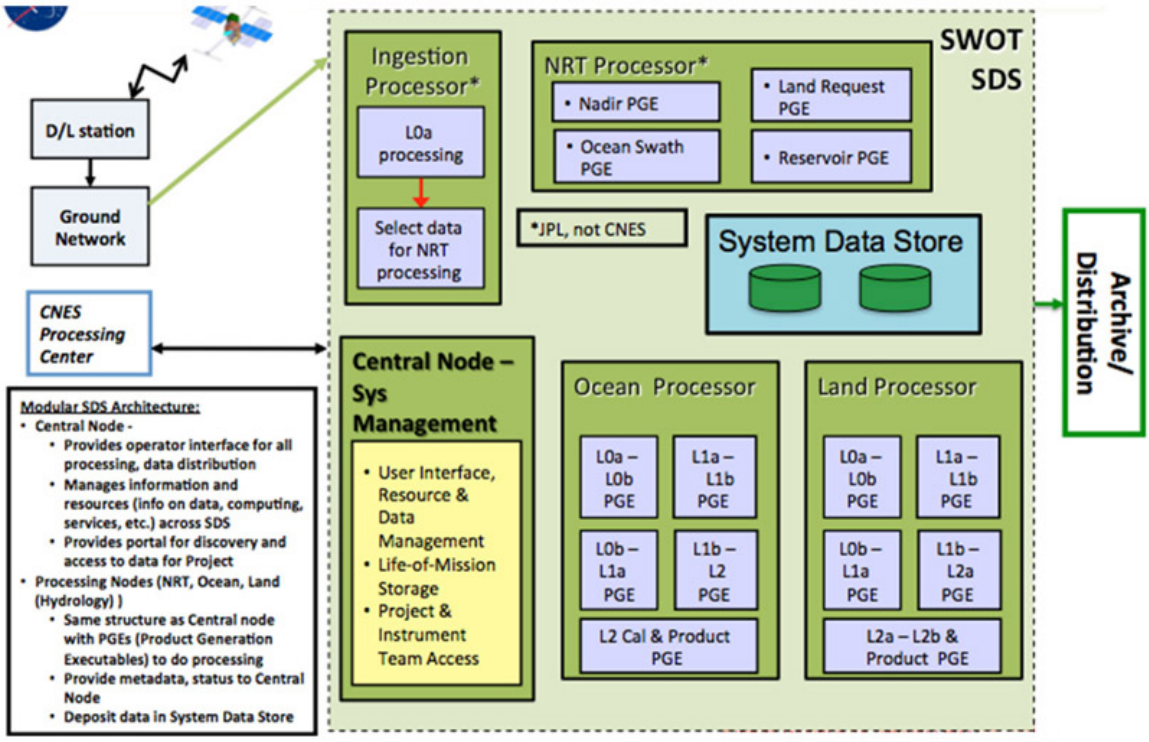

Figure 7.4-3. SDS Block Architecture: A view of SDS showing separate processors for different data types.

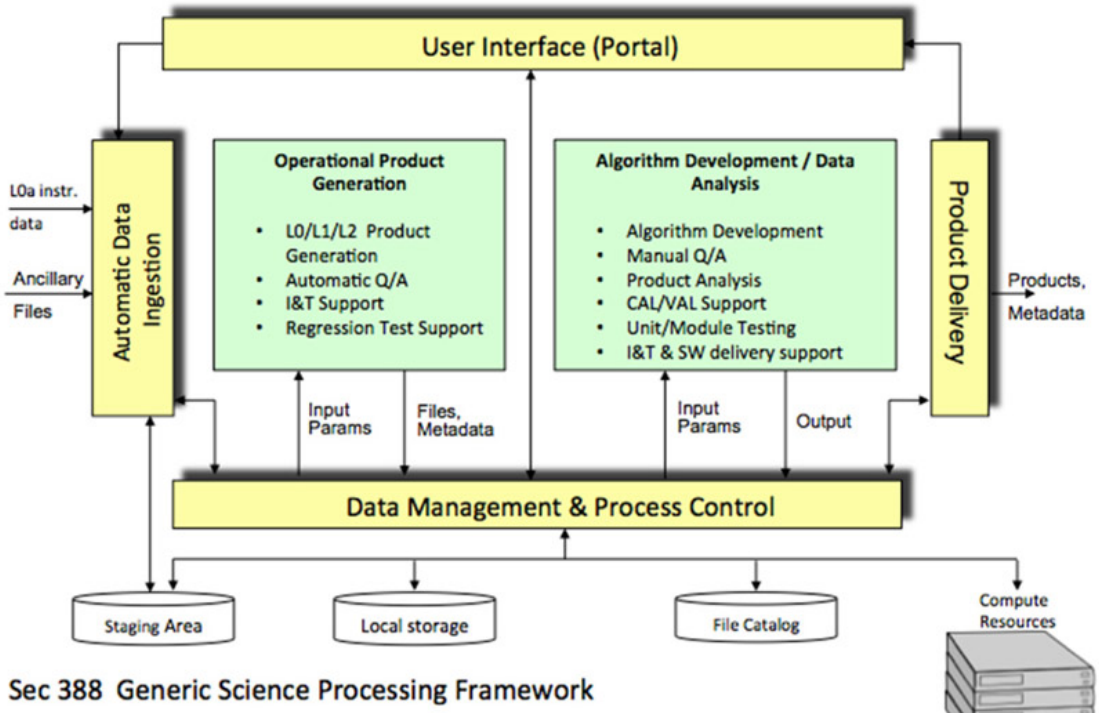

Figure 7.4-4. SDS Architecture based on well-developed infrastructure.

JPL will process all SWOT science data, except for the Jason-class nadir altimeter, which will be done by CNES. CNES will provide the nadir altimeter Level 2 data product (Sensor Geophysical Data Record , or SGDR) to JPL for use in KaRIn processing. It has not yet been determined how JPL and CNES will divide up development, processing, and reprocessing for other data, e.g., KaRIn.

Data go from SDS to CNES and to JPL's Physical Oceanography Distributed Active Archive Center (PO.DAAC) for distribution to science users. Project and selected Science Team members will have access to the SDS for data for cal/val purposes.

Technical Description

**** Preprocessing**

Some preprocessing will take place at the stations and/or the POC to determine data quality and to remove telemetry overhead. The POC will separate instrument engineering from the science data for the instrument analysis software running in the POC and will provide files of clean, merged telemetry packets (Level 0a). Preprocessing will produce files for each instrument separated by half revolution (pass).

Preprocessing will assemble time correlation data involving KaRIn, the spacecraft, and the ground stations to generate instrument time tags accurate to 10 microseconds to meet science requirements.

In addition to science data, several types of ancillary data are needed:

- Payload gyro data
- Spacecraft attitude data
- GPS data for POD
- Time correlation data
- Weather model data
- Ionosphere model data or parameters

**** Instrument Standard Level Processing**

The main processors of SDS are shown in Figure 7.4-3. The architecture of each processor will be based on infrastructure like that used for other JPL Earth-orbiting missions, as shown in Figure 7.4-4. Data ingestion and processing will largely be automated by the Data Management and Process Control module, but MOS teams can control processing through the user interface. The same architecture will be used for algorithm development to ensure a smooth transition to the operational system. The development system will also be used for special processing runs and data analysis during cal/val.

**** Precision Orbit Determination**

The JPL Precision Orbit Determination (POD) system will deliver POD products for KaRIn processing. POD will mainly rely on GPS data but will also be able to utilize DORIS and laser ranging data. Quality analysis of POD orbits will be a key part of POD processing. POD products will be delivered approximately ten days after data acquisition.

**** Jason Altimeter Suite**

CNES will process the Jason altimeter data, radiometer data, and orbit determination data to produce standard altimeter data products.

Operations Approach

The mission will downlink approximately 1 TB of data per day. The Science Data Processing Team of the MOS will operate the SDS. The POD Team will operate the Precision Orbit Determination System.

Key steps include:

- Science Data processed from Level 0a (L0a) to L0b (Preprocessing) as soon as received
- Engineering data extracted and used for instrument health assessment
- Ancillary Data from spacecraft, payload processed as soon as received
- External ancillary data delivery negotiated with providers
- Generation of products from L0b data will be keyed to the availability of POD
- Generation of Near–Real Time (NRT) products is TBD (within 24 hours of data receipt using predicted or quick look orbit)

7.4.2.6 Archive and Distribution Centers

Project teams will have direct access to data within the SDS. General distribution will be handled by PO.DAAC. The large volume of data will be a challenge requiring tools to automate the delivery of data and metadata to PO.DAAC. Data transfer will use common protocols and COTS software.

The Project will supply to PO.DAAC a tool for collecting surface water data pieces (“shards”) to provide useful sets of data for science investigations. Other subsetting and data packaging techniques, particularly for ocean data, will probably be necessary because of the large data volume. These tools will be the responsibility of PO.DAAC.

7.4.2.7 Data Distribution Networks

Exchange of various levels of data products between NASA and CNES will be essential to carrying out data processing and archiving and to support the Science Team. Science Processing Center data exchange will include:

- JPL to CNES: KaRIn L1, L2; POD; cal/val data
- CNES to JPL: Jason Suite L2; cal/val data

In addition, each Science Processing Center will need to exchange data with the archive centers. This will be the responsibility of the respective agencies.

The MOS SDS Science Data Team will handle data transfers. Data exchange between JPL and CNES Science Processing centers will likely require a line rate of about 1 Gbps, depending on details of the products. The high-volume data are processed science data, so security and uptime are not major drivers; therefore, it is expected that commercial lines can be used. An alternative is to install a processing system at CNES that can be used to generate products as needed.

7.4.3 Mission Operations System (Personnel)

The Mission Operations System consists of teams for

- Payload analysis and control
- Science data processing
- Precision Orbit Determination
- Science calibration and validation (cal/val) support

MOS teams will interface with their counterparts in CNES and its contractors to operate the payload and collect science data. Following On-Orbit Checkout, the SDS development personnel will move to the MOS to provide software, algorithm, and infrastructure support for the SDS throughout operations. The SDS personnel will also support the cal/val effort by updating the science processing and regenerating data products to support Science Team activities.

7.4.4 Data Products

Data will be processed through standard data levels in the Science Data System to Level 2b (L2b) data products to be delivered to Science Team members and Project teams for calibration and validation (cal/val). Additional information on processing algorithms is given in the next section. The main products will be

- SWOT Sea Surface Height (SSH) in swath
- SWOT surface water product

The standard L2b products will use the POD, which will be produced approximately 10 days after acquisition. L2b hydrology data will also need to wait for crossover calibration data to be available. Thus, the delivery time for fully calibrated products will be approximately 30 days. NRT products may be developed to support some oceanographic uses and for flood monitoring on land. Depending on timeliness requirements, NRT products will use a less accurate orbit and limited calibration data.

The SSH product will be processed from interferograms generated onboard. Several onboard interferograms will be combined before height determination. SSH will be produced on a fixed grid in alongtrack, cross-track coordinates at a posting of 500 m. (The actual resolution of the data will vary across the swath but is of the order of 1 km.) Each grid cell will have values for height, slope, backscatter (σ_0), significant wave height (SWH, goal), tides, and correction terms such as troposphere, ionosphere, sea state bias. Error estimates on values will also be provided. Cells will be flagged for the apparent presence of rain or ice contamination. Because the grid is fixed and in order to reduce data volume, cell locations and static geophysical fields, such as mean sea surface, will be provided in a reference track.

The surface water product is still under development. The product will be produced from high-rate (~262 Mbps) data over surface water areas. It is required to have 50 m posting, so it is not feasible to do a raster product over all the land. Rather, it will be in the form of triangular interpolated network (TIN) and derived shape files (see http://en.wikipedia.org/wiki/Shapefile and http://www.esri.com/library/whitepapers/pdfs/shapefile.pdf) that provide vector information outlining the water bodies. At each node of a water body location, height, backscatter, corrections (model-derived), and other quantities will be provided. Nodes will be flagged for the apparent presence of layover, rain, or ice contamination. A tool will be provided to collect the pieces of water bodies from multiple swaths over specified time period and geographic area (polygon) for further analysis.

A river discharge product will be produced with support from the Science Team. The Science Team will provide the parameters to implement Manning's equation. Delivery of this product will not start until approximately one year after launch, as a time series of data is needed to derive parameters for the discharge estimate.

Level 1b data [combined, corrected interferograms for ocean data; interferograms "flattened" to a reference DEM for high-rate (land) data] may be made available in limited quantities to Science Team members who request it for special studies. Because of the very large volume of these data, they will not be generally distributed and will not all be kept on-line for the whole mission.

Some characteristics of the principal data products are given in Table 7.4-3.

Additional available data downlink capacity will be used by "synergistic science," most likely coastal ocean or ice areas taken at high rate. Data products for these data types will be defined with the Science Team as the areas and investigations to be supported are defined.

Table 7.4-3. Data Products

Data Product	Products/ Day *	Product Size (GB)	Key Characteristics (Archived, unless otherwise noted)
L0b (Cleaned telemetry)	14	68.0	Telemetry separated by instrument, rev
L1a Ocean	28	0.11	Onboard interferograms
L1a High Rate	~40	~150	Single-look complex images for each swath
L1b Ocean	28	0.13	Combined onboard interferograms with corrections (Not archived)
L1b High Rate	~40	TBC [~100]	Phase flattened interferograms (Not archived)
L2b Nadir Altimeter	28	0.015	Jason-like SGDR produced by CNES
L2b Ocean	28	0. 12	Sea surface height in fixed swath grid
L2b Hydrology	~ 40 plus derived	TBD	Triangular height networks. Derived: Surface water shape files separated by continent, rev; discharge product

*14 = 1/rev, approximately 14 revs/day. Ocean products will be by pass (ascending/descending half revs, 28/day). Land products will be divided by continent, so each rev will have several products.

Additional long-term data products (e.g., a flood plain map) will be produced on annual or longer time scales. The Science Team will produce higher-level products (i.e., Level 3 averaged or gridded data and Level 4 data assimilated with geophysical models).

7.4.5 Algorithms

Data will be processed through standard data levels in the Science Data System to Level 2b (L2b) data products described above to be delivered to Science Team members and the data archive for general distribution.

7.4.5.1 Algorithm Development

JPL and CNES will form a joint algorithm development team. The team will follow these principles during algorithm development:

- Algorithm flow will be specified and iterated by the entire SDS development team
- Data product definitions will be iterated with Science Team
- Alternative algorithms for some data items may be developed and multiple values of the same geophysical quantity may be included in data products
- An algorithm testbed will be set up and prototype processing developed
- The Testbed will read and write the defined data products

- NRT processing will be based on standard algorithms but may not use the processing framework

After the initial development cycle, algorithm specifications will be written for review by the system engineering team and members of the Science Team. CNES and JPL may develop separate processing systems, but they will produce the same format data products with data items agreeing to within specified precisions.

7.4.5.2 Algorithms Needing Significant Science Team Input

A number of algorithms will need significant Science Team input for approaches and, in some cases, operational parameters or models. These algorithms and values include:

- Global DEM for phase unwrapping
- Global a priori water mask
- Wet Troposphere and Ionosphere over land: Model selection and possible other approaches
- Vegetation detection, correction: Approaches, parameters
- Snow, ice flagging: Approaches, parameters
- Mean Sea Surface, Geoid, Bathymetry models to include in SSH product
- Tide models to include in SSH product: Open ocean, internal
- Electromagnetic (EM) Bias: Models including variation across swath
- Wind Speed: Ka-band model function
- Discharge: Parameters for Manning's equation—nominal/a priori and solutions from data during mission
- Flood plain topography: Approaches, support of solutions

The discharge and flood plain products will require a large amount of science team effort not only during algorithm development but also during the first year of the mission. Data from six or more months of the mission will be needed in order to solve for the coefficients of Manning's equation in order to generate meaningful discharge values. The final flood plain product is required at the end of the mission, but developing an estimate from the first annual cycle of data will be important to interpreting all of the hydrology data. Science Team support will be important to completing this effort.

7.4.5.3 Algorithm Flow for KaRIn Processing

**** Ocean Data**

Ocean data will be processed onboard to sets of interferograms. Additional processing on the ground will include:

(1) Computation of phase center position, attitude, speed, acceleration

(2) Correction of phase errors based from spacecraft data and static models

(a) Attitude variations (roll, pitch, yaw)

(b) Baseline dilation (thermal models)

(c) Relative phase delays (loop-back + static calibration, systematic range curvature bias)

(d) Phase screen calibration (systematic distortions, for each azimuth look)

(e) Difference between onboard reference and mean sea level (tide free)

(3) High-frequency roll phase noise reduction (optional)

(4) Estimation of σ_0 and SNR

(5) Estimation of SWH (and its uncertainty) from coherence and SNR

(6) Detection of rain (low SNR), ice (method TBD), and insufficient coherence and plan to raise flags accordingly

(7) Estimation of geolocated heights and associated parameters, combination of looks (squint compensation, interpolation)

(8) Wind speed estimation based on σ_0 and geophysical model

(9) Geophysical corrections

(a) Ionosphere (altimeter and model)

(b) Dry troposphere (numerical weather model)

(c) Wet troposphere (radiometer)

(d) EM bias [SWH and wind speed (or σ_0)]

(e) Tidal corrections (barotropic and internal tides, solid Earth tide)

(f) Inverse barometer correction (NWP)

(10) Range bias estimation (SWOT Ku/C vs. KaRIn nadir ⇨ KaRIn range bias)

(11) Crossover calibration (intra-/inter-mission)

(a) Estimation of attitude errors and range bias at crossovers (mitigate ocean dynamics)

(b) Propagation of estimated attitudes between crossovers (using gyro data, knowledge of thermal snap regions)

(c) Tilt correction of heights based on estimated attitudes (alongtrack grid)

(12) Estimation of sea surface slope (local weighted fitting)

**** High Rate Hydrology Data**

The following steps give the basic land algorithm flow, not including calibration processing, to get triangularly interpolated networks (TINs) of water surface heights:

(1) Determine baseline phase centers, velocities, accelerations for each pulse.

(2) Do range compression, including loop-back calibration.

(3) Presum and do motion compensation.

(4) Do azimuth processing. Produce SLCs at highest spatial resolution. SLCs are the Level 1a product and form the basis for all subsequent processing.

(5) Form interferogram correcting for attitude variations, baseline dilation, relative phase delay (loop-back and static calibrations), phase screen (determined during Calibration phase).

(6) First-stage water mask detection from brightness, interferogram information (correlation, noise), and a priori information.

(7) Rain detection (σ_0 decrease).

(8) Snow, frozen water detection.

(9) Generate two reference interferograms for delta function and actual point target response (PTR) using reference orbit, nominal propagation corrections, and reference DEM.

(10) Identify layover regions (none, acceptable, unacceptable) using two reference interferograms.

(11) Adjust actual PTR reference interferogram to current track for use in unwrapping.

(12) Form differential interferogram between adjusted reference and data. Estimate residual phase corrections (phase bias, attitude errors, baseline dilation) from cross-track fit to residual phase.

(13) Use water mask to extract values from interferogram (data and reference) and image for water. Generate information needed for geolocation.

(14) Perform adaptive averaging on differential interferogram to reduce noise to allow for geolocation, checking of phase unwrapping. Estimate correlation (phase variance). Smooth image to allow for σ_0 estimation.

(15) Identify, correct phase unwrapping errors.

(16) Geolocate water data.

(17) Estimate height errors, σ_0.

(18) Apply geophysical corrections (ionosphere, wet and dry troposphere, tides) to correct height and location.

(19) Clean water body data by removing isolated data using a priori.

(20) Generate TIN of water data based on mask.

(21) Interpolate, smooth heights, errors, σ_0 to TIN vertices (to meet posting and performance requirements).

7.5 Calibration and Validation

7.5.1 Introduction

Although extensive testing and characterization of the SWOT payload will be performed prior to launch, experience with other spaceborne altimeters and interferometers has shown that certain instrument characteristics can only be determined to the desired precision after the instrument is deployed. The goal of the initial calibration phase, which will take place in the one to three months after instrument checkout, will be to determine these constants. After this initial calibration phase, the instrument will transition into a continuous calibration phase, designed to detect drifts in the instrument characteristics over the mission lifetime.

Concurrently with the calibration phase, SWOT will enter a payload performance validation phase. The goal of this validation phase will be to demonstrate that the SWOT payload core measurements (water level elevation random and systematic errors, signal-to-noise performance, data flagging) meet the requirements set in the Science Requirements Document.

An additional calibration and validation phase, which does not involve the core measurements, will concentrate on the global calibration/estimation of river bathymetry and roughness coefficient from the elevation and extent measurements. The purpose of this additional calibration is to enable the production of the SWOT discharge product. This calibration phase, and its associated validation, will occur during the first year of operation. A final calibration and validation of the bathymetry and roughness will occur after the end of the nominal mission, enabling the production of the optimal nominal mission discharge product. The calibration and validation approaches for this phase are still under active development, and are discussed to some degree in section 4.

Additional validation efforts will be required to validate the quality of the floodplain topography map. However, since this product is only available towards the end of the nominal mission, it will not be addressed specifically here.

In section 7.5.2, we review the parameters that need to be calibrated in the altimeter/interferometer system. In section 7.5.3, we present the special requirements of the SWOT mission that led us to the selection of a special temporal sampling phase for the orbit, onboard calibration modes, and to the development of an airborne platform, AirSWOT, to provide a capability for both calibration and validation of SWOT during the mission. Section 7.5.4 presents the calibration strategy for each of the SWOT parameters, while the last section does the same thing for the SWOT validation.

7.5.2 Calibration and Validation Parameters

In order to obtain an elevation from interferometry, one must know the absolute range between a nominal point (e.g., the baseline center) and the center of the pixel to be imaged; any biases in the position of the nominal point; the relative range difference between the two channels; any phase biases between the two interferometric channels; and the baseline length and the orientation of the baseline.

One can associate a parameter to be calibrated, either before or after launch, for each of these parameters, as follows:

- Common Range Delay: This is the average of the range bias between the two channels, and is caused by delays in the instrument that could not be calibrated prior to launch. It is the equivalent of the nadir range bias.
- Differential Range Delay: This is the difference between the two channels. Its main effect will be to cause the two channels to be misregistered, leading to a loss of correlation and a phase bias.
- Static Differential Phase: This is any residual phase between the two channels that is static or varying very slowly (on the scale of month or years). It should not be confused with the instantaneous channel-to-channel phase that can vary due to the changes in temperature or mechanical dilations between channels.
- Static Roll Angle: This is any error in knowledge of the baseline and antenna orientation after space deployment. As with the previous parameter, we only calibrate the static part and recognize that additional roll errors will be present due to uncertainties in the Inertial Motion Unit (IMU) roll estimation. In practice, one cannot differentiate between static roll and static phase biases, and an effective roll (or effective phase) will be the only parameter estimated.
- Baseline Length: This parameter will nominally not be calibrated since it will be known to sufficient accuracy prior to deployment. However, static baseline errors are calibrated as part of the phase screen correction, described below, since they effectively introduce a constant cross-track slope in the phase.
- Reference Point Location: The effect of location errors for the reference point in the nadir direction is (nearly) identical to a common range delay, and will be incorporated into that parameter. Errors in location in the orthogonal plane will lead to geolocation errors. It is assumed that the cross-plane location of the reference point will be known to sufficient accuracy (<10 cm), so that the effect on absolute geolocation can be neglected.
- Phase Screen: Experience has shown that it is impossible in practice to match exactly the far-field phase of both antennas. Differences in the phase far-field pattern, which may be caused by interaction with the baseline and spacecraft structures, will result in phase differences between the channels that vary as a function of look angle, or, equivalently, absolute phase. Unlike the other parameters, the phase screen is not a single value, but a continuous function that

must be estimated across the entire swath. It has never been calibrated prior to deployment.

- Absolute System Gain: Although not strictly necessary for interferometry, the absolute gain of the system is desirable if one wants to relate the wind model function derived by SWOT to that derived by other systems. However, if the model function is derived from SWOT data alone, there is no need for absolute gain calibration.
- Swath-to-Swath Gain Calibration: Although each swath has a different polarization, the restricted set of near-nadir incidence angles implies that a single wind model function will be sufficient for both swaths. In order for this to be the case, the gain in both channels will have to be relatively calibrated.
- Antenna Pattern Relative Gain: Again, this is not required for interferometry, but is required for the estimation of mean squared slope from the decay of the cross section as a function of angle. It will be assumed that both antennas are matched sufficiently prior to launch so that this calibration is not necessary.

The nadir altimeter, on the other hand, is a simpler instrument and for the purposes of SWOT, only the altimeter range bias needs to be calibrated against a reference constellation of altimeters and against the KaRIn interferometer range bias.

The science requirements impose an elevation error accuracy that is defined in the spectral domain. This should be contrasted to the traditional altimeter requirements, where the total error integrated over all scales is specified. In practice, this difference will mean that the validation of the SWOT measurements must be done over an extended test site. This is in contrast to the altimeter, where point test sites (Point Conception, Lampedusa) were sufficient to provide a complete validation of the measurement error budget.

Another difference with traditional altimetry is that a water body extent requirement must also be validated for fresh water bodies. In order to perform this validation, independent and simultaneous determination of water extent must be performed during performance validation.

In addition to the validation of the error budget, the performance of the onboard processor must also be validated and shown to be equivalent to ground processing with an equivalent algorithm.

7.5.3 Special Provisions for Calibration and Validation

The SWOT project has made special provisions to enable the speedy calibration and validation of the instrument performance. These provisions are discussed below.

Phase Calibration Loop and Four-Channel Raw Data Download

By implementing a calibration loop that measures the phase for a significant fraction of the transmit and receive paths for each channel, the bulk of channel phase imbalances,

including all the active RF components, can be accounted for operationally. This calibration loop will significantly reduce the need for the independent calibration of channel-to-channel phase and delay variations. However, the phase calibration loop cannot include the feeds, antennas, or some of the passive elements that may introduce phase imbalance. Since the uncalibrated paths are not active, calibration of static phase and delay differences between the channels should be sufficient to calibrate the paths not included in the phase loop.

In addition, there are provisions for downloading the raw returns from all channels for subsets of the data. For nominal operations, only the returns from two channels (those that transmit and receive from the same antenna) are required for the estimation of elevation. However, the additional two additional channels (transmit from one antenna, receive on the other) can be used to form a “zero-baseline” case, where the phase signal from the ground cancels, and only system effects remain. These data will provide useful information for the independent validation of the phase calibration loop.

Fast Sampling Phase

The calibration of static parameters in the presence of noise and varying parameters will require averaging over multiple observations. For the nominal mission orbit, any given calibration site will be visited on average once every 11 days. Acquiring sufficient number of samples for calibration will require a delay of the nominal mission data flow, since data processing for science products requires that the calibration variables be available. (Notice that the data collected during the calibration phase will, in all likelihood, still be valid for making science data products after the calibration constants are determined.)

In order to expedite the calibration and error budget validation phases, the project has chosen to start the mission with a fast sampling phase that will significantly speed up the acquisition of the calibration of the instrument and its performance validation. This fast sampling phase is achieved by changing the orbit altitude slightly so that the orbit transitions to one of its subcycles. Figure 4-13 shows sample coverage for the two fast sampling orbits currently being considered by the project. These orbits achieve repeat times of 1 or 3 days, potentially enabling the calibration phase to be accomplished somewhere between 10 to 4 times faster than the nominal mission scenario.

The fast sampling phase also allows the investigation of phenomena occurring at time scales smaller than the nominal mission sampling, which will benefit the determination of ocean submesoscale decorrelation times, and the synoptic study of flood wave propagation, among others. Unfortunately, as is evident from Figure 7.5-1, the fast sampling can only be achieved at the cost of poor spatial sampling, and minimizing the calibration time to transition to the nominal mission phase will be an important consideration.

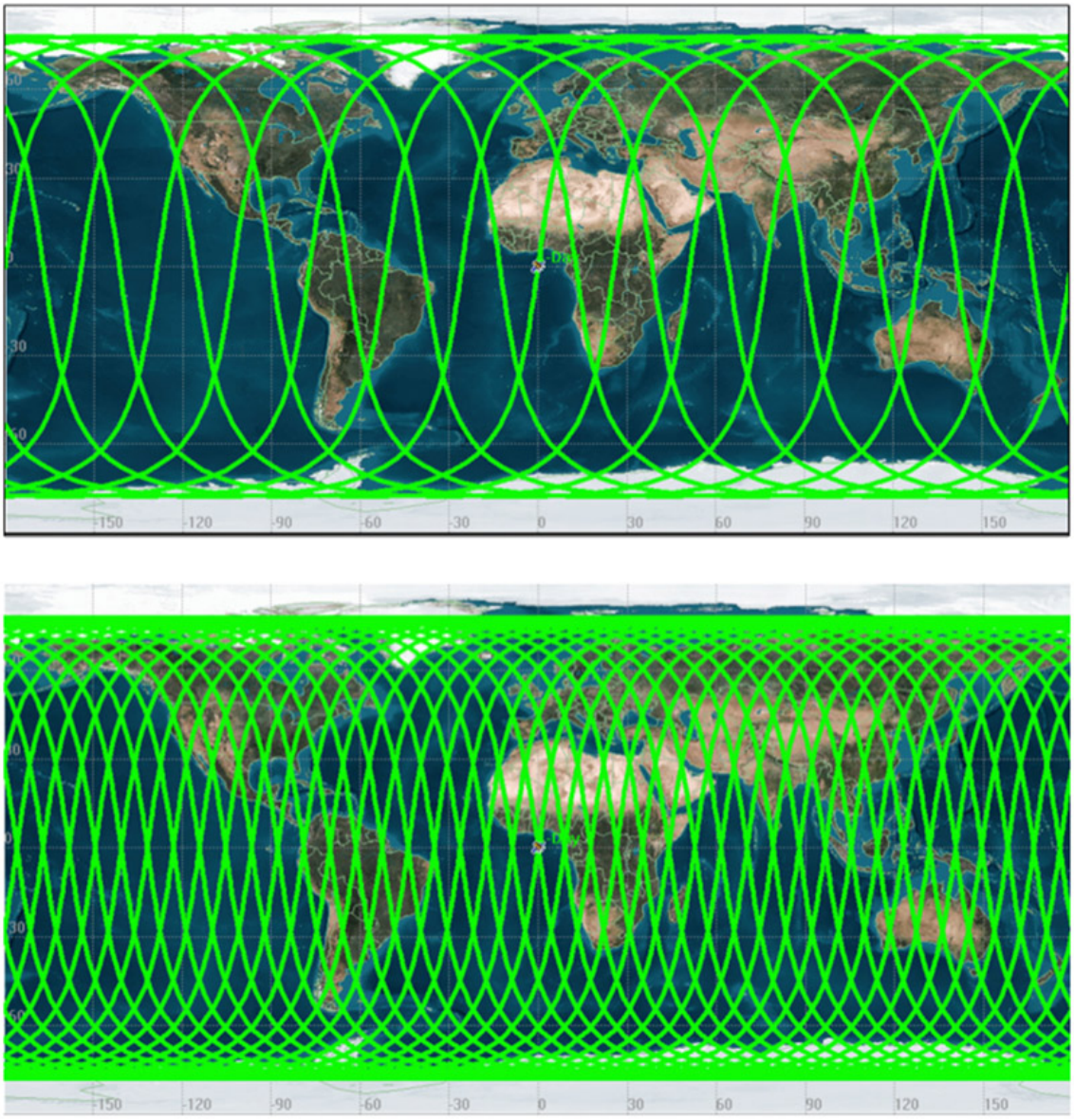

Figure 7.5-1. Ground track configuration for a 1-day (upper panel) or a 3-day (lower panel) repeat orbit for the SWOT fast sampling phase. (Courtesy of S. Nerem, Colorado State University)

AirSWOT

The calibration of the phase screen and the validation of the elevation error spectrum over the entire swath will require SWOT-quality, or better, "truth" measurements over the entire swath. Furthermore, these measurements must be made over the ocean, potentially far from shore. In addition, validation must occur over extended areas for both ocean and land.

All of these requirements can only be met in a cost-efficient manner by using an airborne platform that is able to underfly SWOT at the time of SWOT data collection.

The SWOT project has sponsored the development of an airborne calibration/validation instrument under a NASA Small Business Innovation Research award [D. Moller, PI for Remote Sensing Solutions (RSS)]. The complete instrument payload, called AirSWOT, is currently being integrated and validated jointly by JPL and RSS under sponsorship of NASA's Earth Science and Technology Office (ESTO), and is expected to transition to the project for support of SWOT mission goals in the fall of 2012.

At the core of the AirSWOT payload is a Ka-band interferometric radar (Kaspar), whose main characteristics are given in Table 7.5-1. In essence, Kaspar provides a dual-swath interferometric system. The first swath, from nadir to 1 km, replicates the SWOT incidence angles and range resolution, and will be extremely useful for validating effects such as the variability of the water radar cross section, layover, and vegetation penetration effects. The second swath extends from 1 km to 5 km, and will be useful for extending the elevation measurements to a wider swath (although at a different set of incidence angles and a different range resolution). The random height errors achieved for both swaths are better than what can be achieved by SWOT by at least an order of magnitude.

In addition to a side-looking interferometer, the Kaspar signal from nadir can be processed as a conventional pulse-limited SAR altimeter, to achieve a nadir track of elevation measurements that are insensitive to aircraft roll. These measurements can then be used as cross-calibration to extend the effective AirSWOT swath by juxtaposing smaller 5-km swaths. Figure 7.5-2 illustrates this process.

To provide longer wavelength corrections and positioning, the AirSWOT package includes a state-of-the-art IMU, including a high-precision gyroscope coupled to a GPS receiver. Using this combination, it is possible to achieve an absolute positioning accuracy better than 5 cm (Krabill et al., 2002). Over scales less than 100 km, this error consists mainly of a constant bias and a slow drift, which is sufficient to meet the SWOT spectral requirements. To remove most of the residual bias and drift, AirSWOT can be flown under a conventional Jason-class altimeter.

Table 7.5-1. Kaspar on AirSWOT key system parameters. (Courtesy D. Moller and J. Carswell, Remote Sensing Solutions.).

Parameter		Value	Unit
Center Frequency		35.75	GHz
Peak Transmit Power		40	W
Platform Height		35	kft
Swath Coverage	Inner	0.2-1.4	km
	Outer	0.8-5.0	
Bandwidth	Inner	450	MHz
	Outer	80 to 225 (configurable)	
Incidence Angle Range	Inner	1-6	degrees
	Outer	4-25	
Noise Figure		6	dB

The final component of the AirSWOT payload is a near-infrared camera with pixel resolution <10 m and a swath on the same order as the AirSWOT swath. This camera can be used to validate the SWOT water body delineation measurements.

7.5.4 Calibration of the SWOT Parameters

In this section, we describe briefly how each of the AirSWOT parameters listed in section 7.5.2 is to be calibrated.

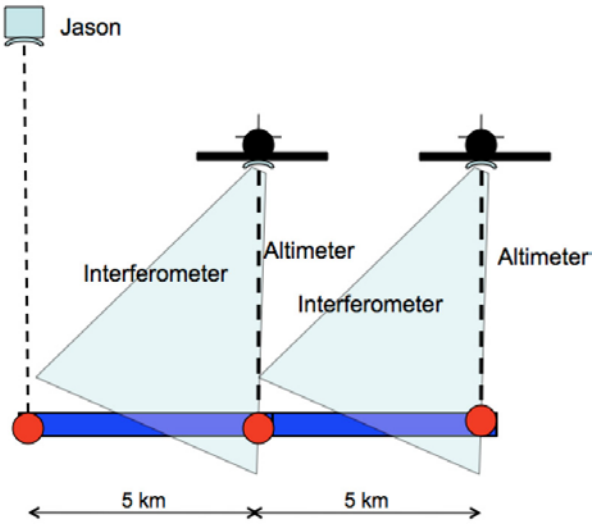

Figure 7.5-2. Conceptual scheme for AirSWOT altimeter calibration and juxtaposition of swaths. A Jason-class altimeter provides a ground track with high-accuracy elevations and high consistency over scales of 100 km. The first AirSWOT 5 km swath residual roll errors are corrected with this ground track; and a new, cross-calibrated nadir altimeter track is measured with the AirSWOT nadir altimeter. The process is iterated to achieve a wider effective swath.

Differential Range Delay

This is the simplest parameter to calibrate, as it can be done without the need of external data. The process to estimate the differential range delay is to perform range cross-correlation measurements between images of the ocean and to vary the relative range delay in the images until the cross-correlation is maximized. The accuracy for this process depends on the number of scenes used for cross-calibration, and the expected accuracy easily exceeds 1/100 of a range pixel. This technique was demonstrated in the calibration of SRTM (Farr et al., 2007).

Phase Screen

AirSWOT under-flights are the primary approach for estimating the phase screen. A 100 km by 140 km AirSWOT swath is built at the time of a SWOT overflight, and the resulting topography mosaic is interpolated to the SWOT alongtrack/cross-track swath coordinate system. The resulting topography is subtracted from the SWOT topography; and, for each alongtrack position, a constant bias and linear trend are removed. The estimated biases and trends are used, together with other data, as explained below, to estimate the static range and roll biases.

The residual topographic variations for each swath can be related to phase variations by means of the equation

$$\delta\phi \approx \frac{x\delta h}{2kB}$$

where δf is the residual phase, δh is the residual height, k is the electromagnetic wavenumber, B is the baseline length, and x is the cross-track distance. Notice that this equation does not depend on the alongtrack position, and one can average in the

alongtrack direction to reduce the random height noise. The subsequent profile is aggregated over multiple under-flights and the final average is fit with a Chebyshev polynomial of relatively low order, to protect against over-fitting. The resulting two functions (one per swath) constitute the interferometric, which is subsequently applied to both low-resolution ocean data and high-resolution land data.

This procedure is similar to the one used in SRTM (Farr et al., 2007), with the exception that, due to the higher precision requirements, AirSWOT data must be used instead of the mean sea surface used in SRTM. By using simultaneous under-flights, one also minimizes the effects of tropospheric delays, since they will be very similar for SWOT and AirSWOT. The temporal variability of the phase screen is not known; and, therefore, the phase screen will be validated, and updated, if required, several times during the nominal mission life.

At the end of the phase screen calibration experiments, one will also have an estimate of the static phase/roll angle bias for each swath. This estimate will be averaged to that obtained from the cross-over calibration described below.

Cross-Over Calibration for Static Phase/Roll Biases

While the AirSWOT under-flights will produce estimates of the static phase/roll bias, the accuracy of the estimates will be limited because we must average over dynamic roll errors that will be present simultaneously. Additional information regarding this bias can be used by assuming the ocean surface does not move significantly between ascending and descending passes at orbit cross-overs (see Figure 4-13 for a global distribution of cross-overs in the fast sampling phase) so that the interferometric phase/roll errors at the cross-over diamonds can be estimated from the KaRIn height differences (Fu and Rodriguez, 2004). (Note that to perform the phase/roll bias estimates, it is not necessary to use the nadir altimeter data.)

Since the KaRIn phase bias will be common between ascending and descending passes, it will cancel when calculating the cross-over differences. However, there will be some differences in the elevation measurements due to changes in the wet troposphere correction and the sea surface height. The tropospheric errors are partially mitigated by application of the radiometer correction, although some random cross-track variations may remain.

The contamination due to the evolution of the sea surface height is partially mitigated by using cross-overs during the fast sampling phase, when the time difference between ascending and descending passes will vary between less than one day to one or three days, depending on the fast sampling orbit chosen. To assess the impact of ocean motion, we use the high resolution ECCO-2 ocean model (see Menemenlis et al., 2008 for a review) of the North Atlantic to simulate the accuracy of phase/roll error retrieval. To obtain bounds for the problem of the effects of ocean motion, the retrieval accuracy is

estimated, including instrument errors but no surface motion, and assuming that the nominal SWOT 22-day orbit determines the cross-over revisit time. The results of this simulation for the residual height error after phase/roll error corrections are presented in Figure 7.5-3. Clearly, the biases can be retrieved with more than sufficient accuracy in the absence of ocean motion. Given the typical temporal correlation time of the ocean surface mesoscale circulation, which is on the order of 20 days (see, e.g., Le Traon et al., 1998), we expect the results from the fast sampling phase to closely match these results, especially if one stays away from areas of significant mesoscale activity.

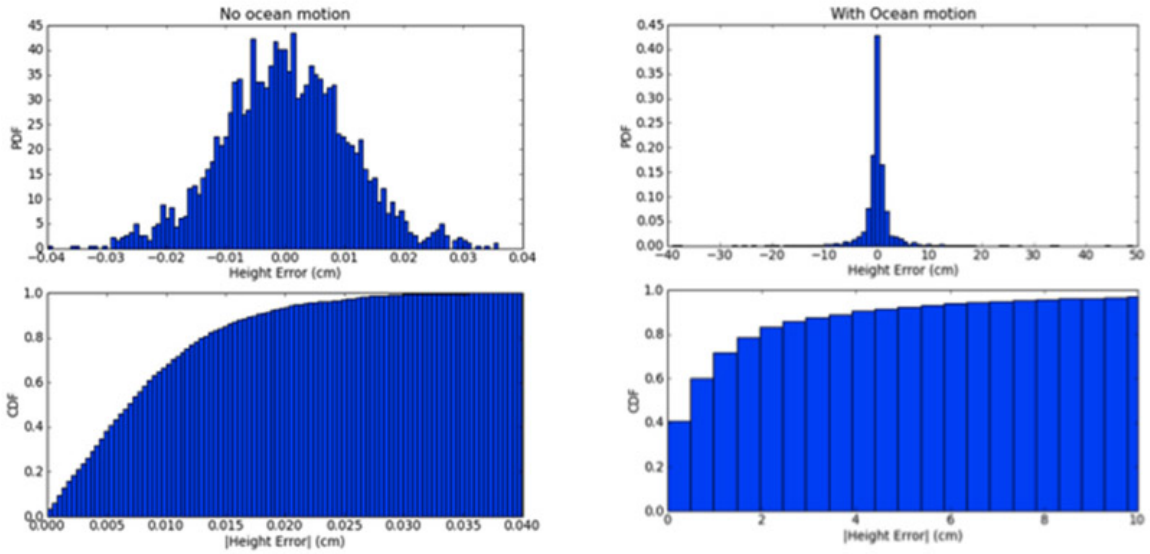

Figure 7.5-3. Probability density function (upper panels) and cumulative distribution function (lower panels) of height errors after correcting for unknown phase/roll errors in the case where there is ocean motion (left column) and in the case when the nominal 22-day orbit cross-over set is used (right column). In the case when no motion is present, almost all the errors are below 0.03 cm. When significant ocean motion is present, 68% of the errors are <1.5 cm, 80% of the errors are <2.0 cm, and 90% of the errors <5.0 cm.

The nominal orbit, on the other hand, will have a significantly degraded performance, which provides additional evidence for the benefits of the fast sampling phase for instrument calibration. The cross-over estimates for the nominal mission are still useful, however, when optimally merged with the data from the onboard gyro, using the known correlations and variances for gyro, phase, and sea surface height. These estimates will be used during the nominal mission to further reduce the dynamic variability of the roll/phase biases over both ocean and land. As an example of the benefits of using this cross-over information, or dynamic ocean calibration, for continuous dynamic calibration, Figure 7.5-4 presents the results of optimal merging ocean and gyro information to improve the roll correction over land significantly over the result that could be obtained using the gyro information alone. Significantly better results will be obtained over the ocean due to the density of cross-over points and the short alongtrack temporal separation between them (although meeting the mission error budget does not rely on this process).

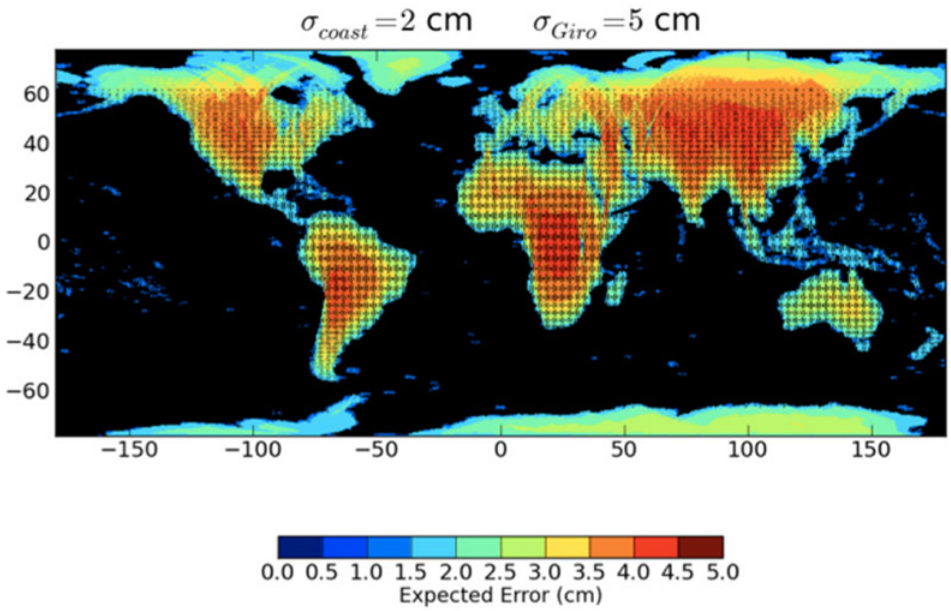

Figure 7.5-4. Expected residual phase/roll errors over land assuming that the ocean cross-over calibration can provide calibration accuracy of 2 cm (1 σ). The results are based on optimal interpolation of the coastal estimates, assuming a known gyro correlation function and a gyro roll uncertainty equivalent to 5 cm (1 σ) of roll error.

Static Range Biases

The problem of absolute range calibration is one of the most challenging for both conventional altimeters and radar interferometers. In fact, for all altimeter systems to date, ad hoc constant bias corrections have been required to ensure consistency for the measured sea surface.

Therefore, for SWOT, rather than requiring that the absolute range be measured precisely, we require that the mean sea surface produced be consistent with that produced by the historical TOPEX/Poseidon–Jason-1–Jason 2 climate data set, which has been cross-calibrated with data collections obtained simultaneously. Both the nadir altimeter and SWOT need to be calibrated to each other and to the reference altimeter data set, including the member of the Jason series operating at the time of the SWOT launch. (Note that if no such satellite exists, the process outlined below will still ensure that the SWOT altimeter and KaRIn are at least consistent with each other.)

As a first step, we cross-calibrate KaRIn and the nadir altimeter on SWOT. Rather than using the ascending-descending cross-overs, which are contaminated with residual errors due to temporal differences in wet troposphere and sea surface dynamics, we use along track data collected at the same time to obtain this calibration. The KaRIn sea surface height (SSH) field is optimally interpolated across the 20 km nadir gap, and the resulting elevations are compared to the altimeter height estimates. Since the ocean SSH spectrum decays quickly with decreasing spatial scale, one expects the contribution due

to interpolation errors to be zero-mean and significantly smaller than 1 cm, especially over regions of low mesoscale activity. Thus, by averaging the interpolated height difference over the entire fast-sampling phase, one obtains an average range difference that is significantly smaller than that required by the SWOT error budget. This process can be further optimized if the optional KaRIn nadir channel is implemented (by adding a nadir-looking receiver to the radiometer antenna), as this would allow direct comparisons of range delay at nadir, without the need for spatial interpolation.

Obtaining consistency with the reference altimeter constellation must rely on cross-over data, which is not collected simultaneously and which will be contaminated by wet troposphere and SSH dynamics. However, assuming slow drifts for the range bias for both systems, an appropriate accuracy can obtained by averaging the observed differences over a suitable time (months).

Radiometric Calibration

Radiometric calibration of SWOT will be obtained by comparing radar cross section for SWOT and AirSWOT when coincident measurements are available at the same set of incidence angles. From this initial calibration, a wind geophysical model function for wind speed as a function of incidence angle will be generated by comparing SWOT cross sections against weather model wind speeds, as is typically done for scatterometer systems (e.g., Wentz and Smith, 1999). The model function will be validated against additional weather model and buoy data, validating also the stability of the system gain.

7.5.5 Validation of SWOT Measurements

Validation of Long-Wavelength Height Errors

To validate the global performance of SWOT, and its consistency with the TOPEX/Poseidon–Jason long-wavelength climate data set, we utilize the cross-over data set obtained by using cross-overs between the KaRIn data, the SWOT altimeter, and the Jason-class operational altimeter operating at the time of the SWOT launch. The resulting global differences will be analyzed using spherical harmonic analysis, and the resulting spectrum will be compared against the long-wavelength spectral requirements for the ocean surface.

Validation of the Ocean Performance from 100 km to 1000 km

For scales larger than the ocean swath, the alongtrack spectra from the SWOT altimeter and KaRIn must coincide (within the noise floor capabilities of the altimeter). Therefore, the KaRIn alongtrack spectrum for these scales will be validated by direct comparison against the simultaneously measured altimeter spectrum. Spectral estimates will be performed for all cross-track pixels in the SWOT swath to validate the consistency of the KaRIn data and the effect of variations in the wet troposphere, EM bias, and ionospheric corrections that are made based on the nadir altimeter and radiometer measurements.

Validation of the Ocean Performance from 10 km to 100 km

The nadir altimeter is unable to resolve these scales due to its noise performance. Therefore, we rely on data collected by AirSWOT over 100 km×140 km regions at the time of SWOT data collection. Since the spectral high-frequency performance of AirSWOT is several orders of magnitude better than SWOT's, the critical high-frequency components of the spectrum can be validated with the required accuracy. In order to perform this spectral validation, the long wavelength components of both the SWOT and the AirSWOT data are removed, mitigating potential long-wavelength IMU-induced drifts in the AirSWOT data. The height differences are then analyzed using two-dimensional Fourier spectra, as well as separate spectra in the cross-track and alongtrack directions.

Validation of the Ocean Onboard Processor

During the fast sampling phase, high-resolution raw data will be transmitted to the ground for selected ocean regions, together with data processed by the onboard processor for the same regions. These data will be processed with hardware and "golden model" software simulators of the onboard processor to validate its performance. The data will also be compared against averaged data produced by an independent high-resolution interferometric processor as an independent validation of the onboard processing approach.

Validation of Surface Water Performance

SWOT's surface water performance will be validated with AirSWOT after the end of the fast sampling phase, since AirSWOT will need to be used daily over the ocean for the calibration and validation of SWOT during this time. The validation sites will be widely distributed to characterize the effects of uncalibrated phase/roll drift in the interior of continents, as well as a variety of lake and river sizes, and topography and vegetation types. In situ observations of lake and river level and slope will be obtained with GPS observations. The lake and river area will be measured using the AirSWOT near-infrared camera at the same time as a SWOT pass. In situ information will also be collected regarding vegetation distribution, height, and canopy characteristics [Leaf Area Index (LAI), canopy closure], as well a high-accuracy digital elevation model of the surrounding topography (for layover studies and calibration of AirSWOT). These measurements will enable the validation of SWOT elevation and surface water extent on a continental basis. This validation period will take place during the first six months to a year after the start of the nominal mission phase.

References

Farr, T., P. Rosen, E. Caro, R. Crippen, R. Duren, S. Hensley, M. Kobrick, M. Paller, E. Rodriguez, L. Roth, D. Seal, S. Shaffer, J. Shimada, J. Umland, M. Werner, M. Oskin, D. Burbank, and D. Alsdorf, 2007: The shuttle radar topography mission. Reviews of Geophysics, **45**, no. doi:10.1029/2005RG000183.

Fu, L., and E. Rodriguez, 2004: High-resolution measurement of ocean surface topography by radar interferometry for oceanographic and geophysical applications. The State of the Planet: Frontiers and Challenges in Geophysics, Vol. 19 of IUGG Geophysical Monograph, 209–224, International Union of Geodesy and Geophysics and the American Geophysical Union.

Krabill, W., W. Abdalati, E. Frederick, S. Manizade, C. Martin, J. Sonntag, R. Swift, R. Thomas, and J. Yungel, 2002: Aircraft laser altimetry measurement of elevation changes of the Greenland ice sheet: Technique and accuracy assessment. Journal of Geodynamics, **34**(3-4), 357–376.

Le Traon, P., F. Nadal, and N. Ducet, 1998: An improved mapping method of multisatellite altimeter data. Journal of Atmospheric and Oceanic Technology, **15**(2), 522–534.

Menemenlis, D., J. Campin, P. Heimbach, and et al., 2008: ECCO2: High resolution global ocean and sea ice data synthesis. Mercator Ocean Quarterly Newsletter, **31**.

Wentz, F., and D. Smith, 1999: A model function for the ocean-normalized radar cross section at 14 GHz derived from NSCAT observations. J. Geophys. Res., **104**(C5), 11,499–11,514.

8 ACRONYMS AND ABBREVIATIONS

Acronym	Definition
ACC	Antarctic Circumpolar Current
ADCP	Acoustic Doppler Current Profiler
AGCM	Atmospheric Global Climate Model
AGU	American Geophysical Union
AMOC	Atlantic Meridional Overturning Circulation
AMR	Advanced Microwave Radiometer
AMSR	Advanced Microwave Scanning Radiometer
ARM	Atmospheric Radiation Measurement
AVHRR	Advanced Very High Resolution Radiometer
CAL/VAL	Calibration and Validation
CHAMP	Challenging Minisatellite Payload
CIA	Central Intelligence Agency
CHL	Chlorophyll
CNES	Centre National d'Etudes Spatiales
COR	Centre d'Operations du Reseau (CNES Network Operations Center)
COTS	Commercial Off the Shelf
DEM	Digital Elevation Model
DESDynI	Deformation, Ecosystem Structure and Dynamics of Ice
DORIS	Doppler Orbitography and Radiopositioning Integrated by Satellite
DUACS	Developing Use of Altimetry for Climate Studies
ECCO	Estimating the Circulation and Climate of the Ocean
ECMWF	European Centre for Medium Range Weather Forecasts
EIK	Extended Interaction Klystron
EKE	Eddy Kinetic Energy
EKE/MKE	Eddy Kinetic Energy/Mean Kinetic Energy
EM	Electromagnetic
ENS-IPSL	Ecole Normale Supérieure-Institut Pierre Simon Laplace
ENVISAT	Environment Satellite (ESA)
ERS	European Remote-sensing Satellite
ESA	European Space Agency
ESTO	Earth Science and Technology Office
FY	Fiscal-year
GAP	Güneydoğu Anadolu Projesi (Turkish acronym)
GBM	Ganges-Brahmaputra-Meghna

GCM	Global Climate Model
GEOSAT	Geodetic Satellite
GFDL	Geophysical Fluid Dynamics Laboratory
GFO	Geosat Follow-On
GIA	Glacial Isostatic Adjustment
GIPSY	GNSS-Inferred Positioning System and Orbit Analysis Simulation Software
GLONASS	Global Navigation Satellite System (Russian)
GNSS	Global Navigation Satellite System
GOCE	Gravity field and steady-state Ocean Circulation Explorer (ESA)
GOCI	Geostationary Ocean Color Imager (Korean)
GOES	Geostationary Operational Environmental Satellite
GPS	Global Positioning System
GRACE	Gravity Recovery and Climate Experiment
HAMSR	High Altitude MMIC (Monolithic Microwave Integrated Circuit) Sounding Radiometer
HEC-RAS	Hydrologic Engineering Center-River Analysis System
HK	Housekeeping
HR	High-Resolution
HYCOM	Hybrid Coordinate Ocean Model
I&T	Integration and Test
ICESat	Ice, Cloud,and land Elevation Satellite
ICOLD	International Commission on Large Dams
IFREMER	French Research Institute for Exploration of the Sea
IFSAR	Interferometry Single Aperture Radar
IGRA	Integrated Global Radiosonde Archive
IMU	Inertial Motion Unit
IPCC	Intergovernmental Panel on Climate Change
IRB	International River Basin
ITRF	International Terrestrial Reference Frame
JERS	Japanese Earth Resources Satellite
JMR	Jason Microwave Radiometer
JPL	Jet Propulsion Laboratory
KaRIn	Ka-Band Radar Interferometer
KE	Kuroshio Extension
LC	Loop Current
LEGOS	Laboratoire d’Etudes en Géophysique et Océanographie Spatiales
LOHAFEX	LOHA is Hindi for iron, FEX stands for Fertilization Experiment

LPO	Laboratoire de Physique des Océans
LRA	Laser Retro-reflector Array
LSM	Land Surface Model
MDL	Minimum Description Length
ML	Mixed Layer
MLD	Mixed Layer Depth
MODIS	Moderate Resolution Imaging Spectroradiometer
MOS	Mission Operations System
MRF	Markov Random Field
MY	Multi-year
NASA	National Aeronautics and Space Administration
NCEP	National Center for Environmental Prediction
NCEP-NCAR	National Centers for Environmental Prediction–National Center for Atmospheric Research
NCODA	Navy Coupled Ocean Data Assimilation
NLOM	Naval Research Laboratory Layered Ocean Model
NNI	Near-Nadir Interferometry
NOAA	National Oceanic and Atmospheric Administration
NOGAPS	Navy Operational Global Atmospheric Prediction System
NP	New Production
NRT	Near Real Time
NWP	Numerical Weather Prediction
OSTM	Ocean Surface Topography Mission
PDO	Pacific Decadal Oscillation
PHYSAT	an algorithm developed to detect the major dominant phytoplankton groups from anomalies of the marine signal measured by ocean color satellites (Alvain, S., et al., 2008: Seasonal distribution and succession of dominant phytoplankton groups in the global ocean: A satellite view, Global Biogeochem. Cycles, **22**, GB3001, doi:10.1029/2007GB003154)
PI	Principal Investigator
POC	Payload Operations Center
POD	Precision Orbit Determination
PO.DAAC	Physical Oceanography Distributed Active Archive Center
POMME	Programme Ocean Multidisciplinaire Meso Echelle
POP	Parallel Ocean Program
PP	Primary Production
PTR	Point Target Response
QG	Quasigeostrophic
RaOb	Radiosonde

RF	Radiofrequency
rms	root mean square
RSS	Remote Sensing Solutions
SAR	Synthetic Apeture Radar
SCC	Spacecraft Control Center
SCICEX	Science Ice Exercise
SDS	Science Data System
SEC	South Equatorial Current
SGDR	Sensor Geophysical Data Record
SHA	Sea Height Anomaly
SHIPS	Statistical Hurricane Intensity Prediction Scheme
SQG	Surface Quasigeostrophic
SRTM	Shuttle Radar Topography Mission
SSC	Swedish Space Corporation
SSH	Sea Surface Height
SSR	Solid State Recorder
SST	Sea Surface Temperature
STCC	Subtropical Countercurrent
SW	Software
SWG	Science Working Group
SWH	Significant Wave Height
SWOT	Surface Water and Ocean Topography
TanDEM-X	TerraSAR-X add-on for Digital Elevation Measurement
TC	Tropical Cyclone
TCHP	Tropical Cyclone Heat Potential
TIN	Triangular Interpolated Network
TOPEX	(Ocean) Topography Experiment
T/P	TOPEX/Poseidon
UNESCO	United Nations Educational, Scientific and Cultural Organization
USGS	United States Geological Survey
WCD	World Commission on Dams
WG	Working Group
WSOA	Wide Swath Ocean Altimeter
XBT	eXpendable Bathy Thermograph